Errata

Page 28. Section 2.1.1.

Add after first sentence; ..... of heat sink. Rupture of the main coolant pipe could not be an initiating mechanism in a 'pool' type of reactor as opposed to a 'loop' type.

Page 61. Line 8:

Replace 'linear' by 'quadratic'.

Page 80. Last paragraph:

Replace 'encounterd' by 'encountered'.

Page 81. Line 10:

Replace 'determins' by 'determines'.

Page 93. Line 2:

Replace 'Menelly' by 'Meneley'.

Page 108. Line 17

Delete '(Meneley 1970)'

Insert after equation (5.2)

"The term representing the movement of the precursors has been neglected since the displacement is likely to be small, but this could be determined from the accompanying Lagrangian calculation".

Page 149. Line 18:

Replace 'change' by 'changes'.

COUPLED NEUTRONIC-HYDRODYNAMIC TREATMENT

OF FAST REACTOR DISASSEMBLY

MOHAMMAD AYUB MIR MSc MPhil DIC

A Thesis Submitted for the Degree of

Doctor of Philosophy,

Faculty of Engineering,

University of London

Nuclear Power Section,

Department of Mechanical Engineering,

Imperial College of Science and Technology

London

January 1981

To

Faisal , Zuhair and Basima.

ABSTRACT

The current approach to reactor safety is outlined and the hypothetical core disruptive accident in an LMFBR is discussed. The events leading to core disruption are described and some of the computer codes which model the various computational phases are summarized. This study essentially deals with modelling and studying the coupled neutronic-thermodynamic-hydrodynamic problem associated with the core disassembly. The physical and the mathematical models of the code BASIMA, developed as part of this study, are discussed. BASIMA is a point kinetic disassembly code which incorporates both the virtual motion (modified Bethe-Tait) and the real hydrodynamic motion models. In order to study the effect of spatial kinetics on the disassembly, a code NEST has also been developed. Various methods of solving the space dependent kinetics problem are also reviewed. NEST uses the alternating direction method. This code is incorporated in a disassembly code DISK which is in the test stage. The numerical results predicted by BASIMA agree with those by VENUS-II. The study with BASIMA confirms the importance of the void content in the reactor. However, it reveals that the sensitivity to the void content depends upon both the displacement reactivity model and the severity of the neutronic excursion. The study shows that when the void content is small the virtual motion model over-estimates the pressure at the centre and under-estimates the

final total energy release. However, the discrepancy in the results of the two models tends to disappear at high void fractions. Comparison of the dynamic flux distributions, calculated by NEST, with stationary flux distribution by the code MARK shows that the time derivative of the flux term acts effctively as an absorption term representing to a 1/v absorber. This absorption tends to soften the neutron energy spectrum in the case of a subcritical system and harden it in the supercritical case.

ACKNOWLEDGEMENTS

I wish to thank Dr A J H Goddard and Dr J L Head for their guidance during the course of this work and for arranging the financial support. Professor P J Grant has been very kind and helpful throughout my stay in Imperial College and I am thankful to him. I also like to thank Dr B Mitchell and Dr S Strachan for their invaluable suggestions during the preparation of this thesis and for the many useful discussions in the preceding years. I sincerely thank Mr F A Hussain, Mr M A Chaudhry and Mrs S Crompton for their help in checking this thesis.

The study was partly supported by the UK Nuclear Installations Inspectorate, to whom I extend my thanks. A lot of credit goes to the Pakistan Atomic Energy Commission for allowing me generous leave for the completion of my studies in the UK. Nevertheless, any conclusions reached in this work are entirely mine and do not necessrily portray the views held by either the UKNII or the PAEC.

I wish to express my gratitude to my parents, brothers and sisters for supporting me morally and encouraging me to complete my studies. Finally I thank my wife Nasreen and children Faisal, Zuhair and Basima for their inspiring affection and understanding.

CONTENTS

LIST OF SYMBOLS

A	Absorbtion and scattering Matrix
A_v, B_v, C_v and D_v	Experimental fitting constants in the expression for the saturated vapour pressure
a, b, c and d	Doppler coefficient parameters
a_f	Thermal Diffusivity of fuel
a_s	Thermal coefficient of expansion for the coolant
$a_{(i,i+1)}$	Coefficients coupling currents in nodes "i" and "i+1"
A_k and B_k	First and second order coefficients in the reactivity input function
B^n	Matrix operator resulting from space time differencing of the diffusion equation
β_i	Fraction of fission neutrons that appear in the ith delayed neutron group
β	Total fraction of delayed neutrons
$C_i(t)$	Concentration at time "t" of the precursors of the i^{th} type
C_{ijk}	The above concentration in node (j,k)
C_f	Specific heat of fuel
C_s	Specific heat of sodium
D	Diagonal matrix formed from matrix B
D_w	Flux convergence ratio
D_g	Neutron diffusion averaged over energy group "g"
D_{gjk}	Diffusion coefficient in group "g", node (j,k)
$D_{i,i+1}$	Diffusion coefficient at the interface "i" dividing the cells (i) and (i+1)

δ_x^2	Second difference operator in the x direction
δ_y^2	Second difference operator in the y direction
δ_{lm}	Kronecker delta
$\delta k_1(t)$	Input reactivity function
δk_2	Reactivity feedback due to the Doppler effect
δk_3	Reactivity feedback due to material displacement
δq	Total nuclear energy deposition during the n^{th} time interval
δQ_{jk}^n	Increment in the internal energy density of the cell (j,k) during the n^{th} time interval
Δt	Time interval
Δr	Radial mesh interval
Δz	Axial mesh interval
E	Internal energy density of the fuel (J/g)
E_m	Internal energy density fuel at the start of the melting transition
E_g	Specific internal energy of gaseous fuel
E_l	Specific internal energy of the saturated vapour
F	Fission column vector
ϕ	Scalar neutron flux vector
$\phi(r,E,t)$	Scalar neutron flux
ϕ_g	Flux averaged over energy group "g"
ϕ_{jk}^g	Flux in group 'g' node (j,k)
ϕ^n	Flux at the end of the n^{th} time interval
$\phi^{(i)}$	i^{th} iterate of the generalized flux vector
f_f	Fuel volume fraction
f_s	Sodium volume fraction
f_{ss}	SS volume fraction

g	g^{th} group of "G" neutron energy groups
f^{g}_{xj}	Resonance self shielding factor for energy group g, process x and material j
h	Coefficient of heat transfer from fuel to coolant
HCDA	Hypothetical Core Disruptive Accident
H_f	Heat of fusion of fuel (J /g)
H_n	Normalized power distribution
j	j^{th} interval of "J" radial mesh itervals
J_i^+	Partial neutron current in the positive normal direction at surface "i"
J_i^-	Partial neutron current in the negative normal direction at surface "i"
$J_{i,i+1}$	Net current at surface "i"
k	k^{th} interval of "K" axial mesh intervals
k_t	Thermal conductivity of fuel
k_0	Initial step reactivity input
$k_2^r(t)$	Contribution to the multiplication factor from region "r" , from Doppler effect, at time "t"
κ	Bulk modulus of expansion
L	Lower triangular component of matrix B
LMFBR	Liquid Metal Fast Breeder Reactor
LOA	Line Of Assurance
LOF	Loss Of Flow
l	index of summation over the fissile isotopes
λ_i	Decay constant of the i^{th} delayed neutron precursor
MFCI	Molten Fuel Coolant Interaction
M_f	Fuel mass in cell (j,k)
M_s	Sodium mass in cell (j,k)

M_{ss}	SS mass in a cell
NEST	Neutronics code with Energy-Space-Time dependence
$n(t)$	Reactor power at time t
p^n_{jk}	Total pressure in cell (j,k) during the n^{th} time interval
p	Pressure consistent with equation of state
p_v	Saturated vapour pressure
p_l	Liquid phase pressure
p'	Pressure due to compression and rarefaction of waves
$p_i(r,t)$	Pressure in the inner mesh cell of interface "i" at time t
$p_{i,i+1}$	Pressure at interface "i"
q	Viscous pressure
$\hat{R}$	Residual Matrix
r,z	Cylinderical coordinate of a point
r_j	Inner coordinate of all Eulerian mesh cells (j,k) ,k=1,...K
r_{jk}	Inner coordinate of the Lagrangian mesh cell (j,k)
r_p	Radius of fuel particle interacting with the coolant.
SS	Stainless Steel
ρ_f	Fuel density
ρ_s	Sodium density
ρ_{ss}	SS density
$\rho_i(t)$	Density of material i at time t
Σ_{ag}	Macroscopic absorbtion cross section in group g
Σ_{fg}	Macroscopic fission cross section in group g
Σ_{sg}	Macroscopic scattering cross section from group g

$\Sigma_{gg'}$	Macroscopic scattering cross section into group g from g′
σ^g_{xj}	Effective microscopic cross section in group g, for process x and material j
$\langle\sigma^g_{0j}\rangle$	Infinite dilution cross section averaged over a standard spectrum
T	Temperature
T_f	Fuel temperature
T_l	Fuel liquidus temperature
T_m	Fuel solidus temperature
T_s	Sodium temperature
T_{ss}	Stainless steel temperature
TOP	Transient Over Power
t^n	Time at the end of the n^{th} time interval
t_h	Time constant for heat transfer in fuel
t_m	Time constant for fuel fragmentation and mixing with the coolant during the MFCI
U	Upper triangular matrix component of B
u_{xx}	Second partial derivative of function "u" in the x direction
u_{yy}	Second partial derivative of function "u" in the y direction
u_t	Partial time derivative of function "u"
$u^{n+1/2}_{jk}$	Value of function "u" during the $n+1^{th}$ time interval, in the cell (j,k)
U^0_{Jk}	Initial energy density in mesh cell (j,k)
U^n_{jk}	Energy density in cell (j,k) at the end of the n^{th} time interval

V_T or V_{jk} Total volume of mesh cell (j,k)

V_{jk}^n Volume of cell (j,k) after the n^{th} interval

V_c Critical volume of fuel

V_s Specific volume

$V_r = V_s / V_c$ Reduced Specific volume of fuel

v_g Averaged velocity of neutrons in energy group "g"

$w(r,z)$ Material reactivity worth distribution

w_{gjk} Logarithmic ratio of the neutron fluxes from successive time intervals

W Weight matrix

w_r^* Normalized weight factors for Doppler contribution from region "r" of the reactor

χ^p Spectrum of emission energies of prompt neutrons

χ_i^d Spectrum of emission energies for the i^{th} precursor of delayed neutrons

z_k Lower axial coordinate of all Eulerian cells (j,k), j=1,...J

z_{jk} Lower axial coordinate of the mesh cell (j,k)

LIST OF TABLES

LIST OF FIGURES

CHAPTER ONE

INTRODUCTION

The discovery of fire marks an important milestone on the path of man's civilisation. The first evidence of its use dates back to the end of the ice age, 370000 years ago. The discovery of preserved remains of a recognizable human along with burnt bones scattered around him in a cave near Pekin, suggests that the 'Pekin man' knew the use of fire (Shapiro,1974). Since taming fire and harnessing it to do his work, man has developed an insatiable appetite for energy. The availability of cheap sources of fossil energy, rapid advances in technology and the breakthrough in human communications in the twentieth century have helped greatly in increasing this appetite and spreading it globally. The effective use of electrical power and its rate of growth are now considered to reflect a country's industrial activity and its modern standard of living. Man's needs are a complex mixture of the material, the intellectual and the spiritual aspects. Energy is the key to the first (Seaborg,1971).

Uptil the last decade, arguments in favour of nuclear power generation were mainly based on the depletion of fossil fuel reserves situation and economic feasibility. Lately however, the geographical location of the sources of fossil energy and the political and economic complexities involved in any interruptions in energy generation, have added significant weight in favour of

the nuclear generation of power. The latter is already making a significant contribution towards the demand of energy, in many countries. Fast breeder reactors, which produce more fissile fuel than they consume, have long been considered the next step in the evolution of commercial nuclear fission reactors. Breeders could in principle increase the utilization of fuel by fifty to a (one) hundred fold as compared with LWRs. At present LWRs are more economical than fast reactors, but the latter would become competitive with the former when the high cost of LWR fuel offsets the high capital cost of the breeders ($1700 million for FFTF and $2000 million for the CRBR). The economic assessment of the breeders was based on relatively optimistic assumptions in the past. A more recent assessment predicts that the economic incentive for introducing the breeders will develop more slowly than previously assumed (Spurgeon et al,1977). Nevertheless, some countries like France have gone ahead in building large breeders motivated by the politico-economic rather than the purely economic incentives.

However with the increasing use of the nuclear energy the concern for public safety has also increased. The world's first experience of nuclear energy in war and the insidious character of nuclear radiation, have naturally aroused strong public reactions, in many countries, to all operations involving radioactive materials. This first experience has created the fear that nuclear energy can destroy the physical basis of life and that radiation may damage irreparably the biological patrimony of mankind (Wallace and Dobzhansky, 1960).

Opposition to nuclear power spread to many liberal democracies in the seventies drawing strength from a substantial measure of international coordination (Williams, 1980). This healthy reaction is to some extent necessary to emphasize the social implications of technology in addition to the political and economic importance.

The design concept of nuclear reactors has gradually developed from the early stage when the aim was to demonstrate the feasibility of nuclear power, to the present state wnen public safety has become the main concern.

The major concern for nuclear power plant safety stems from the possibility, however remote, of the accidental release of radioactive materials in excess of permitted levels to the atmosphere. Much of the safety work on the Liquid Metal Fast Breeder Reactor (LMFBR) is based on the Hypothetical Core Disruptive Accident (HCDA). A fast reactor contains a large mass of fissile material which, in the case of an accident, can rearrange itself in a supercritical configuration, leading to gross melting of the core. This possibility, makes the containment requirements of the LMFBR somewhat distinct from those of thermal reactors.

The current safety approach to the HCDA in LMFBRs is based on the multibarrier containment concept. In the in-depth-defense approach, four defensive lines are envisaged (Alter and Berk,1979):

The first line of assurance (LOA) is the prevention of the

accident by bringing the probability of the occurance of the HCDA to very low levels ($\sim 10^{-6}$ /reactor year). This is assured by maintaining that the design and construction of the power plant must fulfil conservative safety and engineering standards.

If the first LOA fails and the HCDA occurs, then the second LOA functions to terminate the accident with limited core damage and to contain the consequences within the primary system.

In the case of failure of the second, the objective of the third is to control and limit the release of the radioactive materials to the atmosphere.

The objective of the final LOA is to reduce the radiological consequences of the accident to the public, in case the final containment is also breached.

The major part of this work is concerned with modelling some aspects of the second line of assurance. The aim is to model and study the response of the LMFBR to the Transient Over Power and Loss Of Flow accidents after the core configuration is lost and neutronic excursion is terminated by the hydrodynamic motion of the fluid core materials.

The analysis of the HCDA involves modelling the neutronics, thermodynamics and hydrodynamics of the various stages of the accident. These are commonly divided into the following phases: the predisassembly, the disassembly, the post accident heat removal, containment and the radiological consequences phases. These are described in chapter two which also reviews some of the reported computer methods.

Study of the disassembly forms the main aim of this work. A number of computer codes are used to model this phase, which include the VENUS family and EXTRA. Both use the point reactor kinetics model but the former assumes a real hydrodynamic motion of the disrupted core materials, whereas the latter is based on the Bethe-Tait model which assumes a virtual motion of the materials. Real motion codes are more powerful than the virtual motion codes, but the latter are faster and cheaper which makes them highly desirable for parametric studies of the disassembly phase. In order to make a quantitative assessment of the two models, a computer code BASIMA has been developed which incorporates both of the motion models. Chapter three summarizes the physical and the mathematical models used in this code.

The point kinetics model imposes limitations on the accuracy and the scope of application of the aforementioned codes. To overcome this problem a spatial kinetics code NEST has also been developed and incorporated in a disassembly code DISK. In Chapter four the various methods of solving the spatial kinetics problem are reviewed and chapter five explains the mathematical modelling of the NEST and DISK codes.

Results of the numerical calculations are presented and discussed in chapter six and the final chapter summarizes the conclusions of the study.

CHAPTER TWO

THE HYPOTHETICAL CORE DISRUPTIVE ACCIDENT

2.0 INTRODUCTION:

Work on LMFBR safety analysis is mostly related to the so called hypothetical core disruptive accident (HCDA). An important characteristic of a fast reactor is that the large mass of fuel is not arrayed in its most reactive configuration. If the fuel becomes rearranged in a more dense configuration, a positive gain of reactivity ensues. The problem of reactor safety analysis is essentially of a stochastic nature which is inherent in the initiation of the accident, as well as in the sequence of events. The latter form a spectrum of possible accident progression paths associated with each initiator. However the probablistic analysis cannot be used effectively without a strong deterministic base. In this approach, computational methods are developed to model the full spectrum of events. This chapter is limited to this mechanistic approach. It is divided into two sections in parallel with the two step approach to the deterministic assessment of the HCDA, which are:

a) the identification of the potential initiators and the various scenarios of the accident,

b) modelling the various paths of the accident.

2.1 MODES OF ACCIDENT INITIATION AND PROGRESSION

There are various ways in which an LMFBR accident can start and develop, but most of the work on HCDA is concentrated on two main postulated scenarios: the Loss Of Flow (LOF) and the Transient Over Power (TOP) accidents. Other modes include fuel pin failure propagation, loss of heat sink with (and without) scram failure and recriticality after the end of an initial neutronic excursion.

2.1.1 THE LOSS OF FLOW ACCIDENT:

Events leading to a LOF accident can be: coolant channel blockage, coolant pump failure, rupture of the main coolant pipe and the loss of heat sink.

The high heat rating of fast reactors implies that local temperatures rise very rapidly when coolant flow is interrupted during pump coast down. Sodium as coolant, is used at a temperature which is several hundred degrees lower than its saturation temperature (1155 K) at the low operational pressure in the primary system. It has a high surface tension, good conductivity and a low Prandtl number which means that the spatial temperature gradient at the surface of the fuel pin is small and any temperature increase is rapidly transmitted to the bulk of the coolant in a channel (Lewis 1977). Therefore most of the local sodium is heated before boiling starts near the surface of the fuel pin. The nucleation of the bubbles requires vapour pressure large enough to overcome the high surface tension of the medium. When this is satisfied the few bubbles that form expand to come into thermal equilibrium with the surrounding liquid and

in doing so, pressurize the whole channel. This action discourages the formation of further bubbles and tends to force the existing ones to coalesce into a single large bubble. This expanding bubble acts as a high pressure vapour slug which expels the remaining liquid sodium from the ends of the coolant channel. Thus the whole channel is voided within a few milliseconds of the coolant flow interruption (Fauske and Okrent,1977). The vapour bubble would relieve its pressure and condense allowing liquid sodium to reenter and give rise to a chugging motion.

Formation of vapour bubbles usually starts near the core upper blanket boundary , however, a low value of fuel to clad thermal resistance tends to shift the point of bubble nucleation towards the core center (MacFarlane et al,1966;1967). The appearance of void at the top may decrease reactivity in the beginning but as the entire channel starts to void, the reactivity would increase in competition with the Doppler reactivity feedback (Chan et al 1979a). The Doppler coefficient may itself reduce in magnitude due to the sodium voiding effect. After removal of sodium, some heat transfer from the fuel will continue due to the presence of a thin film of coolant which would vaporize rapidly and lead to fuel melting and cladding failure. If the cladding melts it may be relocated upwards by the streaming coolant vapour adding more reactivity to the system. However, if the sodium vapour velocity is not high enough to carry the molten cladding to the upper blanket region, the cladding would move downwards and cause lower blanket flow blockage (Chan et al 1979b). In addition to this, further increase in

reactivity can come from fuel slumping under gravity. The fuel compactive processes compete with the dispersive forces generated by the combined vapour pressures of fuel, stainless steel and coolant and the accumulated pressure of the fission product gases (Chan et al 1979a). During this process, temperature in the low power channels would also increase and may result in cladding failure and molten fuel coolant interaction. The resulting high pressure may expel the remaining coolant from the channel. This extended coolant removal in preferance to the fuel outwards motion would cause a rapid addition of reactivity and a sharp increase in power and result in the so called Loss-Of-Flow-Driven-Transient-Over-Power (LOF-Driven-TOP) accident. The severity of the accident in such a case can be expected to increase because of the higher rate of reactivity input.

2.1.2 THE TRANSIENT OVER POWER ACCIDENT:

A TOP accident may be initiated by a positive insertion of reactivity which results in a rapid increase in power and temperature of the fuel, while the coolant maintains its flow. The sources of reactivity addition can be: excessive control rod withdrawal, passage of entrained gas bubbles through the core or a seismic compaction of the core. The first may be simulated by a ramp function and the latter two cases by a step function reactivity insertion. Both these insertion mechanisms however, may be taken into account if sufficiently wide range of ramp rates are considered (Chan et al 1979a). The transient behaviour is strongly dependent upon the magnitude and the rate of reactivity insertion in addition to the state of the system at

the time of the transient initiation.

The events following a positive ramp reactivity insertion may proceed as follows: power increases while the coolant maintains flow, cladding and fuel heat up and the resulting Doppler reactivity feedback keeps the reactivity below prompt critical. The change in coolant density would tend to decrease the reactivity. With the increase in power and temperature the cladding may melt or rupture under the combined effect of mechanical and thermal loadings and release fission product gases. The coolant may start to boil before cladding has failed except in the case of very low ramp rates of reactivity insertion which involve longer time scales. If cladding fails the molten fuel ejected in the coolant stream may violently interact with it and result in additional reactivity insertion.

The location of the clad failure affects the course of the accident. The most likely place is above the core mid-plane where the temperature is at its highest (Marchaterre 1977). When the molten fuel is ejected into the coolant, it may be quenched and shattered and the particles swept away by the flowing coolant. This removal of fuel away from the core centre, may compensate the reactivity increase due to voiding or other processes and lead to a benign termination of the transient. On the other hand, if the failure occurs at the core mid-plane reactivity may be increased due to the motion of fuel within the fuel pin towards the fuel failure location. The consequences would be most serious if failure happens below the core midplane in which case the coolant flow may carry the ejected fuel particles towards the core midplane and result in larger insertion of reactivity (Lewis,1977).

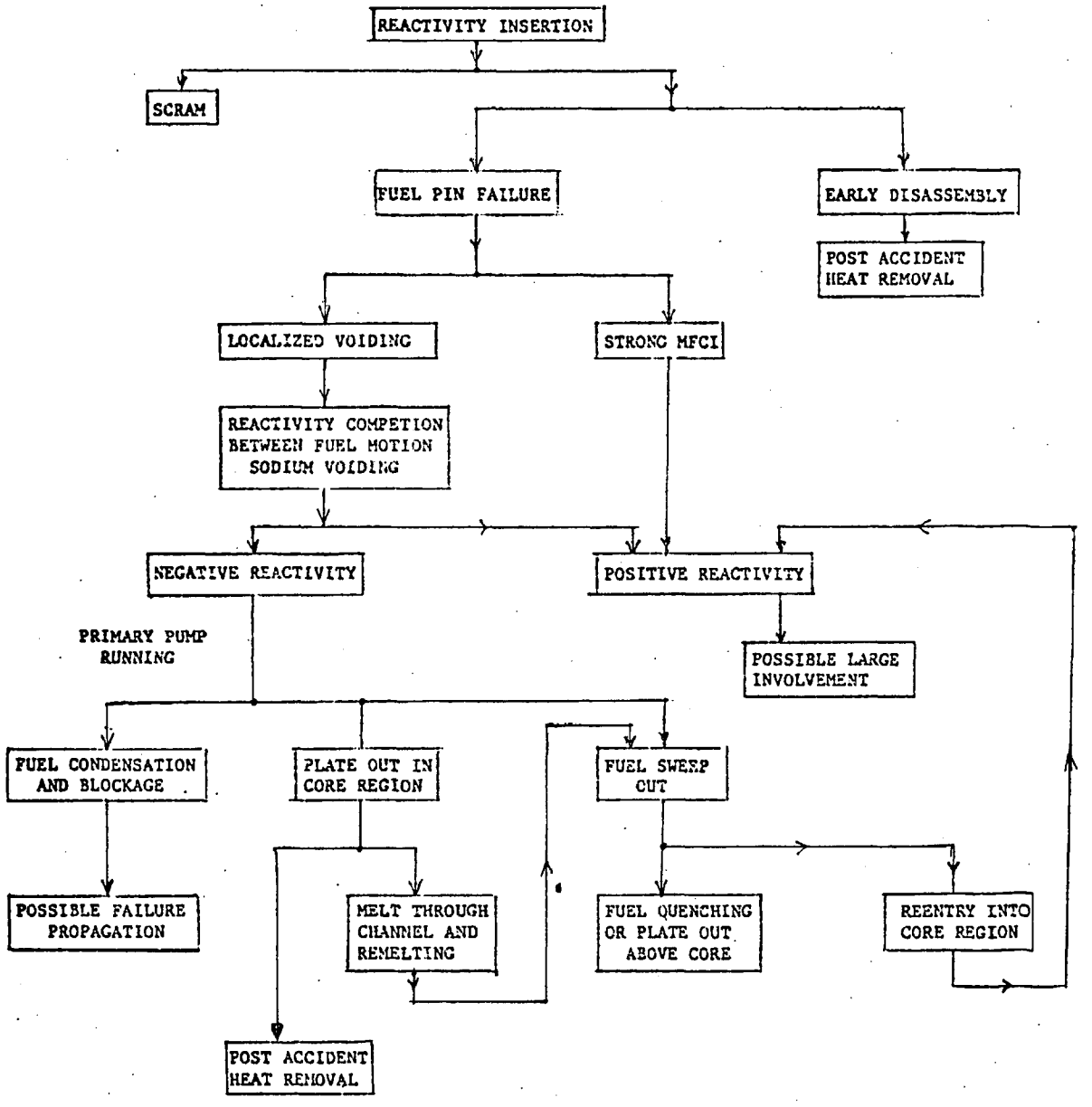

FIG-1 EVENT TREE FOR A TRANSIENT-OVER-POWER ACCIDENT

2.1.3 PROPAGATION OF FUEL PIN FAILURE:

The propagation of a local failure depends upon the response of subassemblies adjacent to the failed pin, to mechanical and thermal loadings generated by the failure. Compared to thermal and thermo-mechanical loads there are few reported investigations of strictly mechanical nature. These investigations include structural response of the subassembly to pressure pulses caused by local MFCIs and sudden releases of fission gases. The models and the parameters used in these investigations differ widely and so do the predicted failure criteria (Crawford et al 1975b). Therefore no explicit conclusions can be drawn about the response of subassembly structure to purely mechanical loads.

The effects of thermal and thermo-mechanical loads, on the other hand, have been more thoroughly investigated and reported. These loads can be caused by over enrichment of fuel, coolant channel blocking or the release of fission gases from a fuel pin.

2.1.3.1 Over Enrichment of Fuel:

Inaccurate loading of enriched fuel pellets in fuel pins, over enriched fuel pins in subassemblies or loading of high enrichment subassemblies in low enrichment zones, would all result in local over power transient and subsequent local failure. However enrichments greater than 130% of normal are required for an over powered fuel pin to produce significant quantities of molten fuel at pin centre line (Crawford et al 1975a).

2.1.3.2 Local Blockage in Fuel Bundles:

Any circulating debris in the primary coolant may block the coolant channel and cause pin failure. The blockage may be:

a) An insulating blockage of low conductivity material which may adhere to the fuel pin and impede local heat transfer from the surface of the pin. Such a blockage may be caused by dry sodium oxide or carbon resulting from the reaction of sodium with an organic material. Small blockages may lead to cladding failure but not to fuel melting .

b) A porous blockage (Kuzay 1979) may be formed by the limited accumulation of debris from a failed fuel pins. Such a blockage will impede the flow of coolant but no melting of fuel is expected for small blockages although cladding may fail and result in the release of fission gases which however, may dislodge the blockage and reallow unimpeded coolant flow.

c) Planar in-core blockage differs from the porous plugging in that the latter allows some coolant flow through itself, whereas the former does not. The coolant would start to boil if more than 20% of the fuel subassembly cross section is blocked with a planar blockage. However, no mechanism of such a blockage can be explicitly identified (Crawford et al 1976a).

d) In addition to the above three cases, blockages can be formed which have mixed characteristics. A possible source of such a blockage is the chemical reaction of the mixed oxide fuel with sodium in a partially failed pin forming

sodium-urano-plutonate. This compound has a considerablly lower density and therefore can lead to swelling of the fuel pin and coolant channel blocking (Rand 1974).

2.1.3.3 Fission Gas Release:

This can occur because of manufacturing defects in the pins and thermo-mechanical stresses during operation. A typical LMFBR fuel pin has an inventory of 2.5 g of fission gases which may attain a pressure of 60 bars after a burn up of 10 kWd/kg (Crawford et al 1975a). The release of high temperature and pressure gases from the fuel pin would produce thermal hydraulic transients which can damage adjacent subassemblies. The effect depends upon the quantity and speed of release.

a) Slow and moderate releases can produce thermal transients through gas jet impingement which would cause gas blanketing and coolant dryout around the point of release, flow starvation due to frictional pressure losses, flow stagnation and entrapment of gas bubbles in grid spacers and other obstructions.

b) Fast Fission Gas Release in addition to gas entrapment, can result in transient reversal of coolant flow and mechanical loads on pins. In a moderate gas release the thermal hydraulic perturbation lasts approximately as long as the gas continues to release, whereas a fast gas release can cause a severe coolant flow reversal lasting longer than the real release duration. The duration of the perturbation in this case may be long enough to allow adjacent pins cladding to be heated to the point of failure.

Experimental investigations show that for short periods of time, the cladding can withstand considerable high temperatures before failure. Therefore an optimistic conclusion may be drawn that failure propagation to several subassemblies adjacent to the accident-striken subassembly in which fuel has melted, is not expected to occur in a reactor operating at normal power and built with a sound engineering design (Marr et al 1976).

2.2 MODELLING OF THE ACCIDENT PATH

The core disruptive accident is a complex physical process which has both microscopic and macroscopic dimensions. The full analysis covers a wide spectrum of events: from steady state fuel behaviour to atmospheric dispersal of radioactive material release. Early attempts of LMFBR accident analysis started with the evaluation of maximum damage to the reactor containment system. This historic background and the different physical characteristics of the accident progression, have lead to the division of the LMFBR HCDA into the following analysis phases:

1. Initiating or predisassembly phase.
2. Disassembly phase.
3. Damage evaluation phase.
4. Post disassembly phase.
5. Post accident heat removal phase.
6. Analysis of the radiological consequences.

In addition to the predisassembly and disassembly phases a third phase is also sometimes defined and is known as the transition phase.

2.2.1 THE PREDISASSEMBLY PHASE:

This initiating phase analysis involves modelling the neutronic, thermodynamic and hydrodynamic behaviour of the LMFBR core from the state of local perturbation to one of the following states:

a) a benign energetic shut down with a coolable intact configuration

b) a gradual meltdown of the fuel and core structure, which leads to the transition phase.

c) or the onset of the disassembly phase when high vapour pressures start to disassemble the core physically.

The predisassembly phase analysis includes the following:

2.2.1.1 Fuel Mechanics and Failure Analysis:

This includes short- and long - time history of fuel restructuring, pore migration, heat transfer, migration of fission gas and its distribution.

Some of the codes which deal with steady and transient state pin failure, include: POROUS, PECT-2T, PECTCLAD (Walter and Padilla 1977), LIFE (Jankus and Weeks 1972) and SIEX (Walter et al 1974). Coolant flow calculations may be performed by using the COBRA family of codes. COBRA-IV (Walter and Padilla 1977) capabilities include: calculation of spatial distributions of temperature and coolant flow, modelling of coolant flow reversal, its recirculation, expulsion and subsequent reentry into the coolant channel.

2.2.1.2 Whole Core Analysis:

Whole core transient analysis includes modelling the response to the neutronic perturbation, sodium boiling and restructuring of molten fuel and cladding. Many large whole core codes, such as MELT and SAS families, have the capability of dealing with the full predisassembly phase including steady state fuel modelling. MELT-III (Walter et al 1974) was developed primarily for the TOP analysis but it has also, a limited capability of dealing with the LOF accident. It incorporates SIEX for fuel pin failure analysis and has a parametric model of molten fuel coolant interaction.

SAS-III (Marchaterre 1977) models both TOP and LOF accidents, moving liquid sodium film and multiple bubble sodium boiling. Other predisassembly codes include CAPRI, SURDYN and FRAX , which are grown up offsprings of MELT-II.

2.2.1.3 Recriticality:

In large reactors there exists the possibility of fuel reconfiguration after meltdown which leads to secondary or even tertiary criticality. The core design and geometry can significantly affect the pattern of molten fuel motion and its potential reconfiguration into a critical system. The fuel, after expulsion from the top of the core, may freeze in top reflector and the reactor may become subcritical. Later on however, it may remelt by the decay heat, reenter the core and result in positive insertion of reactivity and recriticality. The recriticality will depend upon the quantity and the velocity of the reentering fuel and whether it is falling under the force

of gravity alone or is pressure driven.

Other potential sources of reactivity insertion which may lead to recriticality are:

a) Motion of high enrichment fuel from the outer to the inner core.

b) Increased voiding of the remaining coolant from the core during and after an accident.

c) Removal of volatile neutron absorbers from the core by evaporation after meltdown.

The control subassemblies are the last parts to fail in the case of a meltdown and their pattern of failure and motion can significantly affect the path of an accident (Chan et al 1977). In the core region if the cladding melts before the fuel, heat can continue to radiate from the failed pins to the subassembly can walls. This heating, caused mostly by the outer row of fuel pins, would eventually affect wall failure. The melting of the can walls could expose the control subassembly to the radiative heat and would eventually lead to control rod subassembly and structure support failure and subsequent recriticality (Chan et al 1979).

2.2.2 THE TRANSITION PHASE:

Results of predisassembly phase calculations have shown that the consequences of even a meltdown could be accomodated (Walter and Padilla 1977). In mild transients the predisassembly phase may terminate in either a benign shutdown with a geometrically intact and coolable core or result in a slow boiling of the core which leads to a gradual melting of core structure (Marchatere et

al,1976). The slow boiling of the dispersed fuel and steel may end in a coolable configuration without resulting in recriticality or a large release of energy. It is commonly known as the transition phase because it describes the transition of the core from a state of intact fuel geometry, to a state where it behaves as a hydrodynamic fluid.

The accident scenario is as follows :

Low pressures associated with a mild accident are unable to disperse massively the molten fuel and terminate the excursion. The increased energy release melts the subassembly walls which mix with the fuel in the high power channels. Local axial dispersal of fuel causes neutronic shutdown and some fuel material to freeze and plug the axial ends. Decay heat causes boiling and further melting. More molten fuel may be ejected and lead ultimately to a dispersed coolable system (124).

Alternatively, a part of the molten cladding may be swept upwards by the streaming sodium vapours and a part may flow downwards. Both parts may freeze and block the axial removal of the fuel. With the increased energy, the boiling of steel and fuel spreads to other subassemblies. In the case of the FFTF reactor, about three full power seconds of energy are required to effect full core disruption, starting from the state where one fourth of it is disrupted. This bottling up of the core is more likely to occur in reactors with a small sodium void coefficient, such as the FFTF (Ottensen et al.,1976).

This phase is normally analysed by incorporating some of its aspects in either the predisassembly or the disassembly phase

calculations. Subassembly blockage and possible recriticality have been incorporated in the code SAS3A by including FUMO as a subroutine, whereas fuel steel boiling pool behaviour has been linked with the disassembly phase in FX2-POOL (Abramson,1977). SIMMER (Bell et al,1977) is an independent code which is capable of following a relatively long time history of a mild accident. In addition to the transition phase it can also cope with disassembly, extended core motion and recriticality if required. An Eulerian model has been used for the hydrodynamics and a transport theory model employed for the neutronics calculations.

2.2.3 THE DISASSEMBLY PHASE:

The original and now classical"order of magnitude" study of HCDA done by Bethe and Tait, treated the core material as a homogeneous hydrodynamic fluid in spherical geometry (Bethe and Tait 1956). They postulated that in the course of the accident, core compaction results in an increase in reactivity and power and consequently the high vapour pressures cause physical disassembly of the core and termination of the nuclear excursion.

The original Bethe-Tait model was improved subsequently by including Doppler effect, more realistic equations of state and a better neutronics model. Furthermore, the effect of shock waves was incorporated in addition to the capability of handling a two dimensional geometry (McCarthy et al, 1958; Nicholson,1962; Meyer et al 1967; Lee and Pigford 1972). In this approach actual motion of the core is not calculated explicitly and is also

referred to as the virtual motion model in contrast with the real motion model. The virtual motion codes are fast and cheap and still popular in spite of their limitations; examples include: MARS (Hirkawa 1967), AX-1 (Okrent et al 1959) and EXTRA (Edwards and Mather 1973).

In the real motion model, the governing partial differential equations are solved numerically and the displacement feedback calculated from actual motion of the core. VENUS (Sha and Hughes 1970) was the first code of this type and with its modified version VENUS-II (Jackson and Nicholson 1972) have been used as work horses for the disassembly calculations. KADIS (Schmuck,1978), developed in Germany, is another improved version of VENUS. These are two dimensional (r,z geometry) codes which use the Lagrangian model for the hydrodynamics and the point kinetics model for the neutronics calculations. The limitations of the point kinetics have been removed in FX2-VENUS II (Sha et al 1971) by using a quasi static model for the spatial kinetics. The deformation of the mesh, in the Lagrangian hydrodynamics model, gives rise to numerical errors which restrict the applicability of the codes to moderate distortions only. To overcome this limitation an Eulerian hydrodynamics model has been used in the modified version VENUS-III (Walter and Padilla 1977). Thus with FX2-VENUS III extended motion can also be dealt with. The SIMMER codes are primarily for transient phase calculations but disassembly can also be analysed. BASIMA, developed as part of the present work, includes both virtual and actual motion models and uses the point kinetic model for the neutronic calculations.

2.2.4 DAMAGE EVALUATION:

This phase of the HCDA analysis deals with the structural dynamics and the response of the reactor to mechanical and thermal loadings starting from the nuclear shut-down following disassembly of the core, to the point where the expanding core pressure drops to the ambient level and no more plastic work can be performed on the containment.

Early analysis of this problem was performed by uncoupled neutronic hydrodynamic methods. The fluid mechanics part was treated by an uncoupled two-step procedure (Belytschko 1977), in which:

a) fluid mechanics behaviour of the core is studied by treating the structural walls as rigid,

b) the pressure predicted in the first step generates response of the rigid structural walls.

This conservative approach can lead to over designing of some of the reactor components and has lead to the development of coupled hydraulic-structural codes for particular use in LMFBR containment analysis. These are in addition to other available codes like PISCES, HEMP, TOODY, WHAM, STEALTH and SADCAT (Belytchko 1977; Hancock 1977; Chang 1977) which were developed for general structural dynamics applications. REXCO was the first code developed specifically for LMFBR analysis. REXCO-HEP (Chang 1977) is a two dimensional Lagrangian code which copes with the hydrodynamics of the elastic and plastic deformations of

the core. The problem of excessive deformation of the Lagrangian mesh is removed by frequent rezoning of the mesh. ICECO (Zeuch,1979) is an Eulerian code which is capable of treating sodium flow through core support structure openings and other available paths. MICE (Chang 1977) is an extension of ICECO and is characterised by a multifield Eulerian hydrodynamic model. In this model, every thermodynamic state of each fluid is considered as a field. Different fluids are represented by different sets of fields. Each field is governed by its equations of state and motion but are coupled to each other through momentum exchange functions. MICE can cope with five such fields. These codes can analyse the response of the primary system to HCDA to the point of dynamic equilibrium of the system.

2.2.5 HEAT REMOVAL AND CONTAINMENT:

The TOP-HCDA could terminate with a small ejection of molten core debris outside the core but in the LOF-HCDA a large part of the core could melt down and consequently a substantial part of the molten debris could be ejected outside the core. Eventually some of the molten debris could move downwards and melt through the reactor vessel (Gluekler 1977). Thus even after a nuclear shut - down of the reactor, the thermodynamic and hydrodynamic behaviour remains important until it reaches a steady coolable state. The core debris history has to be followed in three locations :

a) within the reactor vessel,

b) within the cavity below the vessel,

c) within the concrete bed at the bottom.

Within the vessel, the heat removal is primarily through quenching in the coolant pool and fragmentation into particles which settle at the bottom surfaces. If the accumulated debris bed dries out, the increased temperature due to loss of cooling can result in vessel failure and downwards flow of the core debris.

Different concepts are used to contain the debris within or below the reactor vessel (Peckover,1973). The SNR-300 design includes a debris catcher tank made of depleted uranium dioxide, cooled by an amalgam of sodium and potasium. The current SUPER PHENIX design is based on a catch-tray concept which consists of a system of horizontal trays immersed in the primary system sodium to quench and fragment the molten debris.

The CRBR design relies on the inherent capabilities of a massive bed of uncooled concrete, which is expected to entomb the non-volatile debris (Glueckler 1977). The basic idea of this approach is based on the chemical reaction of molten sodium with concrete (Baker 1977). The water vapour and carbon dioxide released from the heated concrete react with sodium to form sodium carbonate and hydrogen. The silica react to form silicates. Sodium also reacts with steel and the resulting mixture of oxides, silicates, carbonates and other nonvolatile core materials are expected to settle down and form a layer between the concrete and the molten sodium. The latter would ultimately vaporize. Meanwhile, the molten debris would continue to expand and penetrate the concrete bed until heat equilibrium

is reached between the debris, concrete and the earth below when further penetration is expected to stop. In an alternative design of the CRBR the uncertainties of this concept are circumvented by replacing concrete with a thick bed of magnesia which has debris collection tanks at the top lined with alumina and interspaced with tantalum rods. These materials do not react with sodium and are mutually soluble with the molten debris and therefore are expected to result in a more efficient heat removal (Baker,1977).

The long term thermal and mechanical post accident response of the containment can be studied by using the code CASECO (Peak,1977). This code divides the reactor building into a number of cells and models the thermodynamic and the chemical conditions within the cells, sodium spillage, decay energy and leakage from the building to the atmosphere. The codes SPRAY, SOMIX and SOFIRE (Walter and Padilla 1977) model sodium pool fires and spray fires.

2.2.6 RADIOLOGICAL CONSEQUENCES:

The last line of assurance in the LMFBR safety analysis involves estimation of the exposure of the population at large to the radioactive pollutants released into the atmosphere. For this analysis, the estimation of the radiation source term is of prime importance. In a severe LMFBR accident, typical release fractions are of the following order (Marchaterre 1977):

Table-1

Inert gases	100%
Halogens	1-25%
Volatile solids	0.1-10%
Non volatile solids	0.01-10%

This source term composition does not take into account particle agglomeration and retention of radioactive materials within the sodium system. When sodium drops fall through the cell atmosphere of the heat transport system, they react exothermally with the debris and produce sodium combustion product aerosols (Morewitz 1977). The aerosol and condensation processes can considerably reduce the release of halogens and solids. The mechanics of aerosol transport and particle agglomeration inside the reactor containment structure are modelled in the code HAA-3 (Walter and Padilla 1977).

The development of down-wind plume formation, dispersal of radioactive material and potential exposure to the population can be calculated by conventional methods applicable to all reactors.

2.3 SUMMARY:

The deterministic analysis of the LMFBR accident has been summarized in this chapter. The various accident analysis phases namely, the predisassembly, the disassembly, the transition, damage evaluation, heat removal and containment have been explained. Some of the computer codes used for the study have also been reviewed.

CHAPTER THREE

PHYSICAL AND MATHEMATICAL MODELS

3.0 INTRODUCTION:

The primary aim of LMFBR disassemmbly phase deterministic analysis is the calculation of pressure and energy release in order to estimate potential damage to the reactor containment structure. This phase of the accident is traditionally assumed to start when the core geometry is nearly lost and to end when the power falls a few decades below the peak power. Depending upon the severity of the accident and the initial physical conditions of the reactor, the time scales involved in this phase range from a few milliseconds to a fraction of a millisecond. The space-time dependent solution of this problem involves neutronic, thermodynamic and hydrodynamic calculations. These three aspects are closely coupled and for accurate results, full iteration during each numerical time step is desirable. However, some degree of decoupling has to be incorporated to obtain feasible numerical solutions. For an efficient solution, the iteration in the codes BASIMA and DISK involves only the thermodynamics and hydrodynamics of the problem without significant loss of accuracy. The neutronics aspects have been modelled in two distinct ways:

a) In the point-kinetic model, the thermodynamic change are transmitted via the disassembly reactivity feedback and the hydrodynamic changes via the motion feedback reactivity

b) In the spatial kinetics model the thermal effects are

incorporated in the neutronics compartment, by modifying the effective microscopic cross - sections of the reactor materials. The hydrodynamic effect is modelled by modifying the atomic number densities, thereby affecting spatial and spectral shape of the neutron flux with time. This model will be discussed in chapter five in more detail.

This chapter is divided into three sections which respectively, deal with the physical aspects, the mathematical models and the computational scheme involved in the BASIMA code. In the first section, some of the physical aspects related to the neutronics, thermodynamics and the hydrodynamics of the problem are discussed. These include reactivity feedback mechanisms arising from Doppler and sodium void effects, initial distribution and filling of void spaces in the fuel pins, interaction of molten fuel with the coolant and the selection of the coordinate system for the hydrodynamic calculations. The second section deals with the mathematical formulations and is divided further into the neutronic thermodynamic and hydrodynamic compartments. The last section explains the computational scheme of BASIMA. The discussion here primarily applies to the point kinetics disassembly model, but has many features in common with the disassembly with the space dependent kinetics modelled in DISK.

3.1 PHYSICAL ASPECTS OF LMFBR DISASSEMBLY:

The severity of the accident depends upon the initiating mechanism and the various time dependent constraints, where the

latter ultimately terminate the modelled nuclear excursion. In mathematical terms, the former may be identified with the input reactivity function and the latter with the associated reactivity feedback functions. In the LMFBR disassembly, reactivity feedback processes arise from:

i) Doppler effect,

ii) Sodium void effect,

iii) Thermal expansion and motion of the core material.

In the point kinetics disassembly code BASIMA, the reactivity effect of sodium voiding is assumed to be included in the driving input reactivity function, which is based on predisassembly calculations. The associated thermodynamic and hydrodynamic effects are taken into account by explicitly calculating the Doppler and displacement reactivity feedback. In the spatial kinetics disassembly code DISK, the reactivity effects of voiding are automatically taken into account by modifying the reaction rates in both space and time.

3.1.1 Doppler Effect:

The Doppler reactivity feedback in fast reactors arises from the effect of self shielding on fission and absorption neutron cross-section resonances and their broadening by thermal agitation of the nuclei. The overall effect is positive or negative depending upon the interaction of competing productive and parasitic processes.

The variation of cross-sections with temperature becomes very small at high energies. In the materials of interest in fast reactors, the resonances appear in the intermediate region of the

neutron spectrum, almost entirely below 25 KeV (Hummel and Okrent, The dominant contribution in U-238 arises from the resonances around 1 keV ; in Pu-239 lower energies are more important where self shielding is stronger and in Iron the effect arises from the 1.17 keV resonance.

In small fast reactors, such as EBR-I and EBR-II, the spectrum is hard with a mean neutron energy near 0.1 MeV. The contribution from the mainly U-235 fuel is positive and very small, being less than $10^{-6}/K$ (Hetrick,1971).

In large reactors which have high fertile to fissile material ratio, the effect is negative (order of -10^{-5}) and plays a significant part in reactor safety.

The Doppler effect is also sensitive to the ratios of fuel to sodium and fuel to structural material. Complete voiding of sodium, constituting 50 vol%, in a ceramic - fueled reactor has been reported to reduce the Doppler coefficient by a factor of two. Replacement of sodium with an equal volume of stainless steel tends to soften the spectrum and increase the Doppler coefficient slightly. Use of structural materials other than SS may have undesireable safety aspects. For example, replacing it with niobium may decrease the Doppler effect by a factor of 10 (Bhide and Hummel,1962).

The Doppler coefficient tends to decrease in magnitude with temperature. This temperature variation is sensitive to self overlap of resonances of the fertile material, predominantly in the energy range of 10-50 KeV. The overall behaviour of the Doppler coefficient therefore depends upon the combined effect of

resonance self shielding, self overlapping and the fertile to fissile material ratio. The resonance overlap does not change cross sections by more than 30%, whereas self shielding may reduce the infinite dilution cross sections by a factor of 5 (Hummel and Okrent 1970). When self shielding of resonances is low, the variation of effective cross sections with temperature $\frac{d\sigma}{dT}$, which is proportional to the Doppler coefficient $\frac{dk}{dT}$, behaves as $T^{-3/2}$. As the self shielding becomes stronger, the behaviour changes from T^{-1} to $T^{-1/2}$ and ultimately becomes constant when self shielding becomes strong.

The variation of the Doppler coefficient with the energy of the fertile material resonances also shows a similar pattern. The behavior varies from $T^{-3/2}$ at high energies to a constant value at very low energies. In small fast reactors with high enrichment fuel, the Doppler coefficient behaves as $T^{-3/2}$ since the spectrum is hard, whereas in large oxide fueled fast reactors the coefficient varies as T^{-1}, because the spectrum is softer, the ratio of fertile to fissile material is higher and the self shielding of the resonaces is stronger. The Doppler coefficient of thermal reactors is based on a $T^{-1/2}$ law. In this case the low lying resonances become relatively more important for Doppler effect than in the fast reactor case. (Hetrick,1971).

The code BASIMA, models Doppler coefficient in the general form:

$$\frac{dk}{dT} = a\,T^{-3/2} + b\,T^{-1} + c\,T^{d-1} \qquad (3.1)$$

where: a,b,c and d are constants. However, in the calculations

reported in chapter six, for the FFTF reactor model, a simple T^{-1} behavior of the Doppler coefficient has been assumed (Jackson and Nicholson,1972).

3.1.2 Sodium Void Effect

The sodium void reactivity feedback arises from the combined effect of the physical processes of neutron capture, leakage, and spectral changes.

The capture component is due to change in the macroscopic capture cross-section of sodium. Removal of sodium reduces neutron absorption and so could cause an increase in reactivity.

The leakage component arises from the change in the macroscopic transport cross section of the reactor. Sodium removal enhances neutron leakage and so tends to reduce reactivity.

The spectral component of the void reactivity coefficient, is caused by the change in the elastic and inelastic scattering cross sections of the reactor. Removal of sodium implies reduced scattering of high energy neutrons and a hardening of the spectrum (48). Reduction in neutron scattering also increases self shielding of resonances of the heavy nuclei thereby reducing their effective cross-sections and modifying the reactivity (Teague 1977). The spectral hardening also results in a reduction in the magnitude of the Doppler coefficient. The contribution to Doppler coefficient from capture, leakage and scattering processes are affected by the size and shape of the reactor core and by the actual location of any voiding.

The capture component arises mainly from the 2.85 keV sodium

scattering resonance and is therefor less effective in the hard spectrum of small high-enrichment fuel reactors. In large reactors, the high fertile to fissile material ratio softens the spectrum and therefore increases the importance of capture and spectral components in the sodium void coefficient.

The leakage component is more important in small reactors because of high surface area to volume ratio. In such a reactor, total loss of sodium may produce net reduction in reactivity, whereas in a large reactor positive reactivity feedback could be expected, provided the core is not highly pancaked. Expulsion of sodium near the edge of the reactor would primarily affect the leakage, while expulsion from the central region would preferentially modify the capture and spectral components (48).

In BASIMA the reactivity effect of sodium voiding is assumed to be included in the input reactivity worth distribution data, obtained from predisassembly computations. On the other hand in the spatial kinetics disassembly code DISK, the sodium void effect is implicitly taken into account by modifying the atomic number densities.

3.1.3 Molten Fuel Coolant Interaction (MFCI):

Mixing of molten fuel with liquid coolant in an LMFBR is considered to be a potential hazard in both the fuel element failure propagation and disassembly analysis studies. The MFCI affects the transient in two ways:

a) In a local MFCI the high pressure pulse generated by the interaction would mechanically load the subassembly structure

and may lead to propagation of local failures to other subassemblies. In the predisassembly phase local MFCI may cause rapid expulsion of sodium and large increase in reactivity.

b) During the disassembly phase, MFCI may generate high pressure pulses which can result in rapid disassembly of the core. Although the total generation of energy may decrease due to rapid disassembly of the core, the shock waves generated by the high pressures have a high potential for producing mechanical damage.

The mechanism of MFCI and its effects on the severity of the accident are still open questions. The central issue in any MFCI model is the estimation of heat transfer rate from fuel to the coolant (Caldarolla 1972) and the resulting mechanical work. Based on fundamental thermodynamic principles, early estimates showed that upto 30% of the thermal energy of the molten fuel could be converted into mechanical work (Hicks and Menzies 1965). Such magnitudes of energetic interaction can cause considerable structural damage. Later research in this field, aimed at estimating more practical limits of the mechanical work, has tended to show that large scale explosive interactions are unlikely to occur. This is based on the hypothesis that the mechanism of explosive vapour generation requires very rapid fuel to coolant heat transfer which can only happen if the fuel is finely divided and comes into intimate contact with the coolant. According to this view , fine mixing of hot and cold liquids

requires spontaneous nucleation on contact and that, for the mixed-oxide-fuel-sodium system, the contact temperature is well below the nucleation temperature for sodium (Fauske,1977). Moreover the growth of the vapour film between the two liquids would also impair heat transfer (Teague 1977) and ultimately reduce the explosive energy. Some workers (Board 1974;Board et al,1975) take the view that upon contact with the coolant the surface of the fuel droplets may freeze but crack later, under the high pressure of the liquid fuel inside the droplet. This would lead to the shattering of the large fuel droplet and effect fine mixing of the two fluids. According to this view, the spontaneous nucleation requirement determines only the initial conditions for the development of the vapour explosion, and is not in itself the source of the violent interaction and therefore, irrelevant to the process of vapour explosion development.

The MFCI, nevertheless, has many complexities which may be influenced not only by the physical properties of interacting materials but also by their surroundings. In the reactor environment, the presence of fission product gases, entrained gas bubbles and solid materials in the flowing coolant is expected to promote boiling before homogeneous nucleation can take place in bulk sodium. If homogeneous nucleation is demonstrated to be necessary for explosive interactions, then a sustained MFCI in the reactor environment would be considerd only a remote possibility (Fauske,1973 ;1977). However, this has not been shown to be the case, so in general, vapour explosions may not be ruled out.

3.1.4 Initial Void Space:

The initial void space distribution has a marked affect on the behaviour of temperature, pressure and the total energy generation during the disassembly of the core. This void consists of the voidage due to the porosity of the fuel, boiling in the subassembly and the void due to the gas plenum. The void associated with the porosity of the fuel depends upon the spatial distributions of fuel temperature and power and their histories (O'Dell,1972).

When a central void is present in the fuel pin, the maximum temperature occurs around the periphery of the central void. In the case of a mild accident, the fuel around the pin centre would melt and flow down the void to the bottom of the pin and there melt through the cladding. In strong transients on the other hand, since melting progresses rapidly and the molten fuel expands in volume by about 10%, it would fill the central gap before it could flow under gravity. The molten fuel would ultimately flow through the cracks caused by thermal stress in the fuel and come into direct contact with the cladding and affect its failure (Lewis,1977).

To investigate the effects of void distribution three models of initial void addition have been included in BASIMA and DISK codes. In the first model, sodium void fraction is reduced uniformly in each region of the reactor and made available for fuel expansion. The sodium mass in each cell is modified accordingly. In the second model, a spatially nonuniform void

fraction is added which has a shape similar to the power distribution function. In the third model, the nonuniform void addition model is such that the fuel on expansion completely fills the voidage when it reaches a specified temperature.

In all the three cases, this void creation is in addition to the original void calculated on the basis of coolant-channel design specifications. The former type is referred to here as additional void and the latter as the design void. In the design voiding the composition of materials within the mesh cells of a particular reactor region remains uniform; whereas in the additional void model, since the voidage is created by the initial removal of the coolant, the material composition differ spatially throughout the reactor. Therefore, the path of the accident is expected to be different in the two models. The separate filling of the design and the additional void spaces allows a number of optional ways to fill the initial voidage. The additional void is allowed to be consumed instantaneously but the design void may be filled at a prespecified rate. In the absence of any void in a mesh cell, a small increase in temperature, would expand the fuel and tend to generate a single phase state pressure. The resulting high pressure gradients would accelerate the materials towards the low pressure cells and thus lead to early disassembly of the core. In one option, void filling is switched on when a single phase state is encountered; however, the single phase is suppressed until the void is completely consumed by the expanding fuel.

3.1.5 Coordinate System Selection:

The high pressures generated during and after the disassembly of the core, could potentially deliver several hundred megajoules of mechanical work, depending upon the severity of the accident and the size of the reactor (Teague,1977). Disassembly of such a high magnitude may generate pressure waves in the core similar to mild shocks which result in high material velocities. In three dimensional analysis these are represented by surfaces (or curves in 2-D analysis), across which densities, pressures and velocities change discontinuously. Physically, the shock wave is not a discontinuity, but a thin layer, across which variables change so rapidly, that strict continuum analysis becomes invalid. Mathematically however, the shock may be treated as a discontinuity across which Rankine-Hugonoit conditions of mass, momentum and energy conservation hold (Malvern 1969).

In a numerical treatment, the physical continuum may be discretized by replacing it with a group of meshes. If the physical behaviour is followed at a fixed time-invariant mesh point, the mesh is called Eulerian; if the mesh point is associated with material particles and moves with the material, the mesh is called Lagrangian.

In a Lagrangian coordinate system, the path of material discontinuities are known since the mesh distorts with motion of the discontinuity. The mesh may be chosen so that the discontinuity lies always at a fixed position within a mesh cell. The propagation of shock waves can also be best treated in the Lagrangian system. However the distortion of the grid increases the problems of accurate analysis, which may be partially

remedied by frequent rezoning of the distorted grid (Hancock 1977).

The Eulerian system on the other hand, may be more suitable for modelling mild excursions and extended core motion, where material motion may become more important than pressure wave propagation.

3.2 MATHEMATICAL MODELS

In this section the formulation of the neutronic, thermodynamic and hydrodynamic aspects are briefly presented.

3.2.1 Neutronics:

The various methods of solution of the neutron diffusion equations are discussed in chapter four; in this section therefore, only the point kinetic equations and some of the feedback models are presented.

3.2.1.1 The Point Kinetics Equations:

The time dependent flux distribution $\Phi(r,t)$ is assumed to be separable into a shape function $\phi(r)$ and a time function $n(t)$:

$$\Phi_g(r,t) = \phi_g(r)\, n(t) \tag{3.3}$$

When the space function is normalised to unity, $n(t)$ which is proportional to the total reactor power, satisfies the point kinetics equations (Ash 1979):

$$\left.\begin{aligned} \frac{dn}{dT} &= \frac{\rho^* - \beta}{\Lambda}\, n + \sum_i \lambda_i\, C_i \qquad (3.4) \\ \frac{dC_i}{dt} &= \frac{\beta_i}{\Lambda}\, n - \lambda_i\, C_i \qquad (3.5) \end{aligned}\right\} \quad i = 1, \ldots\ I$$

where,

the reactivity $\rho^*(t)$ is given by:

$$\rho^*(t) = \delta k(t) / (1 + \delta k(t)) \tag{3.6}$$

and the excess multiplication factor $\delta k(t)$ as the sum of the input and various feedback functions:

$$\delta k(t) = \delta k_1(t) + \delta k_2(t) + \delta k_3(t) \tag{3.7}$$

The driving input reactivity function $\delta k_1(t)$, is assumed to be a linear function of time:

$$\begin{aligned} \delta k_1(t) &= \delta k_0 + A_k t + B_k t^2 \qquad t < t_s \\ &= \delta k_0 + A_k t_s + B_k t_s^2 \qquad t > t_s \end{aligned} \tag{3.8}$$

where δk, A_k, B_k and t_s are input parameters,
$\delta k_2(t)$ and $\delta k_3(t)$ represent feedback functions due to Doppler effect and material displacement respectively.

In the space-dependent neutronics disassembly code DISK the Doppler effect is taken into account (see chapter five) by modifying the effective nuclear cross-sections of the materials; the motion feedback by modifying the material densities in the Eulerian system; the input reactivity function by assuming ν, the number of neutrons emitted per fission, to be a function of time $\nu(t)$ similar in form to equation (3.8).

The explicit feedback functions described in the next sections apply only to the disassembly code BASIMA, which is based on the point kinetics model.

3.2.1.2 Doppler Reactivity Feedback:

The Doppler coefficient is assumed to have a general form which takes into account all the cases mentioned in section 3.1.1 (Sha and Hughs 1970):

$$\frac{dk(t)}{dT} = a\, T^{-3/2}(t) + b\, T^{-1}(t) + c\, T^{d-1}(t) \qquad (3.1)$$

where

a,b,c,d are input parameters

The contribution to the multiplication factor from a region r of the reactor, can be written as:

$$k_2^r(t) = -\, 2a\, T^{-1/2}(t) + b\, \ln T(t) + \frac{c}{d}\, T^d(t) + \text{const} \qquad (3.9)$$

The overall Doppler feedback is estimated by summing the weighted regional components:

$$\delta k_2(t) = \sum_r \{\, k_2^r(t) - k_2^r(t_0) \,\}\, w_r^* \qquad (3.10)$$

where w_r^*s are normalized regional weight factors.

3.2.2 THERMODYNAMICS:

When molten fuel-coolant interaction is not initiated, heat transfer from the fuel is ignored. However, during a time interval, the internal energy density of the fluid fuel within a control volume, is assumed to be modified by the nuclear energy increment and the mechanical transfer of energy, to or from the volume, by its compression or expansion. The equation of state, in association with the energy balance, supply densities, pressures and temperatures of the fuels. Since the prime purpose of the code was to study the effect of the hydrodynamic motion model, the pressure of fission product gases in the irradiated

fuel, has not been included. The MFCI model was incorporated so that the effect of localised voiding of the coolant channels could be studied.

3.2.2.1 Equations of State:

Since the fuel is the primary source of pressure generation, it is treated using a detailed equation of state with sodium and steel densities estimated from their compressiblity relationships. Heat transfer from fuel is neglected except when it interacts physically with the coolant. In the last case, the sodium equation of state is used to calculate its own pressure.

The equations of state are in general, functions of the internal energy (or temperature) and density of materials. For fuel it can be written as:

$$P(t) = F_1(E(t),\rho_f(t)) = F_2(T(t),\rho_f(t)) \qquad (3.11)$$

The fuel density ρ_f within a control volume is estimated by assuming the volume to be partitioned among the various components and that it occupies the volume unoccupied by other materials and the void space (Sha and Hughs 1970):

$$\rho_f = M_f \,/\, \left(V_T - \frac{M_s}{\rho_s} - \frac{M_{ss}}{\rho_{ss}} - f_v V_T \right) \qquad (3.12)$$

where the the void fraction f_v is given by equation (3.1) and the densities of sodium and SS are related to the local pressure by:

$$\rho_i(t) = \rho_i(0) \{1 + (\kappa_{1i}/\kappa_{0i}) P\}^{1/\kappa_{1i}} \qquad (3.13)$$

$i = 1,2$

where

i = 1 represents sodium

i = 2 represents SS

$\rho_i(t)$ = density at pressure P(t)

$\rho_i(0)$ = the initial density; k_{0i} and k_{1i} are coefficients in the linear algebraic relationship for the bulk modulus of expansion:

$$\kappa_i = \rho \frac{dP}{d\rho} \tag{3.14a}$$

$$= \kappa_{0i} + \kappa_{1i} P \tag{3.14b}$$

The temperature dependence of these physical coefficients is given in appendix-A.

Two optional equations of state for the fuel have been included in BASIMA: the ANL and the UKAEA equation of state. The first equation is an analytical fit based on Menzies critical data for Uranium dioxide (and assumed to be valid for the mixed Plutonium-Uranium oxide fuel) (Jackson and Nicholson 1972).

Table-2

Critical Constants Of Uranium Dioxide

P_c	2000 atm
T_c	8000 K
V_c	90 cm^3/mol

The ANL equation consists of the original two-phase state equation developed by UKAEA in the form:

$$p_v = A_v \exp (B_v + C_v T + D_v \ln T) \qquad (3.15)$$

and modified to take better account of the density dependence of pressure in the range of 7.5 to 3 g/cm^3 and to provide better extrapolation below the critical density (3 g/cm^3 for UO_2)

The current UKAEA equation of state is in the form of tabulated pressure and temperature values versus the internal energy of the material for different specific volumes. The high energy part of the equation has been obtained by the application of the principle of corresponding states and is based on the data derived by Booth (Allen et al,1974 ;Skidmore and Morris 1962).

In the two phase state, the tabulated values of pressure and temperature conform to the Classius-Clapeyron equation:

$$\frac{dP}{dT} = \frac{P}{T} + \frac{(E_g - E_l)}{(V_g - V_l)} \frac{1}{T} \qquad (3.16)$$

where V_g and V_l are specific volumes of gas and saturated vapour; E_g and E_l the corresponding internal energies.

In the liquid state the behaviour is described by a Grüneisen type equation of state:

$$P = P_r(V) + \frac{\Gamma(V)}{V} (E - E_r(V)) \qquad (3.17)$$

where

$$\Gamma(V) = V\left(\frac{\partial P}{\partial E}\right)_V \qquad (3.18)$$

and $P_r(V)$, $E_r(V)$ and $\Gamma(V)$ are tabulated functions of the specific volume of the materials. The ANL equation of state is shown in figures 2 and 3.

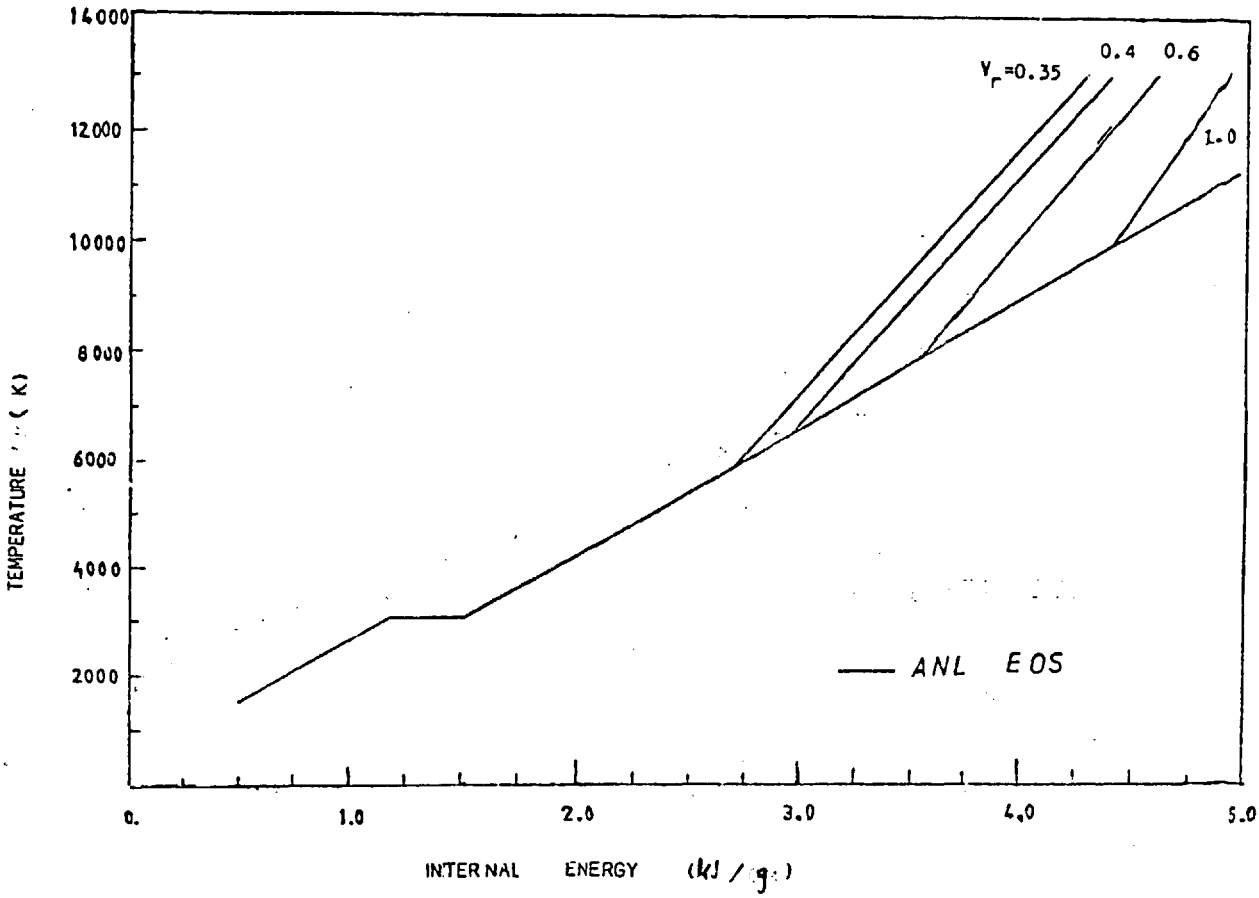

FIG-2 ENERGY TEMPERATURE RELATIONSHIP

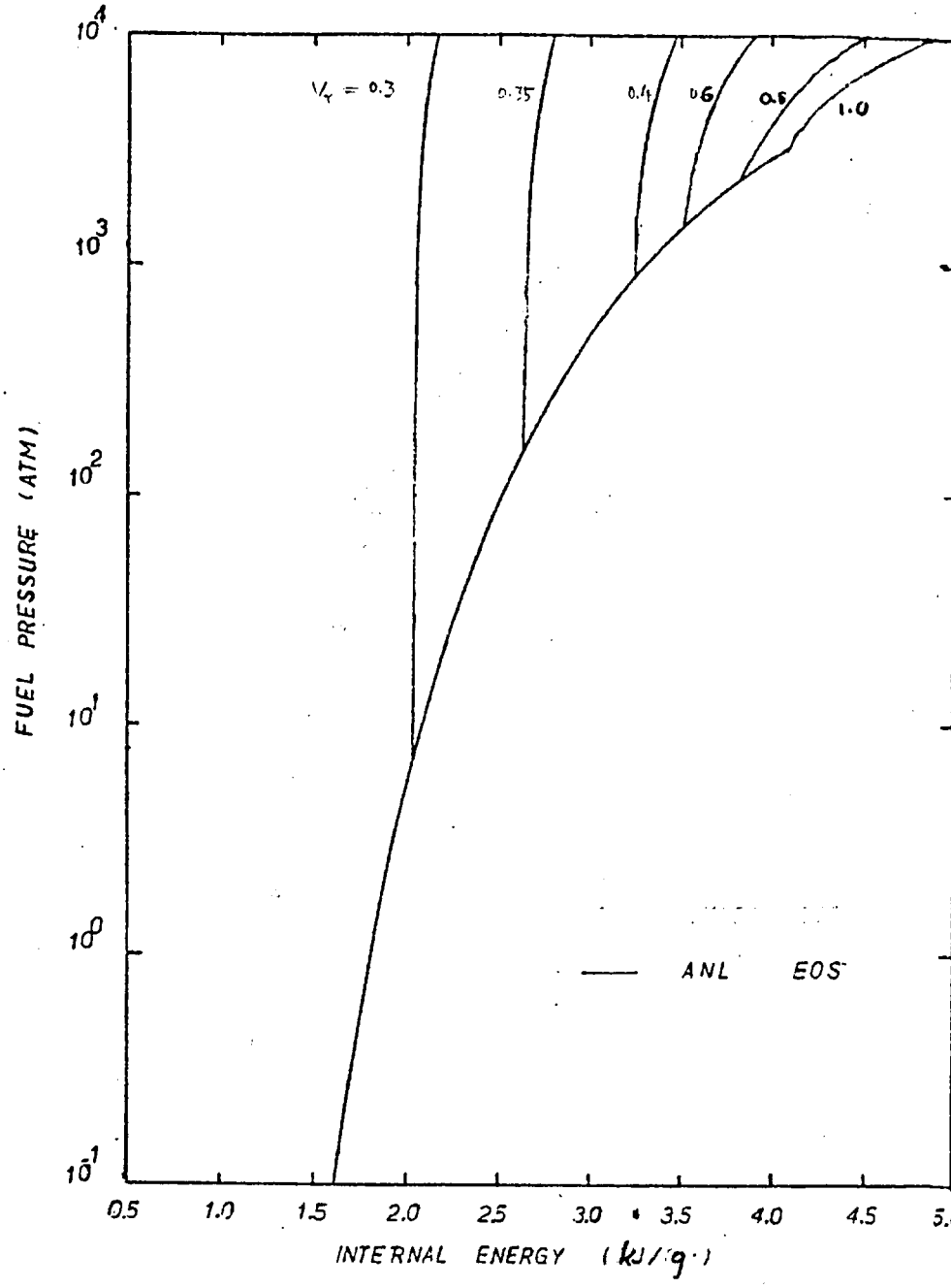

FIG-3 ENERGY PRESSURE RELATIONSHIP

3.2.2.2 Molten Fuel Coolant Interaction Model

The MFCI treatment in both BASIMA and DISK is based on the Cho , Irvin and Wright model (26) which assumes that:

1 fuel and coolant are uniformly mixed,

2. heat transfer is limited by the thermal resistance of the fuel alone,

3. any blanketing effect of the vapour film between the fuel particle and the coolant is ignored.

MFCI is started when either the fuel temperature reaches a specified value or disassembly of the core continues beyond a specified time.

The equations of energy balance for the fuel take the following form:

$$c_f M_f \frac{dT_f}{dt} = - h A (T_f - T_s) \qquad (3.19)$$

and for the coolant,

$$c_s M_s \frac{dT_s}{dt} = h A (T_f - T_s) + 0.1 a_s \frac{M_s}{\rho_s} \frac{dP}{dt} T_s \qquad (3.20)$$

The effective heat transfer coefficient h is given by:

$$h = \frac{k_f}{r_p} + \frac{k_f}{\sqrt{\pi a_f t_h}} \qquad (3.21)$$

The total heat transfer area A for a volume V at time t is given by:

$$A = \frac{3 M_f}{r_p \rho_f} (1 - \frac{t}{t_m}) \qquad (3.22)$$

which takes into account the fragmentation and mixing time constant t_m.

The other symbols are defined as follows:

c_f (J/gK) = The specific heat capacity of fuel

c_s (J/gK) = The specific heat capacity of coolant

T_f (K) = The fuel temperature

T_s (K) = The coolant temperature

M_f (g) = The mass of fuel in the cell

M_s (g) = The mass of coolant in the cell

ρ_f (g/cm^3) = The fuel density

ρ_s (g/cm^3) = The coolant density

α_s (1/ K) = The thermal coefficient of expansion for coolant

P (bar) = The total pressure in the cell

k_f (W/cm K) = The thermal conductivity of fuel

r_p (cm) = The radius of fuel particles

a_f (cm^2/s) = $k_f / c_f \rho_f$

= The thermal diffusivity of fuel

t_h (s) = $r_p^2 / 3a_f$

= The time constant for heat transfer in fuel

t_m (s) = The time constant for fuel fragmentation and mixing

The thermodynamic properties of fuel and coolant are given in appendix-A

In the two-phase state of the fuel, the total pressure is calculated as the sum of fuel and coolant vapour pressures and in the single-phase state by an iterative procedure explained in section 3.3.3.

3.2.3 Hydrodynamics:

3.2.3.1 Treatment of the Shock Waves:

Shock waves may be treated numerically, in a number of ways. In one of the successful methods an artificial dissipative mechanism is introduced in such a way that the shock is smoothed out over a few mesh and time intervals (Neumann and Ritchmayer,1950). This is accomplished by adding a pseudo viscous pressure q to the real preasure p. The effective pressure is then the sum of these two components:

$$P = p + q \tag{3.23}$$

For a plane wave the original expression for q,

$$q = - \frac{(b\,\rho\,\Delta x)^2}{V_s} \frac{\partial V_s}{\partial t} \left| \frac{\partial V_s}{\partial t} \right| \tag{3.24}$$

tends to smear out rarefaction waves unnecessarily and was later modified as below (Ames,1977):

$$q = \begin{cases} \dfrac{(b\,\rho\,\Delta x)^2}{V_s} \left[\dfrac{\partial V_s}{\partial t} \right]^2 & \dfrac{\partial V_s}{\partial t} < 0 \\ 0 & \dfrac{\partial V_s}{\partial t} > 0 \end{cases} \tag{3.25}$$

where the number b is related to the stability conditions and to the number of mesh intervals over which the shock is allowed to spread.

Δx represents the thickness of the mesh slab and

V_s its specific volume.

The method of psuedo viscosity provides numerical solutions which are striclty valid only for plane waves. Nevertheless, the

technique has successfully been used for cylindrical waves in the form (Sha and Walter,1971):

$$q = \begin{cases} \dfrac{1.44\ A\ \rho_0^2}{V_s}\left(\dfrac{\partial V_s}{\partial t}\right)^2 & \dfrac{\partial V_s}{\partial t} < 0 \\ 0 & \dfrac{\partial V_s}{\partial t} > 0 \end{cases} \tag{3.26}$$

where A is the mesh-cell area.

3.2.3.2 Equations of Motion:

The governing equations are obtained by conserving mass momentum and energy within the control volume.

As the grid deforms with the displacement of materials, the equation for the conservation of mass may be written as:

$$\rho(t) = \rho(0)\ \frac{V(0)}{V(t)} \tag{3.27}$$

where $\rho(t)$ and $V(t)$ are the overall density and volume of a mesh cell at time t, $\rho(0)$ and $V(0)$ their initial values.

Observed from the fixed Eulerian coordinates, the spatial pressure gradient accelerates the Lagrangian particle by:

$$\ddot{r} = -\frac{1}{\rho}\frac{\partial P}{\partial r} \tag{3.28}$$

$$\ddot{z} = -\frac{1}{\rho}\frac{\partial P}{\partial z} \tag{3.29}$$

where r and z are the Eulerian coordinates of the particle.

The total pressure P in the Lagrangian mesh is related to the internal energy densities of materials through the equations of state.

3.2.3.3 Material Motion Feedback:

Two options have been included for calculating the displacement reactivity feedback; one based on the virtual motion model and the other on a real hydrodynamic motion model.

3.2.3.3.1 Virtual Motion Model :

In this model no actual motion of the fluids takes place and the reactivity feedback is calculated from the following equation (Hicks and Menzies, 1965):

$$\frac{d^2k}{dt^2} = - \int \text{grad } p \cdot \text{grad } w \, dV \qquad (3.30)$$

where the pressure p is equal to the sum of the actual pressure P and a pressure p′ due to the compression and rarefaction of waves

$$p = P + p' \qquad (3.31)$$

When the core is composed of several zones, the discontinuities at the interfaces may be taken into account by replacing p′ by an interface pressure given by (Lee and Pigford,1972):

$$p_{i,i+1} = \frac{(P_i \rho_{i+1} c_{i+1} + P_{i+1} \rho_i c_i)}{(\rho_i c_i + \rho_{i+1} c_{i+1})} \qquad (3.32)$$

where P_i, ρ_i and c_i represent pressure, material density and acoustic speed on one side of the interface; and P_{i+1}, ρ_{i+1} and c_{i+1} their respective values on the other side.

With this pressure, the reactivity change due to core motion is given by:

$$\frac{d^2k}{dt^2} = -\sum_N \int_{V_i} \text{grad } p_i \text{ grad } w_i \, dV$$

$$- \sum_i (P_{i+1}-P_i) \int ds. \frac{\{\rho_i c_i \text{grad } w_i + \rho_{i+1} c_{i+1} \text{grad } w_{i+1}\}}{(\rho_i c_i + \rho_{i+1} c_{i+1})} \qquad (3.33)$$

This may be integrated twice to obtain the reactivity feedback. In this relation the gradient of the reactivity worth distribution is assumed to remain invariant with respect to time in the Lagrangian coordinate system.

3.2.3.3.2 Real Displacement Feedback:

Here the gradient of worth distribution associated with each Lagrangian cell is assumed to remain invariant with time, which means that the reactivity worth distorts with the material motion in the Eulerian system. The change in the multiplication factor is given by (Sha and Hughs,1970)

$$\delta k_3(t) = \int_V \frac{\rho(r,z,t^n)}{\rho(r,z,0)} \{ \frac{\partial w(r,z)}{\partial r} \Delta r(r,z,t^n) + \frac{\partial w(r,z)}{\partial z} \Delta z(r,z,t^n)\} \, dV \qquad (3.34)$$

where Δr and Δz represent the displacement of the fluid along radial and axial directions respectively.

3.3 THE NUMERICAL PROCEDURE

3.3.1 Layout of the Code BASIMA:

The block diagram of the code is as follows:;

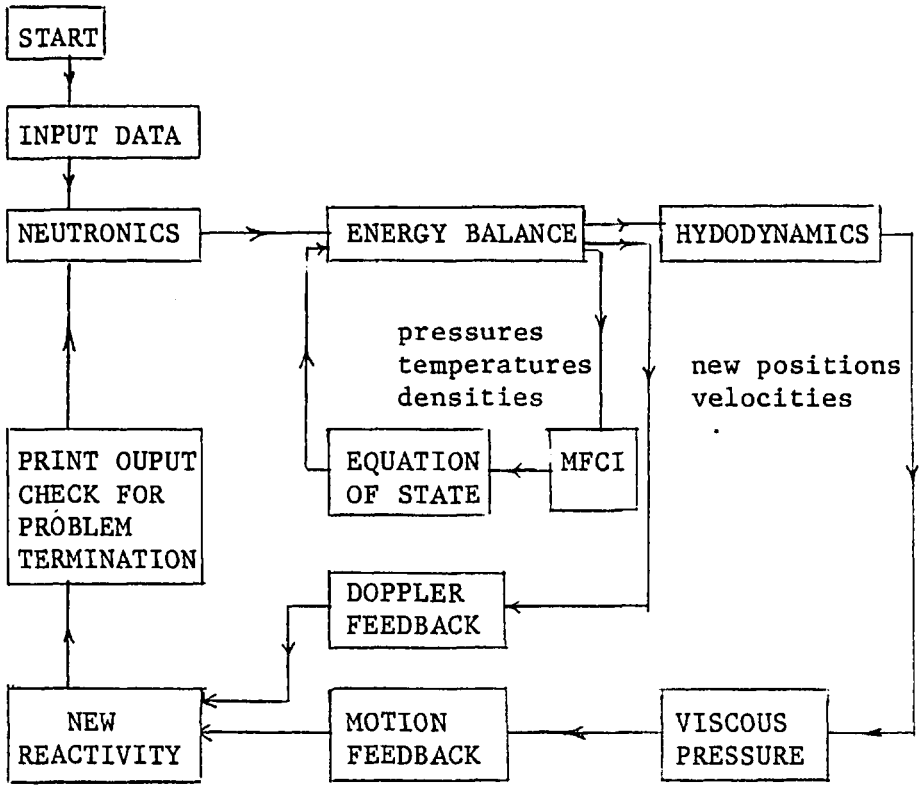

Fig-4 Block Diagram of BASIMA

The programme starts by reading in the reactor geometry, the material, neutronic and thermodynamic data in addition to other data to control the operations of the code. The total energy obtained from the neutronic calculations is distributed over the core in accordance with the input power density distribution function. Cell pressures and temperatures corresponding to the distributed energy density are estimated using appropriate equations of state. Pressure energy density iteration is carried out whenever the liquid state of the fuel is encountered. The fuel is also allowed to interact thermodynamically with the

coolant if the prespecified conditions of MFCI are fulfilled.

When the real hydrodynamics motion option is used, new mesh positions are determined and the reactivity due to material motion and Doppler effect are calculated. In the virtual motion option, the pressure gradients suffice to determine the virtual displacement reactivity feedback and therefore the displacement compartment is skipped over. The motion feedback is also calculated from the appropriate equations. If problem termination criteria are not satisfied, the feedback values are predicted by extrapolating from previous values. The new reactivity is then fed into the neutronics module and the whole cycle repeated.

The temporal and spatial locations of the variables are shown in figures-6a and 6b. The reactor is assumed to be axially symmetric and figure-6b represents a plane section parallel to the central axis of the reactor in which a mesh cell is defined by its lower left indices (j,k). Positions, velocities and acceleration of material particles are defined at the mesh points, whereas energies, temperatures, pressures and densities are defined at the center of mesh cells and are referred to by the half indices (j+1/2,k+1/2) for the cell (j,k).

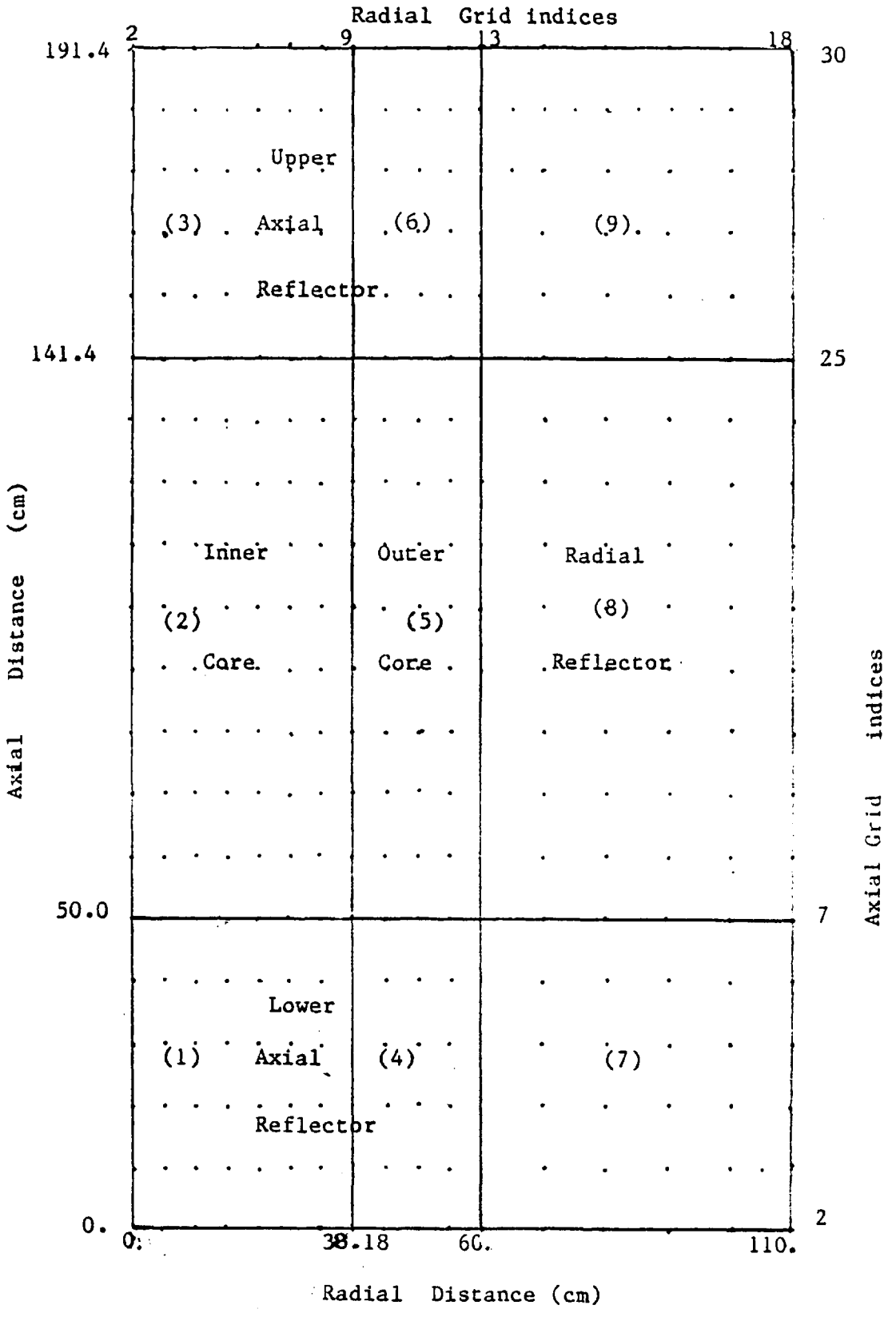

FIG-5 R-Z MESH STRUCTURE

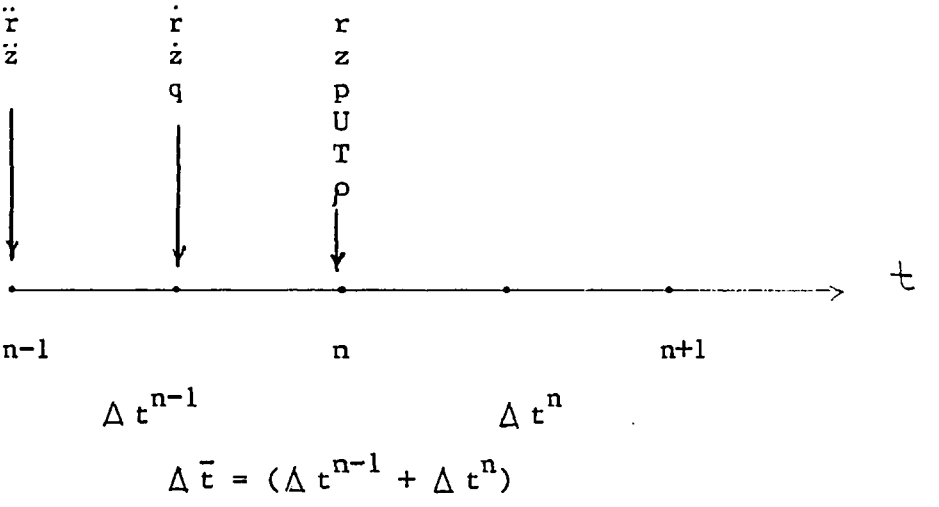

Fig-6a Temporal Location of Variabls.

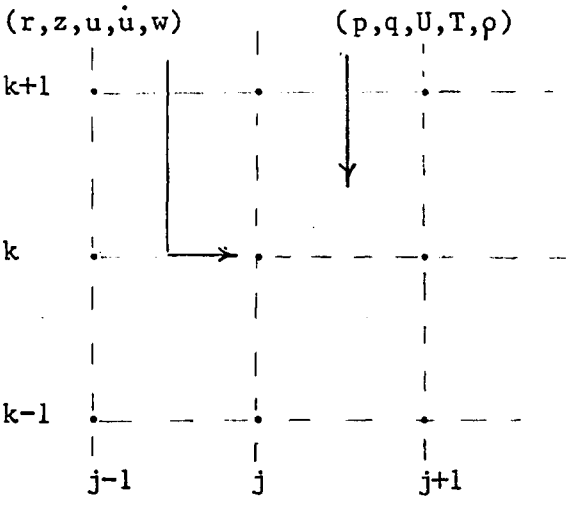

Fig-6b Spatial Locations of Variables

3.3.2 Energy Balance:

The change in internal energy density of the cell during the n^{th} time interval, is given by:

$$\delta Q^n_{jk} = \{ \frac{\delta q^n H_{jk} V^0_{jk} - P^n_{jk} (V^n_{jk} - V^{n-1}_{jk}) 10^{-1}}{V^n_{jk}} \} \qquad (3.35)$$

where

δQ^n_{jk} (J/cm^3) = the increment in the cell internal energy density in the time interval,

δq^n (J/cm^3) = total nuclear energy deposition during the n^{th} interval,

P^n_{jk} (bar) = total pressure in the mesh cell,

V^n_{jk} (cm^3) = mesh cell volume at the end time t^n,

V^0_{jk} (cm^3) = initial cell volume.

The internal energy of the cell is then given by:

$$U^n_{jk} = U^{n-1}_{jk} V^{n-1}_{jk} / V^n_{jk} + \delta Q^n_{jk} \qquad (3.36)$$

The initialisation of the energy densities is done as follows:

$$U^0_{jk} \begin{cases} = \overset{*}{U}{}^0_{jk} = (T^0_f - 273)\, C_v\, \rho_f f_f & T_f < T_m \\ = \overset{*}{U}{}^0_{jk} + \dfrac{(T_f - T_m)}{(T_l - T_m)} H_f \rho_f f_f & T_m < T_f < T_l \\ = \overset{*}{U}{}^0_{jk} + H_f \rho_f f_f & T_f < T_l \end{cases} \qquad (3.37)$$

where

U^n_{jk} (J/cm^3) = the internal energy density in the cell at time t

U^0_{jk} (J/cm^3) = the initial internal energy density,

T^0_{jk} (K) = initial fuel temperature in the cell(j,k),

C_v (J/gK) = the specific heat capacity of the fuel

ρ_f (g/cm^3) = density of the fuel with the cell,

f_f = its volume fraction,

H_f (J/g) = the heat of fusion of the fuel,

T_m (K) = fuel solidus temperature,

T_l (K) = fuel liquidus temperature,

3.3.3 Pressure-Energy-Density Iteration:

The isothermal volume curve encounters a discontinuity at the junction of pure liquid state and two-phase liquid-vapour state. In the latter state the pressure becomes independent of the specific volume. If the fuel state is such that it lies close to the boundary of single and two-phase regions, see figures-2 and 7 , the addition of energy during a time step may take the fuel onto the steep single phase liquid line, with its associated high pressure.

The nuclear energy deposited within a mesh cell during a time step, increases the cells internal energy and provides the necessary work for expansion. This work is positive, if the cell expands; negative, if compressed by its neighbours. The work is estimated by using the volume change from the previous cycle. The latest pressure field is applied to the materials and supplies new densities and internal energy densities which in turn are used to calculate pressures and temperatures at the end of that time step. If the cell remains in a two-phase

liquid-vapour state, the calculation is advanced and the new pressures allowed to displace the mesh. On the other hand, if the fuel goes to single-phase liquid state, iteration becomes necessary, the equation of state being density dependent. If the materials are assumed to be incompressible, the change in volume has no effect in that time step and iteration may not be needed. As real materials are compressible an iterative process involving energy, density and pressure has to be performed.

If the calculations are advanced in time without carrying out the iteration, the high single-phase pressure reached at the end of a time step, may expand the cell during the next step and allow the fuel to flash again to a two-phase liquid-vapour state. The resulting low pressure may decompress the cell and single phase state may establish again. The cell may oscillate between single and double-phase state either indefinitely or for some time depending upon the prevalent conditions in the adjoining cells. These oscillation may happen in such a way that when the fuel in one cell goes to the single-phase state, the adjoining ones may stay in the two phase state. In successive cycles the cells may reverse their phase states and give rise to pressure oscillations between high and low values. Cell oscillations of this kind are obviously not realistic.

A somewhat similar situation is encounterd when a straight forward sequential iteration of density, energy and pressure calculation is attempted. The high pressure, when applied to the fixed volume of the cell, compresses the fluid sodium and stainless steel and makes more volume available for fuel which

expands to the two-phase state, accompanied by low pressure. The previous situation prevails with the exception that since the cell is now isolated from the others it may oscillate indefinitly between single and two phase states.

To overcome this problem, various iteration schemes were tried, some of which had partial success but were discarded because either they were unstable or converged too slowly. Eventually, Newton's iteration method of intersection of chords was found to give satisfactory convergent solutions.

The iteration determins the pressure from the fuel's equation of state, which is consistent with the compresibility relationship of the other materials present. Fig-6 shows the isothermal pressure specific volume behaviour based on the fuel equation of state, along with the relationship based on the compressibilities of sodium and SS. Their point of intersection gives a fuel pressure consistent with all material densities.

The iteration is started when the single phase pressure exceeds the saturation vapour pressure and proceeds as follows:

1. Single phase pressure p_F^0 and the corresponding specific volume of the fuel are used to define a fixed point $A(p_f^0, v_f^0)$ on the fuel pressure volume line which represents the fuel equation of state.
2. The pressure p_f^0 is allowed to compress sodium and stainless steel in the cell, and the fuel to expand to a volume v_c'. The pressure $p_c' = p_f^0$ and v_c' define the point D.

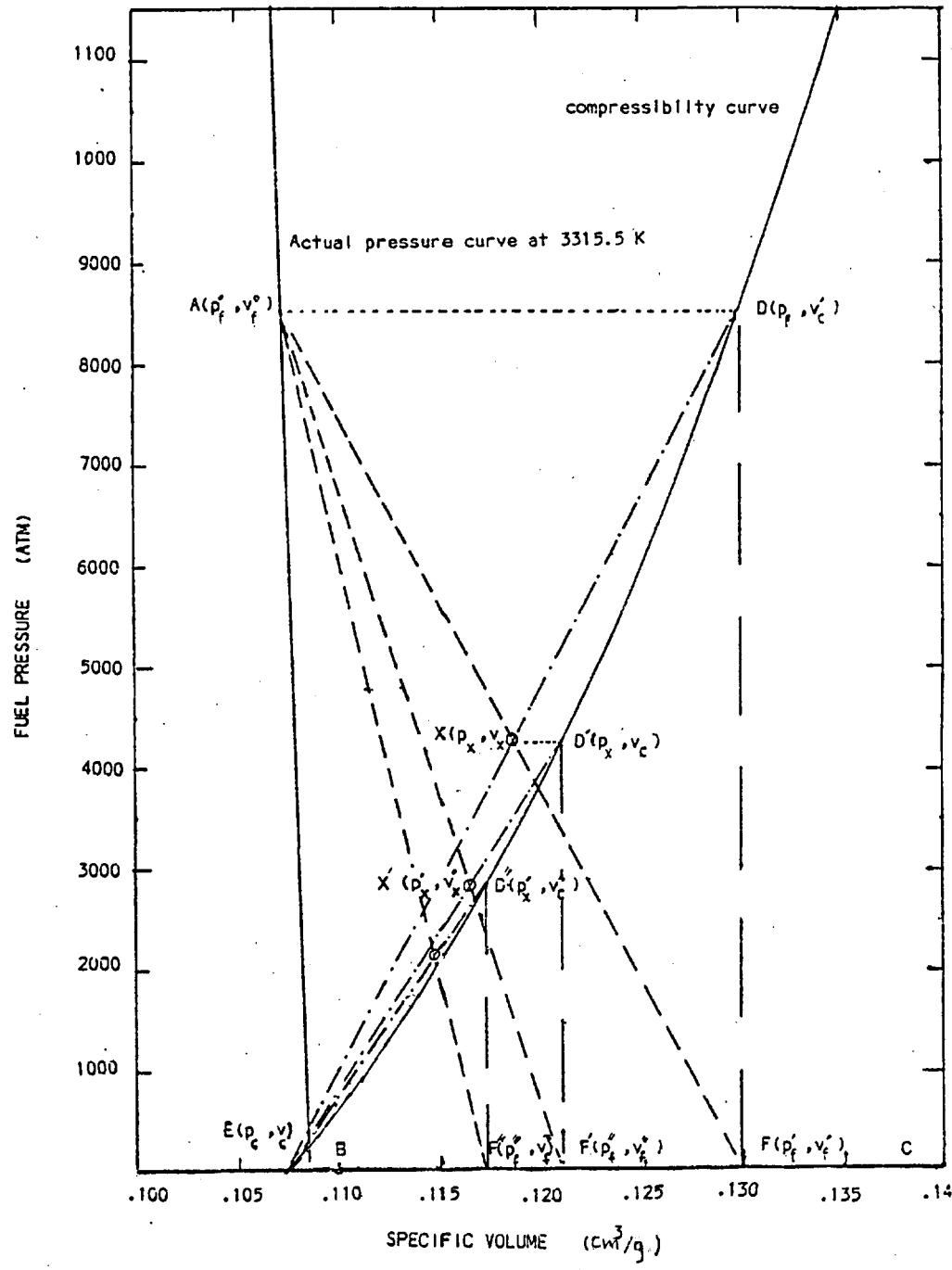

FIG-7 PRESSURE-ENERGY-DENSITY ITERATION SCHEME IN BASIMA

3. A perpendicular dropped from $D(p_f^0, v_c')$ on the pressure volume line defines the point $F(p_f', v_f')$.

4. At the increased specific volume v_f', the fuel in most cases goes to the two phase state and results in a pressure p_f'.

5. The specific volume v_d^0 is calculated from equations (3.12) and (3.13). p_c^0 and v_c^0 specify the coordinates of the fixed point E on the curve based on the compressibility of materials.

6. The gradients m_1 and m_2 of lines AF and DE are given by:

$$m_1 = \frac{(p_f^0 - p_f')}{(v_f^0 - v_f')} \qquad (3.38a)$$

$$m_2 = \frac{(p_c^0 - p_c')}{(v_c^0 - v_c')} \qquad (3.38b)$$

where,

$p_c' = p_F^0$ in the first iteration cycle,

$= p_x$ in the later cycles.

7. The coordinates of the point of intersection of lines AX and XD, defined by:

$$(p_f^0 - p_x) = m_1 (v_f^0 - v_x)$$

$(p_c^0 - p_x) = m_2 (v_c^0 - v_x)$ are determined from:

$$v_x = \frac{\{p_f^0 - p_c^0 + m_2 v_c^0 - m_1 v_f^0\}}{(m_1 - m_2)} \qquad (3.39a)$$

$$p_x = p_f^0 - m_1 (v_f^0 - v_x) \qquad (3.39b)$$

The pressure p_x and the specific volume v_x are then compared with pressure and volume from the compressibility curve ABC and if these are within the specified tolerance limits, the iteration is terminated; otherwise:

8. A new specific volume v_c' is calculated from the compressibility relationship corresponding to the pressure p_x, and these define the coordinates of a new point $D'(p_x, v_c')$.
9. Except for 5, the previous steps are repeated until the points X′ and D′ and the successive pressures fall within the specified convergence limits.

When a single-phase liquid state is encounterd during MFCI, the liquid state iteration is completed, MFCI is initiated, a new sodium temperature calculated, new sodium and SS densities are estimated, pressure-energy-density iteration is carried out again with sodium vapour pressure added to fuel pressure. The iteration is terminated when the fuel temperature calculated from the equation of state becomes consistent with heat transfer to the interacting coolant.

3.4 SUMMARY:

The physical, mathematical and computational models used in the code BASIMA were presented in this chapter. This code deals with the disassembly phase of the LMFBR hypothetical core disruptive accident and covers the three aspects of the problem, namely, the neutronics,the thermodynamics and the hydrodynamics. The first uses the neutron point kinetics model and models the reactivity feedback effects. The second covers internal energy balance, the equations of state and the MFCI. The third deals with the material motion, and for comparative purposes, both the virtual and the real hydrodynamic motion models were included. The results of computations with BASIMA are presented in chapter six.

CHAPTER FOUR

METHODS OF SOLVING THE SPACE DEPENDENT KINETICS EQUATIONS

4.0 INTRODUCTION:

The fundamental aim of reactor kinetics calculations is the estimation of space-time-energy dependent probability distributions. Although it is not possible to predict the individual nuclear events deterministically, a reactor with a statistically large number of neutrons can be considered to behave in a deterministic manner (Henry,1975). This means that if physical characteristics of the reactor are known at time t^n, its behaviour can in principle be predicted for a future time t^{n+1}, with certainty.

The number of nuclear interactions that take place in a reactor per uint time is proportional to the neutron flux and hence, its calculation is of prime importance in reactor physics.

Exact solutions of the Boltzmann transport equation are available only for a few special cases. Therefore, varying degrees of approximation are used to solve this space-time-energy dependent equation. The most popular method is to assume the shape and amplitude of the flux to be fully separable. The time dependent amplitude part gives rise to the point kinetics equations.

In large thermal and fast reactors, small local perturbations cause appreciable spatial deformation of the flux which the point kinetic model fails to cope with. This has lead to an increased

interest in solving the spatial neutron kinetics problem. The solution methods range in cost and accuracy from improved point kinetics method to direct methods involving space, time and energy discretization.

4.1 BASIC EQUATIONS:

Assuming that the multigroup formalism is a sufficiently accurate model, the basic equations may be written in matrix form as follows:

$$V^{-1} \frac{\partial}{\partial t} \Phi = \{\nabla \cdot D\nabla - A + (1-\beta)\, \chi^{p} F^{T}\}\, \Phi + \sum_{i} \chi_i^{d} \lambda_i\, C_i$$

and for the delayed neutron precursor concentrations as:

$$\frac{dC_i}{dt} = \beta_i\, F^{T}\, \Phi - \lambda_i\, C_i \qquad (4.2)$$

where,

$$\phi = \begin{bmatrix} \phi_1 \\ \cdot \\ \cdot \\ \cdot \\ \phi_G \end{bmatrix} \qquad (4.1a)$$

and ϕ_g is the scalar flux averaged over the energy group g,

$$V^{-1} = \begin{bmatrix} 1/v_1 & \cdot & \cdot & 0 \\ \cdot & \cdot & & \cdot \\ \cdot & & \cdot & \cdot \\ \cdot & & & \cdot \\ 0 & & & 1/v_G \end{bmatrix} \qquad (4.1b)$$

v_g = average neutron velocity in group g

$$D = \begin{bmatrix} D_1 & & & 0 \\ \cdot & \cdot & & \\ \cdot & & \cdot & \\ \cdot & & & \cdot \\ 0 & & & D_G \end{bmatrix} \qquad (4.1c)$$

D_g = diffusion coefficient averaged over group g,

The absorption and scattering processes are represented by the matrix A:

$$A = \begin{bmatrix} \Sigma_{a1} & \cdot & \cdot & 0 \\ 0 & \cdot & \cdot & \cdot \\ \cdot & \cdot & \cdot & \cdot \\ \cdot & \cdot & \cdot & \cdot \\ 0 & \cdot & \cdot & \Sigma_{aG} \end{bmatrix} - \begin{bmatrix} \Sigma_{s11} & \cdot & \cdot & \Sigma_{s1G} \\ \cdot & \cdot & \cdot & \cdot \\ \cdot & \cdot & \cdot & \cdot \\ \cdot & \cdot & \cdot & \cdot \\ \Sigma_{sG1} & \cdot & \cdot & \Sigma_{sGG} \end{bmatrix} \qquad (4.1d)$$

F^T is the transpose of the fission column vector F:

$$F = \begin{bmatrix} \nu_1 \Sigma_{f1} \\ \cdot \\ \cdot \\ \cdot \\ \nu_G \Sigma_{fG} \end{bmatrix} \qquad (4.1f)$$

χ^p and χ_i^d, the spectra of prompt and delayed neutrons are:

$$\chi^p = \begin{bmatrix} \chi_1^p \\ \cdot \\ \cdot \\ \cdot \\ \chi_G^p \end{bmatrix} \qquad (4.1g)$$

$$\chi_i^d = \begin{bmatrix} \chi_{i1}^d \\ \cdot \\ \cdot \\ \cdot \\ \chi_{iG}^d \end{bmatrix} \qquad i = 1.....I \qquad (4.1h)$$

λ_i is the decay constant of the i^{th} delayed neutron precursor, β_i the fraction of the i^{th} precursor.

The solution of the space-time-energy dependent kinetic equations can be divided broadly into indirect and direct methods.

4.2 INDIRECT SOLUTION TECHNIQUES:

In this class, approximate solutions are sought by some degree of separation of the time dependence of the flux from its space energy variation. Various methods of solution are available, many of which may be considered as special cases of the general multimode approach.

4.2.1 Multimode Expansion Method:

In these methods, the scalar flux $\phi_g(r,t)$, is represented as a linear combination of known expansion functions or modes with time dependent coefficients:

$$\phi_g(\bar{r},t) = \sum_{l=1}^{\infty} f_{lg}(\bar{r},t)\ n_{lg}(t) \qquad (4.3)$$

where $f_{lg}(r,t)$ are trial functions selected such that the true solution of the problem is approximated by some element in the trial function space.

In addition to the modal expansion matrix $\hat{F}$, another matrix $\hat{W}$ is defined, composed of weight functions and has the same dimensions as $\hat{F}$. In the weighted residual method, the weight functions are selected such that the weighted residual vanishes when integrated over some domain:

$$\int_D \hat{W}\,\hat{R}\,dV = 0 \qquad (4.4)$$

where the domain D may be the whole reactor volume or a node in the nodal method.

The strength or weakness of this method depends upon the

choice of trial and weight functions and this selection is based on physical intuitive grounds (Henry 1975).

4.2.2 Synthesis Methods:

This method is nearly synonymous with the weighted residual method and in reactor physics was first used for three dimensional steady state problems. Historically, the variational flux synthesis and the multichannel synthesis were in competition for some time, till the use of discontinuous trial functions in the first method and a blending procedure in the second method unified the two efforts (Kessler,1970; Stacey 1971a ; Yasinsky 1967; Yasinsky and Kaplan 1967).

The essential idea behind the three-dimensional synthesis technique is the distinctness of the axial from the radial flux shape in the reactor. The flux is then expressed as a linear combination of these two parts:

$$\phi_g(x,y,z) = \sum_{l=1}^{L'} f_{gl}(x,y)\, Z_{gl}(z) \qquad (4.5)$$

where L' is the number of modes used in the approximation to (4.3).

In the multichannel synthesis the radial planes are divided into N subregions S_n (n=1,...N) with each region S_n having its own shape function f_{ngl}, and its own axial component Z_{ngl} , n=1...N (Stacey,1968).

The time synthesis can be approximated by a finite difference representation, or by expanding the flux as follows:

$$\phi(x,y,z,t) = \sum_{l} f_l(x,y,z)\, n_l(t) \qquad (4.6)$$

Another prescription given by Yasinsky . . is:

$$\phi(x,y,z,t) = \sum_{l=1}^{L'} f_l(x,y)\ Z_l(z,t) \qquad (4.7)$$

The elements of f_l are obtained from the static 2-D diffusion equation, solved for different axial planes, while the axially discontinuous blending functions Z_l are obtained by using the variational principle.

4.2.3 Nodal Methods: (Ash 1979, Birkhofer et al 1974, Henry,1972; Werner,1977; Yasinsky,1967; Yasinsky and Kaplan,1967)

In these techniques the reactor is divided into a number of subregions or nodes V_i, over which the flux is spatially averaged:

$$\phi_i = \frac{1}{V_i}\int \phi\ dr \qquad (4.8)$$

The formulation is based either on the concept of net currents or partial currents across the nodal interfaces.

4.2.3.1 Partial Currents Method:

In this method, also known as the gross coupling method, it is assumed that the partial currents directed outwards at an interface x of a node i are proportional to the average flux ϕ in the node:

$$J_i^+ = a_{i,i+1}\ \phi_i \qquad (4.9a)$$

$$J_i^- = a_{i-1,i}\ \phi_i \qquad (4.9b)$$

where partial currents are by definition:

$$J^+ = \frac{1}{4}\phi + \frac{1}{2}J$$

$$J^- = \frac{1}{4}\phi - \frac{1}{2}J \qquad (4.10b)$$

and the coupling coefficients are given by:

$$a_{i,i+1} = \{\frac{1}{4}\int_{V_i} \Phi \, dV + \frac{1}{2}\int_{S_i} D \, \nabla\phi \, ds\} \Big/ \int_{V_i} \phi \, dV$$

$$a_{i-1,i} = \{\frac{1}{4}\int_{V_i} \Phi \, dV - \frac{1}{2}\int_{S_i} D \, \nabla\phi \, ds\} \Big/ \int_{V_i} \phi \, dV$$

where ϕ is a reference flux, obtained from a static solution of the unperturbed system. The coupling coefficient obtained, may be substituted in the neutron balance equation to obtain the nodal equations.

4.2.3.2 The Net Currents Method:

In this method the net current between node i and i+1 is approximated by:

$$J_{i,i+1} = - \frac{D_{i,i+1}}{\Delta x_i}(\phi_{i+1} - \phi_i) \qquad (4.12)$$

where the effective diffusion coefficient is given by:

$$D_{i,i+1} = \frac{2 \, D_i \, D_{i+1}}{D_i + D_{i+1}} \qquad (4.13)$$

and Δx_i is the node centre-to-centre distance.

In both of these methods, the set of coupling coefficients obtained are valid for problems similar to the reference case. More efficient nodal methods compute coupling coefficients from instantaneous fluxes and currents.

4.2.4 The Quasi-static Approach (Ash,1979; Ott and Madell,1966; Ott and Menelly,1969)

This method may be treated as a special case of the multimode approximation in which only the fundamental mode is retained:

$$\Phi(\bar{r},E,t) = \phi(\bar{r},E,t)\ n(t) \qquad (4.14)$$

The flux is split into an amplitude function n(t) and a shape function $\phi(\bar{r},E,t)$. The splitting is such that n(t) embodies the main time dependence or amplitude variation whereas $\phi(\bar{r},E,t)$ contains only the small spatial and spectral flux change. The time dependent shape function can be used as the weight function in equation (4.13) (Galerkin weighting) ; however, it is more common to take the weight functions to be identical to the unperturbed shape functions $\phi(\bar{r},E,0)$ since it is cheaper to calculate their adjoints at the start of the problem.

In order to obtain a unique solution which is positive and finite at all times, the following normalisation is imposed:

$$\iint \frac{\partial}{\partial t}\phi^{*}(\bar{r},E,0)\ V^{-1}\ \phi(\bar{r},E,t)\ dE\ d\bar{r} = 0 \qquad (4.15)$$

The neutron diffusion equation then reduces to a form which is similar to the point kinetic equations (Henry,1972):

$$\frac{dn(t)}{dt} = \left(\frac{\rho^{*} - \beta}{\Lambda}\right) n(t) + \sum_{i}\lambda_i\ C_i + Q(t) \qquad (4.16)$$

$$\frac{dC_i}{dt} = \frac{\beta_i}{\Lambda}\ n(t) - \lambda_i\ C_i \qquad (4.17)$$

where the variables are defined as follows:

$$\rho^{*} = \frac{1}{\bar{F}} \iint \phi^{*}(\bar{r},E,0)\ \{-M + F_p + F_d\}\ \phi(\bar{r},E,t)\ dE\ dr$$

$$M = - \nabla.D \nabla + A \tag{4.19}$$

$$F_p = (1 - \beta) \wedge F^T \tag{4.20}$$

$$F_{di} = \beta_i \wedge F^T \tag{4.21}$$

$$\bar{F} = \iint \phi^*(\bar{r},E,0) \{ F_p + F_d \} \phi(\bar{r},E,t) \, dE \, d\bar{r} \tag{4.22}$$

$$\beta_i = \frac{1}{\bar{F}} \iint \phi^*(\bar{r},E,0) F_{di} \phi(\bar{r},E,t) \, dE \, d\bar{r} \tag{4.23}$$

$$\beta = \sum_i \beta_i \tag{4.24}$$

$$\wedge = \frac{1}{\bar{F}} \iint \phi^*(\bar{r},E,0) \frac{1}{v(E)} \phi(\bar{r},E,t) \, dE \, d\bar{r} \tag{4.25}$$

$$C_i = \int \frac{\beta(t')}{\wedge(t')} n(t') \exp(-\lambda_i(t-t')) \, dt \tag{4.26}$$

The shape function is obtained from:

$$\{ \nabla.D \nabla - A - (1 - \beta) \chi F^T \} \phi(\bar{r},E,t) + \frac{1}{n(t)} \sum_i \chi_i \lambda_i C_i$$

$$= \frac{1}{v} \{ \frac{dn(t)}{dt} \frac{\phi(\bar{r},E,t)}{n(t)} + \frac{\partial \phi(\bar{r},E;t)}{\partial t} \} \tag{4.27}$$

Solutions to this equation, of varying accuracy, may be obtained depending upon the strength of the coupling between the shape and the amplitude functions. Starting from the lowest level, these represent: the adiabatic approximation, the quasi-static and the improved quasi-static approximations.

4.2.4.1 The Adiabatic Approximation

The adiabatic method makes use of the following approximations in equation (4.27):

1. The retardation in the shape of the delayed neutrons is neglected. This means that the delayed neutron distribution instantaneously takes the shape of the prompt neutrons.
2. All time derivatives in the equation describing the shape function are neglected.
3. The reactivities are calculated from already computed shape functions.

With these assumptions, the amplitude and shape equations become completely uncoupled. The shape function can then be determined by solving the stationary eigenvalue problem. Although this is the point kinetic model, it can still be used to solve the spatial kinetics problem by solving the stationary problem periodically and using the new shapes to compute the reactivities for the main temporal calculations.

If assumption 3 is not made, some advantage may be gained but the complexity of the equations becomes comparable to that of the quasi-static equations.

In the adiabatic model used in AX-1 code (Okrent et al 1959), the temporal part is assumed to behave exponentially:

$$\phi(t) = \phi(t_0)\, e^{at} \qquad (4.28)$$

over a finite interval of time.

The adiabatic method assumes that the neutron fluxes attain instantaneous equilibrium after any system perturbation. In so

far as the prompt neutrons are concerned, this is a good assumption, but a poor one for the delayed neutrons. No retardation in the latter's shape function implies that the power density maintains the same distribution in the equilibrium and the dynamic modes (Ash, 1979). This is a poor assumption, particularly for systems having neutron life times typical of thermal spectrum reactors (Ott and Meneley, 1969).

4.2.4.2 The Quasi-Static Method

The adiabatic method may be improved by retaining temporal coupling in the flux shape equation (4.27). However, advantage is taken of the fact that variation in time of the shape function is less important than variation in the amplitude function. The temporal variation of the shape is therefore neglected.

4.2.4.3 The Improved Quasi-static Method

Further improvement can be achieved if all the temporal coupling terms are retained in equation (4.27) which may be solved by backwards differencing the flux shape derivative. The derivative of the amplitude $\frac{dn(t)}{dt}$ may be obtained from the previous time step solution of equation (4.16).

The quasi-static approach works better for fast reactors than for thermal systems. This is because the former have tighter coupling of shape and amplitude equation and respond more rapidly to reactivity perturbations than the latter (Ott and Menelly 1969).

SPARK, QX-1 and FX-2 codes are examples of this approach. The time derivatives of the flux and delayed neutrons shape

functions are neglected for long time intervals during which they are assumed to remain invariant and are calculated whenever the shape is thought to have changed appreciably. The whole procedure results in a series of point kinetic runs with periodic calculation of shape functions and other variables.

In the FX-2 code, a feedback term is included in the delayed neutron equations to take account of the hydrodynamic motion of the precursors in the fuel.

4.3 DIRECT SOLUTION METHODS

In this approach the multigroup spatial kinetic equations are approximated by finite difference equations in space and time. These methods generally require small time intervals over which the equations are solved and hence consume more computer time. The main characteristic of this approach lies in its finite error bounds which makes the method valuable as a standard for the more approximate indirect methods (Ferguson and Hansen,1973; Henry,1972).

The kinetic equations can be written in a compact matrix form as:

$$\frac{d\Phi}{dt} = H\,\Phi \qquad (4.29)$$

where Φ is the extended vector:

$$\Phi = \begin{pmatrix} \phi_1(r,t) \\ \\ \phi_G(r,t) \\ C_1(r,t) \\ \\ \\ C_I(r,t) \end{pmatrix} \tag{4.30}$$

$\phi(r,t)$ = scalar group fluxes,

C_i = i^{th} delayed neutron group precursor concentration and the square matrix H of order (G+I) is defined as:

$$H = \begin{pmatrix} S_{11} & S_{12} \cdots & S_{1G} & F_{11} & F_{12} & & F_{1I} \\ S_{21} & S_{22} \cdots & S_{2G} & F_{21} & F_{22} & & F_{2I} \\ \cdot & \cdot & \cdot & \cdot & \cdot & & \cdot \\ \cdot & \cdots & \cdot & \cdot & & \cdot & \cdot \\ S_{G1} & S_{G2} \cdots & S_{GG} & F_{G1} & \cdot & \cdot \cdot & F_{GI} \\ P_{11} & P_{12} \cdots & P_{1G} & \lambda_1 & & & 0 \\ P_{21} & P_{22} \cdots & P_{2G} & & \lambda_2 & & \cdot \\ \cdot & \cdot & \cdot & \cdot & & \cdot & \cdot \\ \cdot & & \cdot & \cdot & \cdot & & \cdot \\ P_{G1} & P_{G2} \cdots & P_{GI} & 0 & \cdot & \cdot & \lambda_I \end{pmatrix} \tag{4.31}$$

and the components of the matrix H are defined as follows:

$$S_{gg'} = v_g \{\nabla . D_g \nabla - \Sigma_{ag} - \sum_{g \neq g'} \Sigma_{sgg'} + (1-\beta)\, \chi_g \nu_g \Sigma_{fg}\}\, \delta_{gg'} + \Sigma_{sgg'}$$

$$F_{gi} = v_g\, \chi_{gi}\, \lambda_i \tag{4.33}$$

$$P_{ig} = \beta_i\, \nu_g\, \Sigma_{fg} \tag{4.34}$$

and $\delta_{gg'}$ = Kronecker delta,

For a constant H, solution to equation (4.29) can be written as follows:

$$\Phi(t) = e^{Ht}\,\Phi(t_0) \tag{4.35}$$

4.3.1 Time Constants

The time constants involved in equation (4.35) vary widely in magnitude. For fast spectrum systems these may range from a few seconds to a fraction of a microsecond. If such a system is perturbed, the flux adjustment time between energy groups is of the order of the slowing down time, whereas the spatial adjustment is characterised by the relatively longer neutron diffusion time scale (Ferguson and Hansen,1973; Duderstadt,1976; 1979; Wight et al,1971). The delayed neutron precursors take even longer to settle down to a steady state. Since the eigen values associated with the Jacobian of equation (4.35) span several decades in magnitude, this set represents a stiff mathematical system. The stifness ratio, defined as:

$$R_\lambda = \frac{|\lambda_{max}|}{|\lambda_{min}|} \tag{4.36}$$

in the case of kinetic equations, is of the order of 10^9 (Werner,1977). This means that the set of equations describing the spatial reactor kinetics form a very stiff system.

To obtain numerical solutions, stiff equations require very short time steps for the small time constant equations whereas relatively very long time steps are needed to observe any

appreciable change associated with the long time constant equations. Various methods are used to handle stiff differential systems but most of these require storage of many previous time solutions (Gear 1971), which is not feasible for large arrays and many dimensions. In reactor kinetics the most commonly used methods are transformation of equations to a less stiff system and matrix splitting techniques (Werner 1977). In the DISK code a form of splitting is used to soften the stiffness of the kinetic equations.

4.3.2 Spatial Dependence

The spatial discretization of the leakage term V.DV increases the order of the matrix to L*J*K*(G+I) where L,J and K are the spatial mesh divisions in the three coordinate directions; G and I the number of energy and delayed neutron groups respectively.

In one dimension, the extended vector Φ is given by expression (4.30)

Equation (4.29) may be written in generalised difference form (Ferguson and Hansen 1973):

$$\frac{1}{t^{n+1}-t^{n}} \left(\Phi^{n+1} - \Phi^{n} \right) = a\, H^{n+1}\, \Phi^{n+1} - (1-a)\, H^{n}\, \Phi^{n} \qquad (4.37)$$

When

a = 0 , the equation is forwards differenced (FD),

a = 1 , the equation is backwards differenced (BD),

a = 1/2 the equation is centre differenced (Crank-Nicholson scheme)

The simplest of these is the FD scheme in which the equation

becomes explicit. However, in the FD method for solving the kinetics equations, numerical stability conditions severely limit the size of the time steps (Ritchmeyer and Morton 1967). Other differencing schemes give rise to implicit or semi-implicit equations.

4.3.3 Implicit Methods

The time- and space-differenced equations may be written in the form:

$$B^{n+1}\,\Phi^{n+1} = B^{n}\,\Phi^{n} \tag{4.38}$$

The right hand side may be evaluated at time t^n, therefore the problem essentially is of solving the simultaneous set of equations given by:

$$B\,\Phi = Y \tag{4.39}$$

Solving these equations by the elimination method is not feasible because of the large number of variables involved. The most commonly used are the iteration methods.

The matrix B can be decomposed into its diagonal D, lower triangular L and upper triangular U component matrices.

$$B = D + L + U \tag{4.40}$$

The various iterative procedures may be described by the expression:

$$M\,\Phi^{(i+1)} + (B - M)\,\Phi^{(i)} = Y \tag{4.41}$$

where $\Phi^{(i)}$ represents the ith iterate and M is a non-singular matrix of the same rank as B. Various prescriptions for forming the matrix M lead to different iteration schemes.

4.3.3.1 Method of Simultaneous Displacements:

The method was first employed by Jacobi in 1844 and is also known as iteration by total steps. The matrix M is selected to be identical to the diagonal matrix D:

$$M = D \tag{4.42}$$

$$B - M = L + U$$

and the i+1 th solution is given by:

$$\phi^{(i+1)} = - D^{-1} (L + U) \phi^{(i)} + D^{-1} Y \tag{4.43}$$

4.3.3.2 Method of Successive Displacements

This method was used by Gauss in his calculations and was independently discovered by Seidel in 1874 and is also known as iteration by single steps. In this method

$$M = L + D \tag{4.44}$$

which gives:

$$\phi^{(i+1)} = -(L + D)^{-1} U \phi^{(i)} + (L + D)^{-1} Y \tag{4.45}$$

The Jacobi iteration improves the set of variables as a whole, whereas in the Gauss-Seidel method immediate use is made of the improved variables to calculate the formers hence the name of successive displacements. This method converges more rapidly than the other.

4.3.3.3 Relaxation Methods

This is obtained from the general prescription (4.41) by setting:

$$M(x) = D (I + x D^{-1} L) / x \tag{4.46}$$

where x is a relaxation parameter which determines the rapidity of convergence.

The iteration schemes are further divided into the point and block iterative methods. In the first case the solution is modified at single points in the domain whereas in the latter, groups of the components of Φ are modified simultaneously. In the linear iteration method one improves the values of the approximate solutions simultaneously on an entire line of points. Block iteration improves convergence of the solution. The Jacobi method by lines for instance, converges at the same rate as Gauss-Seidel method by points (Ames 1977; Varga 1962). Varga examined successive over relaxation (SOR) by two-line blocks and found that, compared with the single-line block method, the convergence rate improved by a factor of 2. The alternating direction method is a natural extention of the line iteration method.

4.3.4 The Alternating Direction Method

The fully implicit iteration by lines proceeds by scanning the whole mesh line by line in the same direction. In the alternating direction (AD) method, the scanning of a two-dimensional mesh proceeds first in one direction, followed by a scan in the other direction. Both these scans form one complete time cycle.

The AD method was first devised for solving parabolic equations in two directions (Peaceman and Rachford 1955), but it has been reformulated and extended to many dimensions.

The main feature of the differencing scheme is that the resulting equations possess diagonal matrices. For the homogeneous two dimemsional diffusion equation:

$$u_t = u_{xx} + u_{yy} \tag{4.47}$$

the difference equations can be written as

$$\frac{u_{jk}^{n+1/2} - u_{jk}^{n}}{t^{n+1/2} - t^{n}} = \delta_y^2 \, u_{jk}^{n+1/2} + \delta_y^2 \, u_{jk}^{n}$$

and (4.48)

$$\frac{u_{jk}^{n+1} - u_{jk}^{n+1/2}}{t^{n+1} - t^{n+1/2}} = \delta_x^2 \, u_{jk}^{n+1/2} + \delta_y^2 \, u_{jk}^{n+1}$$

where δ_x^2 And and δ_y^2 are second difference operators in the two spatial directions.

In the first half of the time step the equations are implict in one direction and explicit in the other spatial direction; in the second half of the time step, they are assumed to be explicit in the first direction and implicit in the other direction. Each equation taken separately is not unconditionaly stable but the two solved sequentially fulfil the condition.

A form of AD semi-implicit method (also referred to as AD explicit method) has been used in the 2-D code MITKIN. The method has been extended , subsequently, to three dimensions (Ferguson and Hansen, 1973).

The AD scheme used in NEST (Neutronics code with Energy Space Time dependence), and which is incorporated in DISK (DIsassembly code with Spatial Kinetics), is explained in the next chapter.

4.4 SUMMARY

Various methods of solving the space-dependent kinetics equations have been reviewed in this chapter. The techniques were broadly divided into the indirect and the direct catagories and each briefly discussed. The former catagory includes: multimode flux expansion flux synthesis, nodal methods and quasi-steady-state methods. Of the second catagory, the implicit methods have been briefly discussed and the alternating direction method has been presented as a natural extension of the method of successive over relaxation by lines. The AD method, used in the NEST and DISK codes for solving the spatial kinetics problem, is presented in detail in the next chapter.

CHAPTER FIVE

PHYSICAL AND MATHEMATICAL MODELS OF THE CODES NEST AND DISK

5.0 INTRODUCTION:

The point kinetics model used in the LMFBR disassembly code BASIMA has been replaced by a space-dependent kinetics model in the code DISK (LMFBR DIsassembly with a Spatial Kinetics model). This code deals with the three aspects of the disassembly problem namely the neutronics, the thermodynamics and the hydrodynamics. The last two aspects are modelled, essentially, in the same way as in BASIMA. The neutronics modelling, in DISK, differs not only in the inclusion of space dependence in the kinetics equations, but also in the way the various reactivity feedback effects are taken into account. These effects are explicitly calculated in BASIMA, and are used to modify the net reactivity of the system. In the DISK code the feedback effects are taken into account implicitly, by modifying the nuclear reaction rates in response to changes in material concentrations, and their temperatures, with the progress of core disassembly in time.

The code consists of a main overlay which links an independent neutronics overlay with the thermodynamics-hydrodynamics overlay. The former module is related to the latter through transformation of some of the variables from the Lagrangian mesh to the Eulerian system, and vica versa. In the model, the Lagrangian system is associated with the thermodynamics and hydrodynamics and the Eulerian with the neutronics module.

This chapter deals with the physical and mathematical models used in the DISK code. Since the hydrodynamic and thermodynmic models have been discussed in earlier chapters, the main attention here is devoted towards modelling the neutronics and the feedback effects of the disassembly problem.

5.1 THERMODYNAMICS AND HYDRODYNAMICS:

The main function of this compartment is the estimation of pressures, temperatures and densities of materials during the disassembly phase of the accident. The interdependence of these variables makes it necessary to estimate them by an iterative procedure. This is modelled in DISK in the same way as in BASIMA (see chapter 3). However, the estimation of the internal energy density distribution differs in the two codes. In BASIMA, the total nuclear energy increment during a time interval is distributed over the volume in accordance with a specified power distribution function. In DISK, the addition of this energy is based on the time-dependent spatial distribution function. Since the nuclear power distribution is estimated in the Eulerian system, associated with the neutronics module, it is transformed to the Lagrangian system in which the internal energy of the fuel is defined. Except for this energy modification, the thermodynamic and hydrodynamic calculations proceed as in BASIMA.

5.2 NEUTRONICS:

The neutronics of the disassembly problem are treated, in the DISK code, nearly independently of the thermodynamic and hydrodynamic aspects. The space-dependent kinetics equations are

solved in the stationary Eulerian mesh. This avoids the build up of truncation errors which would occur in the distorting Lagrangian mesh. Further this choice allows the use of ordinary numerical methods for spatially finite differencing the equations.

Although motion of the fuel is expected to affect the power generation, it is assumed that the velocity of the moving fluid material is small compared with the neutron velocities and is therefore neglected in the multigroup formalism.

The time dependent multigroup neutron diffusion equations may be written as:

$$\frac{1}{v_g}\frac{\partial \phi^g(r,t)}{\partial t} = \nabla . D^g(r,t)\, \nabla\phi^g(r,t) - (\Sigma_a^g(r,t) + \Sigma_s^g(r,t))\, \phi^g(r,t) + \sum_g \Sigma_s^{g'g}(r,t)\phi^g(r,t) + (1-\beta)\, \chi_p^g \sum_{g'} \nu^{g'}\Sigma_f^{g'}(r,t)\, \phi^{g'}(\bar{r},t) + \sum_i \chi_{id}\, \lambda_i\, C_i(r,t) \qquad g = 1\ldots G \qquad (5.1)$$

The equations for the delayed neutron precursor concentrations may be written as (Meneley,1970):

$$\frac{dC_i(r,t)}{dt} = \beta_i \sum_g \nu^g \Sigma_f^g(r,t)\, \phi^g(r,t) - \lambda_i\, C_i(r,t) \qquad i=1\ldots I \qquad (5.2)$$

It is assumed that the precursor decay constants and the number of delayed neutrons emitted per fission are averaged over all isotopes and are known for the problem considered.

Except for the change in material densities and temperatures during core disassembly, the kinetics equations become decoupled

from the hydrodynamic equations. Therefore an independent spatial kinetics code NEST (Neutronics with Energy Space Time dependence) was developed which, with few modifications, is incorporated in the disassembly code DISK.

5.2.1 Finite Difference Equations:

The two dimensional finite difference equations have been obtained, assuming azimuthal symmetry, by integrating over an annular cylindrical node. Assuming that the reactor properties within each node are given by their values averaged over the volume of the node, the various terms of the integrated form of equation (5.1) may be written as:

$$\int_V \frac{1}{v_g} \frac{\partial \phi^g(\bar{r},t)}{\partial t} \, dV = V_{jk} \frac{1}{v_g} \frac{\partial \phi^g_{jk}}{\partial t} \tag{5.3}$$

$$\int_V (\Sigma^g_a(\bar{r},t) + \Sigma^g_s(\bar{r},t)) \, \phi^g(\bar{r},t) \, dV = V_{jk} \, (\Sigma^g_{ajk} + \Sigma^g_{sjk}) \, \phi^g_{jk} \tag{5.4}$$

$$\int_V (1 - \beta) \, \chi^g_p \sum_{g'} \nu^{g'} \Sigma^{g'}_f(\bar{r},t) \, \phi^{g'}(\bar{r},t) \, dV = V_{jk} \, (1-\beta) \, \chi^g_p \sum_{g'} \nu^{g'} \Sigma^{g'}_{fjk} \, \phi^{g'}_{jk} \tag{5.5}$$

$$\int_V \sum_{g'} \Sigma^{gg'}_s(\bar{r},t) \, \phi^{g'}(r,t) + \sum_i \lambda_i \, \chi^g_{di} \, C_i(\bar{r},t) \, dV = V_{jk} \left(\sum_{g'} \Sigma^{gg'}_{sjk} \, \phi^{g'}_{jk} + \sum_i \lambda_i \, \chi^g_{di} \, C_{ijk} \right) \tag{5.6}$$

where t has been suppressed on the r.h.s. By applying Green's theorem, the diffusion term may be written as:

$$\int_V \nabla \cdot D^g(\vec{r},t)\ \nabla \phi^g(\vec{r},t)\ dV$$

$$= \int_S D^g(\vec{r},t)\ \nabla \phi^g(\vec{r},t)\ d\vec{S}$$

$$= V_{jk}\ \frac{X_{j+1\ k}}{(r_{j+1}^2 - r_j^2)}\left(\phi^g_{j+1\ k} - \phi^g_{j\ k}\right)$$

$$- \frac{X_{j\ k}}{(r_{j+1}^2 - r_j^2)}\left(\phi^g_{j\ k} - \phi^g_{j-1\ k}\right)$$

$$+ \frac{Y_{j\ k+1}}{(z_{k+1} - z_k)}\left(\phi^g_{j\ k+1} - \phi^g_{j\ k}\right)$$

$$- \frac{Y_{j\ k}}{(z_{k+1} - z_k)}\left(\phi^g_{j\ k} - \phi^g_{j\ k-1}\right) \qquad (5.7)$$

where

$$X_{jk} = \frac{4\ r_j(r_{j+1}+r_{j-1})\ D^g_{jk}\ D^g_{j-1k}}{\{D^g_{j-1k}\ (r^2_{j+1}-r^2_j) + D^g_{jk}\ (r^2_j - r^2_{i-1})\}}$$

$$Y_{jk} = \frac{2\ D^g_{jk}\ D^g_{jk-1}}{\{D^g_{jk-1}\ (z_{k+1}-z_k) + D^g_{jk}\ (z_k - z_{k-1})\}} \qquad (5.9)$$

Equation (5.7) may be written as:

$$\int \nabla \cdot D^g(\bar{r},t)\ \nabla\ \phi^g(\bar{r},t)\ dV$$

$$= V_{jk}\ \frac{\{\ X_{j+1k}\ \phi^g_{j+1k} - (X_{jk} + X_{jk})\ \phi^g_{jk} + X_{jk}\ \phi^g_{j-1k}\ \}}{(r^2_{j+1} - r^2_j)}$$

$$+\ \frac{\{\ Y_{jk+1}\ \phi^g_{jk+1} - (Y_{jk+1} + Y_{jk})\ \phi^g_{jk} + Y_{jk}\ \phi^g_{jk-1}\}}{(z_{k+1} - z_k)} \qquad (5.10)$$

When these are substituted in the integrated form of equation (5.1), it reduces to:

$$\frac{1}{v_g}\frac{\partial\ \phi^g_{jk}}{\partial t} = \frac{\{\ X_{j+1k}\ \phi^g_{j+1k} - (X_{jk} + X_{jk})\ \phi^g_{jk} + X_{jk}\ \phi^g_{j-1k}\ \}}{(r^2_{j+1} - r^2_j)}$$

$$+\ \frac{\{\ Y_{jk+1}\ \phi^g_{jk+1} - (Y_{jk+1} + Y_{jk})\ \phi^g_{jk} + Y_{jk}\ \phi^g_{jk-1}\ \}}{(z_{k+1} - z_k)}$$

$$-\ M_{jk} + P_{jk} \qquad (5.11)$$

where M and P are removal and production terms defined as:

$$M_{jk} = (\Sigma^g_{ajk} + \Sigma^g_{sjk})\ \phi^g_{jk} \qquad (5.12)$$

$$P_{jk} = (1 - \beta)\ \chi^g_p \sum_{g'} \nu^{g'} \Sigma^{g'}_{fjk} + \phi^{g'}_{jk} \sum_{g'} \Sigma^{gg'}_{sjk}\ \phi^{g'}_{jk}$$

$$+ \sum_i \lambda_i\ \chi^g_{di}\ C_{ijk} \qquad (5.13)$$

In the model, the solution from time $t = t^n$ to $t = t^{n+2}$ is advanced in two alternating direction time steps each of duration

$$\Delta t = (\ t^{n+2} - t^n\ )\ /\ 2$$

In the first time step, the time differenced equation may be written as:

$$\frac{1}{v_g \Delta t} \left(\phi_{j\,k}^{n+1} - \phi_{j\,k}^{n} \right)$$

$$= \frac{\{ X_{j+1k}\, \phi_{j+1k}^{n+1} - (X_{j+1k} + X_{jk})\, \phi_{jk}^{n+1} + X_{jk}\, \phi_{j-1k}^{n+1} \}}{(r_{j+1}^2 - r_j^2)}$$

$$+ \frac{\{ Y_{jk+1}\, \phi_{jk+1}^{n} - (Y_{jk+1} + Y_{jk})\, \phi_{jk}^{n} + Y_{jk}\, \phi_{jk-1}^{n} \}}{(z_{k+1} - z_k)}$$

$$- M_{jk}^{n} + P_{jk}^{n} \qquad (5.14)$$

and in the second direction as:

$$\frac{1}{v_g \Delta t} \left(\phi_{jk}^{n+2} - \phi_{jk}^{n+2} \right)$$

$$= \frac{\{ X_{j+1k}\, \phi_{jk}^{n+1} + (X_{j+1k} + X_{j+1k})\, \phi_{jk}^{n+1} + X_{jk}\, \phi_{j-1k}^{n+1} \}}{(r_{j+1}^2 - r_j^2)}$$

$$+ \frac{\{ Y_{jk+1}\, \phi_{jk+1}^{n+2} - (Y_{jk+1} + Y_{jk+1})\, \phi_{jk}^{n+2} + Y_{jk}\, \phi_{jk-1}^{n+2} \}}{(z_{k+1} - z_k)}$$

$$- M_{jk}^{n+1} + P_{jk}^{n+1} \qquad (5.15)$$

Since the neutron cross sections are assumed to remain constant during the full time interval $\Delta t = t^{n+2} - t^{n}$, the superscript

referring to time steps has been suppressed in the diffusion factors X_{jk} and Y_{jk}. Equations (5.14) and (5.15) can be written as:

$$X_{j+1k}\ \phi^{n+1}_{j+1k} - (X_{j+1k}+X_{jk}+e_r)\ \phi^{n+1}_{jk} + X_{jk}\ \phi^{n+1}_{j-1k} = F^n_{jk}$$
$$k = 1,....K \qquad (5.16)$$

$$Y_{jk+1}\ \phi^{n+2}_{jk+1} - (Y_{jk+1}+Y_{jk}+e_z)\ \phi^{n+2}_{jk} + Y_{jk}\ \phi^{n+2}_{jk-1} = G^{n+1}_{jk}$$
$$j = 1,....J \qquad (5.17)$$

where

$$F^n_{jk} = -\{Y_{jk+1}\ \phi^n_{jk+1} - (Y_{jk+1}+Y_{jk}-e_z)\ \phi^n_{jk}$$
$$+ Y_{jk}\ \phi^n_{jk-1}\}\ \left(\frac{\Delta r^2}{\Delta z}\right) + \{M^n_{jk} - P^n_{jk}\}\ \Delta r^2 \text{ and} \qquad (5.18)$$

$$G^{n+1}_{jk} = -\{X_{j+1k}\ \phi^{n+1}_{j+1k} - (X_{j+1k} + X_{jk} - e_r)\ \phi^{n+1}_{jk}$$
$$+ X_{jk}\ \phi^{n+1}_{j-1k}\}\ \left(\frac{\Delta z}{\Delta r^2}\right) + \{M^n_{jk} - P^n_{jk}\}\ \Delta z \qquad (5.19)$$

$$e_r = \frac{1}{v_g}\frac{\Delta r^2}{\Delta t} \qquad (5.20)$$

$$e_z = \frac{1}{v_g}\frac{\Delta z}{\Delta t} \qquad (5.21)$$

$$\Delta r^2 = (r^2_{j+1} - r^2_j) \qquad (5.22)$$

$$\Delta z = (z_{k+1} - z_k) \qquad (5.23)$$

Equation (5.16) and (5.18) give consistent solutions as long as: $\frac{\Delta r^2}{\Delta t}$, $\frac{\Delta z}{\Delta t}$ and $\frac{\Delta r^2}{\Delta z}$ remain finite when: Δt, Δz and

Δr^2 tend towards zero. The equations are constrained by the following boundary conditions:

a) All fluxes vanish outside the reactor boundary,

b) Radial flux gradients vanish along the central axial line of the cylindrical core.

Equations (5.16) may be written as:

$$
\begin{aligned}
(X_{2k}+e_r)\phi_{1k}^{n+1} - X_{2k}\phi_{2k}^{n+1} &= F_{1k}^{n} \\
X_{2k}\phi_{1\,k}^{n+1} - (X_{2k}+X_{3k}+e_r)\phi_{2\,k}^{n+1} + X_{3k}\phi_{3\,k}^{n+1} &= F_{2k}^{n} \\
&\cdots \\
X_{jk}\phi_{j-1k}^{n+1} - (X_{jk}+X_{j+1k}+e_r)\phi_{j\,k}^{n+1} + X_{j+1k}\phi_{j+1k}^{n+1} &= F_{jk}^{n} \qquad (5.24) \\
&\cdots \\
X_{Jk}\phi_{J-1k}^{n+1} - (X_{J-1k}+X_{Jk}+e_r)\phi_{J\,k}^{n+1} &= F_{Jk}^{n}
\end{aligned}
$$

When the boundary conditions are incorporated the set (5.24) may be written as:

$$
\begin{bmatrix}
C_{1k} & A_{2k} & 0 & & & & 0 \\
A_{2k} & C_{2k} & A_{2k} & 0 & & & \\
\cdots & \cdots & \cdots & \cdots & & & \\
 & 0 & A_{ik} & C_{ik} & A_{i+1k} & 0 & \\
\cdots & \cdots & \cdots & \cdots & \cdots & \cdots & \cdots \\
 & & & 0 & A_{J-1k} & C_{J-1k} & A_{Jk} \\
0 & & & & 0 & A_{Jk} & C_{Jk}
\end{bmatrix}
\begin{bmatrix} \phi_{1k} \\ \phi_{2k} \\ \cdots \\ \phi_{ik} \\ \cdots \\ \phi_{J-1k} \\ \phi_{Jk} \end{bmatrix}
=
\begin{bmatrix} F_{1k} \\ F_{2k} \\ \cdots \\ F_{ik} \\ \cdots \\ F_{J-1k} \\ F_{Jk} \end{bmatrix}
$$

$$\text{for} \quad k = 1 \ldots K \qquad (5.25)$$

where,

$$\begin{aligned} A_{ik} &= X_{ik} && i = 2, \ldots J \\ C_{1k} &= -\{ X_{2k} + e_r \} && \\ C_{ik} &= -\{ X_{ik} + X_{i+1k} + e_r \} && i = 2, \ldots J \end{aligned} \tag{5.26}$$

Similarly equation (5.17) may also be written as:

$$\begin{bmatrix} C'_{j1} & A'_{j2} & 0 & \cdots & 0 \\ A'_{j2} & C'_{j2} & A'_{j3} & 0 & \cdots \\ \cdots & \cdots & \cdots & \cdots & \cdots \\ 0 & A'_{ji} & C'_{ji} & A'_{ji+1} & 0 \\ \cdots & \cdots & \cdots & \cdots & \cdots \\ & & 0 & A'_{jK-1} & C'_{jK-1} A'_{jK} \\ 0 & \cdots & \cdots & 0 & A'_{jK} \quad C'_{jK} \end{bmatrix} \begin{bmatrix} \phi_{j1} \\ \phi_{j2} \\ \cdots \\ \phi_{ji} \\ \cdots \\ \phi_{jK-1} \\ \phi_{jK} \end{bmatrix} = \begin{bmatrix} F'_{j1} \\ F'_{j2} \\ \cdots \\ F'_{ji} \\ \cdots \\ F'_{jK-1} \\ F'_{jK} \end{bmatrix}$$

$$\text{for} \qquad j = 1 \ldots J \tag{5.27}$$

where

and $C'_{jK} = -\{ Y_{jK} + e_z \}$

$$\left.\begin{aligned} A'_{ji} &= Y_{ji} \\ C'_{ji} &= -\{ Y_{ji} + Y_{ji+1} + e_z \} \\ F'_{ji} &= G_{ji} \end{aligned}\right\} \text{ for } i < K \tag{5.29}$$

The mesh is first scanned in the axial direction by solving the set of equations (5.24) for each axial plane k. In each of these planes, neutron fluxes at time t^{n+1}, are evaluated in terms of variables defined in planes k-1, k and k+1 at time t^n. This set of equations is solved at each axial position and for each energy groups used for the computation. This procedure advances

the flux solutions to the intermediate time t^{n+1}. The mesh is then scanned in the radial direction by solving the set (5.27) for each radial position and energy group. The sequential axial and radial scanning completes one full time cycle.

The concentrations of delayed neutron precursors are advanced in time by simply forward differencing the spatially integrated form of equation (5.2), which gives:

$$C_{ijk}^{n+1} = \Delta t \ \beta_i \sum_g \nu^g \sigma_{fjk}^{gn} \phi_{jk}^{gn} - (\Delta t \ \lambda_i \ C_{ijk}^{n} - 1) \qquad (5.29)$$

5.2.2 Solution of The Tridiagonal Matrix:

Both sets of equations (5.25) and (5.27) may be written in a simplified forms as:

$$\begin{aligned} c_1 \phi_1 + a_1 \phi_2 &= f_1 \\ \cdots & \cdots \\ a_i \phi_{i-1} + c_i \phi_i + a_{i+1} \phi_{i+1} &= f_i \\ \cdots & \cdots \\ a_N \phi_{N-1} + c_N \phi_N &= f_N \end{aligned} \qquad (5.30)$$

These equations are solved by the following algorithm (Carnahan et al 1969, Ames 1977):

$$\phi_N = d_N \qquad (5.31)$$

$$\phi_i = d_i - \frac{a_{i+1} \phi_{i+1}}{b_i} \qquad i = N-1, N-2 \ldots, 1 \qquad (5.32)$$

where d_i and b_i are given by the recursion relations:

$$b_1 = c_1 \tag{5.33a}$$

$$d_1 = \frac{f_1}{b_1} \tag{5.33b}$$

$$b_i = c_i - \frac{a_i^2}{b_{i-1}} \qquad i = 2,3,\ldots N \tag{5.33c}$$

$$d_i = \frac{f_i - a_i\, d_{i-1}}{b_i} \qquad i = 2,3\ldots N \tag{5.33d}$$

5.2.3 Modelling of the Reactivity Feedback Effects:

Reactivity feedback, arising from hydrodynamic motion and changes in temperature, is not calculated explicitly in the DISK code but is taken implicitly into account by modifying the nuclear reaction rates as disassembly of the core progresses in time. In BASIMA these are explicitly estimated and the net reactivity of the reactor modified accordingly.

DISK models the hydrodynamic motion in the Lagrangian mesh system which distorts with the moving fluid, whereas the neutronics are dealt with in the stationary Eulerian mesh past which the material moves. Variables which undergo change in one system have to be transformed to the other system when they are used there. These include material densities and temperatures, estimated in the Lagrangian system, and nuclear energy distribution, calculated in the Eulerian system. The nuclear energy is transformed into the Lagrangian mesh because internal

energy balancing involves local pressures and volume changes of the distorted Lagrangian mesh cells.

Since the total mass of materials within the distorting Lagrangian cells is assumed to be conserved, densities of materials change with the cell distortion. Consequently, the densities in the corresponding Eulerian cells, also undergo changes during the disassembly. The changed atomic concentrations effect changes in the nuclear reaction rates within both the Lagrangian and the Eulerian mesh cells. When proper allowance is made for any change in the masses of materials, the modification of atomic concentrations takes account of reactivity feedback effects caused by material displacement, sodium voiding or any other change in material composition. Furthermore, feedback due to the Doppler effect is also incorporated by modifying the microscopic neutron cross sections in response to changes in temperature of the medium. Since the internal energy balance and temperature estimation is performed in the Lagrangian mesh, the temperatures are also transformed to the Eulerian mesh for the neutronic calculations. Thus all reactivity feedback effects are taken into account automatically, by modifying both the effective neutron cross sections and the atomic concentrations both of which change the nuclear reaction rates with time, during the disassembly of the core.

In transforming variables from one system to the other, it is assumed that the transformed variables are continuous, with well defined derivatives and hence, Taylor's expansion may be used to estimate the value of a function at (r,z) in terms of its value

at (r_0,z_0):

$$f(r,z) = f(r_0,z_0) + (r-r_0)\left.\frac{\partial f}{\partial r}\right|_{r=r_0} + (z-z_0)\left.\frac{\partial f}{\partial z}\right|_{z=z_0} \qquad (5.34)$$

Further, it is assumed that the values of functions in both mesh systems are associated with their respective cell centroids, defined for an Eulerian cell by:

$$\tilde{R} = (R_j + R_{j+1}) / 2 \qquad (5.35a)$$

$$\tilde{Z} = (Z_k + Z_{k+1}) / 2 \qquad (5.35b)$$

and for a Lagrangian cell by:

$$\tilde{r} = (r_{j,k} + r_{j+1,k} + r_{j,k+1} + r_{j+1,k+1}) / 4 \qquad (5.36a)$$

$$\tilde{z} = (z_{j,k} + z_{j+1,k} + z_{j,k+1} + z_{j+1,k+1}) / 4 \qquad (5.36b)$$

The Taylor equation is used to relate values of functions at the centroids of one mesh system in terms of known values at the centroids of the other system. The partial derivatives are obtained by centre differencing the functions.

This method of mapping tends to smooth out density effects caused by narrow compression waves, but since these waves have been assumed to be spread over more than one cell width (section 3.2.3.1), this is not expected to affect the results adversely.

5.2.4 Effective Neutron Cross Sections

For a process x the group microscopic cross-section for a single isotope is calculated by assuming the cross-section to be a function of temperature:

$$\sigma_{xg} = a_{xg} + b_{xg} T + c_{xg} T^2 \qquad (5.37)$$

where the constants a_{xg}, b_{xg} and c_{xg} estimated from known cross section values at three fixed temperatures.

The spatial kinetics calculations reported in chapter six, were performed by using few-group effective cross-sections generated by the code DEFILE (Mitchell 1979). This code generates effective cross-sections from the 26 energy group ABBN data set (Abagyan et al 1964), by applying the resonance self-shielding factor method (Kidman 1971; Kidman et al 1972).

In this method, instead of averaging the fine group cross-sections over a particular spectrum, tabulated avaraged cross-sections and correction factors are used to generate effective cross-sections for a particular mix. The effective cross-section for a process x, group g and isotope j is defined as:

$$\bar{\sigma}^g_{xj} = f^g_{xj} \langle \sigma^g_{xj} \rangle \qquad (5.38)$$

where the bracketted cross-section is averaged over a standard (1/E and fission) spectrum and is independent of both the temperature and the composition of the mix. Strictly, the self-shielding factor 'f' is a function of temperature, atomic concentrations and resonance parameters (Segev 1974). However, for practical applications, Bondarenko simplified this by

assuming the self-shielding factor to be a function of temperature and a background cross-section σ_{0j}^{g}. This is the total cross-section of all other materials in the mix referred to the element under consideration:

$$\sigma_{0j}^{g} = \frac{1}{N_j} \sum_{i \neq j} N_i \, \sigma_{tj}^{g} \qquad (5.39)$$

where N_k is the atomic density of the k^{th} constituent and σ_{tj}^{g} its effective total cross-section. The background cross-section takes care of all parameters except temperature.

This prescription allows construction of tables of fixed cross-sections and of correction factors for discrete values of temperature as a function of the dilution. The effective cross-sections for particular values of temperature and composition are estimated by interpolation. The ABBN cross section set is fairly old but the prescription is very popular and has resulted in codes like ETOX (Schenter et al, 1969) which calculate group constants using basic data from the Evaluated Nuclear Data Files (ENDF/B).

The main advantage of this method is the separation of group constants estimation for a particular mix, from detailed integration over the resonance structure. The main disadvantage of the method is that energy dependence of other cross-sections in the mix is not fully reflected in the self-shielding factor of a particular isotope. The contribution of narrow resonances of the fuel to the cross-sections is affected by the resonances of the other materials. In a typical LMFBR fuel, the resonances of U-238 and Pu-239 are affected by the large (912 b) scattering

resonance of sodium at 2.85 keV which if neglected, would imply over-estimation of self-shielding and hence of Doppler effect. One plausible solution is to average the scattering resonance cross-section over energy and include this in the infinite dilution cross-section. This tends to underestimate the self-shielding and hence the Doppler effect. Nevertheless, this prescription is considered to be superior to the previous one, which ignores the sodium scattering resonance (Stacey,1971b; Segeve,1974; Antonakos et al 1972).

The few-group cross-sections generation model in the code DEFILE, follows the first prescription and neglects background resonances in obtaining the infinite dilution cross-sections. Therefore, these cross-sections are expected to lead to an over-estimation of the Doppler effect. The cross-sections required by NEST and DISK do not assume any particular group-constants generation model, however, this discussion may be useful when the results are compared with other codes.

5.2.5 Quasi-Steady State Fluxes

Real steady state can be established only if the effective multiplication factor equals unity, obtained when neutron balance is maintained. When this is not the case, the overall power level and the neutron group-fluxes change with time. The disassembly phase is started when the reactor is already in the supercritical state. In the absence of initial flux distributions, these are calculated in NEST by solving the space-dependent kinetics equations. The fluxes obtained after the transients have settled down are

therefore referred to here as quasi-steady state fluxes.

These and the delayed neutron concentrations are calculated by assuming arbitrary initial distributions and then proceeding with kinetic calculations. However at the end of each time step, the fluxes are normalised such that the total power is conserved. The flux adjustment between energy groups is achieved fairly rapidly, but the spatial adjustment takes relatively longer, particularly, in the unfueled regions where the flux level increases mainly by diffusion from the fueled regions. This happens because the energy adjustment is primarily associated with the slowing down time, whereas the spatial adjustment is characterised by the neutron diffusion time.

The reactor is assumed to reach a quasi-steady state when neutron fluxes for all energy groups change by the same rate everywhere in the reactor. This is checked by monitoring a convergence number D_ω, defined by:

$$D_w = \frac{\omega_{max} - \omega_{min}}{\omega_{min}} \tag{5.40}$$

where ω_{max} and ω_{min} are the maximum and minimum values of the frequency functions ω_{gjk} which represent the logarithmic variation of flux with time:

$$\omega_{gjk} = \frac{1}{\Delta t} \ln \left(\phi^{n}_{gjk} / \phi^{n-1}_{gjk} \right) \tag{5.41}$$

Before the quasi-steady state has been established, or in the transient state following a perturbation, ω_{gjk} have different values in each energy group and spatial location. During the

flux adjustment time, ω's are positive or negative, depending upon whether the flux is increasing or decreasing at the point under consideration. As the transients fade away, all ω's tend to reach a single value. This means that in the quasi-steady state, all fluxes increase or decrease at the same rate. The solution of the kinetics equations can then be written as:

$$\phi_{gjk}^{n+1} = \phi_{gjk}^{n} \; e^{\omega \Delta t} \tag{5.42}$$

During the search for the quasi-steady state, convergence of the solution is accelerated by using the above equation to advance the solution, by a relatively long time, without performing detailed space energy dependent calculations which require shorter time steps. For this purpose, instead of a single value of ω, space energy dependent ω_{gjk}s are used, provided the discrepancy between different ω_{gjk}s is not excessively large, otherwise numerical instability may ensue. This discrepancy is monitored by the convergence number D_ω, defined by equation (5.40). The extrapolation procedure is started when D_ω becomes less than a specified number e_ω. For the quasi-steady state problem, investigated in chapter six, $e_\omega = 10$ ensured stable extrapolation. After each extrapolating time cycle has been completed, it is followed by a few normal cycles to reduce the magnified transients.

As the system approaches the quasi-steady state, D_ω tends to become zero. However, the solution is assumed to have converged when D_ω becomes less than a prespecified number E_ω

When a criticality search is intended, quasi-steady state

calculations are performed with the aim of reducing all ω's to zero by varying either the material compositions or, fictitiously, the number of neutrons produced per fission. However, these changes are made only after the transients have faded away to avoid any numerical instability. After the variation of flux becomes uniform, the material concentrations or the neutronic constants can be changed and the calculations repeated till criticality is achieved. The search for the critical system is not required during the disassembly phase calculations. Since this phase is started with the reactor in the super critical state, the quasi-steady state fluxes are more appropriate for the calculations than steady state solutions.

In the model, it is assumed that the delayed neutron precursors take the same spatial distribution as that of the reactor power, after each time step, during the determination of the quasi-steady state fluxes.

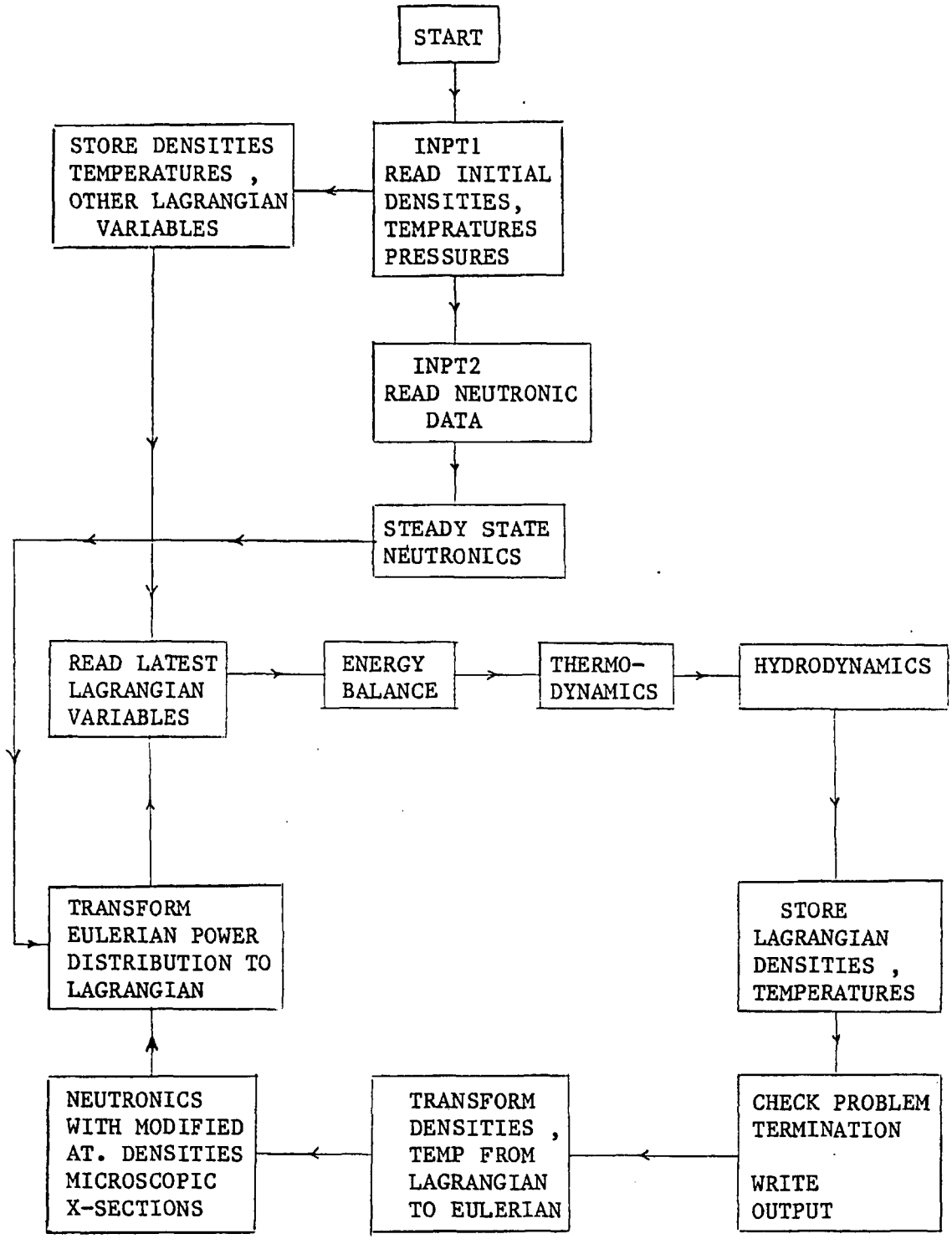

Fig- 8 Block diagram of DISK

5.3 LAYOUT OF DISK:

The overall layout of the code is shown in figure-8. It consists of a main and two primary overlays. The first deals with the thermodynamics and hydrodynamics and the second with the neutronics and the transformation of variables from the Eulerian to the Lagrangian mesh and vica versa.

The code starts by reading in the hydrodynamic and thermodynamic data. This includes reactor mesh geometry, initial material compositions, pressures, energy density and temperature distributions. These are stored on a tape associated with the Lagrangian mesh. This is followed by reading in the neutronic data which includes initial total power level, delayed neutron precursor concentrations and their constants, effective neutron microscopic cross-sections evaluated at three temperatures for each isotope and energy group. If the initial neutron flux and precursor distributions are supplied they are read in; otherwise an initial guess is made and the exact distribution calculated by calling the quasi-steady-state flux subroutine. The flow of the programme is such that the transformed variables are not retransformed back to the original mesh system. Instead, before being transformed, the variables are temporarily stored and read back when the transformed variables have served their purpose. This insures that the truncation errors, arising from the transformation, are not carried forward in time but are limited to that step. The effect of truncation on the reactivity feedback, within a time step, is tolerated however.

5.4 SUMMARY

The physical and mathematical models used in the disassembly code DISK, have been presented in this chapter. Here, the main emphasis has been placed on the neutronics since the hydrodynamic and thermodynamic modelling of DISK is essentially similar to that of BASIMA. Therefore, those features which are in common with BASIMA were omitted from the discussion. In this chapter, two aspects of the neutronic problem were dealt with, namely, the solution of the spatial kinetics equations and modelling of the reactivity feedback effects. The former was dealt with by developing a spatial kinetics code NEST. This was incorporated in DISK along with the feedback models. The reactivity feedback is taken into account by modifing the nuclear reaction rates with time, in response to changes in the temperature-dependent neutron cross sections and isotopic concentrations. The effect of temperature on the neutron cross-sections was incorporated through the use of the f-factor method. The choice of the cross-section set and its effect on the Doppler reactivity feedback has been discussed. Modelling of the feedback due to material displacement or voiding has also been explained in this chapter. Lastly the overall layout of DISK has been explained briefly.

CHAPTER SIX

PRESENTATION AND DISCUSSION OF THE RESULTS OF NUMERICAL MODELS

6.0 INTRODUCTION:

This chapter consists of four main sections; the first three are concerned with results from the point kinetics model disassembly code BASIMA and the fourth with preliminary results from the NEST (Neutronics with Energy Space Time dependence) code.

In section 6.1 a comparison of the results using BASIMA has been made with reported disassembly calculations using the VENUS-II code. Section 6.2 deals with the effects of the magnitude and distribution of void spaces on the course of the disassembly. The effect of void spaces has been taken up again in section 6.3 with emphasis on the material motion model. In the final section results of quasi-steady-state calculation of neutron flux have been presented.

6.1 BASIMA vs. VENUS-II:

6.1.1 Initial Conditions:

The disassembly-phase calculations depend upon the initial conditions of the reactor as well as upon the physical models

used for the analysis of this phase of the LMFBR accident. For comparison of BASIMA results with those from VENUS-II, output from a predisassembly-phase calculation using the code MELT-II for the FFTF reactor model have been used (Nicholson and Jackson, 1972 and 1974). In this comparison, as far as possible, the initial conditions have been made similar, but certain differences are evident particularly in the initial void addition model. This gave rise to some discrepancies in the results, which will be discussed in detail later.

The neutronic input data includes:

a) Initial power level and distribution,

b) Delayed neutron concentrations and constants,

c) Prompt neutron life time,

d) Doppler reactivity coefficients

e) Material reactivity worth distributions.

The thermodynamic data includes:

a) Temperature distributions of fuel and other materials in the reactor

b) Parameters of the equations of state.

c) Physical constants and parameters for the molten fuel coolant interaction.

The hydrodynamics data consists of

a) Material compositions,

b) Spatial positions of mesh points and

c) Initial pressures and velocities of mesh points.

Although both spatial and temporal variations of thermodynamic and hydrodynamic aspects are dealt with in BASIMA

and VENUS II, the neutronics are dealt with in the point kinetics model. Furthermore, it is assumed that in the Lagrangian mesh, the spatial power distribution remains unchanged.

The three aspects of the problem,however, are interconnected through the net reactivity of the reactor. The driving reactivity function contains most of the information regarding the type and the severity of the accident in both the predisassembly and the disassembly phases.

The results reported in this section are based on a transient over power excursion corresponding to an initial reactivity input of $ 1.09 and an insertion rate of $ 100 /s. The initiating mechanism for this severe excursion was a $ 5 /s reactivity insertion accompanied by failure to scram and followed by fission gas release and partial voiding of the core.

6.1.2 Comparison of Results:

Since the course of the disassembly is determined to a great extent by the amount and the spatial distribution of the initial void spaces in the reactor, comparison of results has been made keeping this point in view. Tables-7 and 8 summarize results of the $ 100 /s excursion obtained by using VENUS II and BASIMA, respectively. Table-7 is based on table-17 and fig-34 of Nicholson and Jackson, 1974. The void percentages given in the two tables are not the same because of the differences in the modelling of the void-addition mechanism. The void percentage in table-7 is in addition to the porosity voidage whereas in table-8, the porosity voids were assumed in the present calculations to be left unfilled by the molten fuel. The

distiction between the porosity and the additional sodium void, however, disappears as the void percentage increases.

The variables in the two tables have been plotted against the void percentage in figures-12 to 17. The BASIMA calculations correspond to the option with a uniform distribution of void volume, whereas the VENUS-II results correspond to a non-uniform void addition. Therefore for comparative purposes two curves have been plotted for each variable in table-7: the first, plotted against the core volume-weighted void fraction, and the second, against the core centre void fraction. The VENUS-II curves can be displaced by 0.022 units along the void fraction axis, so compensating approximately, for the unfilled void in the BASIMA runs.

6.1.2.1 Temperature:

The variation of the maximum fuel temperature with the initial void content predicted by BASIMA, in fig-12, closely follows the VENUS behaviour. However, the behaviour of temperature during the disassembly period is slightly different. In fig-13, the central temperature estimated by BASIMA is plotted for increasing values of the void volume percentage. In addition to these, VENUS temperatures depicting the unvoided and the voided core cases are also superimposed on the previous curves. Each of these curves may be divided into three parts: an early part in which the temperature increases at an increasing rate; a middle part where it increases at nearly a constant rate; and an end part, where it increases at a decreasing rate which tends towards zero as the disassembly nears termination point. The

temperature at the centre, in the early part of the disassembly, increases at the same rate in both BASIMA and VENUS II, but the slope of the linear part from the former becomes slightly greater than that from the latter. Since in this middle region of the curves the instantaneous temperatures are higher from BASIMA than from VENUS II, the Doppler reactivity effect calculated by the former is stronger than that predicted by the latter. The higher negative Doppler reactivity feedback contributes towards a more rapid reduction of the net reactivity and hence the power. The total energy therefore reaches a maximum level earlier than predicted by VENUS-II. Consequently the end part of the BASIMA curve starts earlier than that of VENUS-II. This neutralises the effect of greater slope of the middle part and consequently results in earlier termination of the disassembly and lower final temperatures than VENUS-II. The discrepancy in the sodium-out case was less than 0.3%.

Therefore it may be concluded that the small discrepancy in fuel temperatures estimated by BASIMA and VENUS-II which exists mainly during the middle part of the disassembly, tends to disappear as the disassembly approaches termination point.

6.1.2.2 Pressure:

The clearest difference between BASIMA and VENUS II results is exhibited by the pressure behaviour during and at the end of the disassembly phase. The discrepancy lies mainly in the single phase liquid state. In this region, BASIMA predicts pressure-time peaks which are narrower than those of VENUS-II. The narrowing of the width of the peaks is associated with an

increase in the height of these peaks. The two effects have a compensating effect on the total nuclear energy generation. The higher pressures in BASIMA act for shorter durations with the result that the core disassembles in nearly the same time as that predicted by VENUS-II. The discrepancy is greatest in the low void region where, as explained in subsection 6.3.1.2, the pressure is most sensitive to variation in the void percentage. However the discrepancy becomes small at the end of the disassembly phase. Fig-14 shows the pressure variation with the void volume at the end of the phase in the two codes. Since the pressure at the end is governed by the saturated vapour pressure equation, which depends upon the temperature, it behaves in a similar way to temperature.

6.1.2.3 Total Power:

For the excursion started by a $1.09 reactivity step and driven by a $ 100 /s ramp reactivity insertion, the power-time curve exhibits a single broad peak, as long as the central few channels are not preferentially voided of sodium. The shape of the curve and the time at which the power starts to turn over, depend upon the percentage of void volume in the core, in addition to the neutronic parameters. Fig-29 shows the time variation of power calculated by BASIMA for various uniformly added void fractions. The peak power and the corresponding turn-over time from BASIMA and VENUS-II are shown in figs-15 and 16. In both codes the power peak increases in height at a decreasing rate, with increase in the void fraction. Above 6% void volume in BASIMA (3.7% in VENUS-II) the height of the power

peaks become invariant of the void fraction. In this range the magnitude of the power peaks predicted by each of the two codes differ by about 1.3%. The power turn over times in fig-16 show a similar behaviour. However, the power turns over earlier in BASIMA than in VENUS-II. The maximum discrepancy between the two is 12.6% and is principally due to the higher reactivity feedback in BASIMA.

6.1.2.4 Total Energy:

Fig-17 shows the sensitivity of the maximum total energy predicted by BASIMA and VENUS-II during core disassembly, to changes in the void volume fraction. Taking account of the void percentage difference between BASIMA and VENUS-II, these curves nearly overlap for all values of void space. The discrepancies in the power-peak times and the height of the peaks are compensated to a large extent by the difference in the disassembly time. The last entry in table-7 from VENUS-II corresponds to a \$20 /s reactivity ramp and an initial power level of $6.101\ 10^5$ MW, instead of \$ 100 /s insertion rate and $7.806\ 10^5$ MW , for the other entries. Furthermore, the initial temperature distribution is also different.

6.1.2.5 Reactivity:

The variation of net reactivity with time depends upon the initial void fraction in the core. In both BASIMA and VENUS II the net reactivity is assumed to be the sum of the time dependent input reactivity and the feedback reactivities due to material displacement and Doppler effect. Although the Doppler

coefficient is not independent of the material composition of the reactor, it was treated as constant in both calculations even when the core was partially voided of sodium. Similarly the material reactivity worth distribution was assumed to remain constant. For exact calculations the changes in Doppler coefficient and material worth distribution have to be taken into account. However,the above mentioned assumptions were convenient for the present comparative and parametric studies. Since the disassembly begins with the fuel already at high temperatures, the Doppler reactivity feedback also starts from a high value in contrast with the displacement feedback which starts from zero.

When a large volume of void is present in the core, the central region of the core stays in the two-phase state for the entire duration of the disassembly or for a large portion of it. In this case, because of the low pressures in the early part of the disassembly, the displacement feedback increases very slowly in comparison with the Doppler feedback. This allows the Doppler effect to take the leading role in reducing the net reactivity of the reactor. On the other hand when the void volume is small, high single-phase fuel pressures cause rapid outwards motion of the fluid material. Therefore, the motion feedback becomes more effective from the early stages of the disassembly phase, with the result that the total power starts to decrease earlier than in the previous case.

Before the displacement feedback becomes effective, the increase in power remains mainly affected by the input and the Doppler reactivities. For the $ 100 /s excursion, below 6%

void volume the power turn-over time decreases with decrease in the void percentage. The turn-over time gives some measure of the relative effectiveness of the reactivity feedback mechanisms. In the void region where the turn over time varies with the void volume, before the power reaches its peak, the displacement feedback plays an effective role in reducing the reactivity and increases in importance as the void percentage is decreased. However, in the large void region the increase in the displacement feedback comes too late to affect the power turn-over time.

The earlier turn-over time in BASIMA as compared with VENUS-II (see fig-16) implies that the negative feedbacks are higher in the former code. If the reactivity was to follow the same trend in the remainder of the disassembly time, the disassembly would be expected to terminate earlier in BASIMA. On the contrary, BASIMA predicts a longer disassembly time which implies that after the power turn-over, net reactivity falls at a lower rate in BASIMA than in VENUS=II. Thus the power peak in BASIMA becomes lower and broader.

Therefore it may be concluded that in the early part of the disassembly the feedback processes are stronger in BASIMA but in the later part, they are stronger in VENUS-II. Furthermore, in the absence of the single phase state, or before its appearance, the Doppler feedback determines the initial course of the disassembly, but in the later part and in the low void cases, the displacement feedback plays the leading role.

Since the discrepancy in power turn-over times persists even

in the high void region where the single_phase state does not occur, this suggests that high single-phase pressures are not the only cause of the higher negative reactivity feedback in BASIMA results. Since the other reactivity variation mechanisms are the same, the Doppler feedback emerges as the likeliest cause of the discrepancy. The stronger reactivity feedback in the early part of disassembly implies that the corresponding temperatures from BASIMA would be higher in the early part but lower in the later part, as compared with VENUS-II. This conclusion is further supported by the behaviour of temperature, in the high-void range, predicted by BASIMA as compared with the fully voided case of VENUS-II (fig-16).

6.2 EFFECT OF VOID DISTRIBUTION:

In this section the effects of the spatial distribution and the magnitude of initial void content are discussed. For this study two void distribution models were considered; the first distributes the void space uniformly over each reactor region, and the second distributes it non—uniformly. For comparison purposes only the power-shape weighted void distribution has been used, although a number of non-uniform distribution models have been included in BASIMA.

6.2.1 Uniformly Distributed Void

6.2.1.1 Temperature:

The rise in the fuel temperature is directly related to the increase in its internal energy density and specific volume.

During the early part of the disassembly phase when the driving pressures are low and the mesh distortion is small, the main contribution comes from the energy density factor. During this period, the total energy density increases nearly linearly with time, whereas near the end of the disassembly, it tends to level off to a maximum. The specific volume factor becomes more effective when high fuel pressures cause significant mesh displacement distortion. Both these factors tend to check the increase in temperature of the fuel during the course of core disassembly. This point will be discussed in more detail in section 6.3.1.1.

The shape of the temperature vs time curves depends upon the initial conditions of the fuel. In those mesh cells where the fuel is in the molten state, the temperature increases smoothly, but where it is below the melting temperature or is in the melting transition, flat regions appear. Once the melting transition is over, the temperature rises smoothly again. Figs-18 to 21 show the temperature variation with time, in the case of \$70 /s ramp reactivity input, in three mesh positions: cell (2,16) at the core centre, cell (9,16) lying at the inner-outer core interface and cell (2,24) adjoining the core-reflector interface. The temperature variation is shown for uniform initial void additions of 3%, 6%, 8% and 10%. The three selected mesh cells start from different phase states: cell (2,16) in the molten state, cell (9,16) undergoing the melting transition and cell (2,24) below the melting temperature. In cell(2,24), the early linear part corresponds to the solid

state and the flat part to the melting transition.

In the 3% void case, the small energy generation does not allow complete melting of the fuel in cell (2,24). But when the void volume exceeds 6%, the generated energy is sufficient to take the fuel through the melting transition.

The different void cases show that in the case of moderate voidage fractions, increase in voidage tends to prolong the linear parts of the curves, but the increase in duration becomes smaller as the core is further voided of sodium. The temperature in the 10% void case behaves in nearly the same way as the 8% case and the difference tends to disappear at still higher void fractions.

6.2.1.2 Pressure:

Figs 22 to 25 show the pressure of the fuel in the case of $70 /s excursion, in the representative cells (2,16), (9,16), 2,24) for uniformly distributed void volumes of 3%, 6%, 8% and 10%. Above 8%, the pressure varies smoothly with time, but below that the variation exhibits a discontinuous pattern. This is characterized by high pressure peaks corresponding to the single-phase liquid state of the fuel, superimposed on the continuous vapour-liquid state line.

In the 3% void case, the void volume is insufficient to accommodate the fuel vapour and therefore it goes immediately to the single-phase state. If after the internal adjustment of densities within the mesh cells, high pressures associated with single-phase state persist in successive time steps. These pressures impart large accelerations to the fluid particles and

cause steady enlargement of the pressurized cells. According to the equation of state of the liquid fuel, an increase in the specific volume tends to decrease its pressure. If during this time the increase in the internal energy is not able to maintain the fuel in the liquid state, it flashes to the two-phase vapour-liquid state and would stay there until further addition of energy can reestablish the single-phase state.

If the central cells are not voided of sodium in preference to the rest of the core, they may continue to expand driven by the momentum gained already by the fluids, even if the pressure reduces. This expansion can become large enough to preclude further establishment of the single-phase state. This becomes particularly true prior to the end of the disassembly-phase. Therefore in most cases, the fuel ends up in the two-phase state.

The same applies to cell(9,16), with the exception that the single-phase is encountered here much later than at the centre and the pressure peak becomes broader. This is because the void in the inner cells cushions, to a great extent, the effects of the high-pressure peaks. This becomes particularly more pronounced when a pressure threshold for material motion is assumed. In such a case, pressure propagation becomes supressed until it exceeds a specified value. The outer cells remain sheltered for some time from the effects of central high pressure. Thus unlike the centre, the distortion of the outer part of the mesh remains relatively small and slow and therefore, the outer pressure peaks become broader in time. In the calculations reported here, a radial threshold of 20 atm was assumed.

In the case of 6% uniformly distributed void volume, the onset of the single-phase state recedes in time in each of the three mesh cells. Furthermore, the heights of the pressure peaks shorten and the frequency of their occurence becomes less. The availability of more void makes it difficult for the single-phase state to become established in the fuel. In this case, only two pressure peaks appear at the centre and only a single peak in each of the cells (9,16) and (2,24)

At 8% void 'volume, the peaks disappear completely from the centre and the inner-outer core interface cell and appear only in the core-reflector interface cell(2,24). This peak however, appears very late during the disassembly and even this disappears when the void volume is increased to 10%. The flat regions of pressure-time lines correspond to the melting transition during which the rate of increase in temperature remains very small.

In the two-phase state, since the pressure depends on the temperature alone for most of the disassembly phase, the pressure increases at one rate almost independently of the void fraction. Only a slight difference in magnitude appears near the end of the disassembly in parallel with the behaviour of fuel temperature.

6.2.1.3 Total Energy and Power:

Fig-30 is a plot of the variation of total energy release with time during disassembly driven by $70 /s ramp reactivity, for different percentages of void volume. This plot shows that for all void cases, the energy increases at nearly a constant rate for the large part of the disassembly time. In the later part of the disassembly, the rate of increase of energy becomes

progressively smaller. The nearly linear part of each curve corresponds to the time during which power and net reactivity decrease rapidly. This has been explained in more detail in section 6.1.2. The overlapping of the linear parts is due to the similar variation of the net reactivity in the early part of each curve. In this region the displacement feedback is largely ineffective and therefore the net reactivity depends mainly on the input reactivity function and the magnitude of the Doppler coefficient, Tdk/dT. In these runs, a constant value -0.004 of the Doppler coefficient was assumed for all void values. In reality, for the FFTF core, the Doppler coefficient decreases in magnitude with increase in the void fraction. For the fully voided case, Tdk/dT decreases to -0.0025 (Nicholson and Jackson 1974). The material reactivity worth distribution also changes with change in the void content, but it too was assumed to remain fixed. Had these effects been included, the linear parts would have had different slopes. Since the Doppler feedback plays the most significant role in reducing the reactivity during the early part of the disassembly particularly when the void percentage is high, the power peaking is expected to occur later and the height of the peaks to be greater. Table-9 shows the effects of the change in the Doppler coefficient from -0.004 to -0.0025, in the fully voided core.

In the second case, the decreased Doppler coefficient caused a 40% increase in the height of the power peak and 29% increase in the power turn-over time. However, the increased reactivity feedback caused a decrease of 16% in the total disassembly time

with the result that the total energy increased by only 28%.

Both of the first two cases correspond to a reactivity insertion of \$1.09 and \$100 /s , which is excessively high for the coolant flow coast-down accident. For this case Nicholson and Jackson take lower initial power and reactivity input values (see tables-5 and 6), which result in a total energy release comparable to the over-power case.

The total energy at the end of the disassembly phase is plotted in figs 71 and 89 as a function of the void content for \$70 /s and \$ 100 /s excursions respectively. Qualitatively, both excursions exhibit a similar behaviour. In both cases, the energy acts as a monotonic function of the void volume fraction. The sensitivity of energy to void content decreases rapidly at high void percentages. However, this conclusion rests on the assumption of constancy of the Doppler coefficient and other reactivity feedback parameters. In reality, the two energy curves would increase at a slightly higher rate in the high void region than shown in figs 71 and 89. This is evident from table-9 where in the second case only the Doppler coefficient Tdk/dT has been changed. The void percentage above which the sensitivity of energy apparently becomes low, depends upon the severity of the excursion. In the \$70 /s excursion, this happens when the void volume exceeds 8%, whereas in the \$ 100 /s case, this occurs above 10% void. In addition to shifting towards the high void side, the \$ 100 /s curve increases substantially in height. The difference between energies of the two cases increases from approximately 5% at low

void content to about 14% at high values. Thus if the Doppler coeffficient is modified as the core is voided of sodium, the sensitivity of maximum energy release to the void content is expected to increase at higher rates than shown in figs 71 and 89.

Nevertheless, it may be concluded that the energy release increases monotonically with increase in the uniformly distributed void content.

6.2.2 Power-Shaped Void Distribution:

6.2.2.1 Temperature:

The temperature variation with time is shown in figs-31 to 35, for the 3%, 4%, 6%, 8% and 10% power shaped void addition cases. Compared to fig-18 to 21 of the uniformly distributed void cases, the plots show that for the same void fraction at the centre, the disassembly is terminated earlier in the power-shaped distribution cases.

The discrepancy between the two void addition models tends to disappear as the void fraction increases. At 10% void volume the variations of temperature with time, shown in figs-35 and 21, become similar. This is because at high void fractions the temperature becomes relatively insensitive to the void fraction and therefore, the discrepancy between the two tends to disappear.

6.2.2.2 Pressure

Figs-36 to 40 show the variation of pressure with time in the power-shaped void addition model for a \$70 /s ramp reactivity

excursion. In these plots the void percentage refers to the maximum at the centre and is distributed over the core in proportion to the normalized power distribution. Because of the shape of the void in this model, the void percentage averaged over the core volume is less in magnitude than the uniformly distributed void and therefore, in general, the single-phase state is expected to set in earlier in the former than the latter void model, for the same percentage of void at the centre. Reducing average void percentage, tends to condense the time scale of pressure time curve.

Fig-36 for the 3% power-shaped void case corresponds to fig-22 for the uniformly distributed void case. The second peak in the latter moves closer to the first peak and the two merge into a single broad peak. The third and the fourth peaks also occur earlier than predicted by the uniform void model. In parallel with the central mesh cell, the pressure peaks in the inner-outer core interface cell(9,16) also move similarly to the left on the time axis. In cell(2,24), lying at the interface of the core and the reflector regions, the first broad peak occurs while the fuel is still in the solid state and therefore is physically unrealistic. This broad peak is caused by the unavailability of sufficient void space for the expanding solid fuel. The two later peaks which are present also in the uniformly distributed void case, occur earlier following the overall trend.

The same trend manifests itself in fig-38 for the 6% power-shaped void cases corresponding to fig-23 for the uniform void case.

In the 8% case, a pressure peak appears in cell(9,16) near the end of the disassembly phase but is absent in fig-24 of the uniform void case. The pressure peak in cell(2,24), in line with the general trend, occurs earlier.

In all these cases, in addition to a shortening of the disassembly time, this void model, increases the height of the pressure peaks and these become instrumental in early termination of the excursion.

The difference between the two models tends to disappear as the void percentage becomes high. At 10% void volume, the two models give nearly identical pressures in each of the cells (2,16) and (9,16). However a pressure peak persists in cell(2,24) due to the insufficient void space, but this is expected to vanish as still more power_ shaped void volume is added to the core.

6.2.2.3 Power and Total Energy:

The overall shape of power and total energy variation curves using the power_ shaped void addition model figs-44 and 45, resemble figs-29 and 30 from the uniformly distributed void model.

For the same value of central void, the average value is lower in the former. Therefore the power falls earlier and the energy generation reaches a lower level than in the latter. However a different picture emerges if the comparison is made with reference to the average value of the void instead of the maximum value at the centre. For the present problem, a 10% void

volume corresponds approximately to a 6% average value. Hence for the same average void value, the power shaped distribution gives higher power and total energy output. The high void at the centre (the power being maximum there) compared with the rest of the core, tends to delay its disassembly. This effect is most pronounced in the low-void region where the disassembly process is most sensitive to change in the void volume.

If the core is preferentially voided at the centre, with the rest of the core remaining unvoided, the high single-phase state pressures in the outer regions may drive the fuel towards the low two-phase state pressure region at the centre and result in a positive reactivity feedback. This would continue till the pressure at the centre becomes high enough to reverse the motion and cause disassembly of the core. The disassembly in such a case would take longer and result in a greater generation of total energy. Although the power-shaped void addition model does not cause this kind of fuel motion (in this problem), it effectively reduces the magnitude of the displacement feedback and hence increases the disassembly time.

6.3 EFFECT OF THE MATERIAL DISPLACEMENT MODEL:

The choice of the material motion model has a marked effect on the time variation of power, temperatures and pressures during the course of the core disassembly.

Any discrepancy in results from the two models depends to a great extent on the percentage and location of void space in the reactor. The results presented in this section are based on the assumption of constancy of the Doppler coefficient and the

material reactivity worth distributions. The implications of this assumption have been dealt with in subsection 6.2.1.3 .

6.3.1 Temperature:

In this section effects of the material motion model on the behaviour of fuel temperature are discussed and the contribution of other factors which influence the spatial and temporal variation of fuel temperature are analysed.

6.3.1.1 Temperature Variation During The Disassembly:

When no heat transfer from fuel to coolant is envisaged, fuel temperature is affected by two interdependent factors namely the density and the energy density. However energy transfer can occur also through mechanical motion of the mesh cells.

6.3.1.1.1 The Density Factor:

During the course of the disassembly, density of the core materials change in both motion models in response to changes in pressure and volume. In the real motion model, the density changes because of the following reasons:

a) change in the volume of the Lagrangian mesh cell,
b) compression of the cell materials other than the fuel by pressure within the cell,
c) salting in of the time dependent void space during the disassembly phase.

In the disassembly analysis model used here, it is assumed that the cell masses remain invariant with time. The time dependent salting in of the void is made from the void already present, but which is made available for fuel expansion at a

prescribed rate. The effect of change in the fuel reduced volume becomes important when the volume available for the fuel is not large enough to allow it to expand and flash into the two-phase vapour-liquid state.

It is evident from the pressure-energy-density dependent equation of state shown in figure-2 that as long as the fuel remains in the two-phase vapor-liquid state, the temperature depends only on the local energy density. But in the single-phase liquid state in addition to the energy the temperature also depends upon the density of the fuel. Within a mesh cell if the reduced volume of the fuel is incremented while its energy density is held constant, the liquid fuel is expected to rebalance itself at a lower temperature.

Furthermore figure-2 show that the slopes of the single-phase state pressure-energy density curves are greater than the slopes of the temperature-energy density curves. Compared with the pressure behaviour, the temperature is less sensitive to change in specific volume of the liquid fuel throughout the energy range of interest.

In the virtual motion model, no real motion takes place, and therefore the change in density arises from points b and c only. Thus in this model although the fuel density undergoes continuous change, the overall cell density remains invariant. However, the change in the fuel density in this case is related directly to the instantaneous local pressure, whereas in the real motion model it depends upon the cumulative motion, past history of pressure and its spatial distribution in addition to the

instantaneous local values. Because of this, the effectiveness of point "b" becomes diluted in the real motion model, but remains strong in the other model. Figs-72 and 73 show the time variation of fuel temperature in the case of a \$100 /s ramp reactivity excursion using real and virtual motion models respectively. In the former, the temperature increases smoothly with increase in the void volume and the curves tend to overlap above 14%.

The virtual motion curves in fig-73, on other hand, exhibit a different behaviour. Upto 6% void volume, the temperature behaves like the real motion model but in the case of 8% void, the rate of change of the temperature gradient experiences a sudden change at 1850 μs and then continues to vary smoothly again until the end of the disassembly. At higher void percentages the sudden change occurs later in time. However at 18% void volume, the curve no longer experiences this change and the temperature rises smoothly through out the disassembly phase. This behaviour is thought to be mainly due to the density factor. Fig-86 shows that at 8% void volume the virtual motion model gives the maximum final disassembly pressure at the centre. Because of the compression of materials other than fuel by the high single-phase pressure, the specific volume of the fuel increases and hence the temperature also increases in conformity with the equation of state. Further increase in the void fraction results in a decrease in pressure accompanied by a decrease in the specific volume. Therefore pressure and temperature continue to decrease with increase in void until the

large specific volume precludes establishment of the single-phase state. The change in material densities produced by the change in the initial void space is common to both motion models and is in addition to the changes due to effects a, b and c.

6.3.1.1.2 The Energy Density Factor:

When heat transfer is ignored and the point kinetics model is used, the space-time change in the energy density of the fuel arises from:

a) the changes in the power level and its distribution function ,

b) the amount of work done by or on the moving cells.

As explained later in section 6.3.4 the power level of the reactor starts to fall earlier in the case of the virtual motion model. When the void volume is relatively small (less than 7% for a \$70 /s and 8% for \$100 /s ramp reactivity input) energy densities and hence the temperature at all points remain higher in the case of the real motion model. Since the power level increases at nearly the same rate in both motion models until it reaches a maximum, the corresponding temperatures also increase in the same manner.

6.3.1.1.3 The Work Factor:

Since in the virtual motion model actual motion of the materials does not take place, the energy density of the cell and hence the fuel is not modified by this factor. In the real motion model on the other hand, pressure within a mesh cell can be relieved by the physical motion of the materials and thus

energy transfer from one cell to another may take place. This space-time variation in the energy modifies the temperature distribution of the fuel as the accident progresses. The energy transfer from a cell is positive or negative depending upon whether the cell is in the process of expansion or contraction. The expanding cells expend energy which is gained by the compressed cells.

This factor is relatively small because of the assumption of moderate material motion, nevertheless the expansion of the inner parts of the core tends to retard the increase in energy and temperature of the local fuel. In the outer core effects of material motion manifest themselves by compressing the cells near the inner-outer core and the core-reflector interfaces. This compression is expected to increase the energy and hence the temperature of those cells. This increase in energy would continue until the compression can be passed on to the reflector and/or reflected back to the inner core. The presence or the absence of the void spaces within the reflector would affect the propagation of these pressure waves.

Fig 46 to 51 show the change with time of the radial distributions of temperature, pressure and reduced volume of the fuel predicted by the two motion models, for a core voided by 3%. The 160 μs curves reveal that in its early stages, the disassembly progresses nearly identically in the two models. Of the three variables, the temperature shows the slowest response to the motion model. In fact, upto 560 μs the temperature distributions, from the two models, remain similar. On the other

hand, the pressure and the fuel density start to deviate at an earlier stage.

The change in the shape of the spatial distribution of temperature with time is not entirely due to these factors alone but is also caused by change in the phase state of the melting fuel, during which the increase in the temperature remains very small, although the energy density continues to increase steadily. In the equation of state used here, this melting transition is assumed to occur over one Kelvin . This causes the temperature to increase more in those regions of the core, where to start with, the fuel is either near to or in the molten state. Initially only the central region of the core and the core-reflector interface regions fulfil this condition and therefore the temperature rises rapidly in these core locations.

When only a small void space is available for fuel expansion, a cell may undergo repeated phase changes caused by compressions and decompressions of the moving material. The effect of work on temperature in that case becomes difficult to isolate.

On the other hand when a sufficiently large void volume is available, fuel in the central region continues to expand steadily and remains in the two_phase vapour-liquid state till the termination of the dissassembly. Because of the systematic expansion of the central cells, the effects of the work factor becomes more apparent. Figs 57 and 58 show the temperature variation in the core voided uniformly by 13% as predicted by the real and virtual motion models. Within the inner-outer core interface cell (9,16), the temperature predicted by the real

motion remains higher than given by the virtual motion model, but in the central cell (2,16) the temperature behaves differently. In the early part of the disassembly the two temperatures increase in unison but after 2.6 milliseconds from the start of disassembly the temperature given by the virtual motion model becomes greater than that from the other model.

This lower temperature at the centre, given by the real motion model, arises from the combined effects of the following factors:

a) The outwards transfer of energy from the centre in the form of mechanical energy by the expansion of the central region. The mechanical energy transfer during the disassembly remains small except when the driving pressures are high or extensive motion of the material takes place,

b) The increase in the specific volume of the cell in general and the fuel in particular due to the expansion of the Lagrangian mesh cell,

c) The increased volume available to the fuel due to the higher initial void fraction.

In the virtual motion model mechanical transfer of energy does not take place and therefore the energy density of the fuel in the central part of the core is not reduced by the expansion. As far as the density is concerned, except when the inner-few coolant channels are preferentially voided and cause inward motion of the material, the specific volume of the fuel at the centre remains lower in this model than in the real motion model.

The relatively low specific volume of the fuel in conjunction with the higher energy density and low void fraction results in a higher fuel temperature in the virtual motion model.

At higher initial void fractions the difference in the fuel temperatures from the two models tends to disappear. The effect of the initial void space can be seen more clearly in fig-67, 84 and 85 where the end of disassembly temperatures have been plotted as a function of the void percentage for both motion models. The first curve corresponds to \$70 /s and the other two to \$100 /s reactivity excursions.

6.3.1.2 Final Temperatures:

In the real motion model initially, the end temperature at the centre rises rapidly with increase in the void percentage. Above 6%, the increase gradually slows down and above 8% the change in the slope of the temperature versus void curve becomes very small. Following the behaviour of the total energy of the reactor, the energy of the central cell also tends to level off to a maximum in this range of void values. Additional void space in the core does not continue this increase in energy.

Below 8% void volume, the end of disassembly fuel temperature increases less rapidly in the virtual than the real motion model. Instead of increasing continuously as in the latter the end temperature reaches a peak value at about 11% void volume and then begins to fall gradually upto about 13%. Here the difference between the temperature in the two models nearly disappears. Above 13% voidage, the difference in the two temperatures is expected to remain very small. In addition to

the high void fraction, the difference in the temperatures also disappears at 8% void volume where the two curves cross each other.

Thus at high void volumes, the fuel temperature variations become nearly identical in the two motion models. The void volume at which this happens depends upon the reactivity insertion rate during the disassembly phase. For the \$70 /s excursion, the discrepancy in temperatures at the core centre disappeared when the void volume exceeded 15% (fig-67) whereas for the \$ 100 /s case in fig-84 this occurred above 18%.

6.3.2 Pressure:

The main difference between the pressures obtained by the real motion and the virtual motion models is that the former allows pressure propagation and hence its relief while the latter does not. The pressure from the two models differs not only in magnitude but also in its spatial and temporal characteristics.

As mentioned in section 6.2.1.2 the pressure build up and propagation in the reactor depends greatly on the available void space. When the void space is small, the expanding liquid fuel exerts high pressure in both real and virtual motion models. As more void space is made available the onset of the single-phase state is further delayed. The build up of pressure is, however, different in the two motion models.

6.3.2.1 Pressure Variation During the Disassembly:

In the real motion model, after establishment of a single-phase state of fuel in a cell, interaction of that cell with its

neighbours may give rise to fluctuations in the phase state. However, in most cases the disassembly terminates with the fuel in the vapour-liquid state in the central region. Since the motion is small near the core reflector interface, phase fluctuaions may continue in this location. These phase changes are further enhanced by the transfer of mechanical energy from the expanding central cells to the outer parts.

In the virtual motion model, the effect of spatial pressure shape on the reactivity feedback is taken into account instantaneously, but the spatial effects of pressure on the internal energy and overall cell volume are neglected. Any spatial perturbation remains localised and does not affect other cells, except indirectly through the net reactivity and its effect on the total energy of the reactor. Once the fuel in a mesh cell goes into the single-phase liquid state, the only mechanism of pressure restraint is the self compression of the cell materials. The pressure in the cell therefore, increases continuously but with a tendency to level off near the end of the disassembly. Thus unlike the real motion model, once the single-phase state has set in, the cell remains in this state. The continuously high pressures hasten the disassembly of the core and result in less generation of energy in the reactor.

In the real motion model, a single-phase state would typically be established later than in the virtual motion case, for the same initial condition. This results from the specific volume of fuel changing steadily, in the former model, even before the establishment of the single-phase state in the fuel.

Although the cell enlargement caused by the vapor pressure is small, it helps to maintain the fuel in the two phase state for a longer time. Fig-78 to 83 show the pressure variation with time at the core centre caused by a \$100 /s reactivity excursion, for 3, 4, 6, 8, 10 and 18 percent void volume addition. The time difference associated with the appearance of a single-phase state in the two motion models is most obvious in fig-81 for 6% voidage. Here the single-phase is delayed in the real motion case by about 90 μs. This delay continues to increase steadily with increase in the void percentage and helps in the elimination of the single-phase state altogether when the void content becomes high. In the real motion curve in fig-78, this phase state does not appear at the centre, but it continues to remain in the virtual motion case. In the latter, the single-phase state is not eliminated until the void volume approaches 18% (figs -75 and 83).

The magnitude of the initial void addition also affects the final pressures, temperature, total energy and the reactivity feedback.

6.3.2.2 Final Pressures:

The final disassembly presssures are important in estimating the maximum explosive energy release in the LMFBR accident. These pressures are affected greatly by the initial void space available for fuel expansion and are shown in fig-68 and 69 for the \$70 /s excursion and fig-86 and 87 for the \$ 100 /s case.

The real-motion end pressure increases steadily with the

increase in the void percentage to about 7% (8% in the $ 100 /s case), above which the rate of increase becomes very small.

The variation of the end pressure with void space is more dramatic in the virtual motion model. In the first case, upto about 7% initial void, it continues to increase but at a higher rate than the real motion model. Above 7% instead of levelling off, the central fuel pressure starts to decrease with increase in the void space. With further addition of void, the virtual motion pressure tends to approach the real motion pressure and at 13% void, they coincide. This behaviour is thought to be due to the competing effects of the change in the density and the energy density of the fuel in the liquid state. An increase in the energy density tends to increase the fuel pressure. On the other hand an increase in the specific volume of the fuel caused by more void addition or otherwise has the opposite effect. The increase in the total energy becomes very slow beyond 7% void volume and therefore the energy density factor becomes increasingly over shadowed by the fuel density factor. At low void fractions the energy density factor dominates whereas when the void fraction is high the density factor plays the major role. At about 7% initial uniform void addition, the two factors balance each other. Above this percentage the pressure begins to decrease with increase in the void fraction and ultimately the void space becomes large enough to accommodate production of the vapour-liquid state. Further addition of void simply increases the fraction of the vapour in the two-phase state fuel.

The pressure in the inner-outer core interface cell(9,16)

also exhibits similar behaviour, but the reversal happens at a much lower void percentage. The high-pressure point at 7% in fig-65 for the real motion model, is due to the single-phase fuel resulting from the compression of cells in this location, by the outwardly moving mesh cells on the inner side of the interface. The two curves in fig-61 coincide earlier than the curves for the core centre because away from the centre the mechanical energy transfer , pressures and hence the mesh distortion is relatively very small. Obviously the less the motion of the material, the less the effective differences between the two motion models.

The void volume fraction at which the fuel pressures associated with the two motion models behave nearly identically, varies with the severity of the accident. For an excursion driven by a reactivity insertion rate of \$70 /s, the discrepancy in pressure variation at the core cenre disappears when the void volume exceeded 13% (fig-68), which increases to about 18% (fig-86) in the case of a \$ 100 /s excursion. Away from the centre, the difference in pressures disappears at lower void fractions. In the inner-outer core interface cell(9,16), this happens above 8% (fig-69) and 10% (fig-87) in the cases of \$70 /s and \$ 100 /s excursions respectively.

Thus it can be concluded that the discrepancy between the end pressures given by the real and virtual motion models effectively disappears when large void spaces are present initially in the FFTF core.

6.3.3 Reactivity

As long as the motion reactivity feedback remains small the variation with time of the Doppler and the net reactivities associated with the real and the virtual motion models also remain small. As the displacement feedback becomes large, the time variation of both Doppler and net reactivities become different in the two models.

6.3.3.1 Doppler Feedback:

Upto the time when the power begins to decrease, the Doppler effect dominates the reactivity feedback processes. During this period the fuel temperature continues to increase everywhere, but beyond this point the increase slows down and so does the magnitude of the Doppler feedback. At this stage the reactivity feedback due to material motion, whether real or virtual, starts to increase rapidly and dominates the course of the nuclear excursion.

The Doppler reactivity tends to follow the trend of the total energy variation rather than the temperature of a particular mesh cell. The magnitude of the feedback depends upon both the percentage of the void volume and the choice of the motion model.

Fig-70 shows the maximum reactivity feedback due to Doppler effect as a function of the initial void fraction, in the case of a \$70 /s excursion.

In both motion models the Doppler feedback values decrease at decreasing rates with increase in the void fraction in the core. Upto about 6% initial void addition, the discrepancy between the two curves increases steadily; but after reaching a maximum, it decreases with more void addition until it disappears at about

11%. Upto this percentage, the feedback due to the virtual motion model remains lower in magnitude than the real motion case. Above 11% void volume, the feedback from the former becomes slightly greater than from the latter. This behaviour is consistent with the variation of fuel temperature with void percentage in fig-70. Upto 7% the temperature from the former remains lower than from the latter model but after that the temperature from the virtual motion becomes higher. At still higher void fractions, the two models give practically identical temperatures.

However the cross-over of the Doppler reactivity curves does not occur at the same void fraction as that for the central temperature curves. This is because the temperature cross-over is limited to the central region of the core, while the fuel temperature continues to rise steadily in the rest of the core. Since the Doppler feedback is averaged over the whole core, the decreased contribution from the centre is compensated by the increased contribution from the rest of the reactor core.

6.3.3.2 Motion Feedback:

A plot of the end of disassembly motion feedback, similar to fig-67, does not allow meaningful conclusions to be drawn. This is because the motion feedback increases very rapidly near the end, whereas the Doppler feedback tends to level off at this time. The variation of the former, during a time step, becomes too large and any meaningfull comparison would require very small, and so inefficient, time steps near the end of the disassembly. Since pressures and energies are the prime source

of interest in the LMFBR accident analysis, and these vary slowly near the end, the inaccuracy in the motion feedback is not expected to affect the end results significantly.

The variaton of the motion reactivity with time is shown in fig-63b for uniform initial void additions of 4%, 6%,9% and 13% in the case of $70 /s excursion. Unlike the Doppler feedback, the motion feedback is directly related to the material motion; therefore it is expected to be more sensitive to changes in the void volume.

For approximately the first two thirds of the disassembly time the reactivity feedback increases very slowly in magintude but in the last part, it increases at an increasing rate. At a fixed void volume, the discrepancy between the real and the virtual motion reactivity feedback increases as the disassembly progresses in time and becomes greatest at the end.

In the 4%, 6% and 9% cases in fig-63b, the gradients of the virtual motion curves change at a faster rate than those of the real motion curves. However, the difference in the rates decreases as the void volume increases. Therefore, motion reactivity curves corresponding to the two motion models tend to approach each other as the void volume fraction becomes larger.

In the 13% void case in fig-63a, upto about 1.5 millisecond into the disassembly, the two curves behave identically but then the reactivity feedback from the virtual motion curve increases at a higher rate than that in the real motion curve. After 2.5 millisecond, the change in slope becomes very small in the former whereas, it continues to change normally in the latter. Thus

near the end the slope of the former becomes less than that of the latter. The two curves therefore intersect at about 2.9 millisecond. Since the motion reactivity feedback is important near the end of the disassembly, the net reactivity changes more slowly near the end in the virtual motion model for the 13% void case. This prolongs the disassembly time.

This behaviour is due to the fact that the displacement reactivity feedback in the virtual motion model is related directly to pressure gradients in the core, whereas in the real motion model, it is related to the actual displacement of the materials. In this range of the initial void percentages, the end pressures in the virtual motion model tend to decrease with the addition of more void. In most cases of the real motion model, even when the accelerating pressure gradients become very small, the momentum gained earlier in the disassembly continues to displace the material outwards with the result that the displacement reactivity feedback continues to increase steadily. This becomes more pronounced as the disassembly nears the termination point.

6.3.4 Total Power:

The time variation of total power depends mainly on the variation of net reactivity of the reactor. When the negative feedbacks are small, the net reactivity and consequently the power are governed by the input reactivity function. Therefore in the early part of the disassembly, reactor power variation associated with the real and the virtual motion models remains nearly identical. As motion becomes more effective, the

reactivities change at different rates in the two motion models and therefore the power variations also behave differently. igs 29 and 55 show the time variation of reactor power associated with the two motion models for various void fractions, in the case of $70 /s excursion.

When the void percentage is small (<5%), the time variation of power in the two models differs markedly; but as the percentage becomes high, the difference tends to disappear.

When the void exceeds 5%, very little change occurs in either the power level or the time at which it reaches the peak. However, the maximum power level in the virtual motion model remains slightly lower than in the real motion model. This is because the high single-phase state, pressures in the former occur slightly earlier than in the latter. It is also apparent from figs 29 and 49 that in the moderate void region, power variation in the former model is more affected by change in the void fraction than in the latter model. This is because the end pressure is very sensitive to change in the void fraction in the virtual motion model.

Above 7% void volume addition in the real motion model, power variation with time becomes less sensitive to change in the void percentage and the disassembly tends to end at the same time. In the virtual motion model this happens at larger void fractions (>13%), when the relatively high single-phase pressures no longer appear in the central region of the core. The power decreases at a lower rate than in the real motion model and therefore the disassembly takes longer to terminate. The initial power level

affects the disassembly also through the Doppler reactivity feedback. At the start of the disassembly and in the absence of heat transfer, the temperatures are dictated by the initial power level and its spatial distribution. The higher the initial power, the larger the Doppler feedback and therefore the greater the restraining effect on the rate of power increase. The small Doppler feedback associated with the low initial power level helps to prolong the disassembly phase and results in increased energy generation.

6.3.5 Total Energy:

The variation of total energy during core disassembly driven by \$70 /s ramp reactivity insertion, is shown in figs 30 and 50 in the real and virtual motion models respectively. For about two thirds of the disassembly time, the energy increases in nearly a linear way but gradually levelling off to a maximum. This linear part corresponds to the nearly flat parts of the power vs time curves in figs 29 and 55 for the real and the virtual motion models respectively. The linear parts of figs 30 and 50 remain coincident for a long time and most of the energy generation occurs during this time. The two energy curves diverge when the corresponding power variations become different.

The maximum energy has been plotted also as a function of the initial void fraction in figs 71 and 89 for the \$70 /s and \$ 100 /s excursions respectively. These show that the maximum generated energies, obtained by using the real and the virtual models, increase rapidly initially for an increase in the pre-set void volume fraction but tend to reach a maximum value at large

void fractions.

In the $70 /s excursion case, the two curves nearly coincide at approximately 10% void volume whereas, in the $ 100 /s case this happens when the void volume exceeds 12%. In the first case the maximum discrepancy occurs at a void volume of 6.5% whereas in the second case this happens at about 7%. Upto this percentage the slope of the real motion curve is greater than that of the virtual motion curve but above this percentage the slope of the former curve becomes less than that of the latter. This means that below this void volume fraction the sensitivity of total energy to the void fraction is greater in the real model than in the virtual motion model, but above that the energy becomes more sensitive in the latter. At 10% void volume and above, the slopes of the two curves become nearly identical.

The magnitude of the energy in the virtual motion model remains smaller than in the real motion model for void volumes less than 10% with the maximum difference occuring at about 6%. In the virtual motion model this is the void percentage at which both the end pressure at the centre and the Doppler reactivity feedback also reach their maximum values.

6.4 DYNAMIC INITIAL FLUX DISTRIBUTION:

The results of two group neutron diffusion calculations, using the code NEST, are presented in figures 90 to 93. The quasi-steady state radial flux distributions are compared with steady state fluxes predicted by the code MARC. The comparison shows that in the core region. the radial flux distribution for the upper energy group, predicted by NEST, is lower in magnitude than estimated by MARC, but in the unfueled region the former predicts a slightly higher flux than the latter. In the lower energy group, the flux distributions are similar in the core, but in the reflector region, NEST predicts a higher distribution than MARC.

The overall behaviour of the flux distribution implies that the energy spectrum of the NEST flux is softer than the MARC flux spectrum. This softening of the flux is a natural consequence of solving the time dependent equation.

The MARC flux distribution is obtained by solving the stationary eigenvalue equation:

$$L\,\phi_{eff} = \frac{1}{k_{eff}}\,M\,\phi_{eff} \qquad (6.1)$$

where the operators L and M represent total loss and total production, respectively. This equation describes the actual reactor configuration but which is made critical, if not already in a critical state, by a fictitious value of k_{eff}. The steady state flux distributions and the neutron multiplication factor k_{eff} correspond to the lowest lambda mode (reactivity mode) obtained by solving the, instantaneously, stationary equation

$$L(t)\ \phi = \frac{1}{\lambda} M(t)\ \phi \qquad (6.2)$$

The eigenvalues of this equation are modified by the delayed neutrons.

The NEST flux distributions correspond to solutions of the time dependent neutron density equation:

$$\frac{\partial N}{\partial t} = K\ N \qquad (6.3)$$

The operator K encompasses both removal and production. This equation also satisfies the omega mode eigenvalue equation:

$$K\ N = \omega_n N \qquad (6.4)$$
$$= \omega_n \frac{\Phi}{v}$$

Equation (6.3) can be written as:

$$\frac{1}{v}\frac{\partial \phi_n}{\partial t} = \frac{\omega_n}{v}\ \phi_n \qquad (6.5)$$

Solving the dynamic equation (6.5) is equivalent to varying the concentration of a $\frac{1}{v}$ absorber to achieve criticality. Therfore for a positive value of ω, the spectrum of the dynamic diffusion equation would become hardened, whereas for a negative value it would be softend in comparison with the static spectrum (Bell and Glasstone, 1971). In the present problem $\omega = -.119\ 10^{-6}$ and therefore, as expected, the dynamic neutron spectrum estimated by NEST is softer than the static spectrum predicted by MARC.

The behaviour of the flux convergence number D_ω is shown in fig-92. In the present problem the initial power and material compositions were specified, and therefore an arbitrary initial

distribution, flat in the reflector and a cosine in the core, was assumed to start the calculations. Since the initial fluxes are inconsistent, the frequencies ω_{gjk} vary widely. The convergence number D_ω measures the maximum discrepancy between the values. As the transients fade away, D_ω decreases rapidly and ultimately tends towards zero.

In the converged state, all frequencies tend to assume a single value which implies that all fluxes increase or decrease at the same rate.

6.5 SUMMARY

Results of computations using the codes BASIMA and NEST, were presented in this chapter. NEST solves the space dependent neutron kinetics equations by an alternating direction method. This code was used, in section-6.4, to calculate the dynamic initial flux distribution to initiate the disassembly code DISK. The flux distributions were compared with solutions of the stationary diffusion equations obtained by using the code MARK. The two results exhibit good agreement when the difference between static and dynamic solutions is taken into account.

The major part of the chapter was devoted to the results of disassembly calculations using BASIMA. In the first section, the results for the FFTF reactor model were compared with the reported results with VENUS-2. The overall behaviour of the two codes was found to be similar. In the second section, the effects of void distribution on the core disassembly were investigated. The disassembly was found to be highly sensitive to the void content in the core. However, this sensitivity

decreased steadily as the void fraction became increasingly high. In the third section, the differences between the results of the real and the virtual hydrodynamics were investigated. The results show that the discrepancy, arising from the two options, becomes high at moderate void fractions (6% to 8%) but tends to decrease at high void fractions. The results reemphasize the importance of the void spaces in the reactor during the core disassembly.

CHAPTER SEVEN

CONCLUSIONS

This study of the deterministic analysis of the LMFBR accident pertains, principally, to the disassembly phase of the HCDA. The results of the study were mainly produced by BASIMA, a point kinetics LMFBR disassembly code incorporating both real and virtual displacement models, developed for this study. To replace the point kinetic model in BASIMA, a spatial kinetics code NEST was also developed and incorporated in a disassembly code DISK. Testing of the different parts of DISK was made but full commissioning was not completed. Therefore results produced by BASIMA and NEST only were included in this study.

7.1 DISASSEMBLY CALCULATIONS WITH BASIMA:

The disassembly predictions by BASIMA for the FFTF reactor model compared well with similar calculations reported for VENUS-2 (Nicholson and Jackson,1974). The code was then used to study the effect of spatial void distribution and that of the material displacement models on the course of the disassembly phase of the accident.

The disassembly was found to be sensitive to the content and distribution of the void spaces in both the virtual and the real motion options. This sensitivity was higher in the case of greater voiding at the core centre than when the core was voided

uniformly. This was due to the implosive tendency caused by the low two-phase pressure in the central region in contrast with the high single-phase pressures in the outer regions. Even when the fluid fuel did not move inwards physically, preferential voiding of the central region led to a reduction of the velocities of the outwardly moving material and resulted in a slowing down of core disassembly and consequently a greater release of total energy. However, the sensitivity of the energy generation to voidage decreased steadily as the void volume was increased and ultimately became nearly insensitive to the void content.

Investigation of the effects of the choice between virtual and real hydrodynamics revealed that the disassembly with the former option was more sensitive to the void content than with the latter. The discrepancy between the results increased with the void fraction initially, but after reaching a maximum, tended to decrease rapidly and nearly disappeared at high void fractions. This discrepancy was found to depend, also, on the severity of the accident and the power distribution in the reactor.

In the case of an excursion driven by a \$70 /sec reactivity ramp, the maximum discrepancies in pressure and energy generation occurred around 6.5% uniform void addition. The difference in the total energies, in the two models, disappeared at about 10%, while the discrepancies in pressure disappeared at approximately 13% void volume addition. In the case of a \$100 /sec excursion, the maximum differences occurred at about 7% and disappeared at 12% for total energy, and 18% for pressure.

The behaviour of temperature with void addition was similar to that of the pressure. However, the temperature in the virtual model started from a lower value than in the real motion case. As the void volume increased, figs-59 and 76, the temperature in the virtual option continued to increase, while the other tended to level off. After reaching a maximum, the former started to decrease and approached the real option curve at high void fractions. In the low void range (< 8%), the temperature behaviour was similar in both the excursions but above 8% the discrepancy in temperatures due to the different motion models increased in magnitude and the peak of the temperature-void curve shifted towards the high_void side as the excursion increased in severity.

The differences in behaviour of the disassembly in the high void range became most conspicuous near the end of the disassembly. In this time range, sustained displacement of the materials resulted in a higher reactivity feedback in the real motion model than in the other.

However, in the high void range, the behaviour of pressure and temperature became similar in the two models and relatively insensitive to changes in the void content.

In the mesh cell lying at the middle of the core-reflector interface, where the power level was lower than at the centre, the discrepancy arising from the virtual and real motion options disappeared at lower void fractions than at the centre. In the $70 /s excursion case, the discrepancy in pressure disappeared above 8% void volume (compared with 13% at the centre) and in the

$100 /s case, it disappeared above 10% (compared with 18% at the centre).

These results reveal that the differences between the displacement feedback models become most effective when the fuel exists in the compressed liquid state. The high pressures in the real displacement model are relieved by the physical motion of the fluid material but in the other model these can only be relieved through compression of materials within a mesh cell by the local pressure. In the liquid state, the behaviour of specific volume of the fuel and its internal energy density determines the sensitivity of the disassembly to voiding. An increase in void volume increases the specific volume of the fuel and in conformity with the equation of state, tends to increase (upto $V_r = 1.0$) both the pressure and temperature of the fuel. On the other hand, an increase in the internal energy of the fuel tends to increase the two variables. However, the total energy becomes progressively insensitive to voiding. Therefore at low void volume fractions, the behaviour of pressure and temperature is primarily determined by that of the internal energy, but at high void fractions, the void factor predominates. The two competing factors gave rise to the peculiar shape of the pressure void curve, fig-79, for the virtual motion model.

However, the virtual motion model continued to underestimate the total energy generation, even when the void percentage became high. Although the discrepancy after disappearing initially increased slowly with void addition, its magnitude remained relatively small in the high-void range.

The conclusions reached so far were based on the simplifying assumption that the material reactivity worth distribution and the Doppler coefficient remain invariant with respect to the void content. Since the effect of coolant voiding on reactivity feedback depends upon the actual void distribution in the reactor, this was left to be investigated by DISK.

The Doppler coefficient would be expected to remain insensitive to the choice between the motion models, except through changes in the material densities in the real displacement option. Nevertheless, the relative difference in the total energy releases using void corrected Doppler coefficients in the two motion options is not expected to be too different than if invariance of the coefficient is assumed. The previous conclusions are expected to remain valid.

Therefore, it can be concluded that when the core is highly voided, virtual displacement codes like EXTRA can be expected to predict disassembly behaviour similar to that of the real motion codes, such as VENUS-2. But when the void content is small, the former model is expected to underestimate the total energy release and overestimate the pressure generation.

These conclusions were based on the results obtained by using an ANL type equation of state. The use of a vapour-liquid phase state equation, in the low void range, would obscure the effective differences between the two motion models. Thus if the code EXTRA is to be used even in the low void range, then a two-phase equation of state may be a better choice than an equation which caters for the single-phase state also.

7.2 SPATIAL KINETICS CALCULATIONS WITH NEST:

NEST was used to generate multigroup neutron flux distributions to initiate the spatial kinetics calculations by DISK. The dynamic initial distributions are obtained in NEST, by proceeding with space dependent kinetics calculations, but in which the total power is normalised after each time step. This normalization is suppressed when real time-advanced solutions are sought, during the disassembly or otherwise.

In this study, the dynamic flux distributions for an arbitrary reactor configuration, were compared with static distributions, obtained by using the code MARC. The comparison revealed that the energy spectrum of the NEST flux was softer than that of the MAR spectrum.

The difference has been attributed to the term $\frac{1}{v}\frac{\partial\phi}{\partial t}$, which produces an effect equivalent to that of a $\frac{1}{v}$ absorber. This term is positive or negative, depending upon whether the reactor is supercritical or subcritical. For positive omega mode eigenvalues, the spectrum of the dynamic spectrum becomes hardened and for negative values it becomes softened in comparison with the static flux spectrum (Bell and Glasstone,1971).

Therefore in the supercritical state, at the start of the disassembly phase, the energy spectrum of the dynamic flux is expected to be harder than the spectrum obtained by solving the static neutron balance equations.

The effect of the $\frac{1}{v}$ absorber is proportional to the magnitude of the omega mode eigenvalue, associated with the equation, and therefore the discrepancy between the dynamic and

the static spectrums is expected to be greater for excursions driven by larger reactivity inputs.

The use of the static spectrum for initiating the disassembly phase would imply an underestimation of the driving reactivity and consequently also of the total energy release.

TABLE - 3 INITIAL MATERIAL DENSITIES

	Fuel (g/cm^3)	SS (g/cm^3)	Sodium (g/cm^3)
Core	10.0	7.92	0.85
Radial Reflector	0.0	8.35	0.85
Axial Reflector	0.0	8.25	0.85

TABLE-4 INITIAL VOLUME FRACTIONS OF MATERIALS

	Fuel	SS	Sodium
Core	0.333	0.252	0.39
Radial Reflector	0.0	0.702	0.275
Axial Reflector	0.0	0.582	0.39

TABLE - 5 REACTIVITY INPUT AND INITIAL POWER*

Initial Condition	Over-Power Accident	Loss of Flow Accident
Power	$7.806\ 10^{11}$ W	$6.101\ 10^{10}$ W
Step Reactivity	1.09 $	1.01 $
Ramp Reactivity	100 $/s	20 $/s

* (Nicholson and Jackson , 1974)

TABLE - 6 DELAYED NEUTRON PARAMETERS*

Group	β_i	λ_i (s^{-1})	Delayed Neutron Concentrations (TOP) 10^{12}(W)	(LOF) 10^{12}(W)
1	0.00008	0.013	4.998	4.81
2	0.00063	0.0316	17.7	16.25
3	0.00057	0.136	5.567	4.12
4	0.00107	0.344	6.811	3.83
5	0.00049	1.33	7.16	2.245
6	0.00017	3.61	0.668	0.166

$\beta = 0.00301$

$\Lambda = 5.0\ 10^{-7}$ s

TABLE-7

EFFECT OF VOID CONTENT ON THE DISASSEMBLY AS PREDICTED BY VENUS-II

FOR A 100 DOLLAR/SECOND REACTIVITY EXCURSION

Temp Rise to Fill Voids (° K)	Total Energy (MJ)	Peak Power (10^{12} W)	Time at Peak Power (μs)	End Central Pressure (atm)	End Centre Temprature (° K)	Void Volume Weighted	Void At Core Centre
No Void	563	0.861	260	3.8	4104	2.2%	2.2%
500	1310	1.073	840	37.6	4906	3.8%	3.55%
1000	1870	1.187	1280	126.2	5509	5.2%	5.1%
1500	2370	1.217	1500	287.0	6037	6.9%	7.05%
2000	2580	1.217	1510	382.0	6253	8.5%	9.2%
No Sodium	2620	1.206	1500	399.0	6287	Fully	Voided

TABLE-8

EFFECT OF VOID CONTENT ON THE DISASSEMBLY AS PREDICTED BY BASIMA

FOR A 100 DOLLAR/SECOND REACTIVITY EXCURSION

Uniform Void Addition	Total Energy (MJ)	Peak Power (10^{12} W)	Time at Peak Power (μs)	End Centre Pressure (atm)	End Centre Temperature (K)
2%	486	0.836	200	2.8	4021
3%	1013	1.003	620	17.0	4588
4%	1442	1.1204	920	51.4	5046
6%	2138	1.120	1280	200.4	5792
8%	2524	1.201	1320	356.6	6199
10%	2576	1.201	1320	379.8	6248
12%	2592	1.201	1320	387.4	6263
18%	2606	1.200	1320	393.4	6277

TABLE-9

EFFECT OF VARIATION OF THE DOPPLER COEFFICIENT ON DISASSEMBLY

OF THE FULLY VOIDED CORE

Doppler Coefficient	Total Energy	Peak Power	Time at Peak Power	End Centre Pressure	End Central Temprature	Initial Power	Reactivity Step	Reactivity Ramp
T dk/dT	(MJ)	(10^{12}W)	(μs)	(atm)	(K)	10^{12}W	($)	($)
-0.004	2606	1.200	1320	390.0	6269	0.7806	1.09	100
-0.0025	3301	1.876	1700	874.0	7007	0.7806	1.09	100
-0.0025	2620	1.206	1500	399.0	6287	0.6101	1.01	20

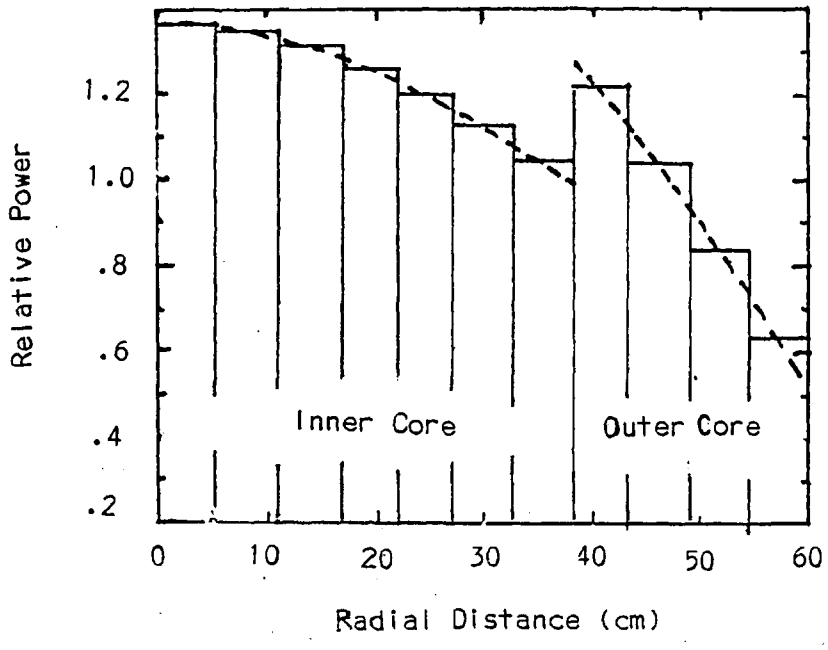

FIG-9 Radial and Axial Power Distribution for Both BASIMA and VENUS-II

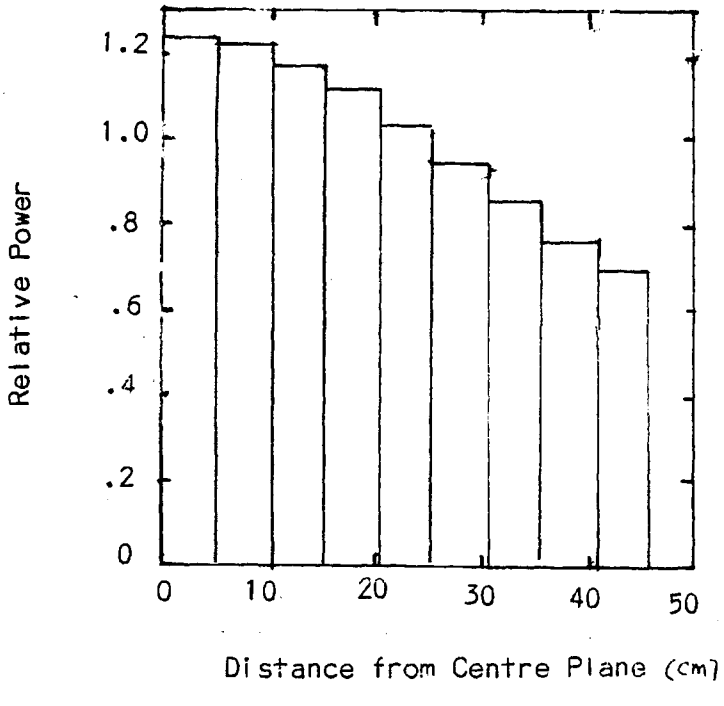

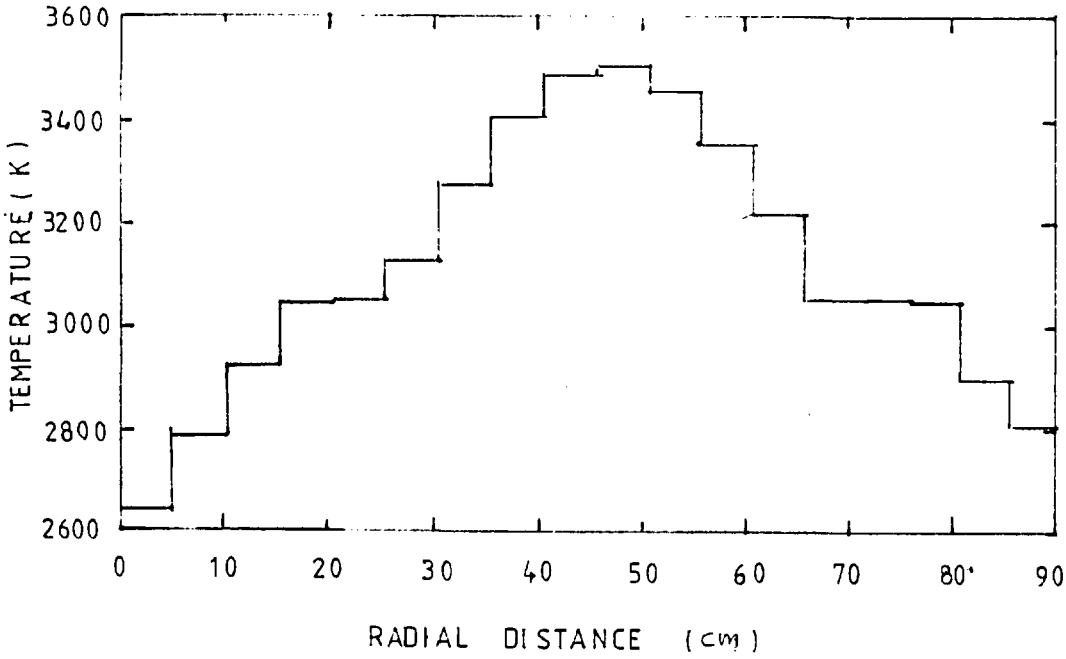

FIG - 10 RADIAL AND AXIAL TEMPERATURE DISTRIBUTIONS

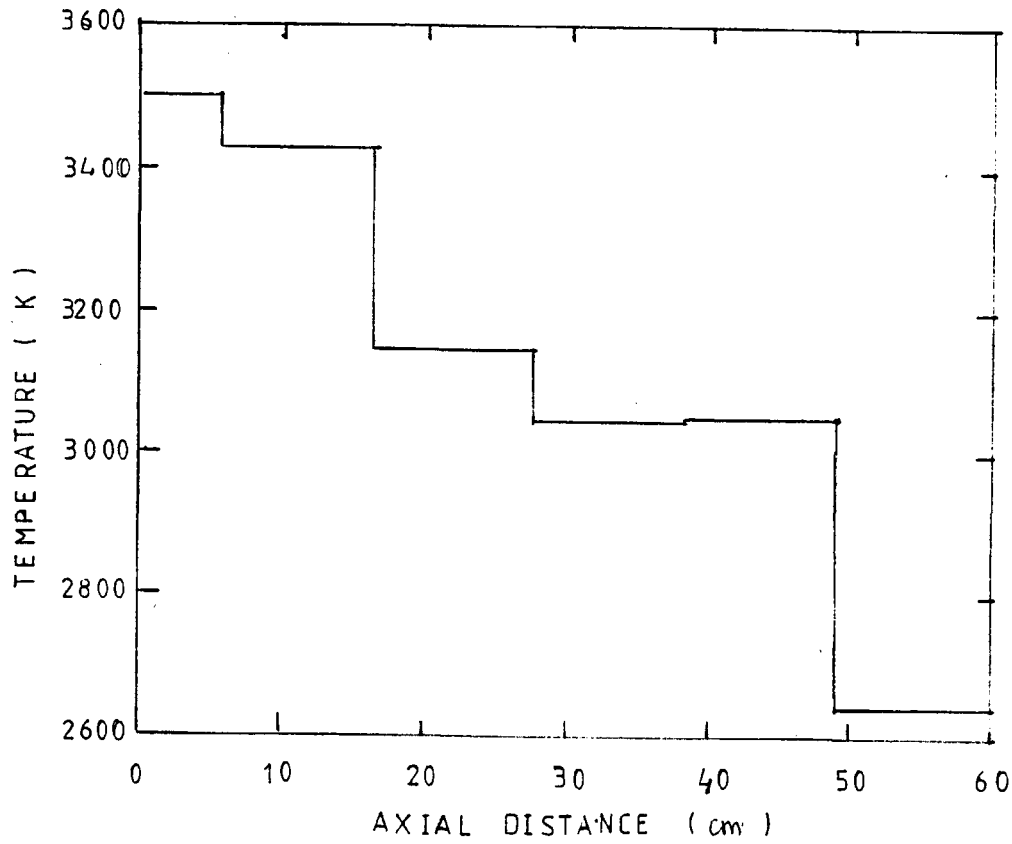

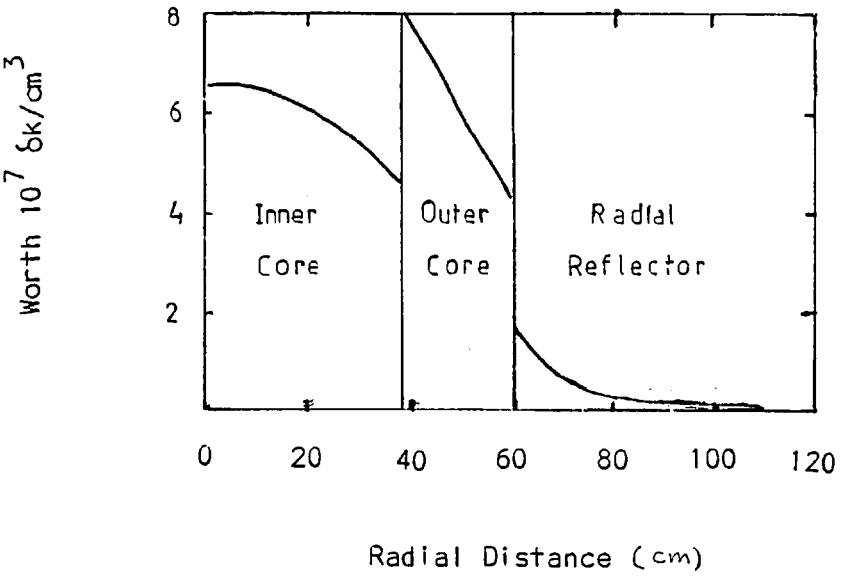

FIG-11 MATERIAL REACTIVITY REACTIVITY WORTH DISTRIBUTION

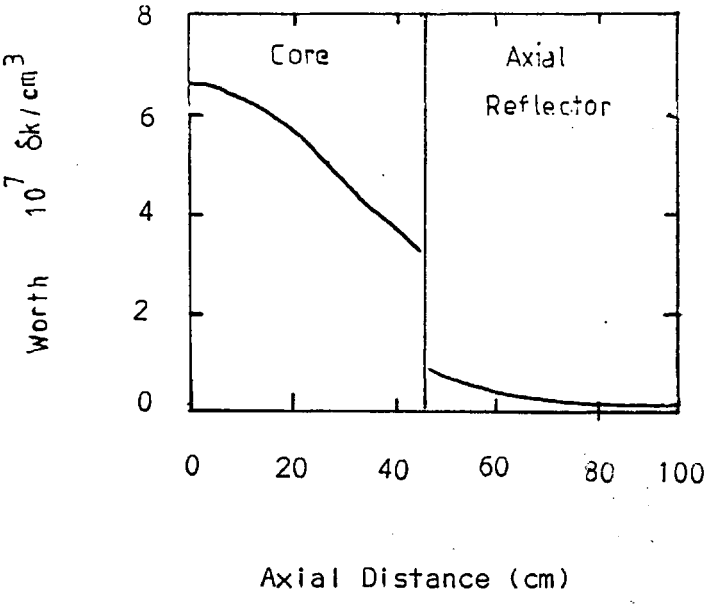

Fig- 12 Central temperature at end of disassembly from BASIMA and VENUS-II as a function of void

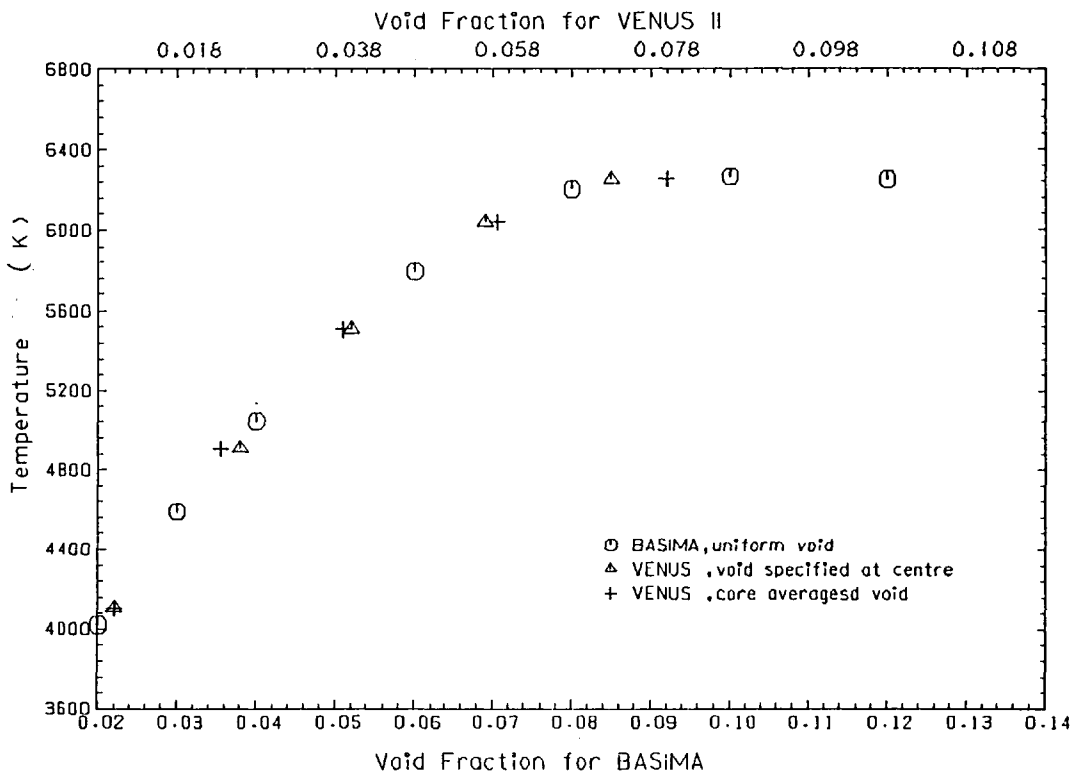

FIG-13

Central Temperature Predicted by BASIMA and VENUS-II

During Core Disassembly Driven by 100 $/s Reactivity

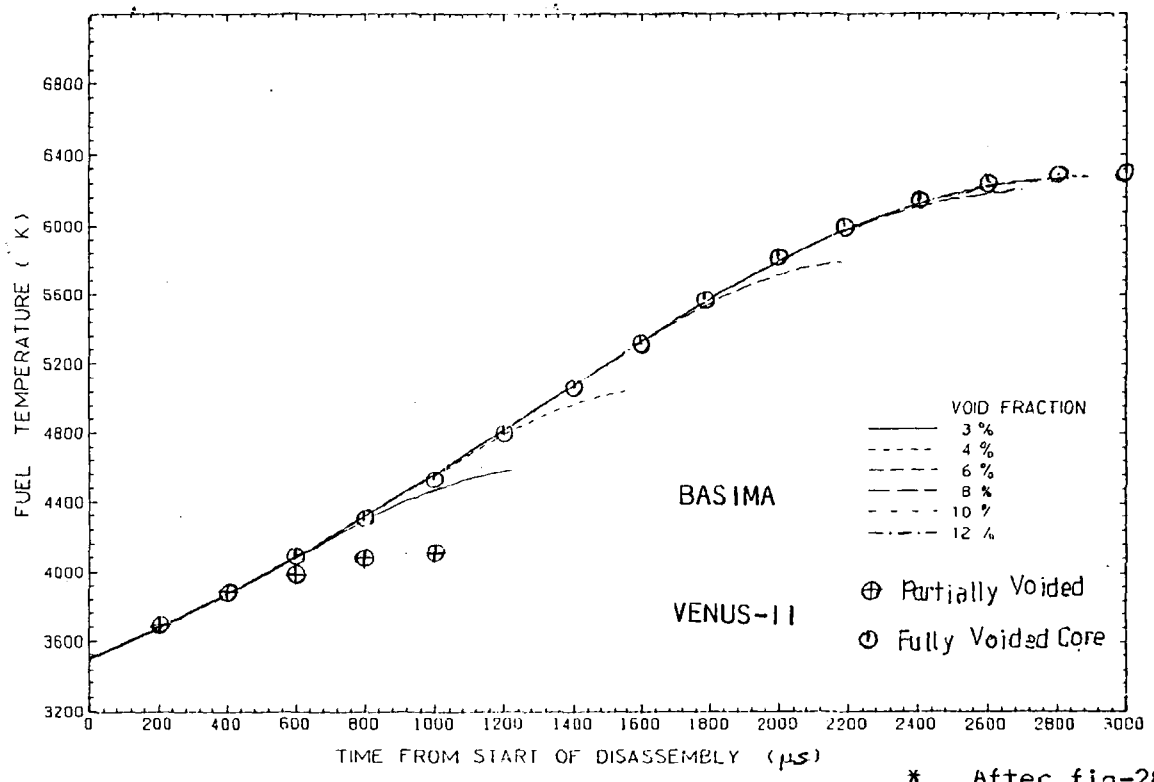

* After fig-28 (Nichlson and Jackson 1974)

** After fig-41 " " "

Fig- 14 Central pressure at end of disassembly from BASIMA and VENUS-II as a function of void

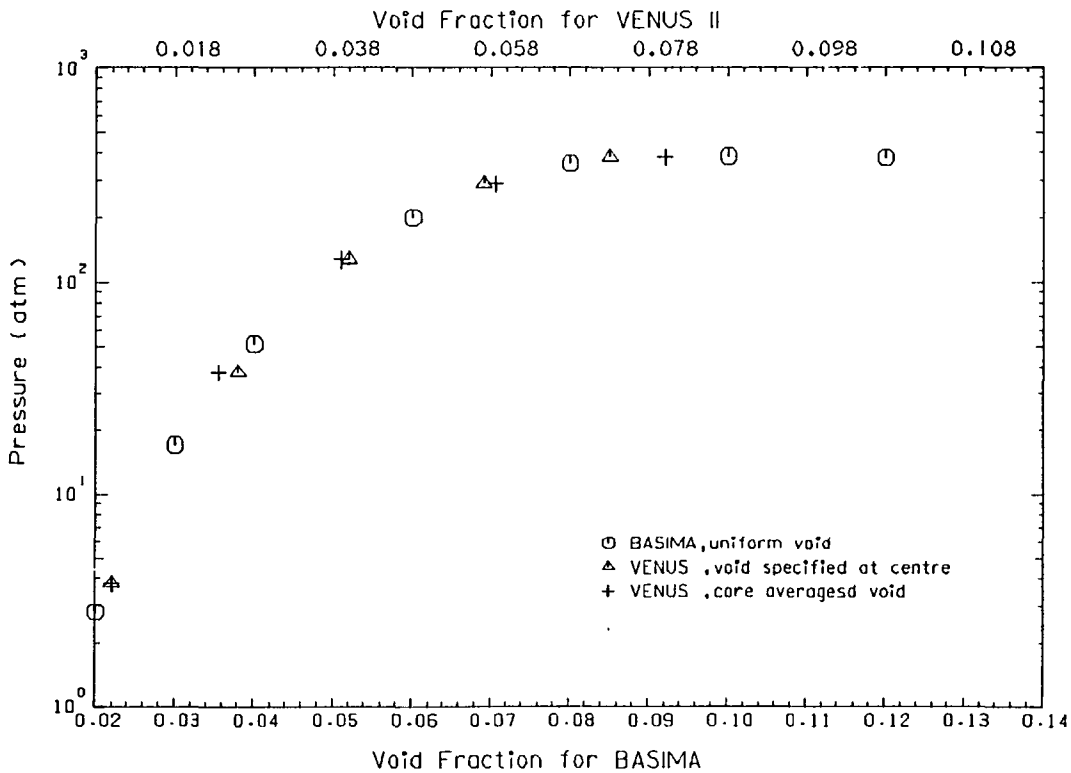

Fig -15 Peak power reached during disassembly, using BASIMA and VENUS-II

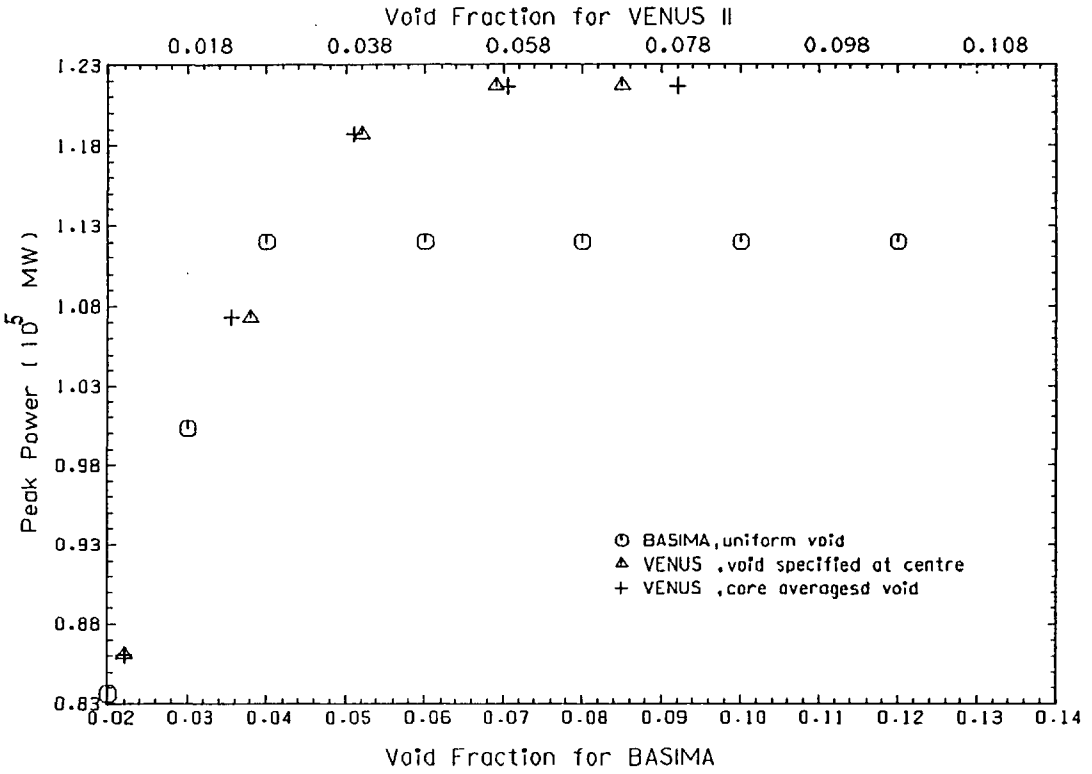

Fig-16 Time at peak power as a function of void fraction, in BASIMA and VENUS-II

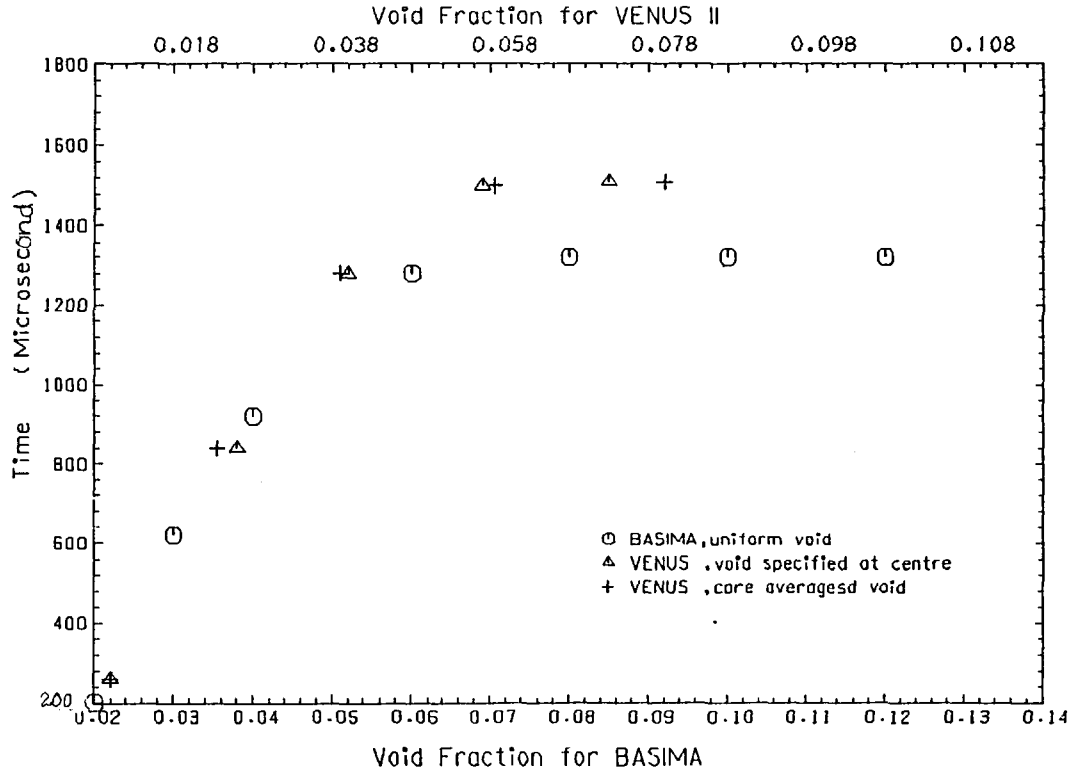

Fig_17 Total energy generated during disassembly, using BASIMA and VENUS-II

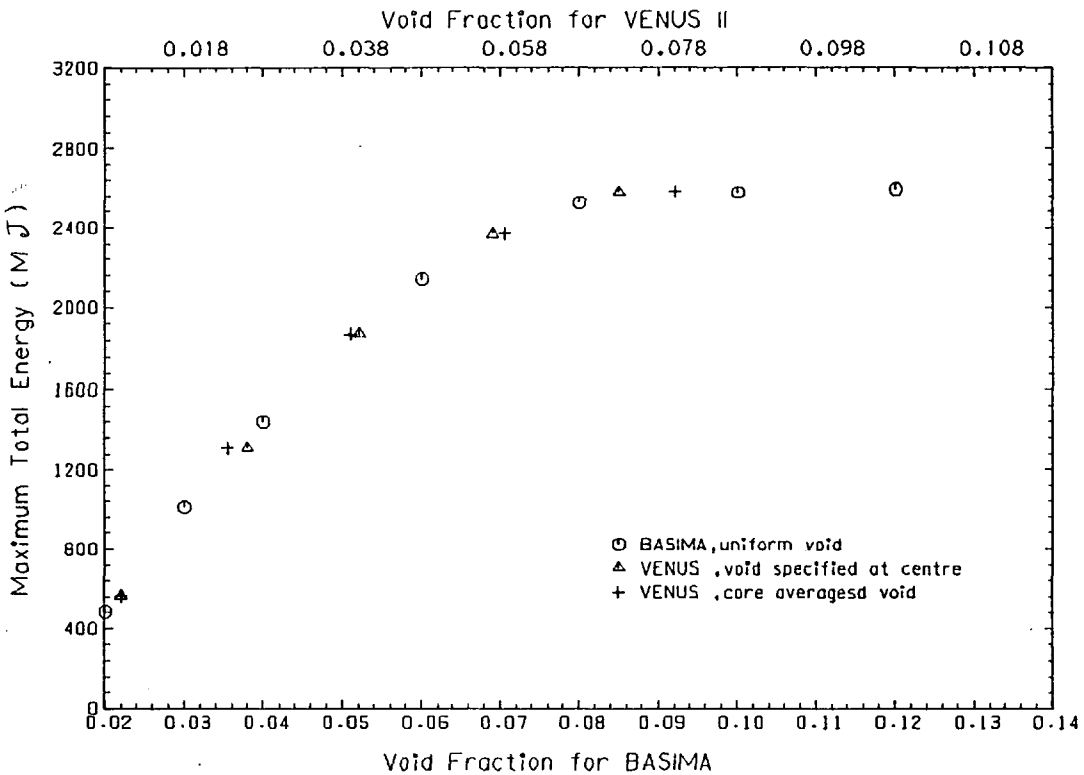

FIG 18 FUEL TEMPERATURE VARIATION DURING DISASSEMBLY OF A CORE HAVING AN ADDITIONAL VOID OF 3%, USING THE REAL MOTION MODEL

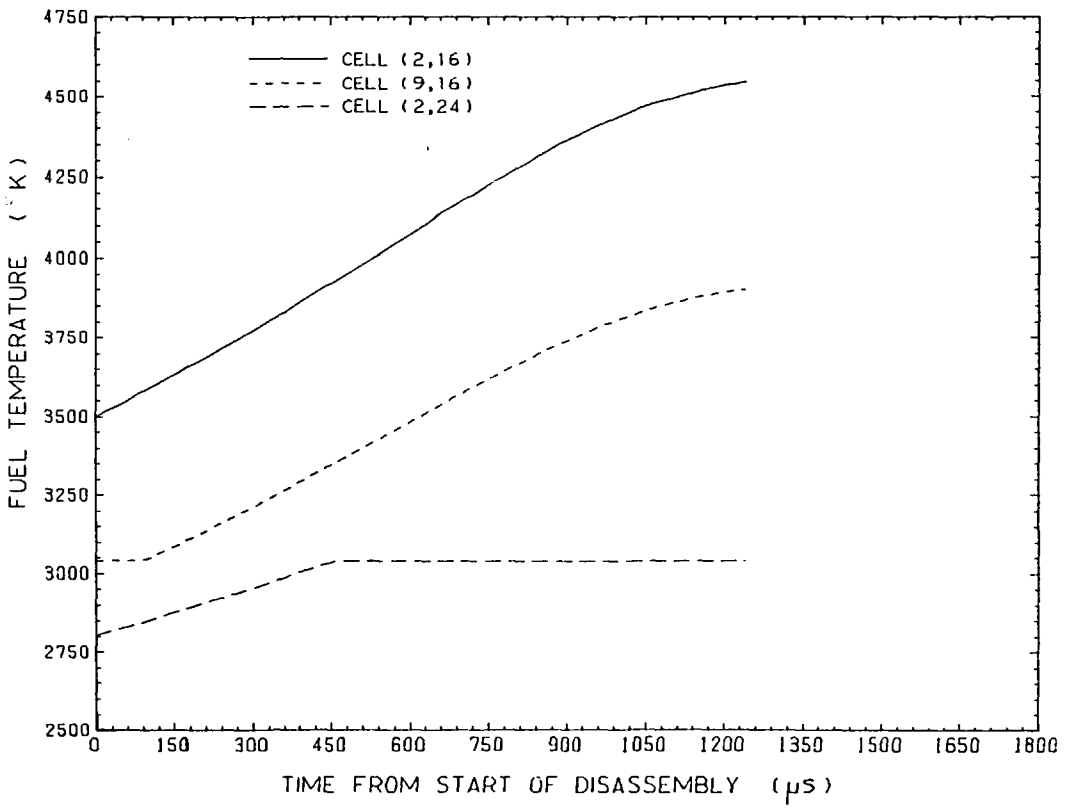

FIG-19 FUEL TEMPERATURE VARIATION DURING DISASSEMBLY OF A CORE HAVING AN ADDITIONAL VOID OF 6% USING THE REAL MOTION MODEL

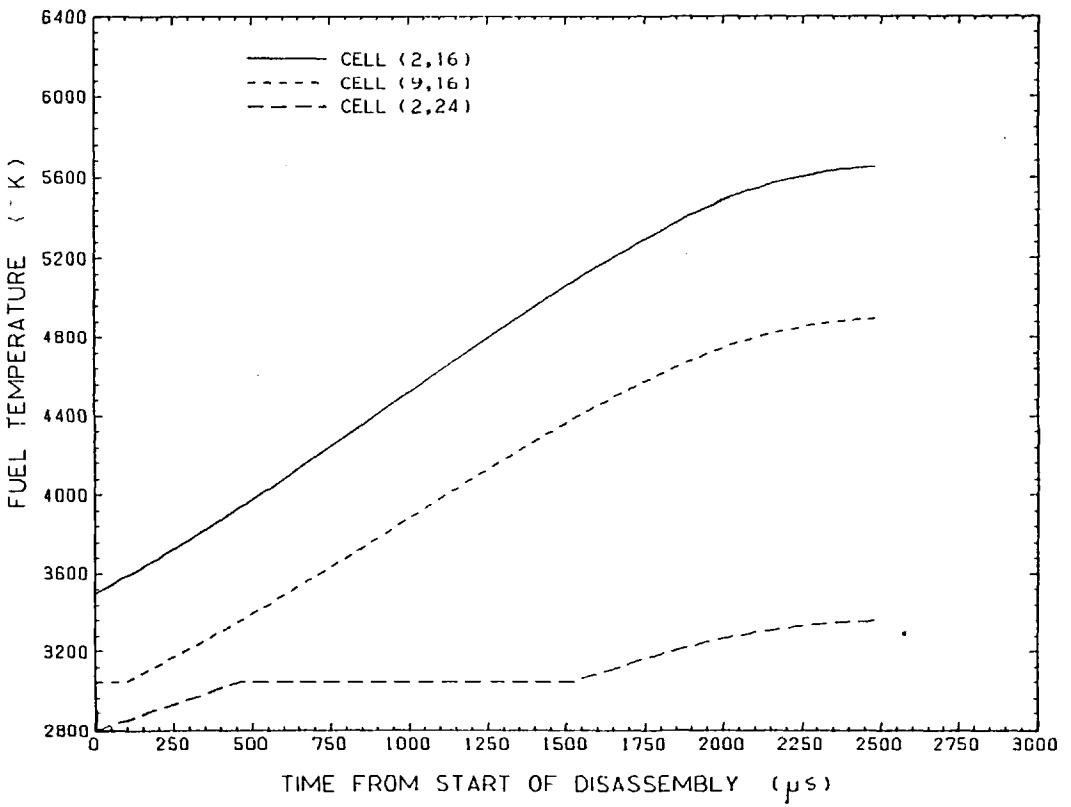

FIG-20 FUEL TEMPERATURE VARIATION DURING DISASSEMBLY OF A CORE HAVING AN ADDITIONAL VOID OF 8% IN THE REAL MOTION MODEL

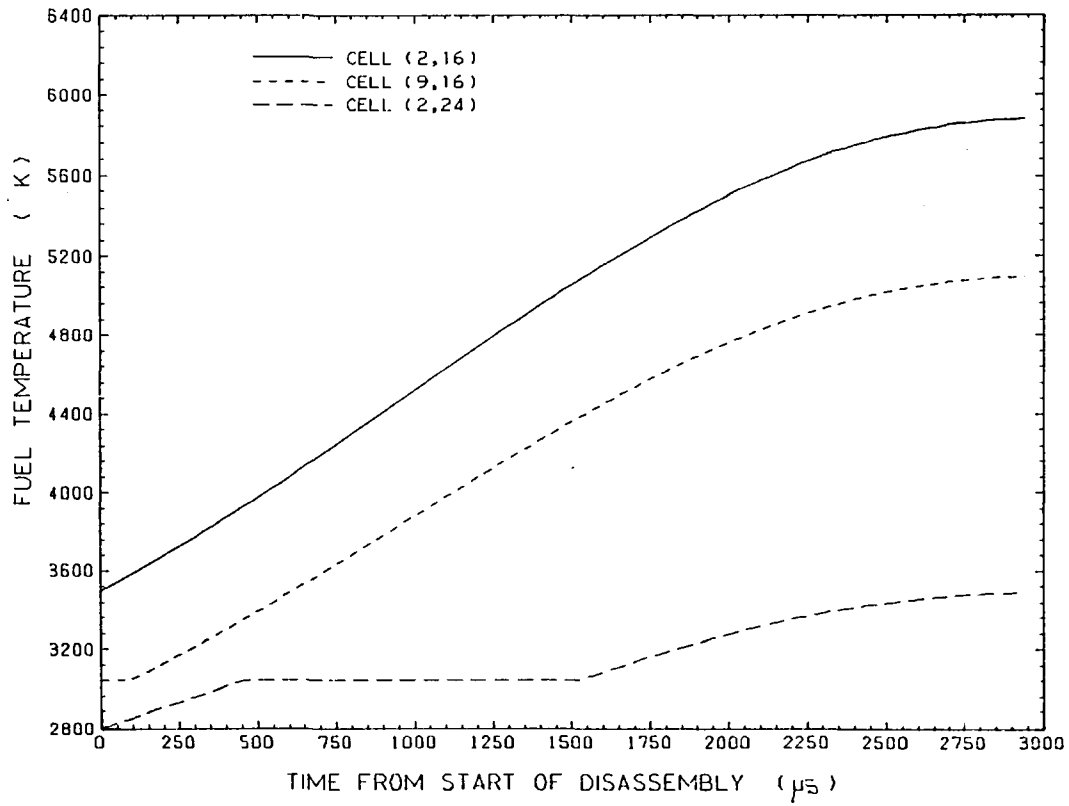

FIG-21 FUEL TEMPERATURE VARIATION DURING DISASSEMBLY OF A CORE HAVING AN ADDITIONAL VOID OF 10% IN THE REAL MOTION MODEL

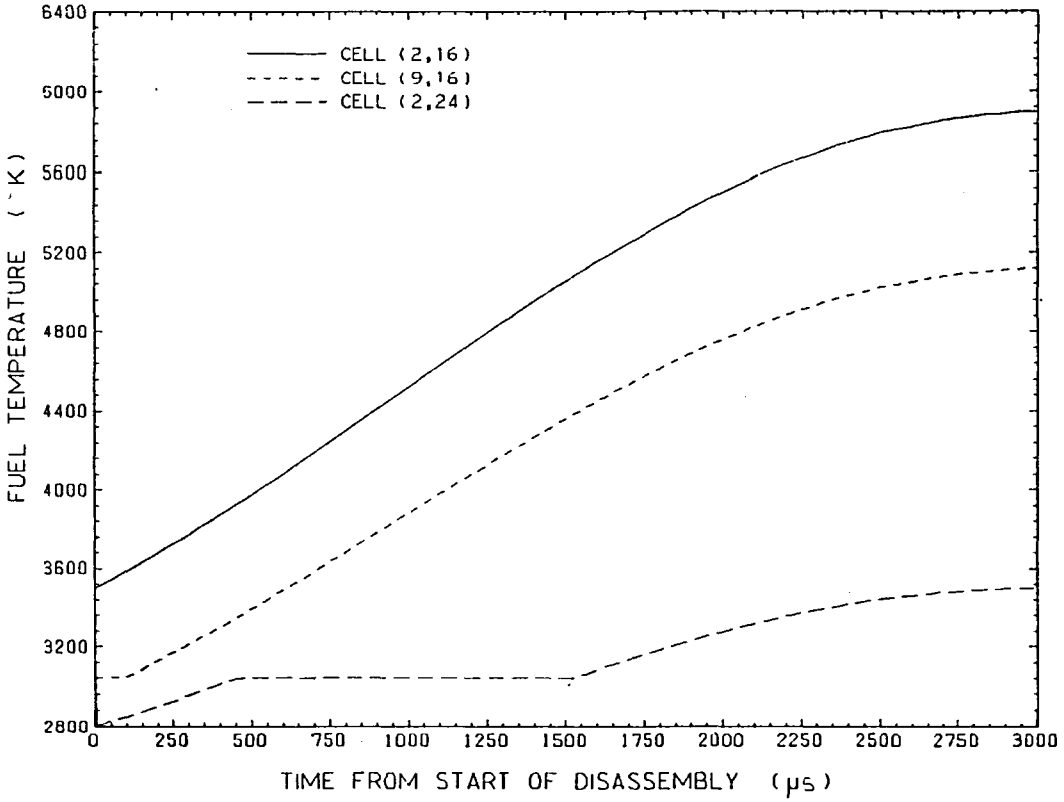

FIG_22 FUEL PRESSURE VARIATION WITH TIME AT THREE POSITIONS IN A CORE HAVING AN ADDITIONAL VOID OF 3% USING THE REAL MOTION MODEL

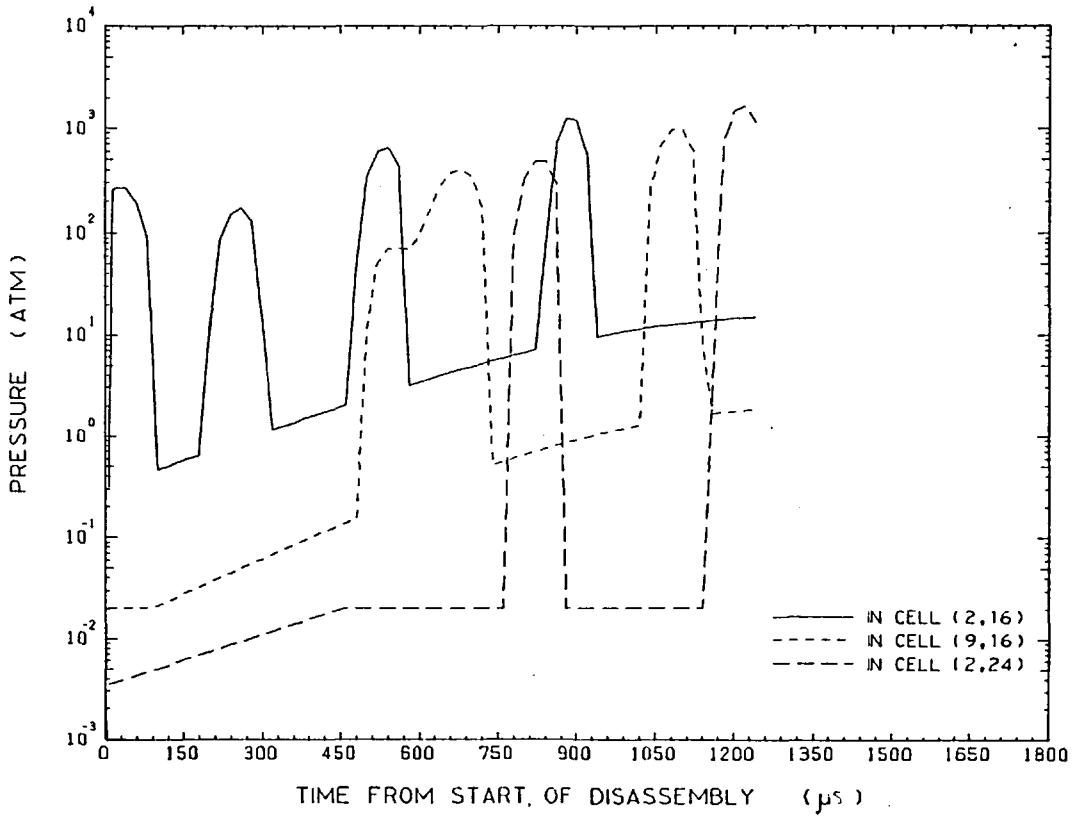

FIG-23 FUEL PRESSURE VARIATION WITH TIME AT THREE POSITIONS
IN A CORE HAVING AN ADDITIONAL VOID OF 6% IN THE REAL MOTION MODEL

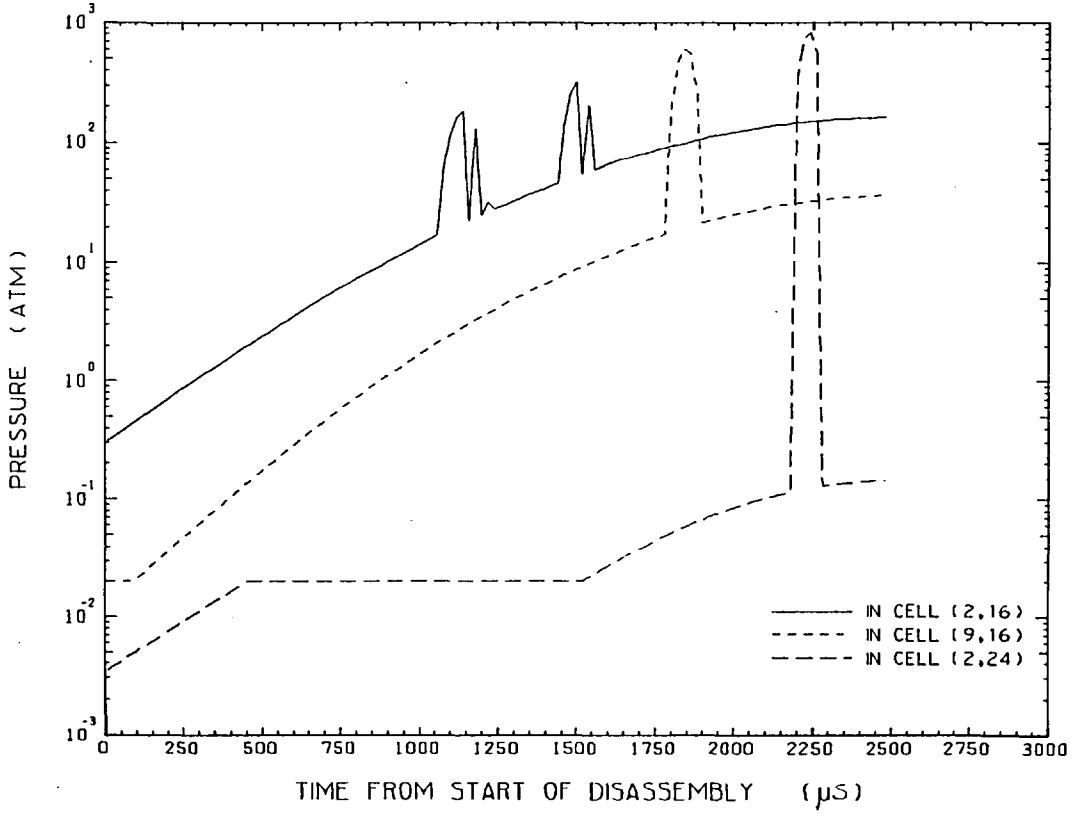

FIG-24 FUEL PRESSURE VARIATION WITH TIME AT THREE POSITIONS
IN A CORE HAVING AN ADDITIONAL VOID OF 8% , IN THE REAL MOTION MODEL

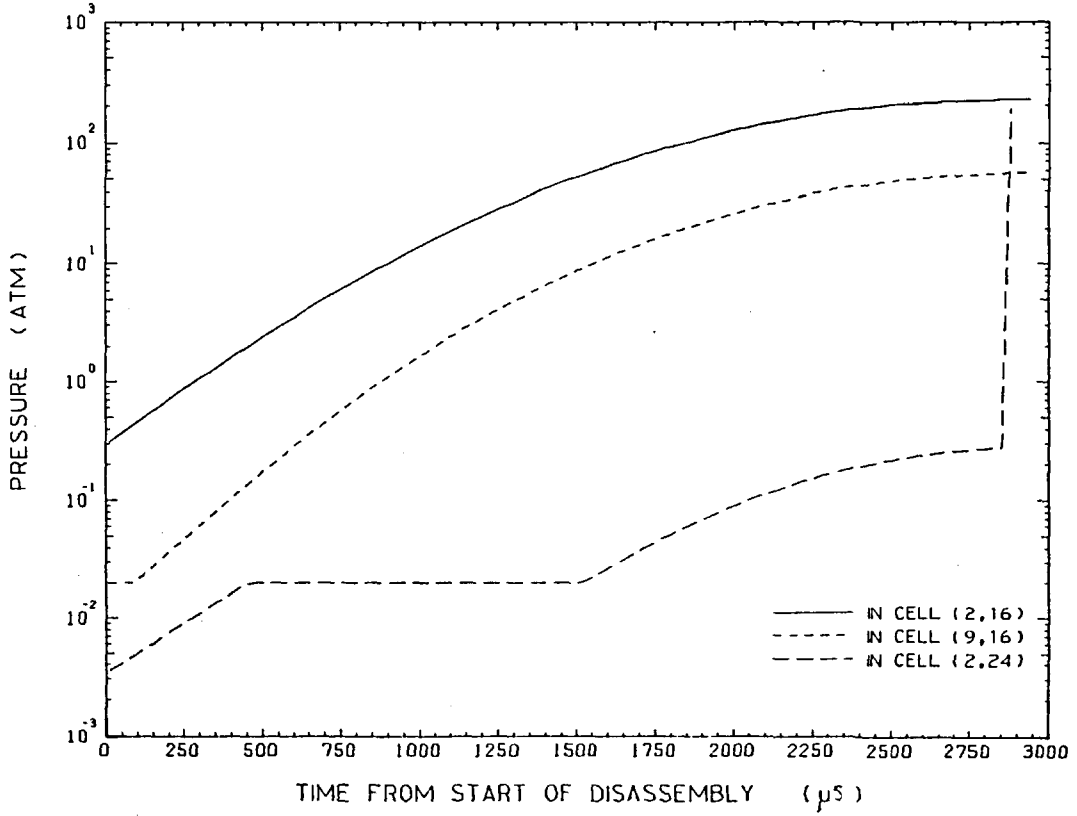

FIG-25 FUEL PRESSURE VARIATION WITH TIME AT THREE POSITIONS IN A CORE VOIDED BY 10% , IN THE REAL MOTION MODEL

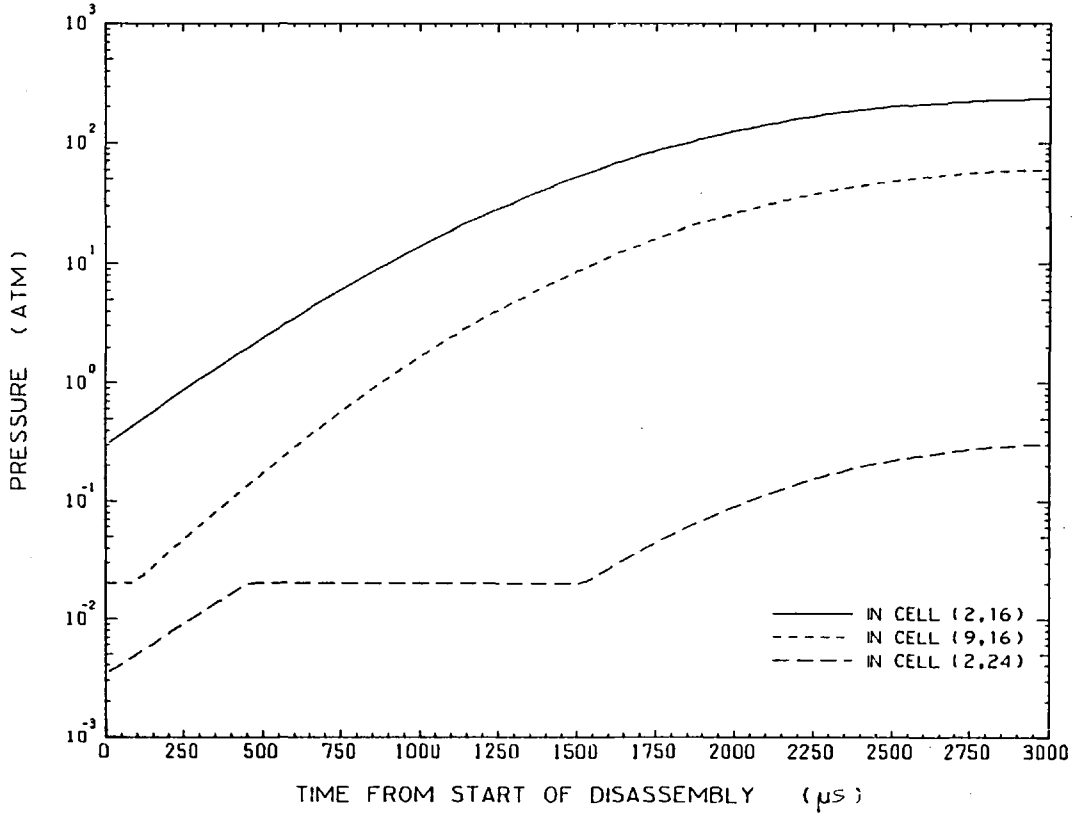

FIG-26

Variation of Doppler Reactivity with Time During Disassembly of a Uniformly Voided Core, Driven by 70 $/s. Reactivity Assuming Real Motion

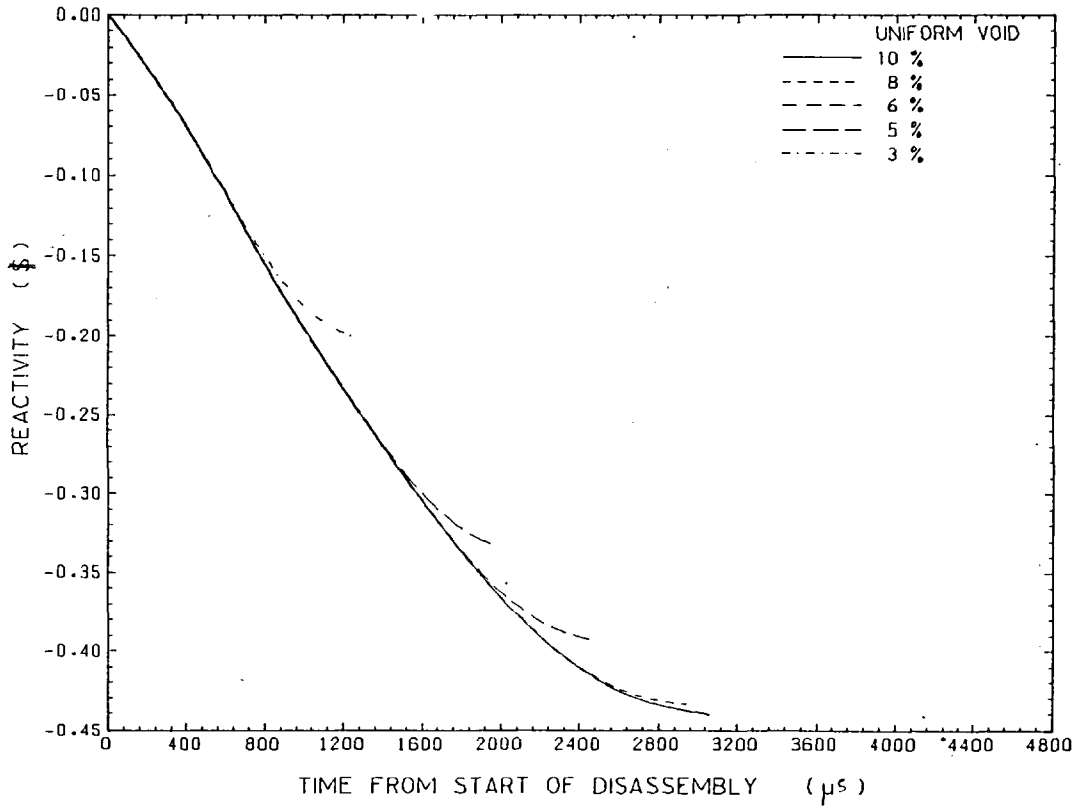

FIG-27

Variation of Displacement Reactivity with Time During Disassembly of a Uniformly Voided Core, Driven by 70 $/s Reactivity Assuming Real Motion

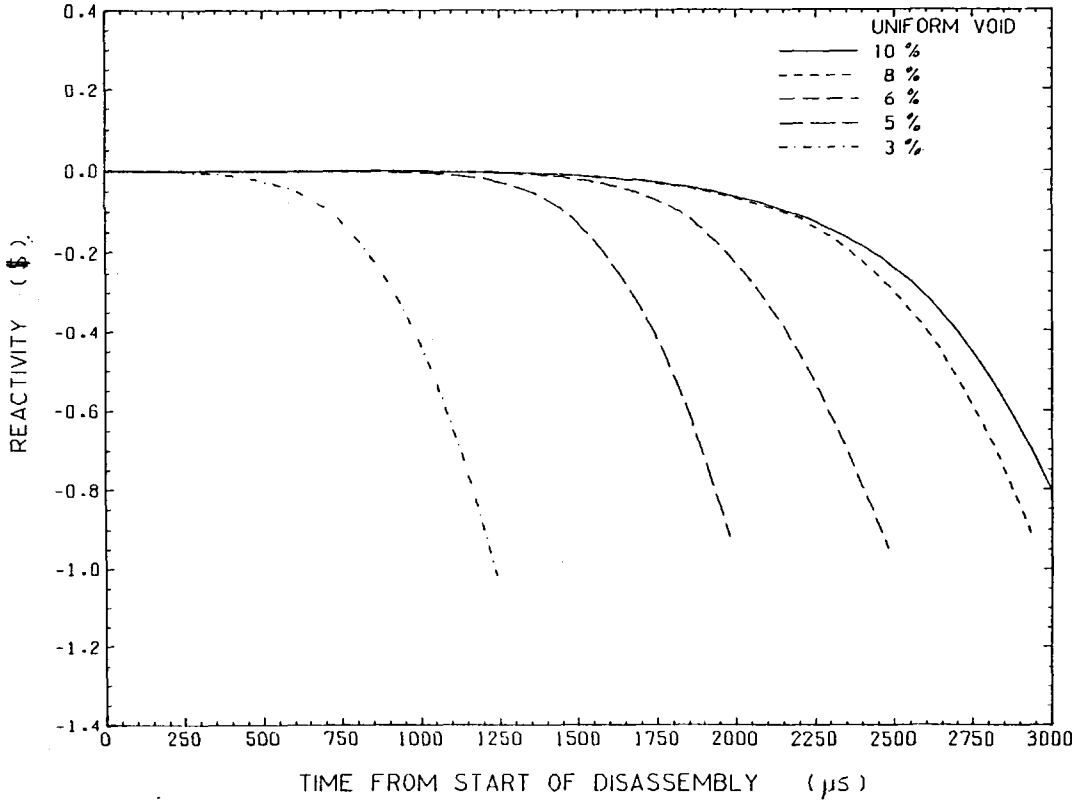

FIG-28

Variation of Net Reactivity with Time During Disassembly of a Uniformly Voided Core, Driven by 70 $/s Reactivity Assuming Real Motion

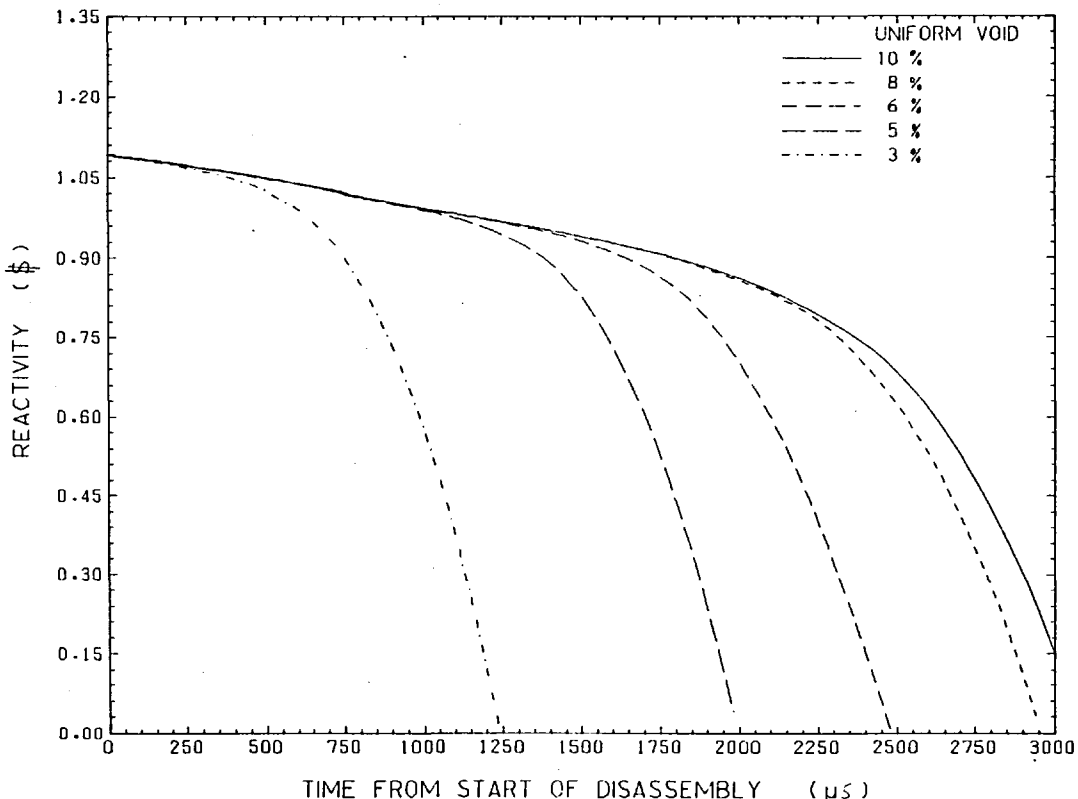

FIG-29

Variation of Total Power with Time During Disassembly

of a Uniformly Voided Core, Driven by 70 $/s Reactivity

Assuming Real Motion

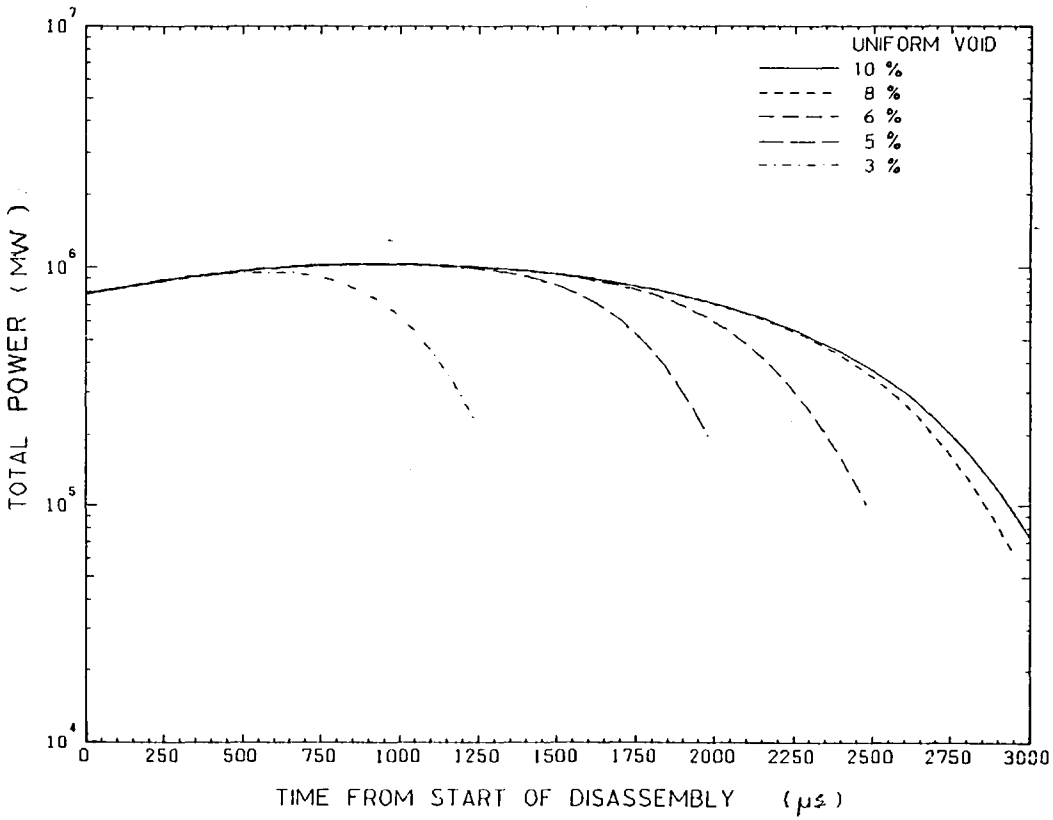

FIG-30

Variation of Total Energy with Time During Disassembly of a Uniformly Voided Core, Driven by 70 $/s Reactivity Assuming Real Motion

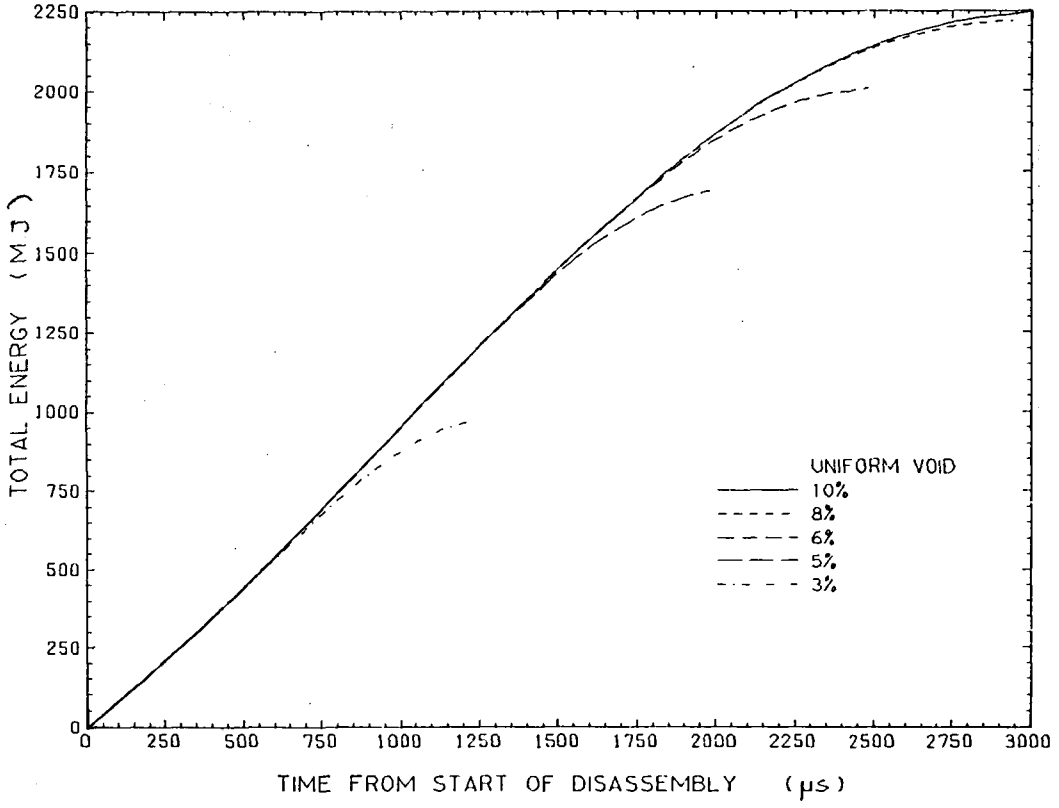

FIG - 31 FUEL TEMPERATURE VARIATION WITH TIME IN THE REAL MOTION MODEL, FOR POWER WEIGHTED INITIAL VOID ADDITION OF 3 %

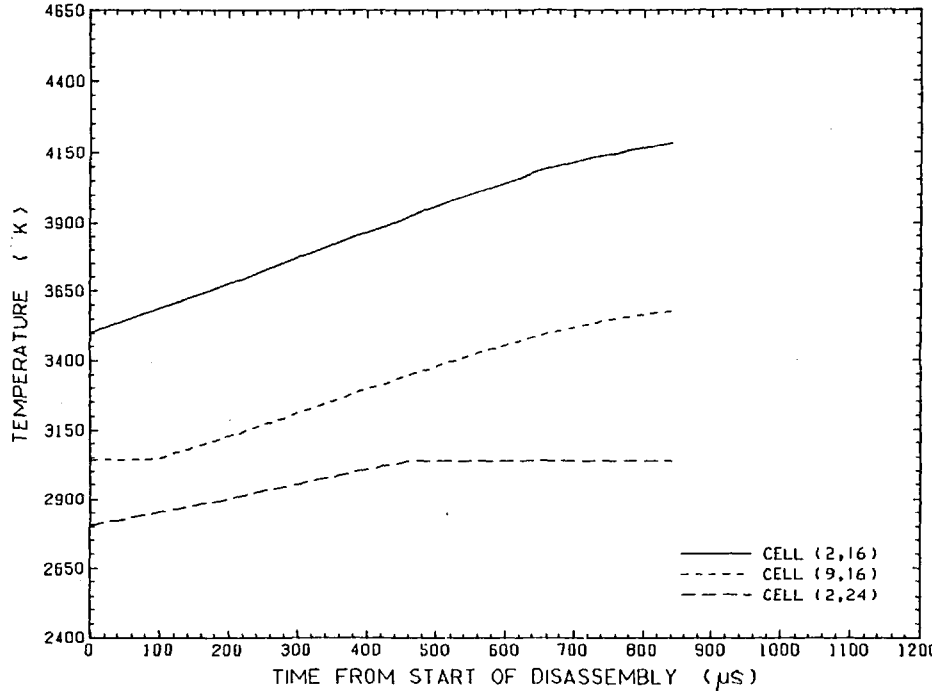

FIG -32 FUEL TEMPERATURE VARIATION WITH TIME IN THE REAL MOTION MODEL, FOR POWER WEIGHTED INITIAL VOID ADDITION OF 4 %

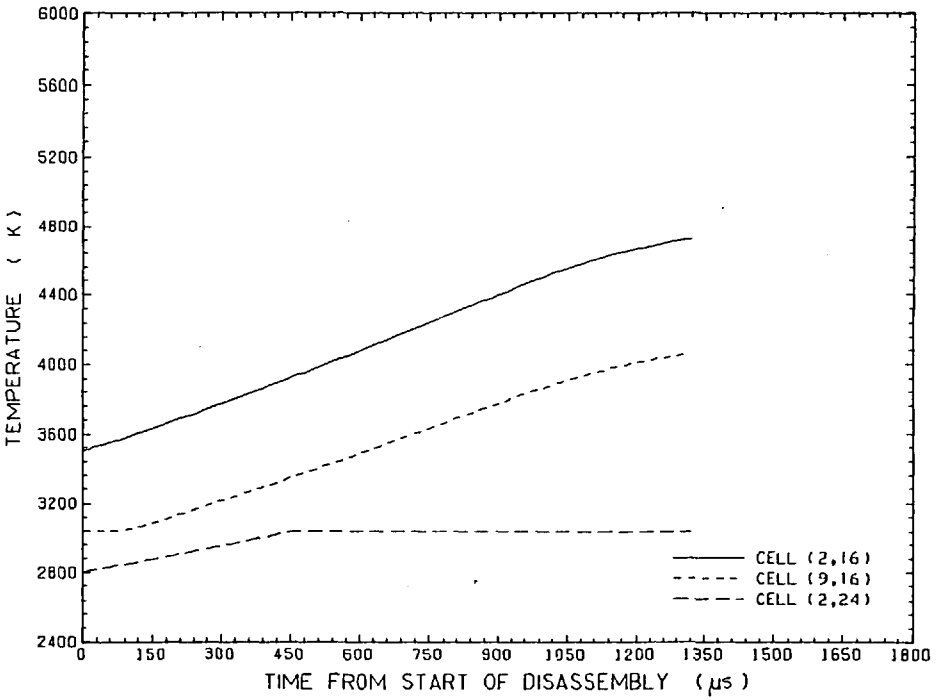

FIG - 33 FUEL TEMPERATURE VARIATION WITH TIME IN THE REAL MOTION MODEL, FOR POWER WEIGHTED INITIAL VOID ADDITION OF 6 %

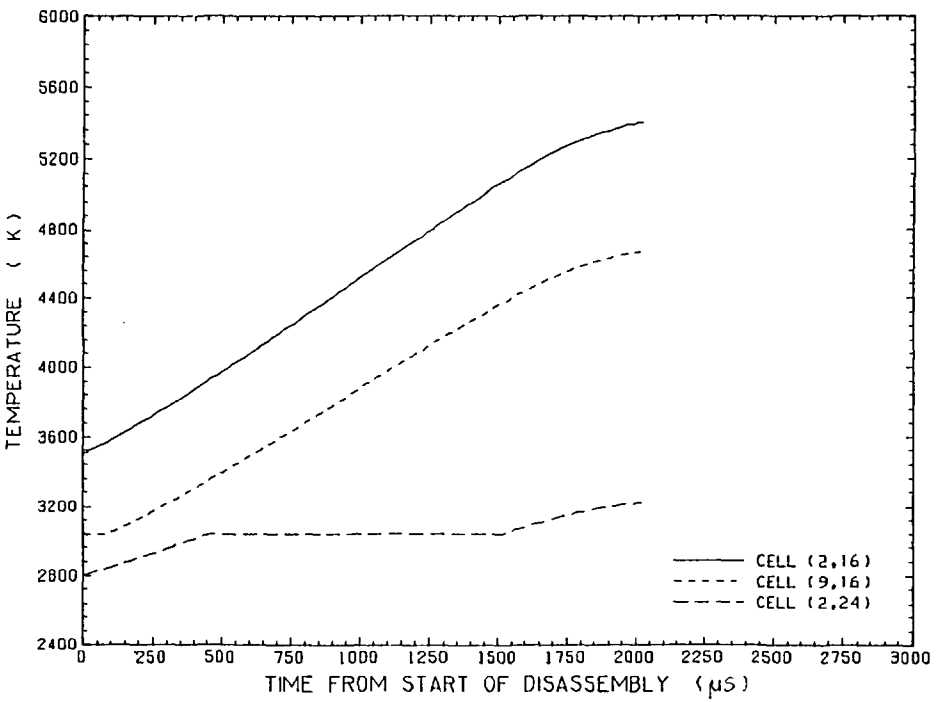

FIG—34 FUEL TEMPERATURE VARIATION WITH TIME IN THE REAL MOTION MODEL, FOR POWER WEIGHTED INITIAL VOID ADDITION OF 8 %

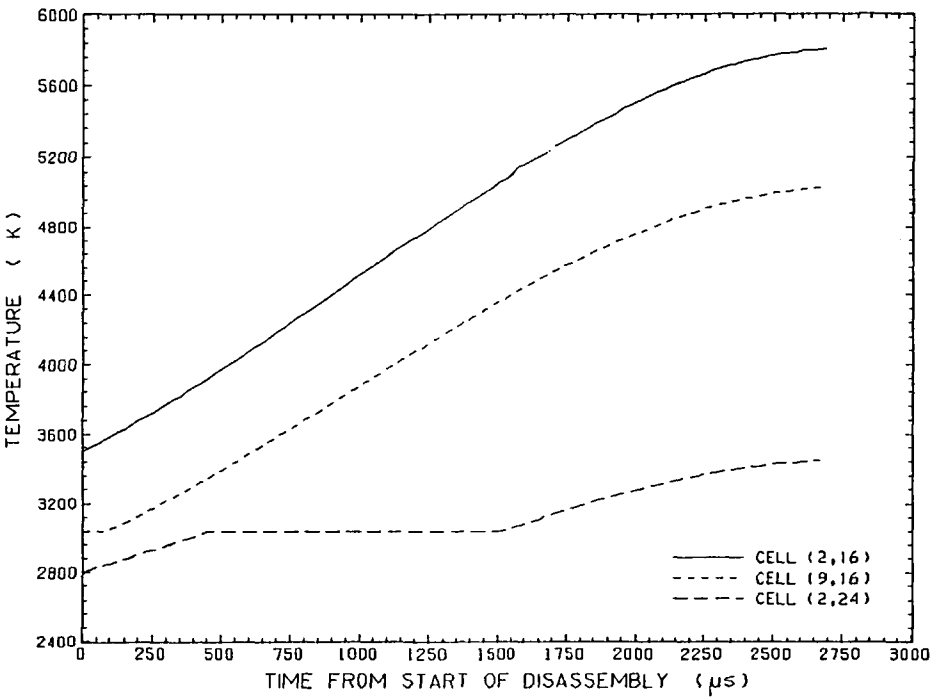

FIG-35 FUEL TEMPERATURE VARIATION WITH TIME IN THE REAL MOTION MODEL, FOR POWER WEIGHTED INITIAL VOID ADDITION OF 10 %

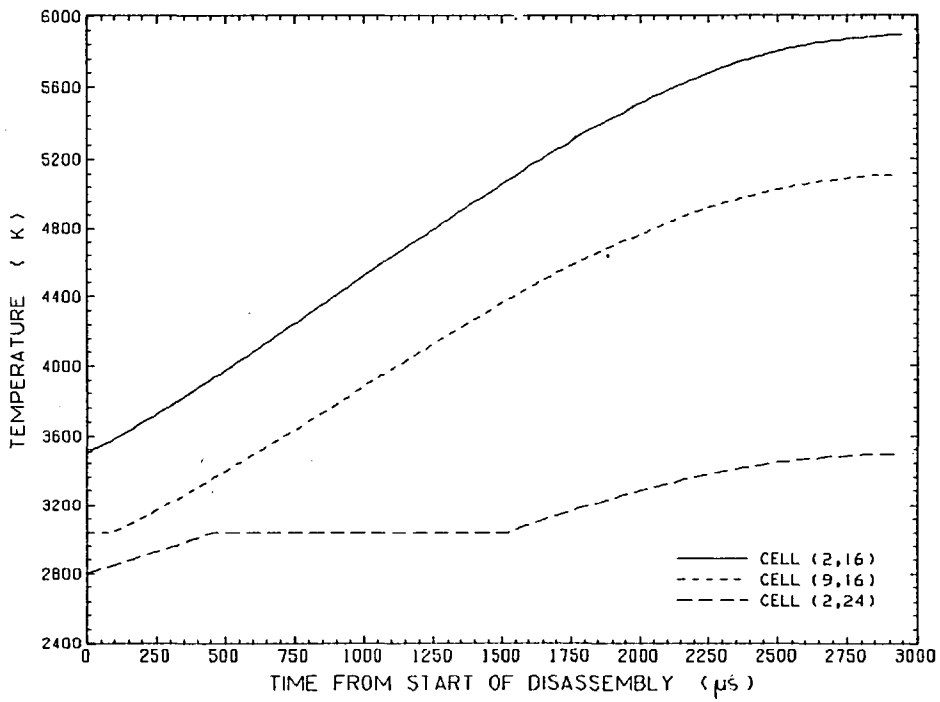

FIG-36 PRESSURE VARIATION WITH TIME IN THE REAL MOTION MODEL, FOR THE POWER WEIGHTED VOID ADDITION OF 3 %

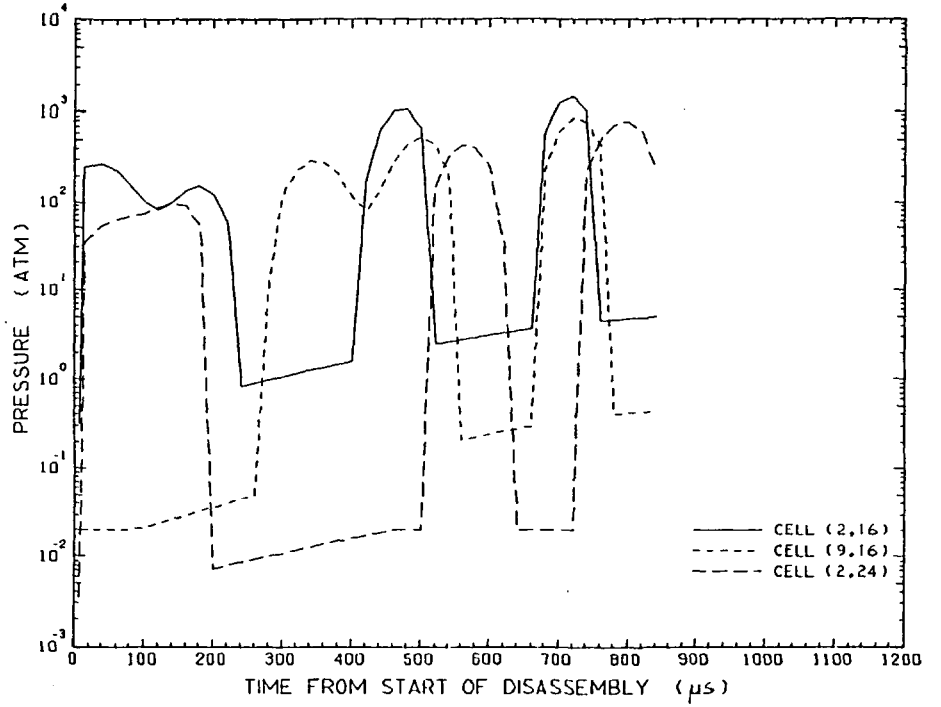

FIG-37 PRESSURE VARIATION WITH TIME IN THE REAL MOTION MODEL, FOR THE POWER WEIGHTED VOID ADDITION OF 4 %

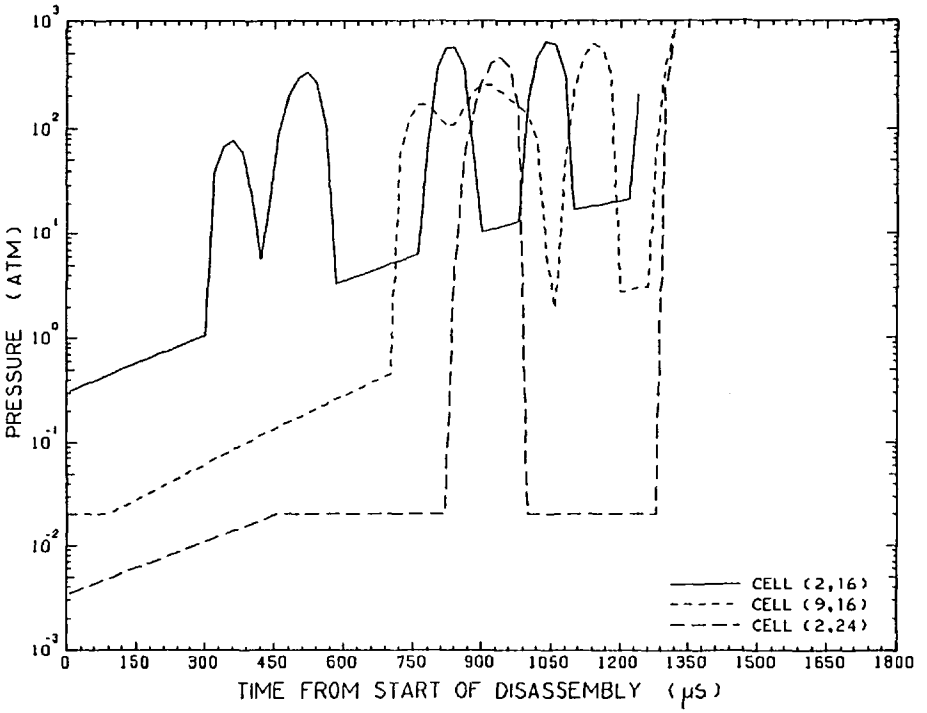

FIG 38 PRESSURE VARIATION WITH TIME IN THE REAL MOTION MODEL, FOR THE POWER WEIGHTED VOID ADDITION OF 6 %

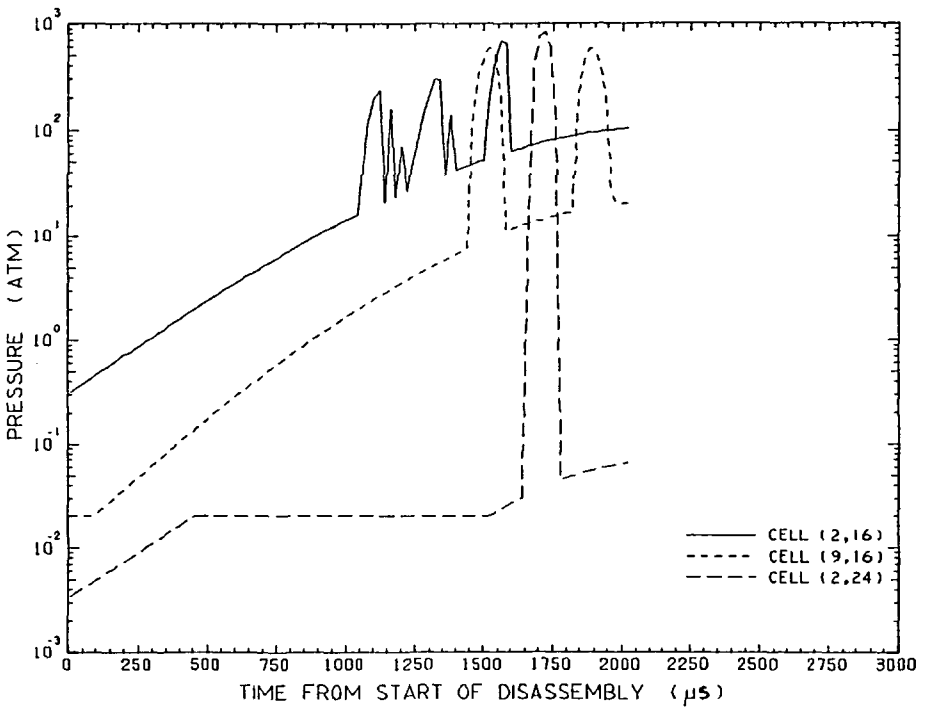

FIG –39 PRESSURE VARIATION WITH TIME IN THE REAL MOTION MODEL,
FOR THE POWER WEIGHTED VOID ADDITION OF 8 %

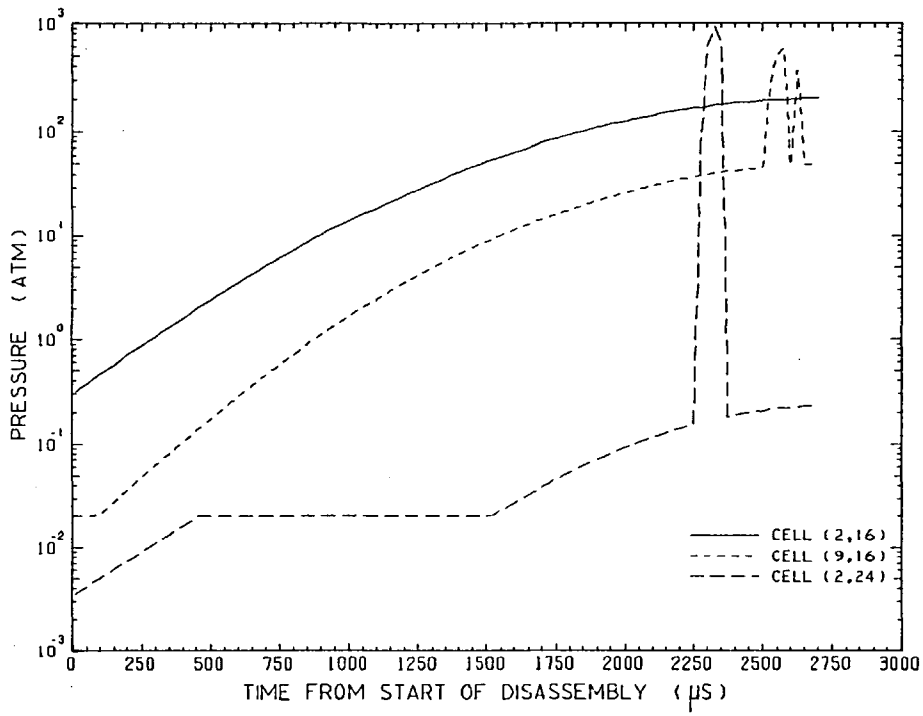

FIG. 40 PRESSURE VARIATION WITH TIME IN THE REAL MOTION MODEL, FOR THE POWER WEIGHTED VOID ADDITION OF 10 %

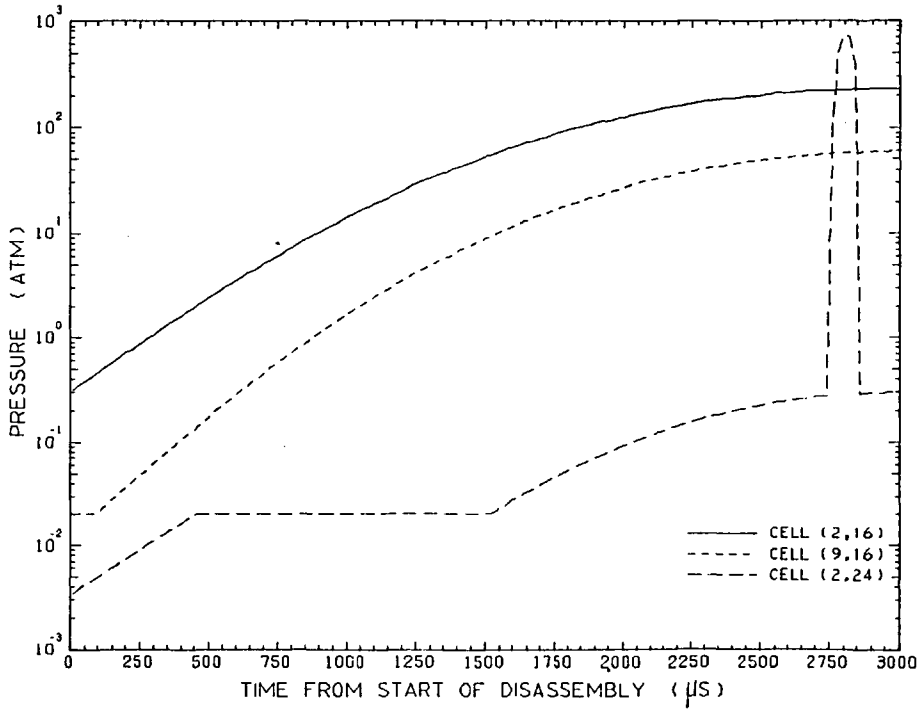

FIG-41 EFFECT OF NON UNIFORM ADDITION OF VOID ON THE DOPPLER FEEDBACK VARIATION IN THE DISASSEMBLING CORE USING THE REAL MOTION MODEL

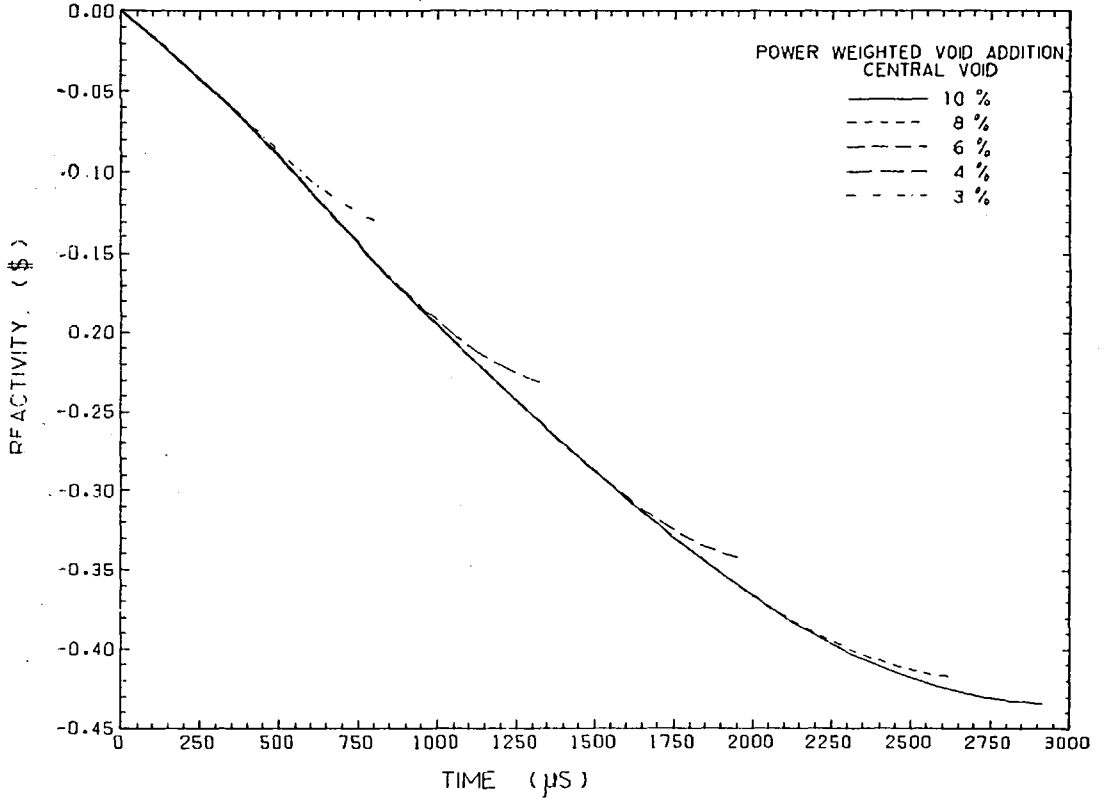

FIG-42 EFFECT OF NON UNIFORM ADDITION OF VOID ON THE DISPLACEMENT FEEDBACK VARIATION IN THE DISASSEMBLING CORE USING THE REAL MOTION MODEL

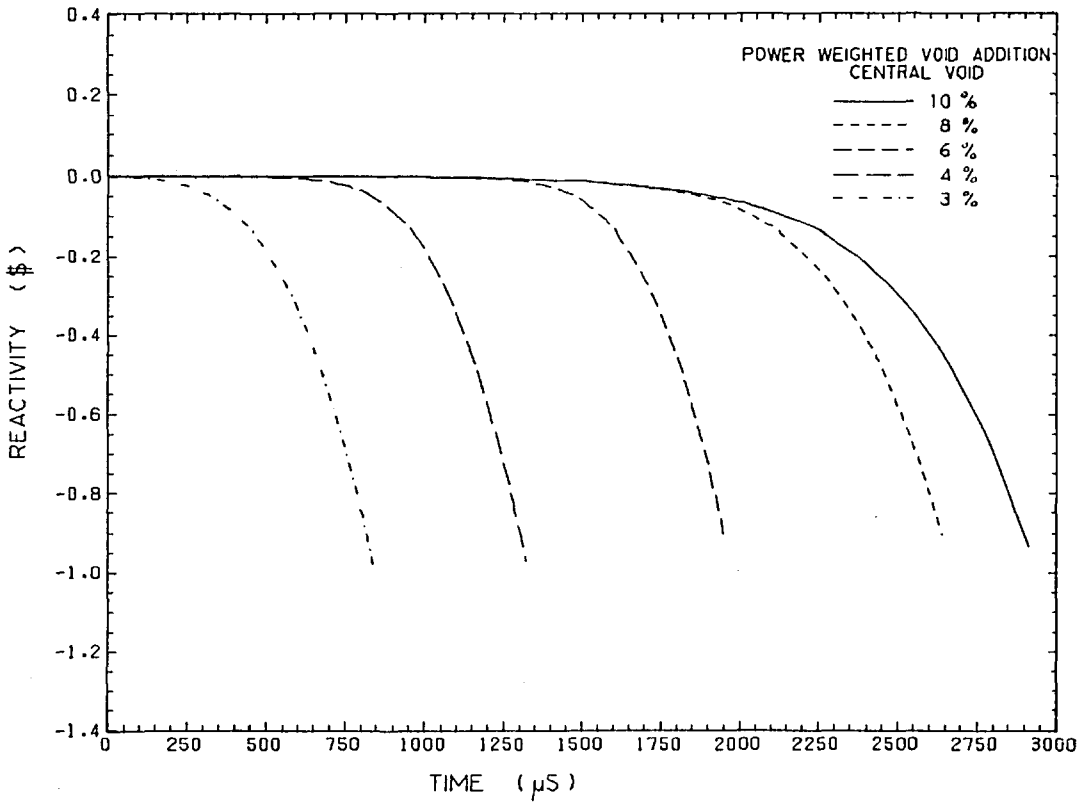

FIG-43 EFFECT OF UNIFORM ADDITION OF VOID ON THE NET REACTIVITY VARIATION IN THE DISASSEMBLING CORE USING THE REAL MOTION MODEL

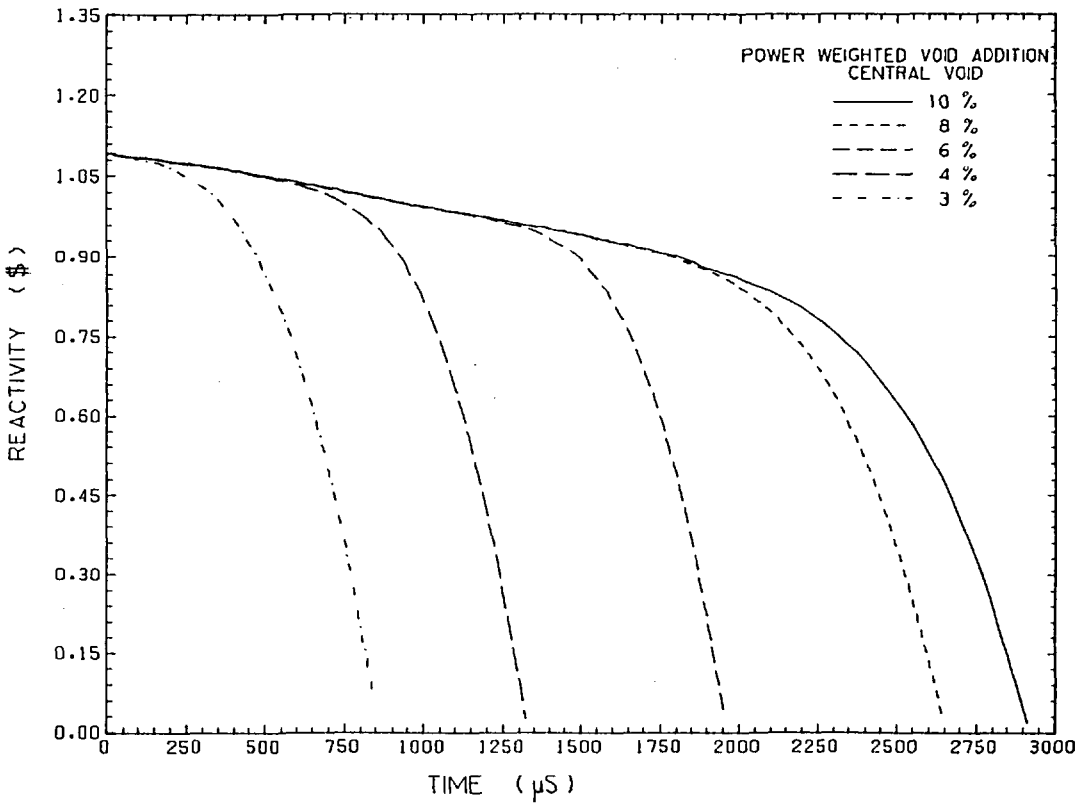

FIG — 44

EFFECT OF NON UNIFORM ADDITION OF VOID ON THE TOTAL POWER VARIATION IN THE DISASSEMBLING CORE USING THE REAL MOTION MODEL

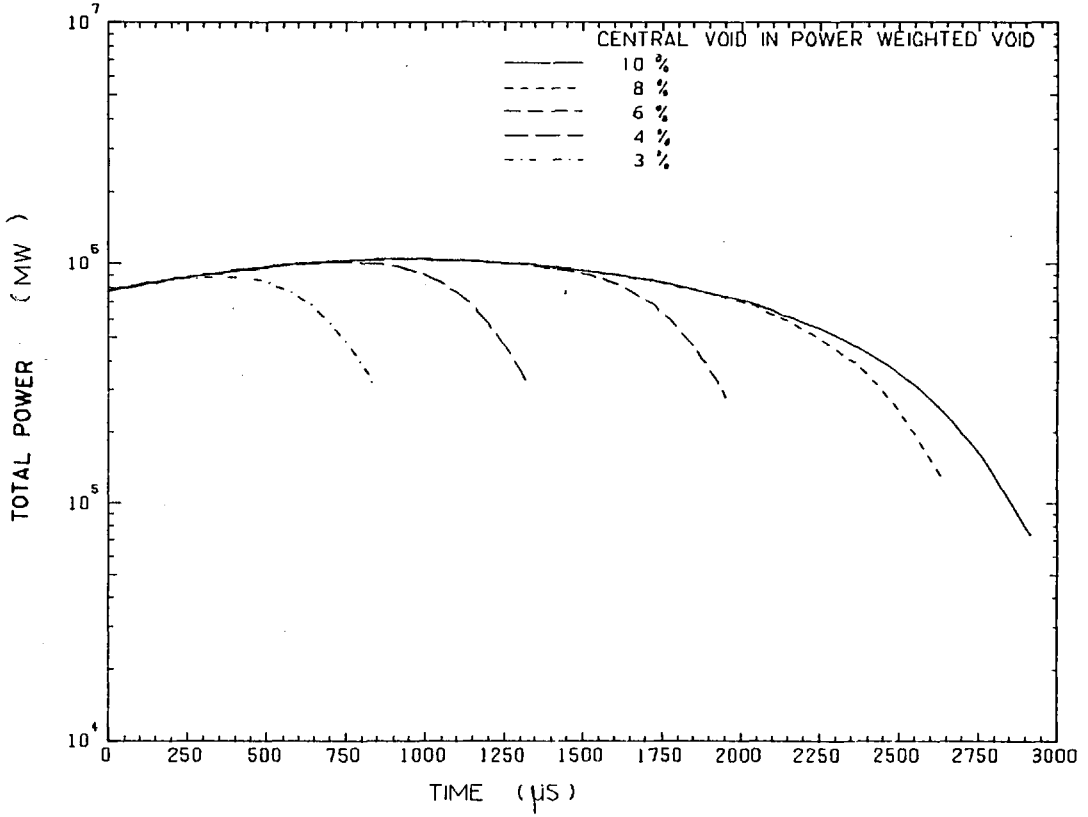

FIG 4.5 EFFECT NON UNIFORM VOID ADDITION TO THE TOTAL ENERGY VARIATION IN THE DISASSEMBLING CORE USING THE REAL MOTION MODEL

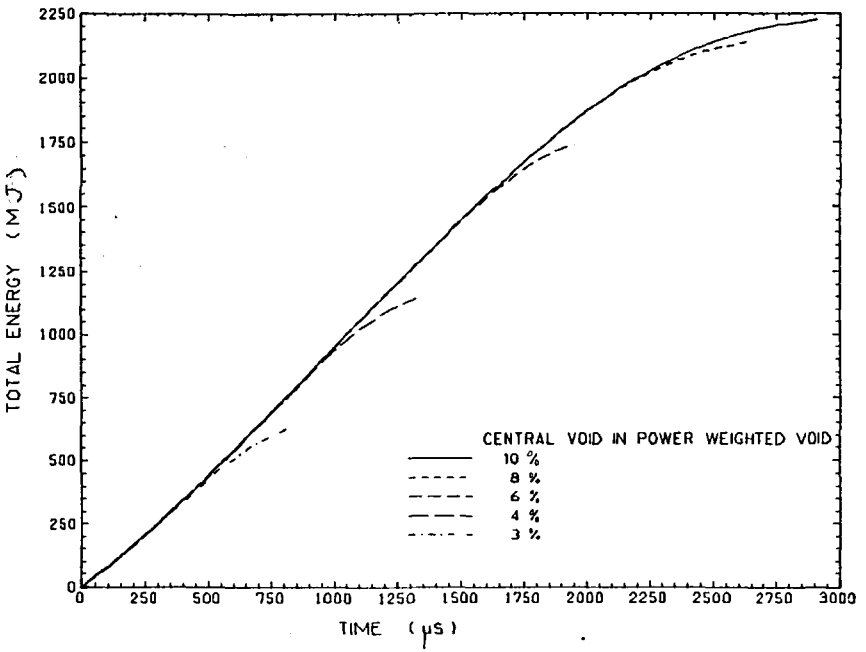

FIG-46

Variation of Doppler Reactivity with Time During Disassembly of a Uniformly Voided Core, Driven by 70 $/s Reactivity Assuming virtual Motion

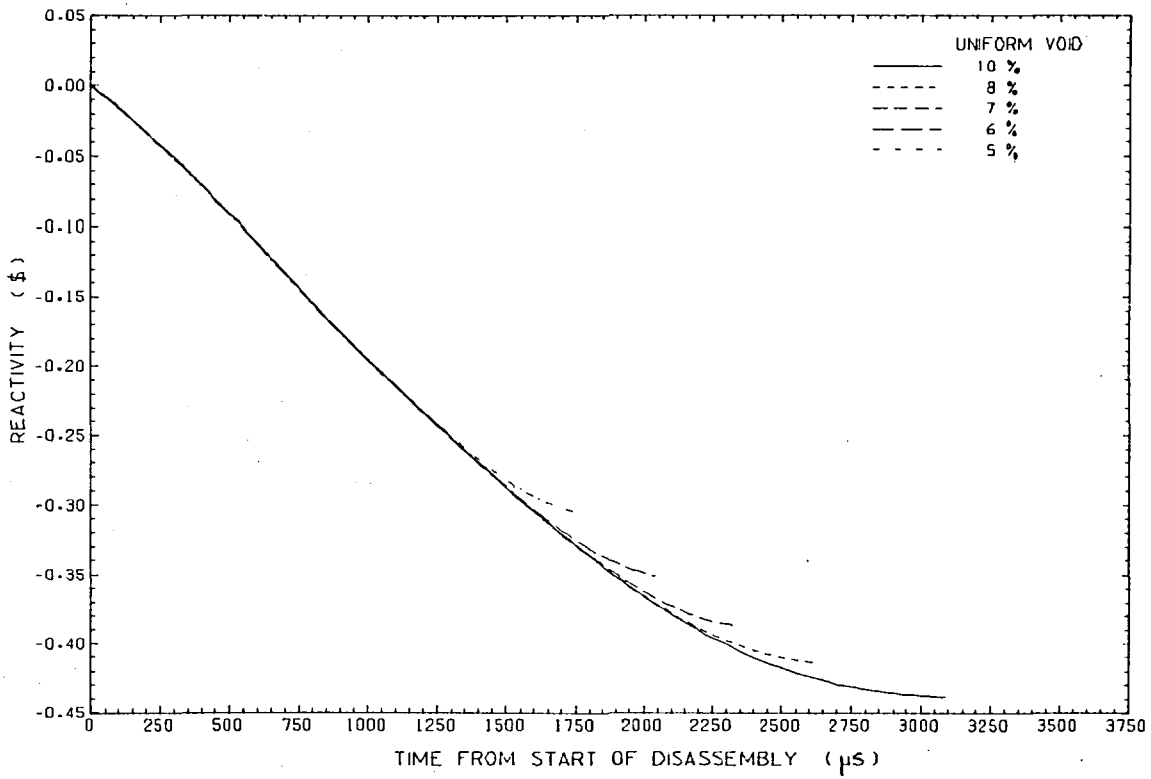

FIG-47

Variation of Virtaul Motion Reactivity with Time During Disassembly

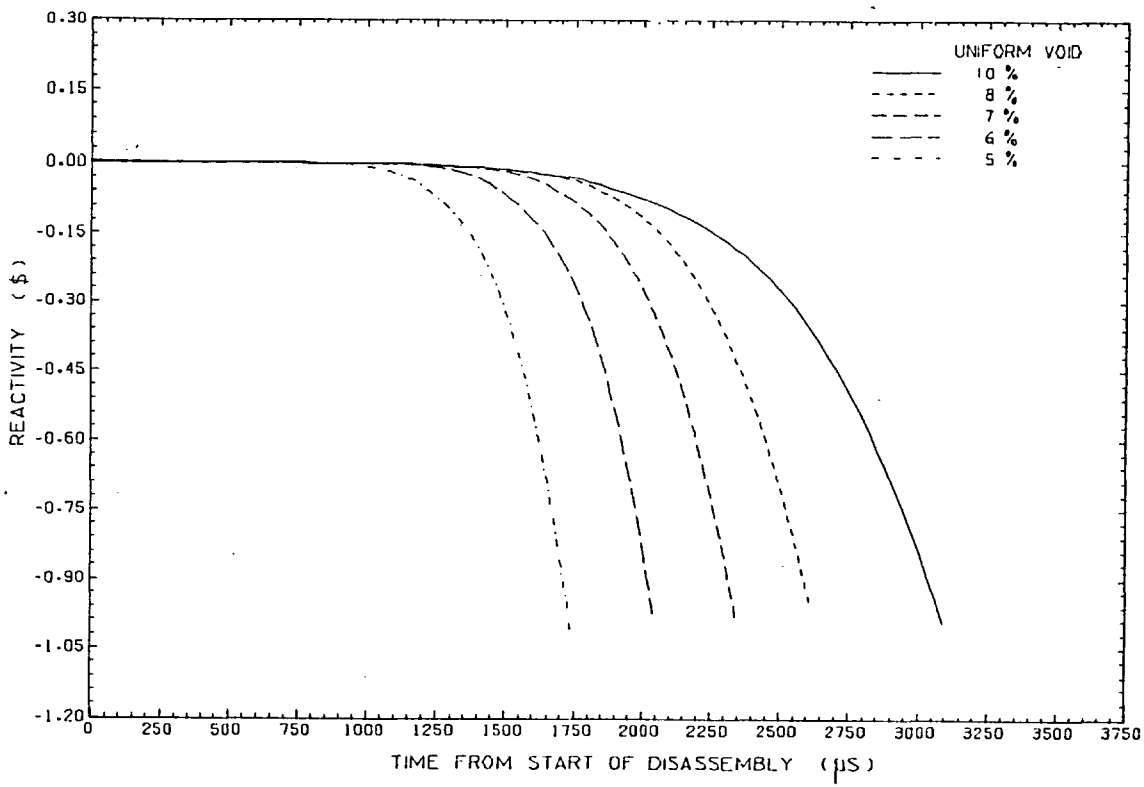

FIG-48

Variation of Net Reactivity with Time During Disassembly of a Uniformly Voided Core, Driven by 70 $/s Reactivity Assuming virtual Motion

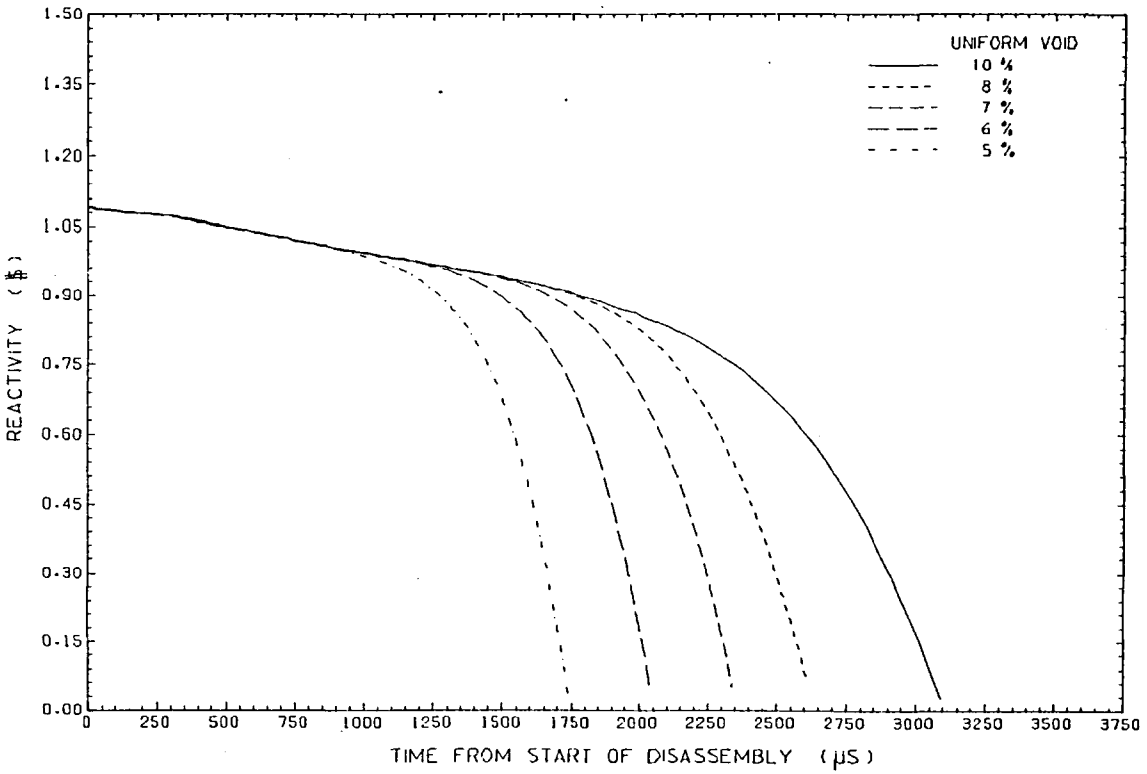

FIG-49

Variation of Total Power with Time During Disassembly

of a Uniformly Voided Core, Driven by 70 $/s Reactivity

Assuming Virtual Motion

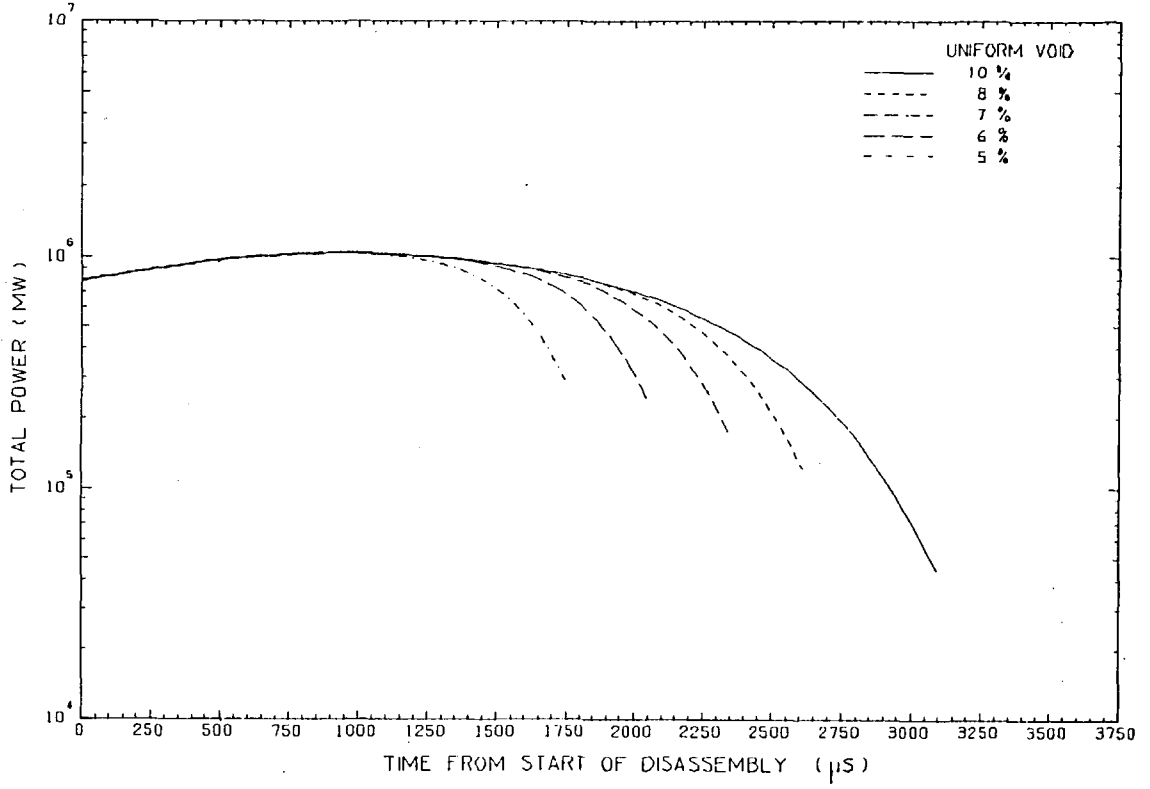

FIG-50

Variation of Total Energy with Time During Disassembly

of a Uniformly Voided Core, Driven by 70 $/s Reactivity

Assuming Virtual Motion

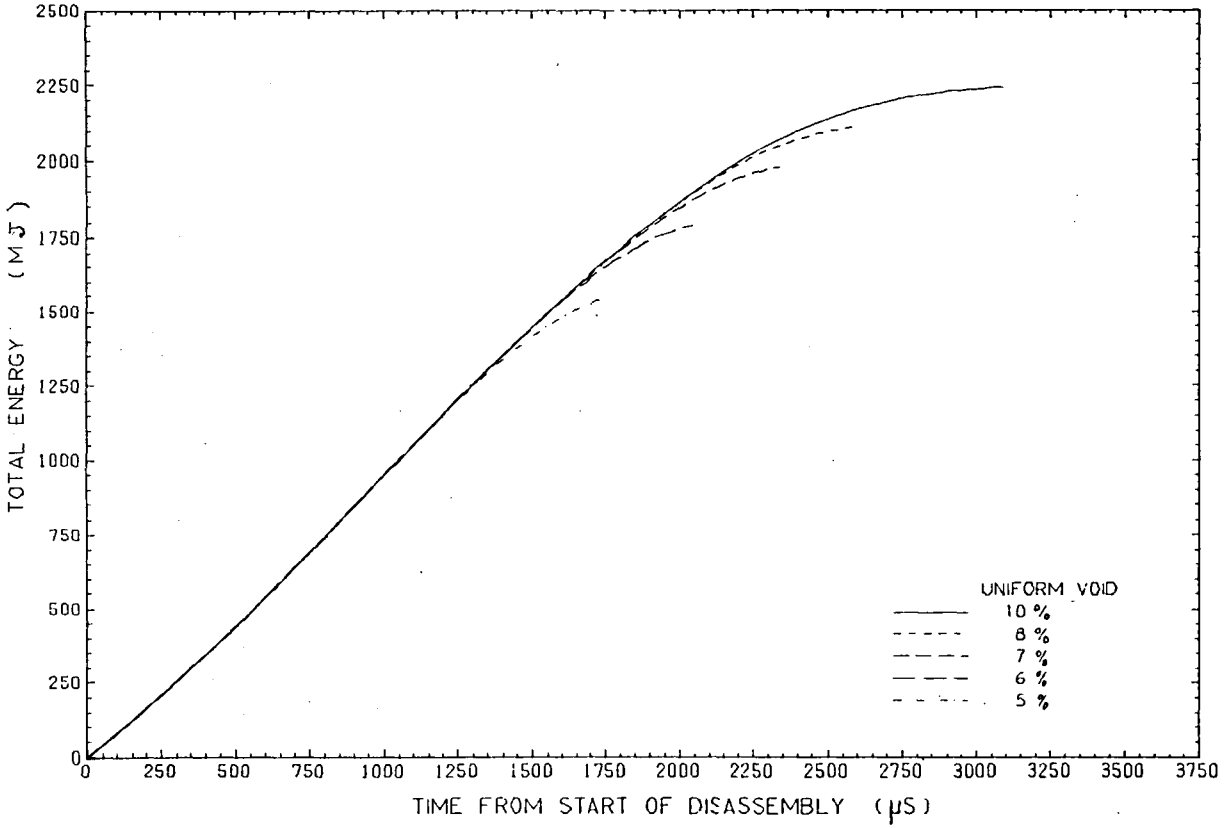

FIG - 51

TEMPERATURE DISTRIBUTION AFTER 560 MICROSECONDS FOR A 70 $/s EXCURSION, IN A CORE VOIDED UNIFORMLY BY 3%, IN BOTH THE REAL AND VIRTUAL MOTION MODELS

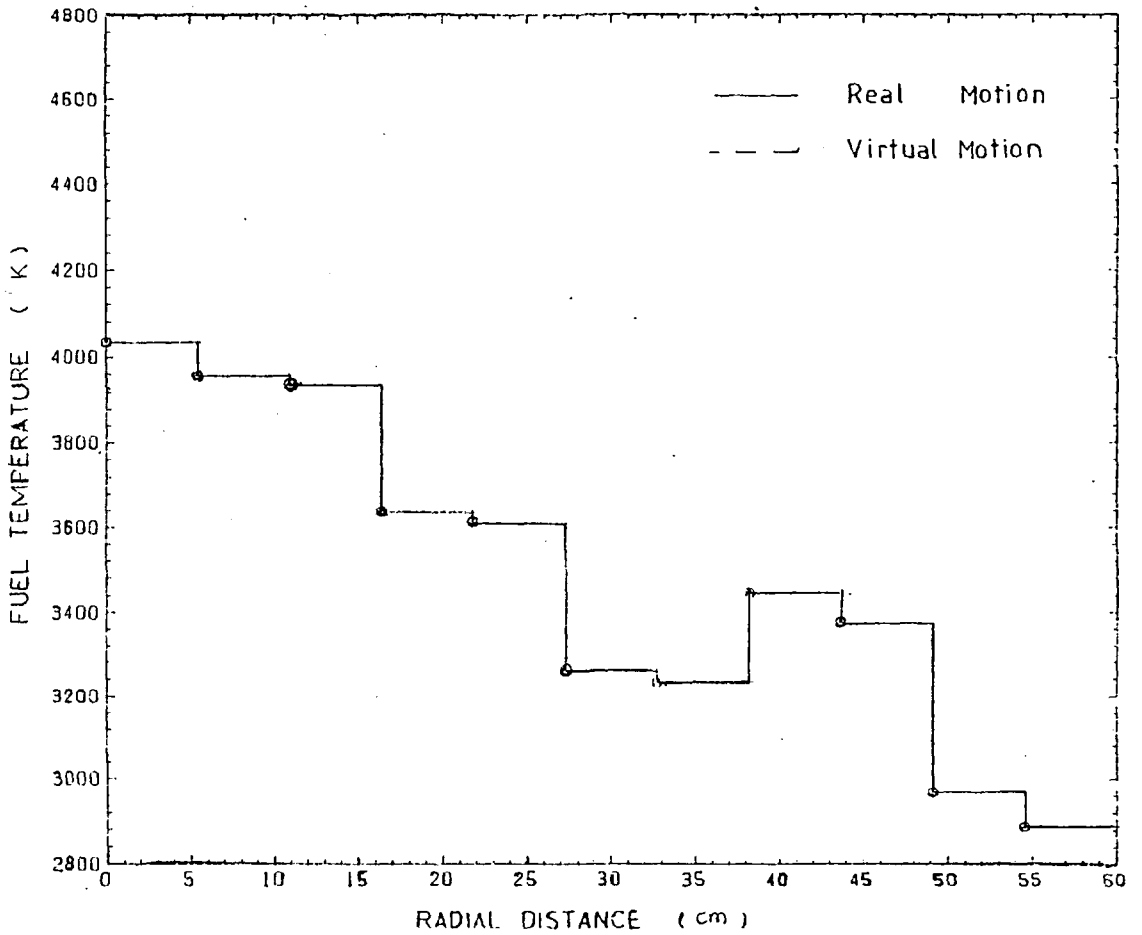

FIG - 52

TEMPERATURE DISTRIBUTION AFTER 960 MICROSECONDS FOR A 70 $/s EXCURSION, IN A CORE VOIDED UNIFORMLY BY 3%, IN BOTH THE REAL AND VIRTUAL MOTION MODELS

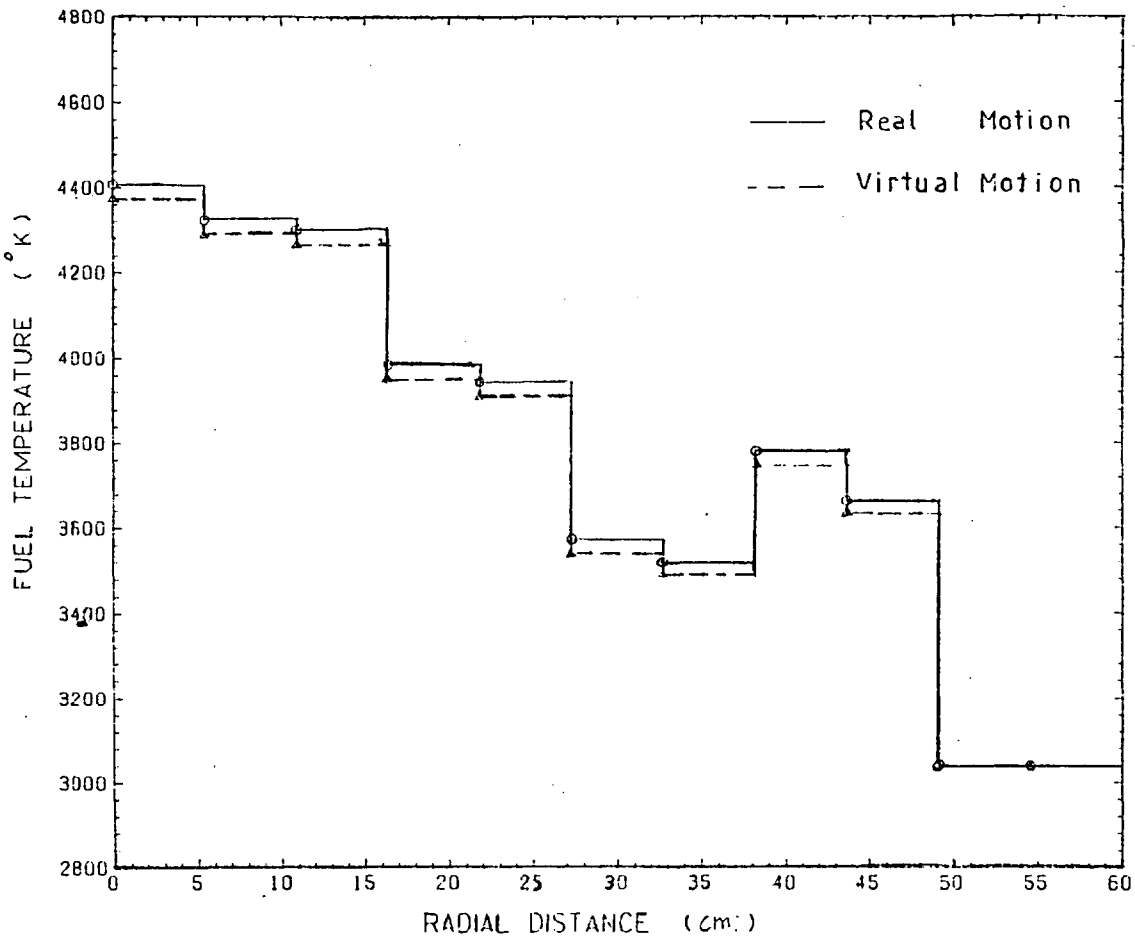

FIG - 53

PRESSURE DISTRIBUTION AFTER 160 MICROSECONDS FOR A 70 $/s EXCURSION, IN A CORE VOIDED UNIFORMLY BY 3%, IN BOTH THE REAL AND VIRTUAL MOTION MODELS

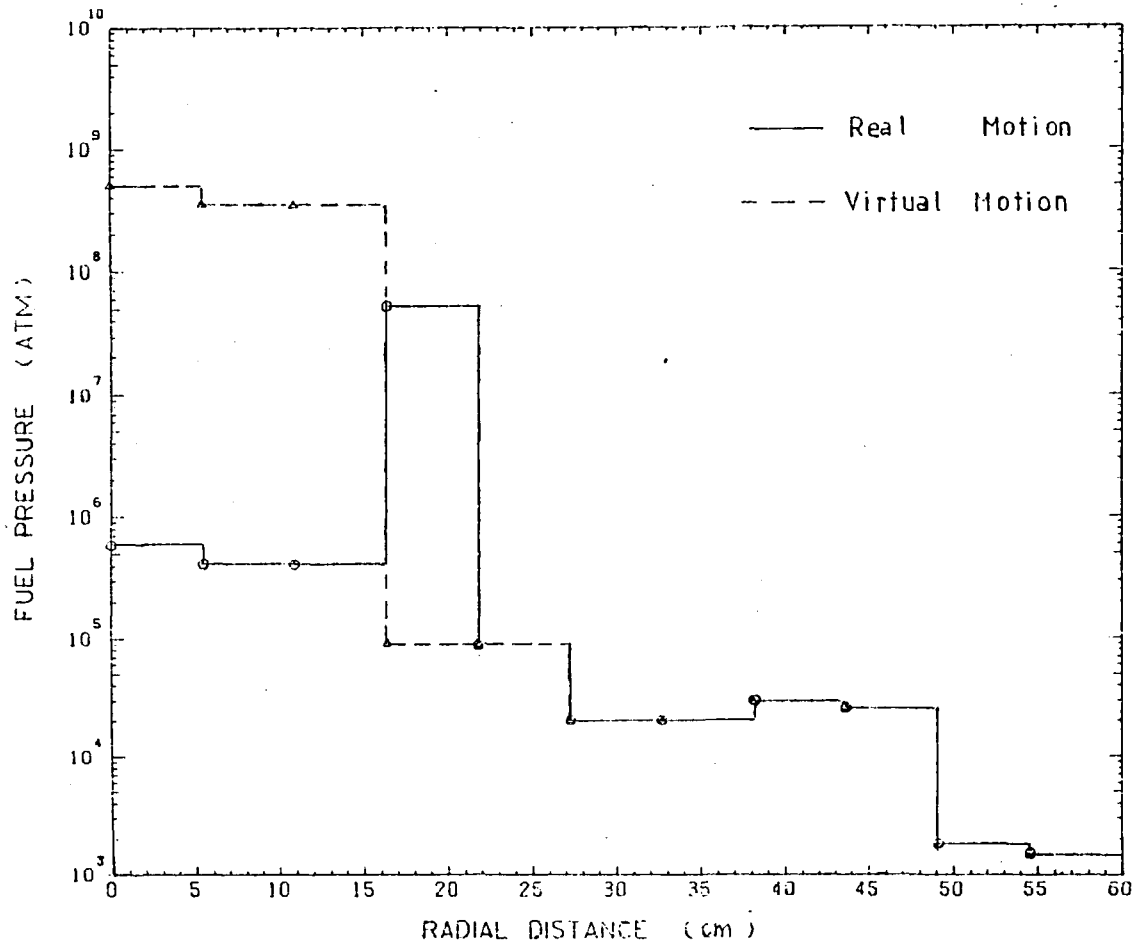

FIG- 54

PRESSURE DISTRIBUTION AFTER 560 MICROSECONDS FOR A 70 $/s EXCURSION, IN A CORE VOIDED UNIFORMLY BY 3%, IN BOTH THE REAL AND VIRTUAL MOTION MODELS

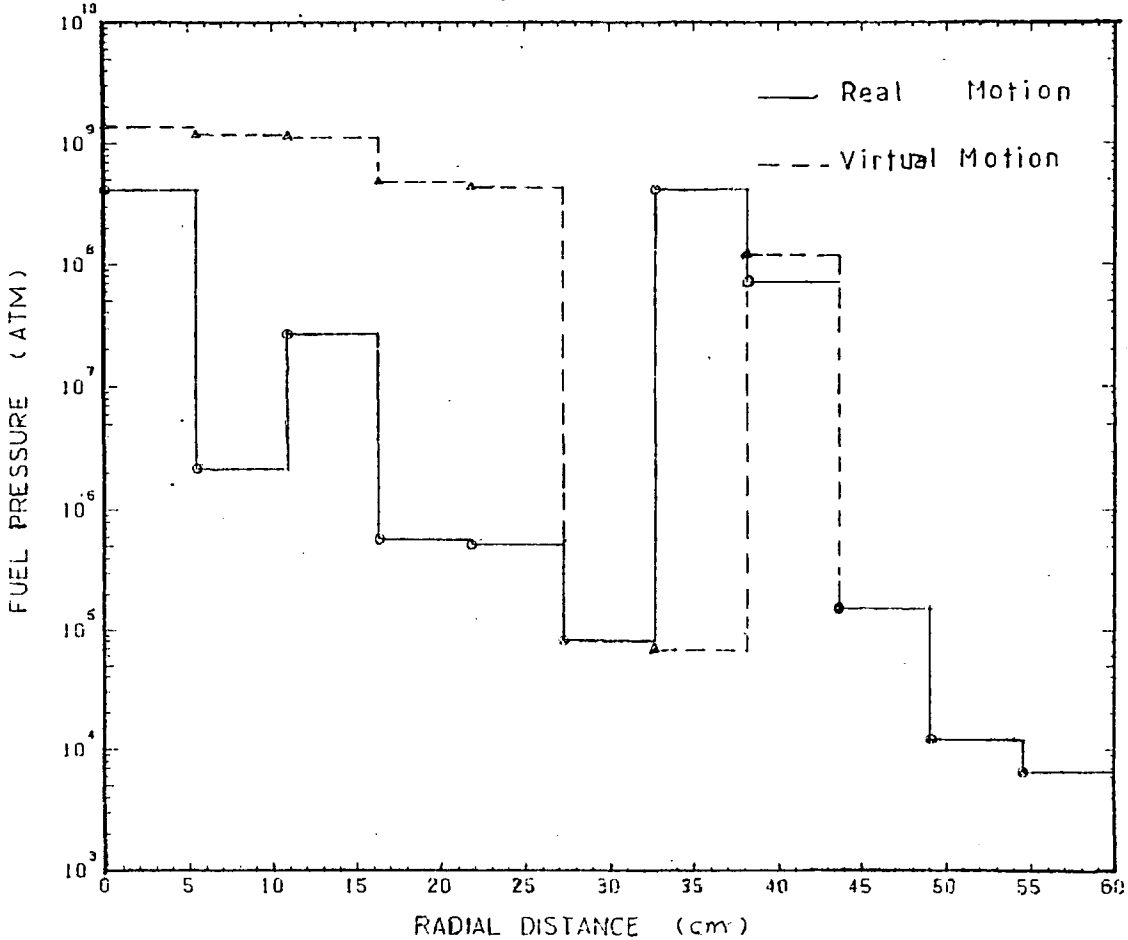

FIG - 55

PRESSURE DISTRIBUTION AFTER 960 MICROSECONDS FOR A 70 $/s EXCURSION, IN A CORE VOIDED UNIFORMLY BY 3%, IN BOTH THE REAL AND VIRTUAL MOTION MODELS

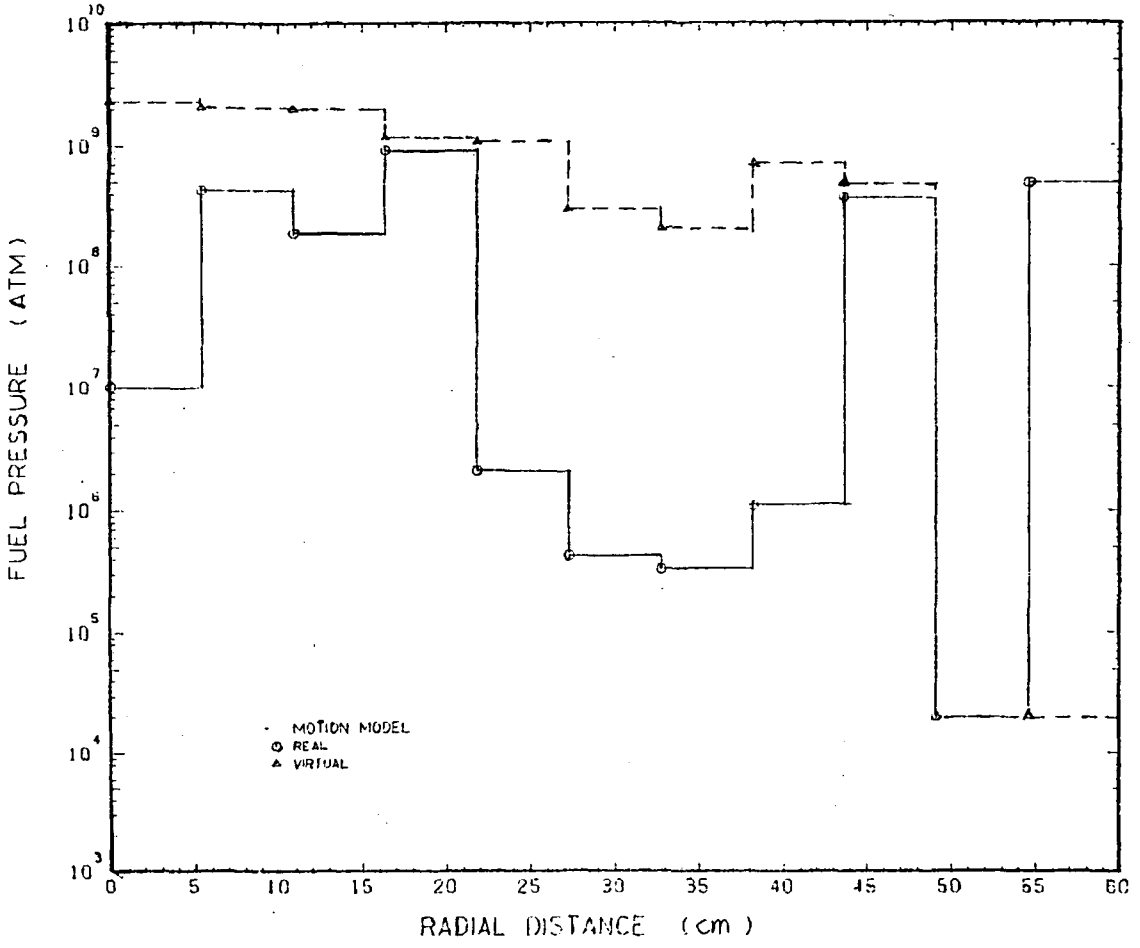

FIG-56

REDUCED VOLUME DISTRIBUTION AFTER 960 MICROSECONDS FOR A 70 $/s EXCURSION, IN A CORE VOIDED UNIFORMLY BY 3%, IN BOTH THE REAL AND VIRTUAL MOTION MODELS

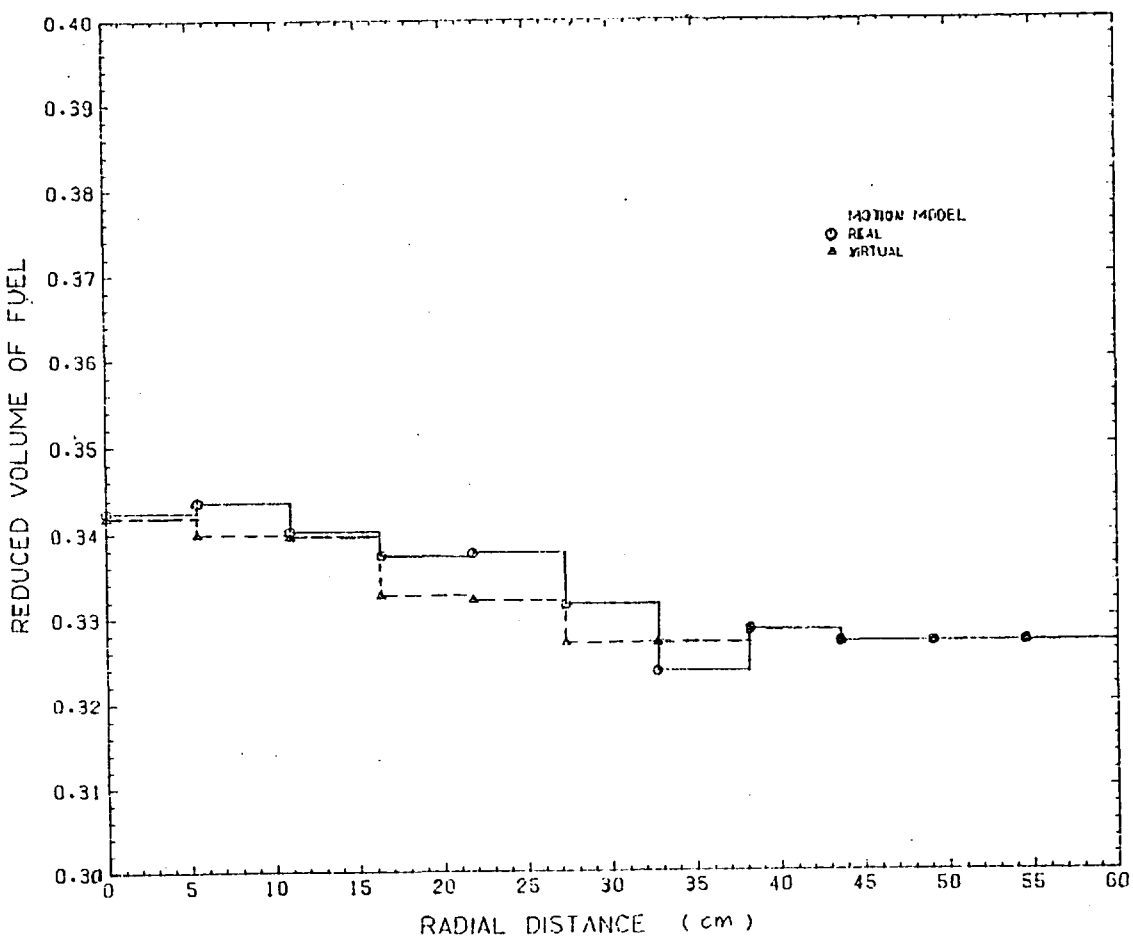

FIG – 57

TEMPERATURE VARIATION IN THE REAL AND THE VIRTUAL MOTION MODELS
FOR AN INITIAL UNIFORM VOID OF 13 %

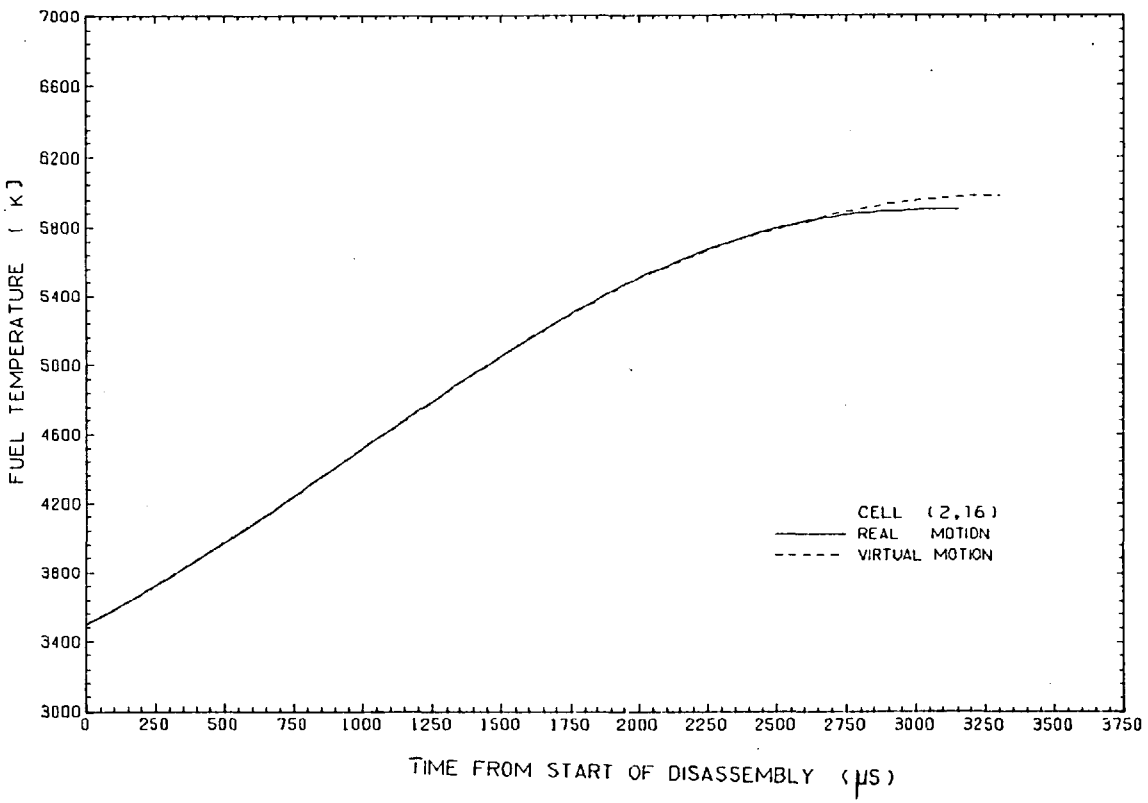

FIG_58

TEMPERATURE VARIATION IN THE REAL AND THE VIRTUAL MOTION MODELS
FOR AN INITIAL UNIFORM VOID OF 13 %

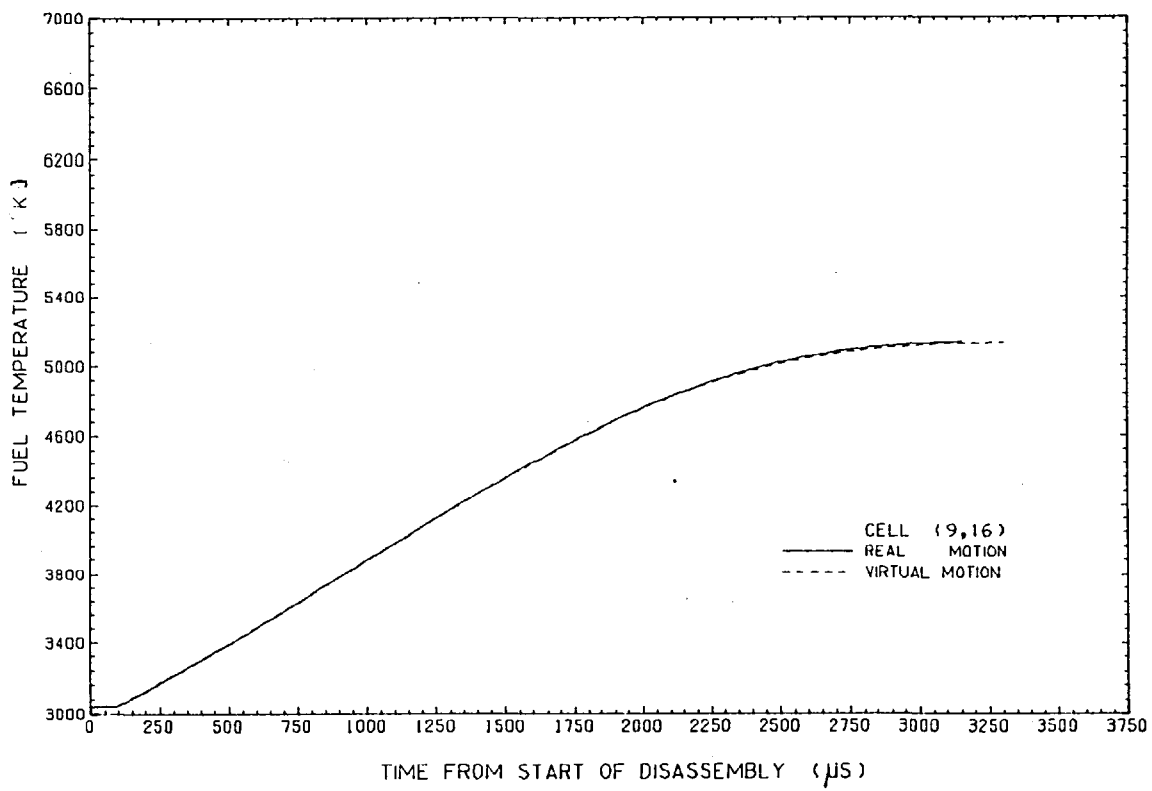

FIG - 59

PRESSURE VARIATION IN THE REAL AND THE VIRTUAL MOTION MODELS FOR AN INITIAL UNIFORM VOID OF 13 %

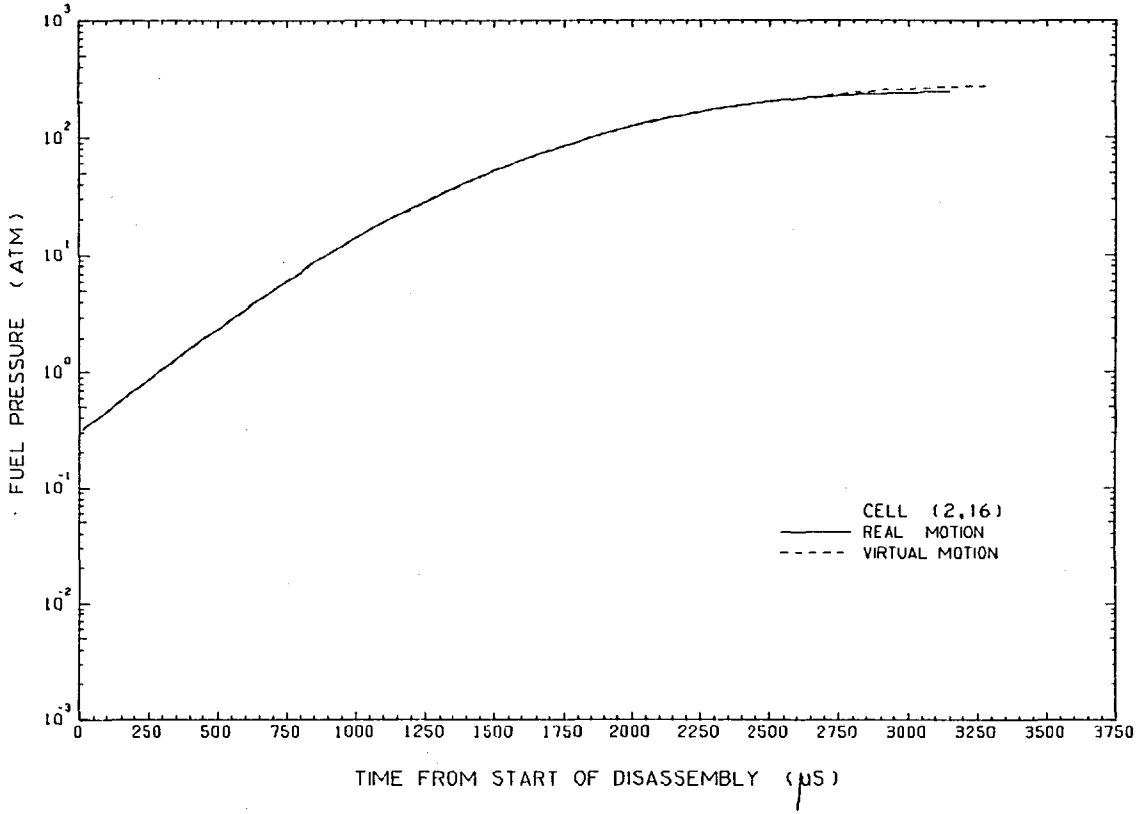

FIG-6 o

PRESSURE VARIATION IN THE REAL AND THE VIRTUAL MOTION MODELS FOR AN INITIAL UNIFORM VOID OF 13 %

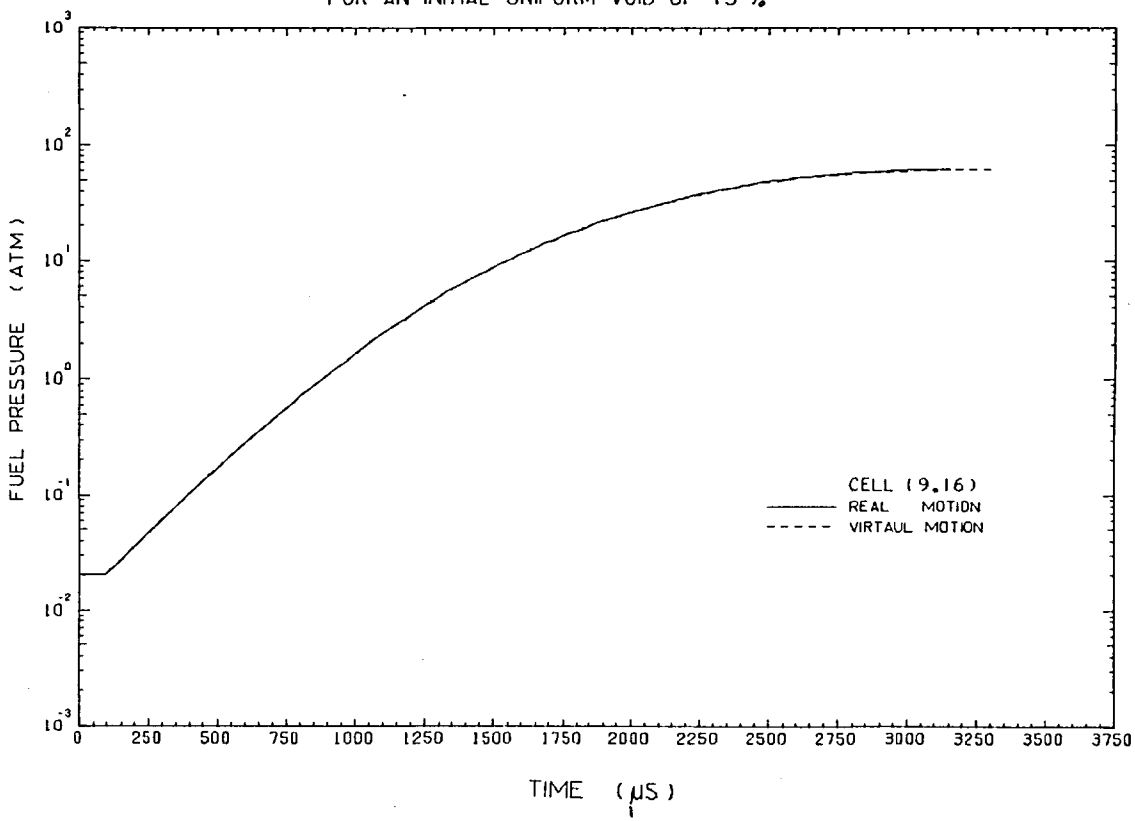

FIG - 61

PRESSURE VARIATION IN THE REAL AND THE VIRTUAL MOTION MODELS FOR AN INITIAL UNIFORM VOID OF 13 %

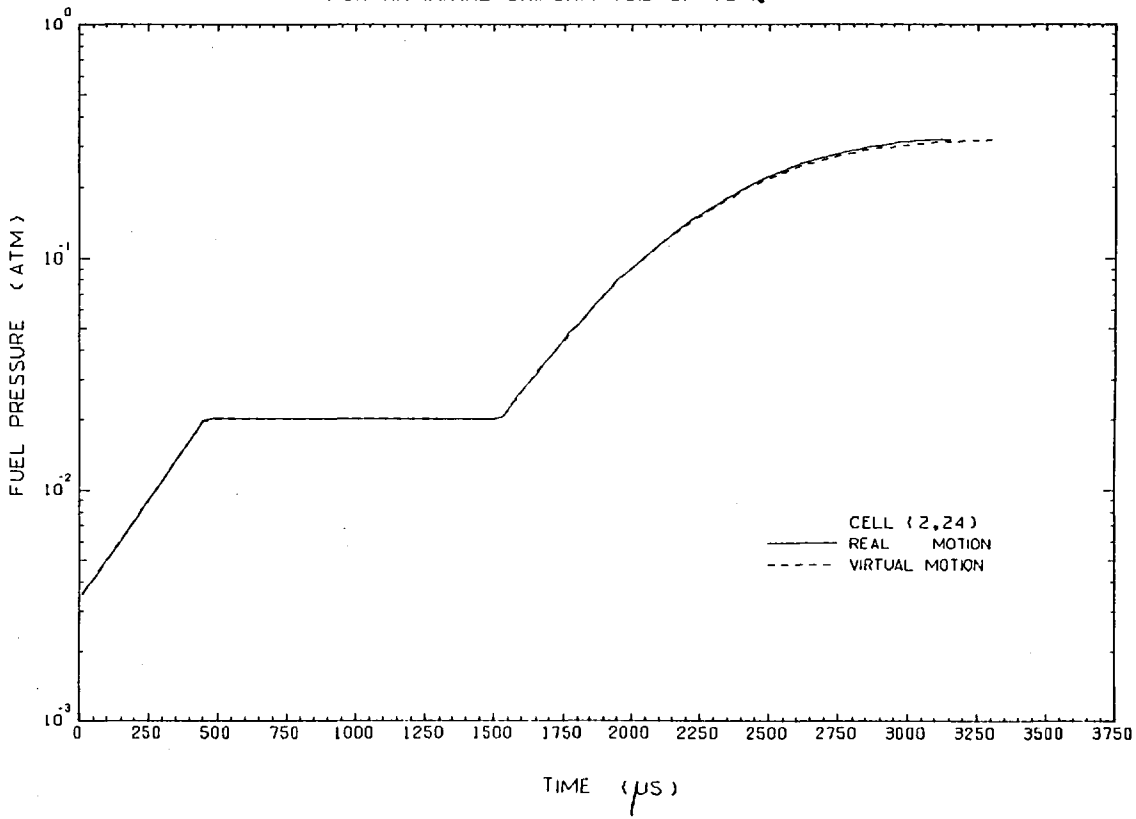

FIG – 62

DOPPLER FEEDBACK VARIATION IN THE REAL AND THE VIRTUAL MOTION MODELS FOR AN INITIAL UNIFORM VOID ADDITION OF 13 %

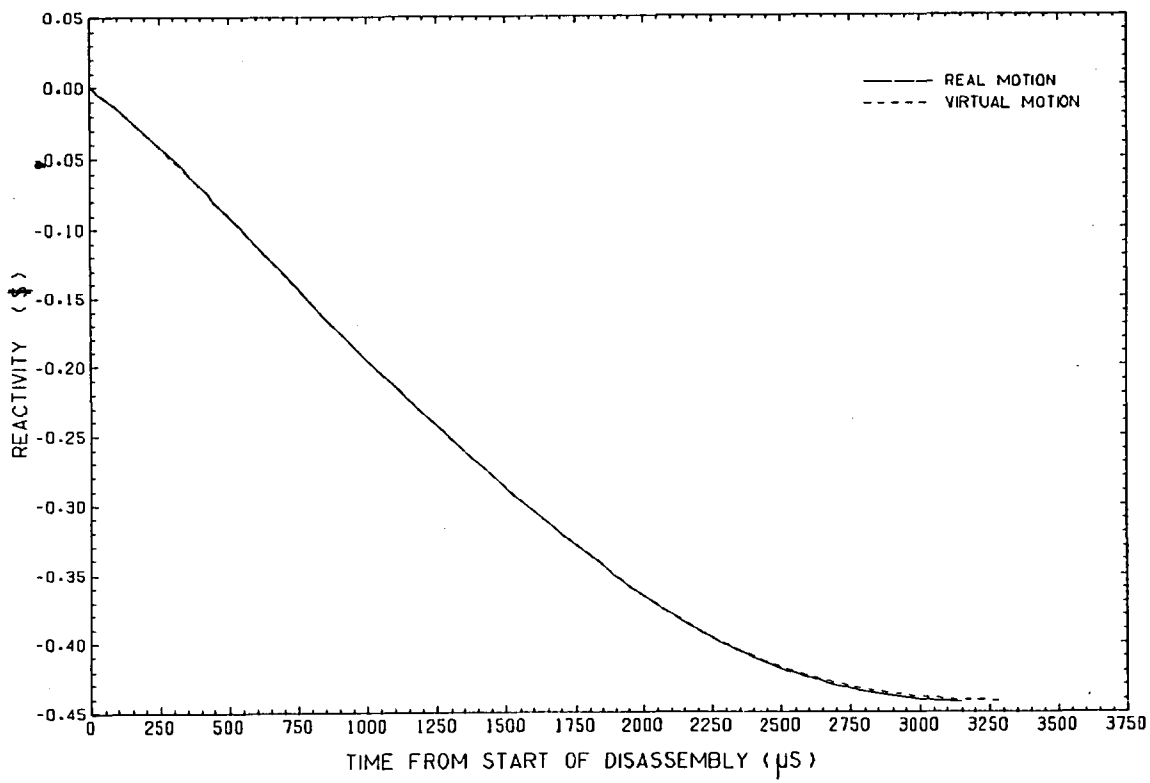

FIG - 63A

MOTION FEEDBACK VARIATION IN THE REAL AND THE VIRTUAL MOTION MODELS
FOR AN INITIAL UNIFORM VOID ADDITION OF 13 %

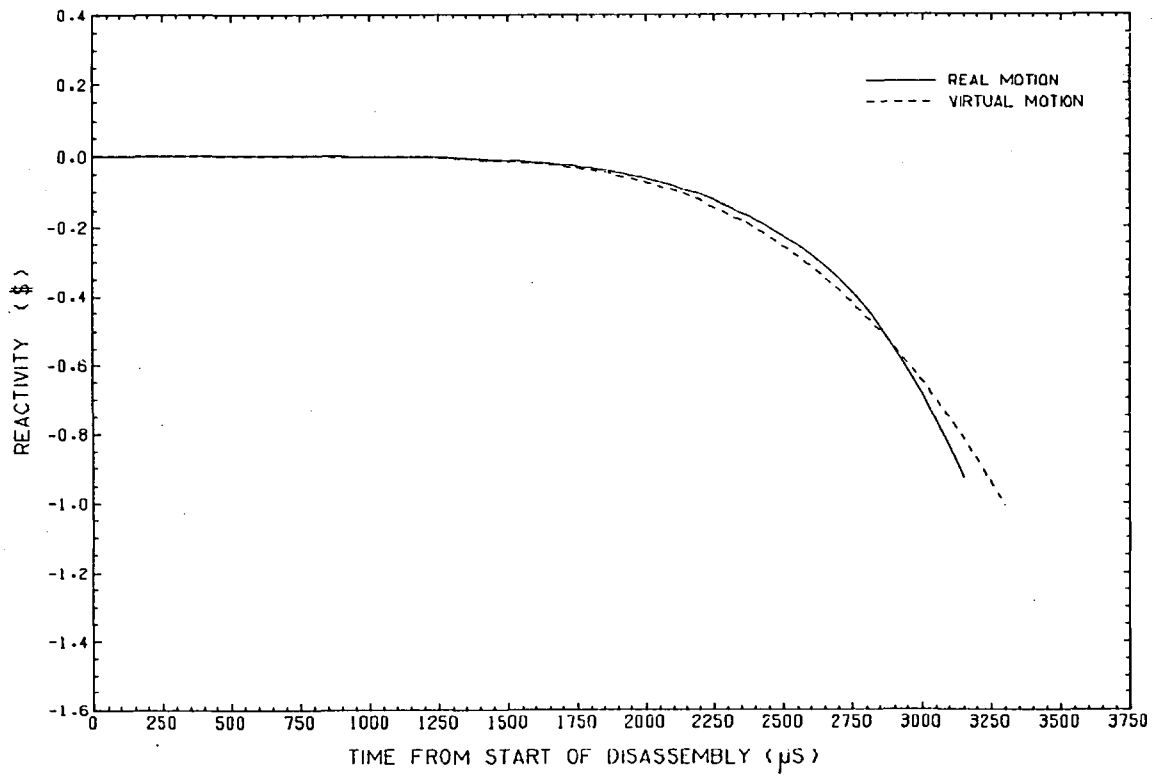

FIG- 63B
MOTION REACTIVITY FEEDBACK VARIATION DURING DISASSEMBLY DRIVEN BY $70/s WITH UNIFORM VOID ADDITION IN BOTH THE REAL AND VIRTUAL MOTION MODELS

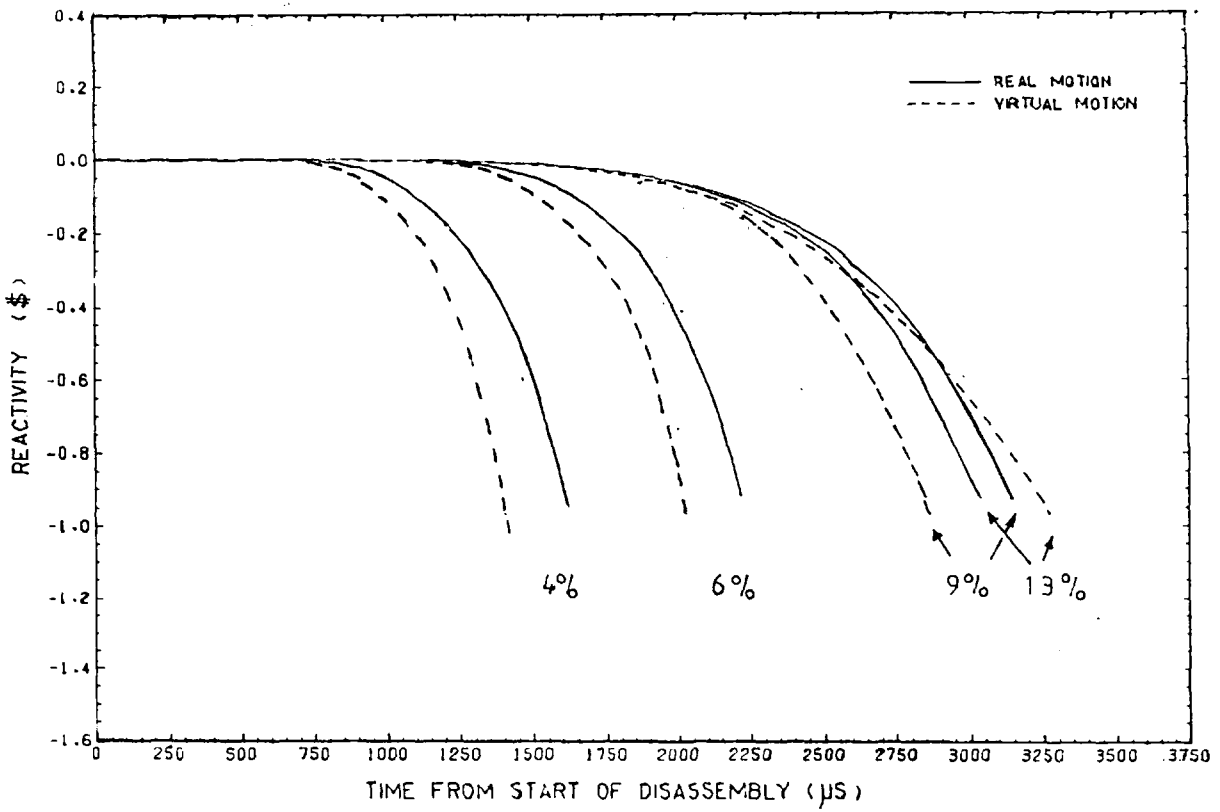

FIG - 64

NET REACTIVITY VARIATION IN THE REAL AND THE VIRTUAL MOTION MODELS
FOR AN INITIAL UNIFORM VOID ADDITION OF 13 %

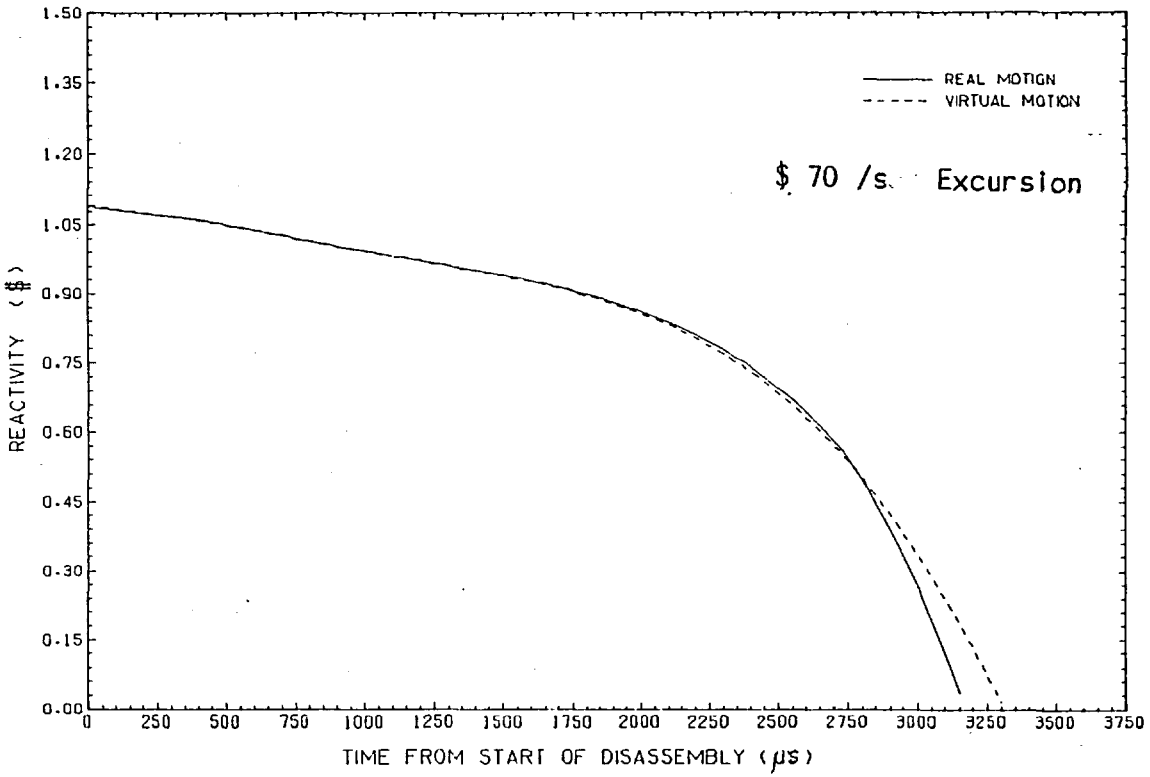

FIG - 6 5

TOTAL POWER VARIATION IN THE REAL AND THE VIRTUAL MOTION MODELS
FOR AN INITIAL UNIFORM VOID ADDITION OF 13 %

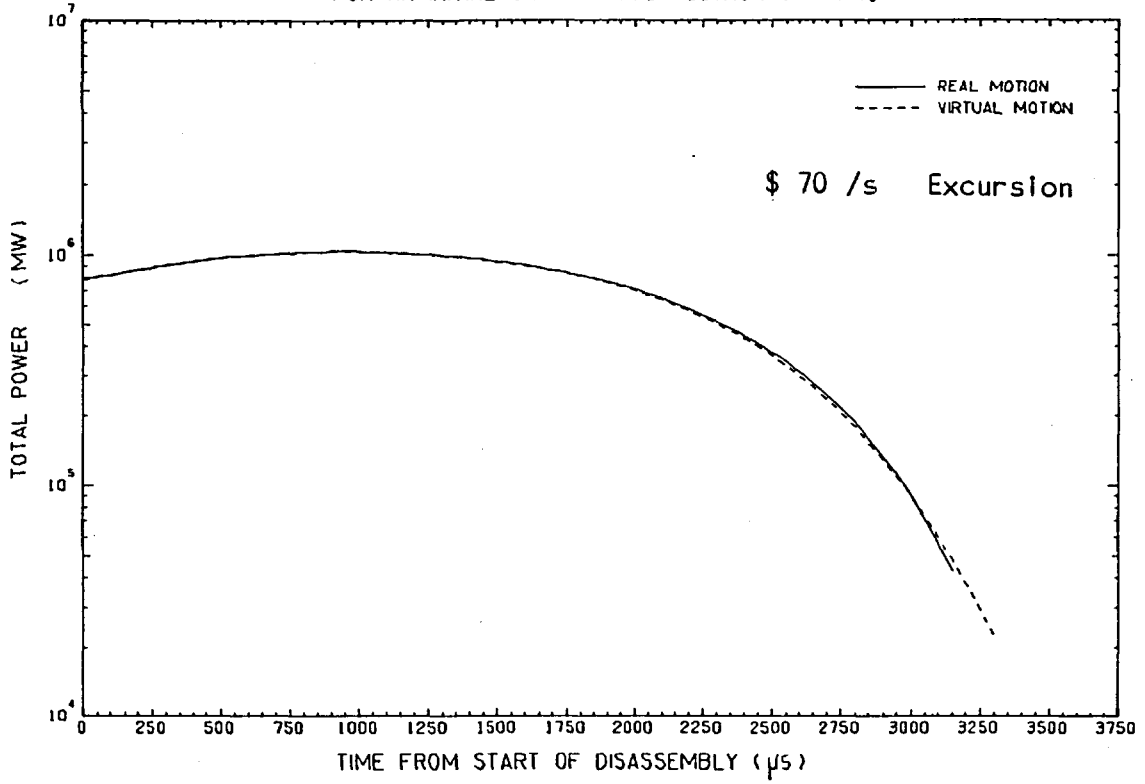

FIG – 66

TOTAL ENERGY VARIATION IN THE REAL AND THE VIRTUAL MOTION MODELS

FOR AN INITIAL UNIFORM VOID ADDITION OF 13 %

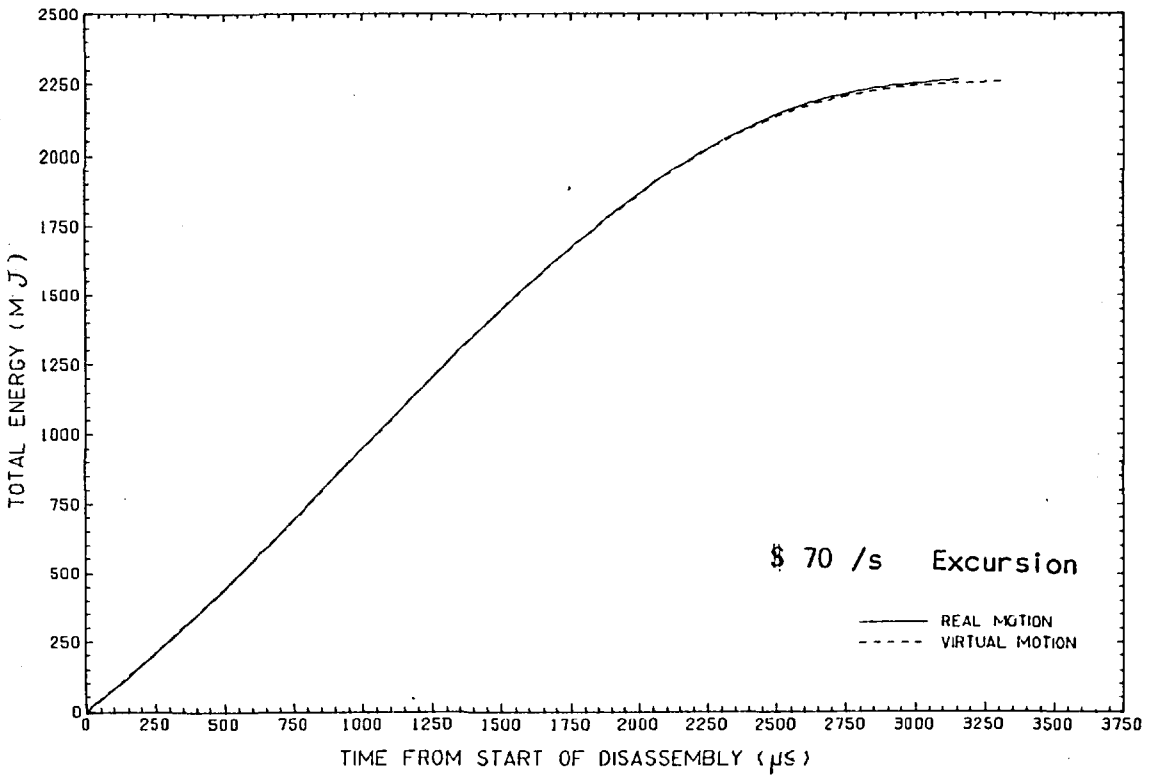

FIG - 67

CENTRAL TEMPERATURE AT THE END OF DISASSEMBLY AS A FUNCTION OF THE INITIAL VOID FRACTION , IN THE REAL AND VIRTUAL MOTION MODELS

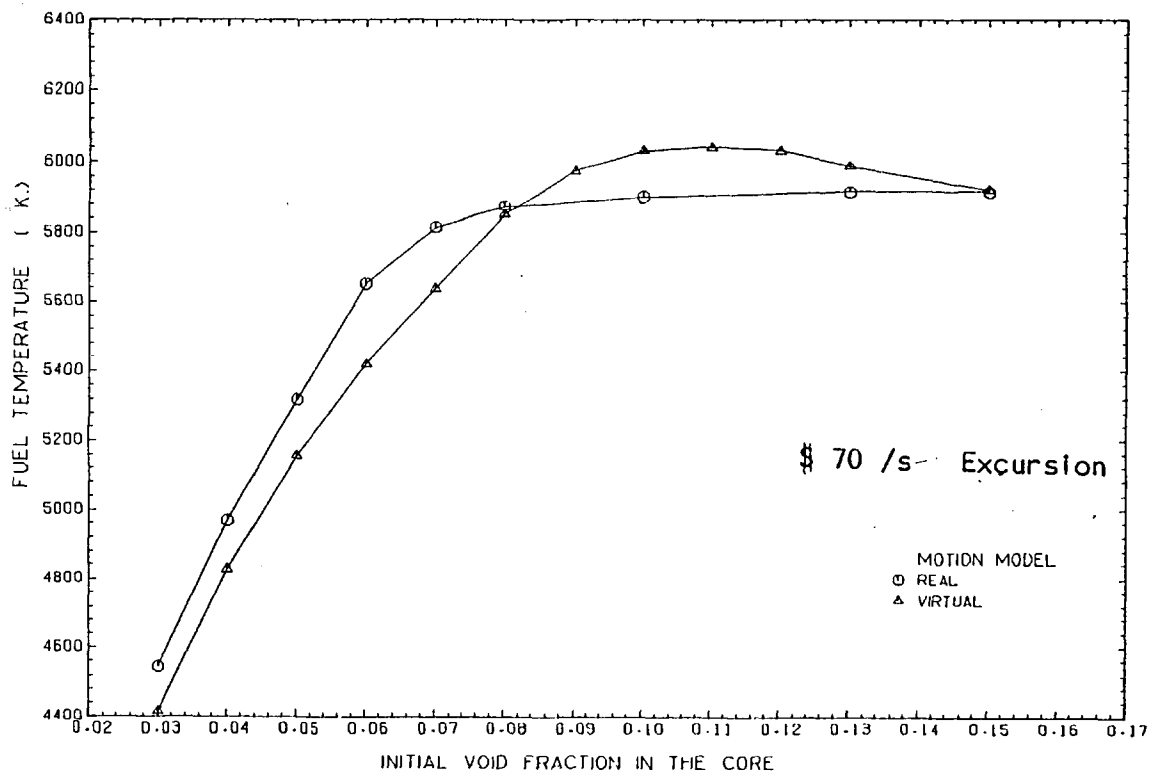

FIG - 68

CENTRAL PRESSURE AT THE END OF DISASSEMBLY AS A FUNCTION OF INITIAL VOID FRACTION , IN THE REAL AND VIRTUAL MOTION MODELS

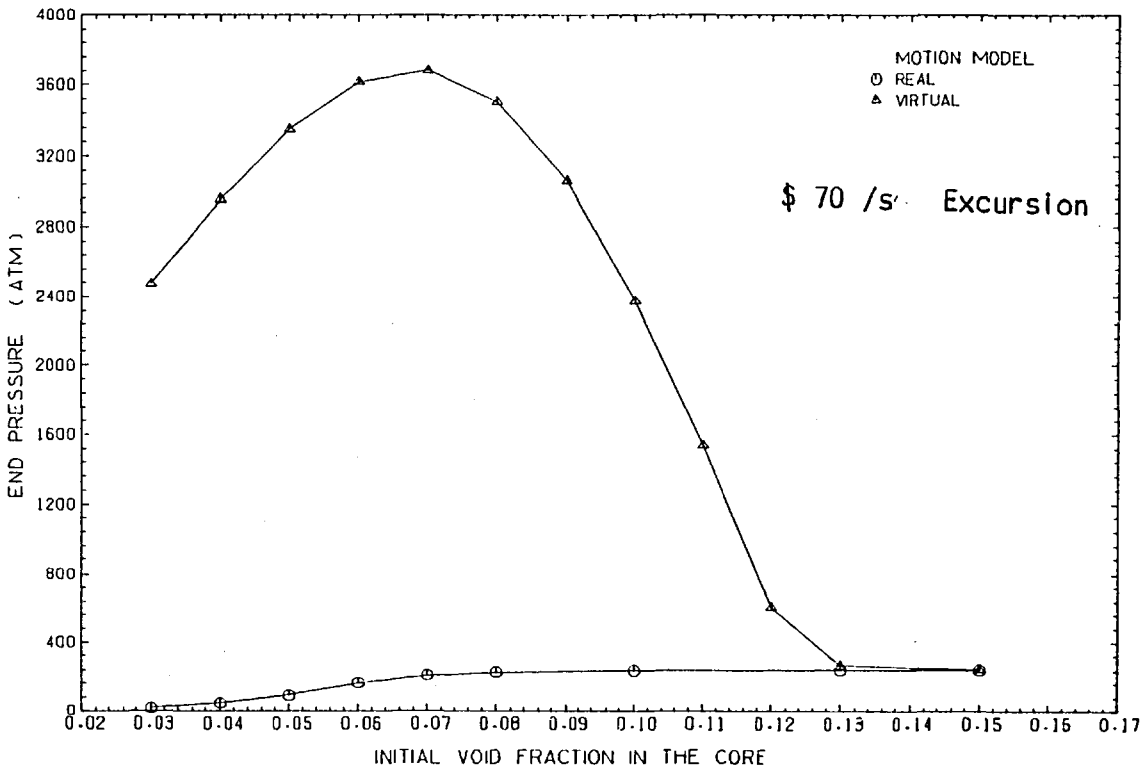

FIG - 69

PRESSURE IN CELL (9,16) AT THE END OF DISASSEMBLY AS A FUNCTION OF THE INITIAL VOID FRACTION , IN THE REAL AND VIRTUAL MOTION MODELS

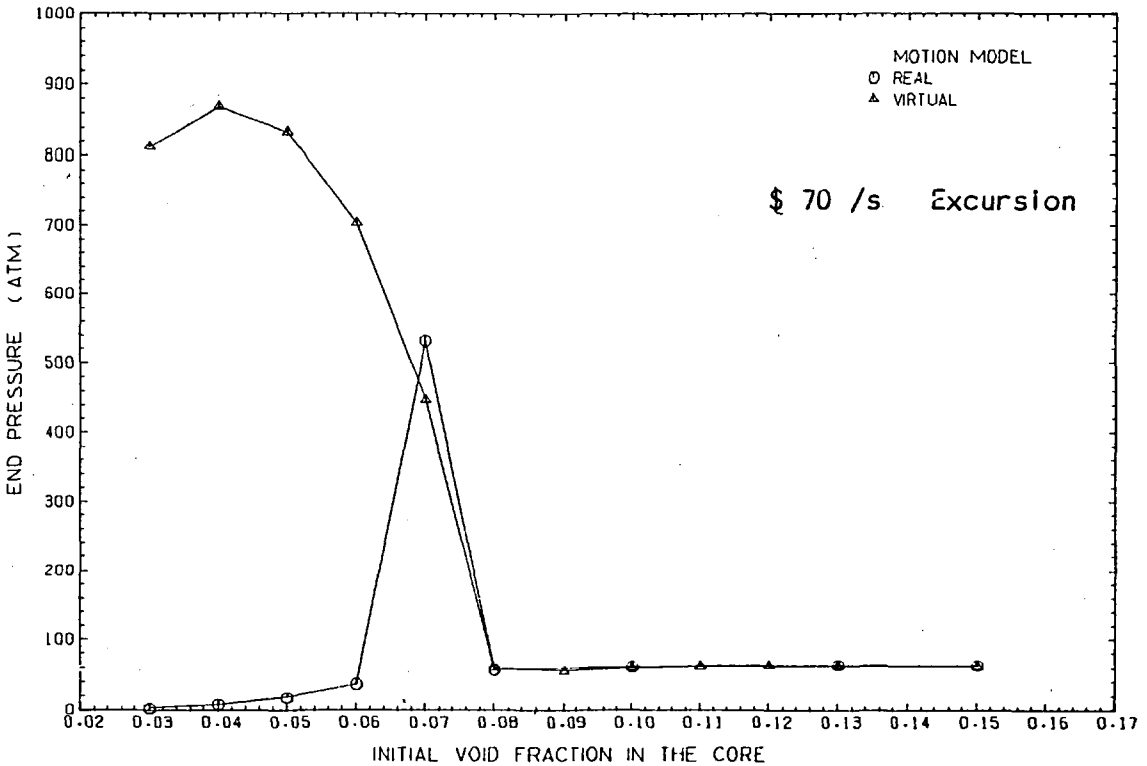

FIG - 70

DOPPLER FEEDBACK AT THE END OF THE DISASSEMBLY AS A FUNCTION OF THE INITIAL VOID FRACTION , IN THE REAL AND VIRTUAL MOTION MODELS

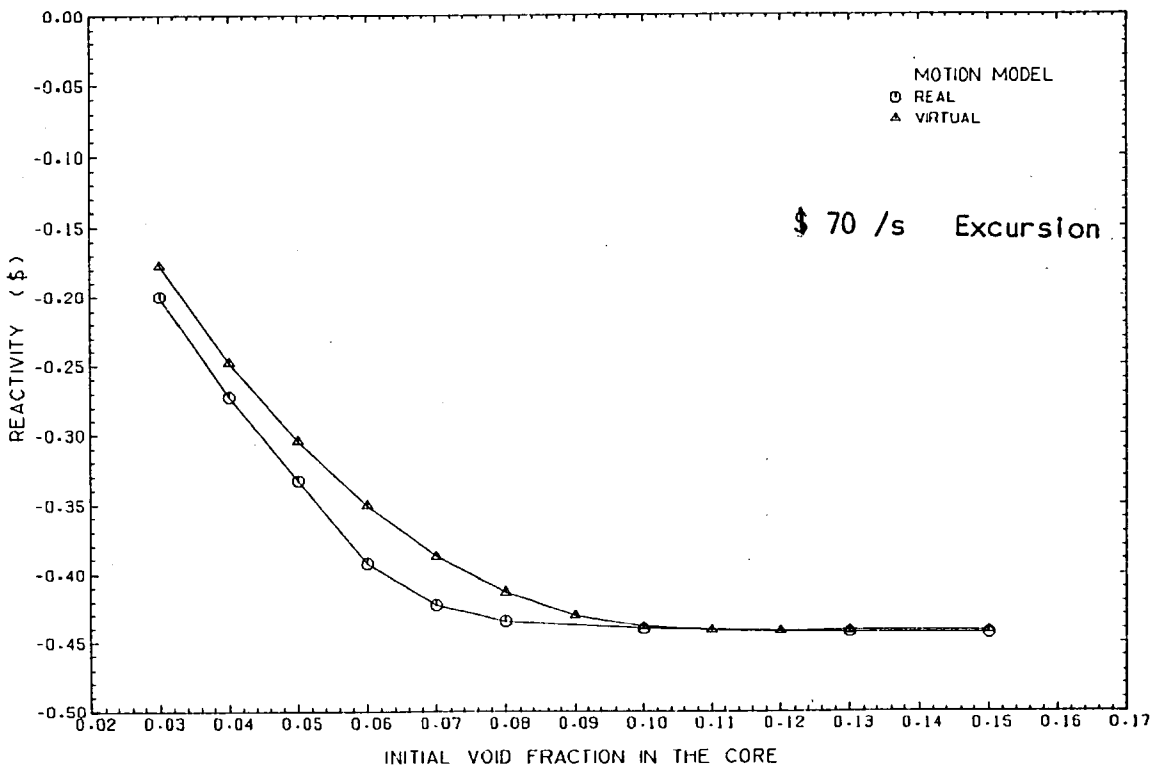

FIG - 71.

TOTAL ENERGY AT THE END OF DISASSEMBLY AS A FUNCTION OF THE INITIAL VOID FRACTION , IN THE REAL AND VIRTUAL MOTION MODELS

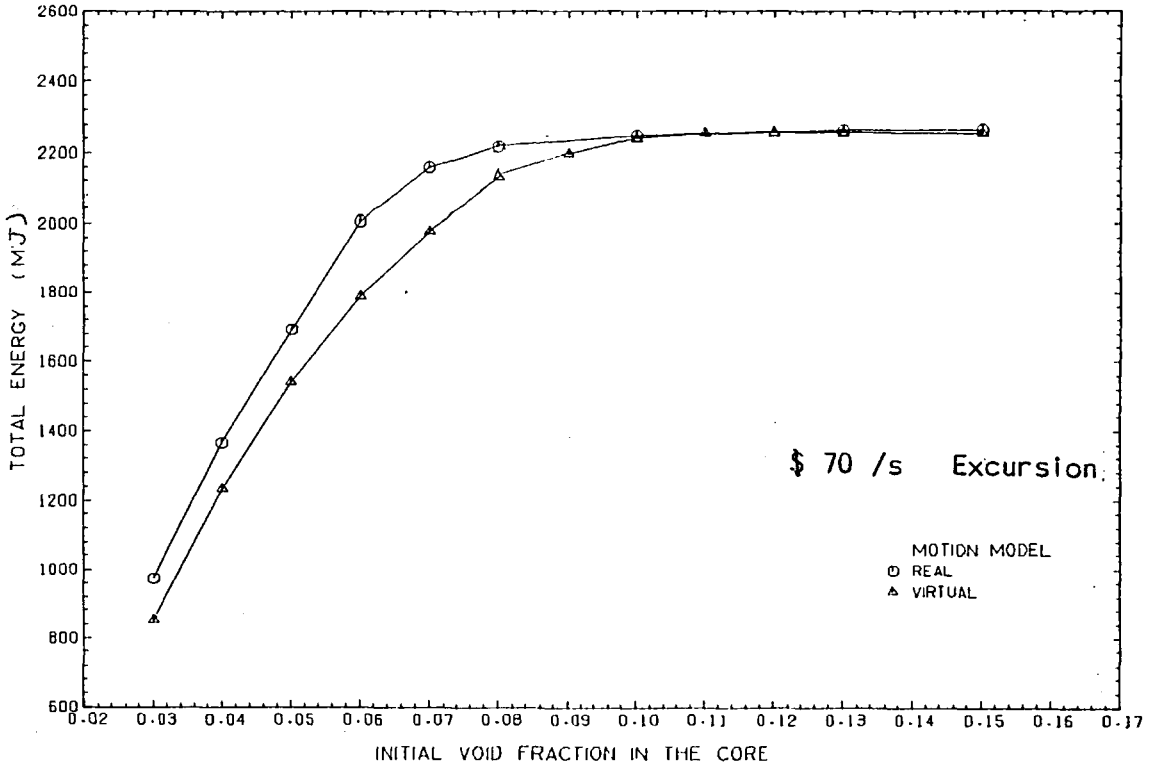

FIG - 72

VARIATION OF FUEL TEMPERATURE AT THE CENTRE DURING DISASSEMBLY DRIVEN BY 100 $ /s RAMP REACTIVITY, IN THE REAL MOTION MODEL

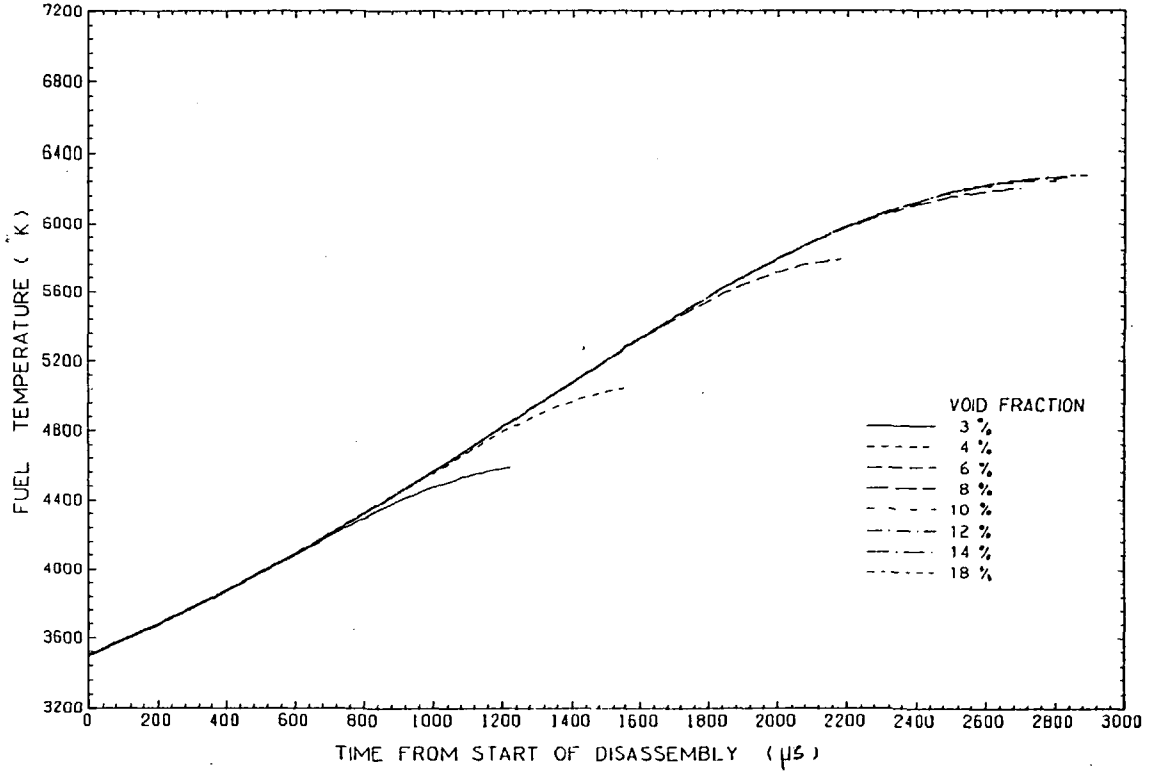

FIG - 73 A

VARIATION OF FUEL TEMPERATURE AT THE CENTRE DURING DISASSEMBLY DRIVEN BY 100 $ /s RAMP REACTIVITY , IN THE VIRTUAL MOTION MODEL

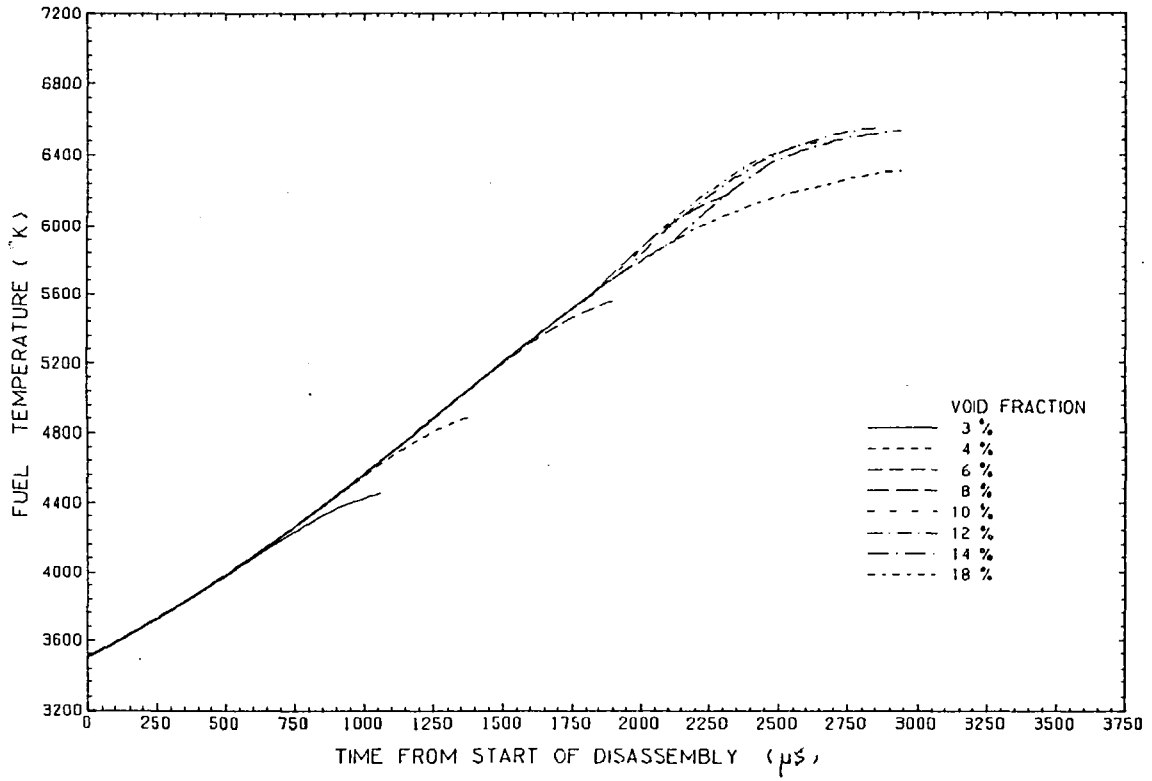

FIG - 73 B

VARIATION OF FUEL TEMPERATURE AT THE CENTRE DURING DISASSEMBLY DRIVEN BY 100 $ /$ RAMP REACTIVITY , IN THE VIRTUAL MOTION MODEL

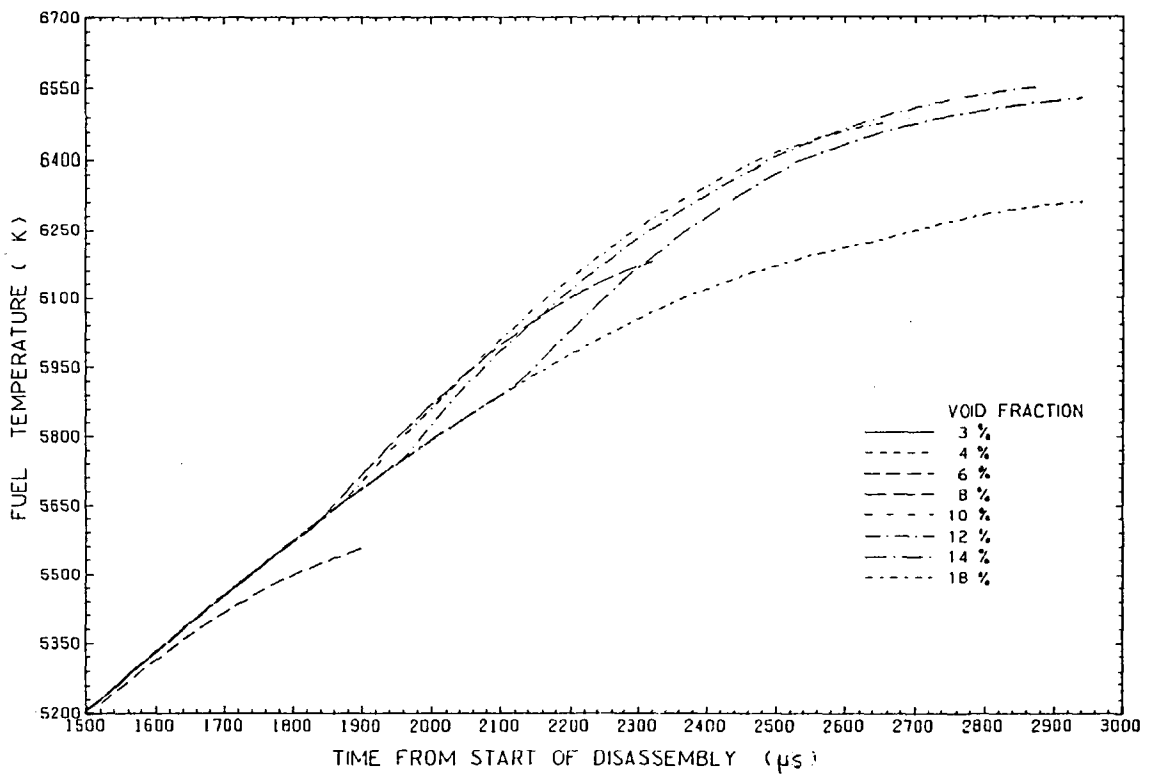

FIG - 74

VARIATION OF FUEL PRESSURE IN CELL (2,16) DURING DISASSEMBLY, DRIVEN BY 100 $ /s RAMP REACTIVITY, IN THE REAL MOTION MODEL

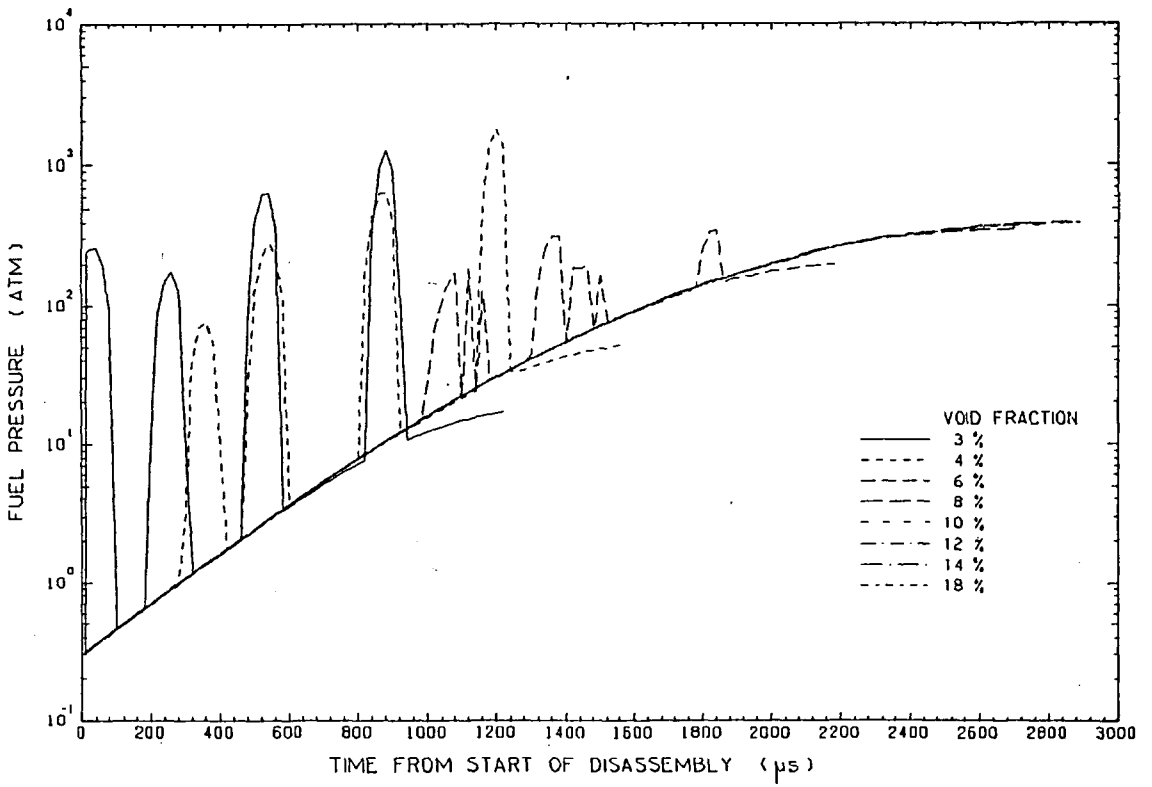

FIG - 75 PRESSURE VARIATION WITH TIME, IN THE VIRTUAL MOTION MODEL FOR VARIOUS UNIFORMLY DISTRIBUTED VOID FRACTIONS, IN 100 $/$ DISASSEMBLY

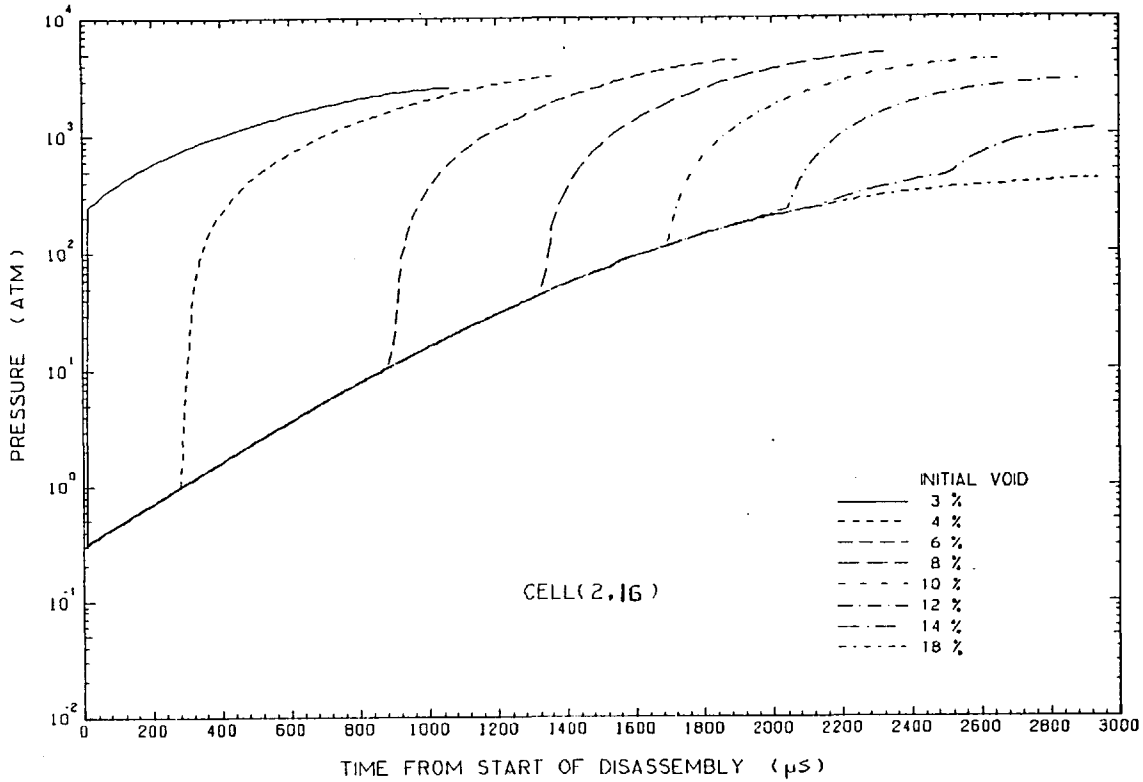

FIG - 76

VARIATION OF FUEL PRESSURE IN CELL (9,16) DURING DISASSEMBLY, DRIVEN BY 100 $ /s RAMP REACTIVITY, IN THE REAL MOTION MODEL

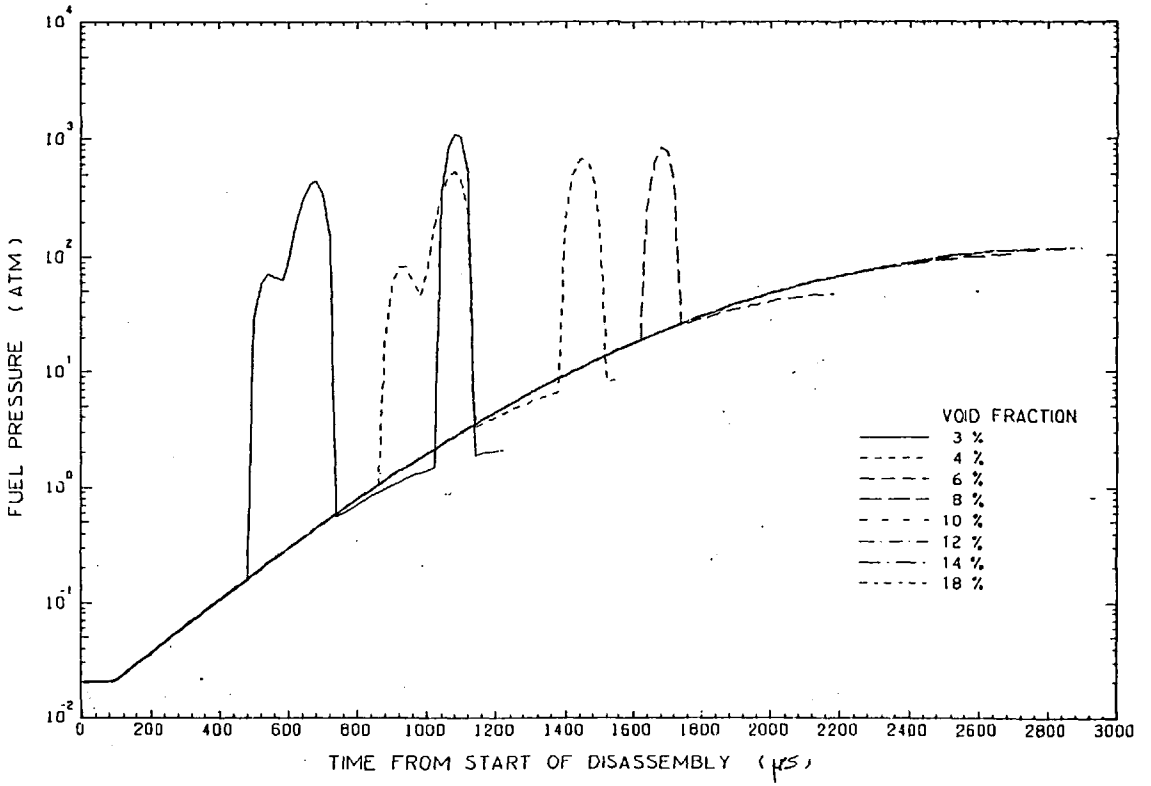

FIG 77 PRESSURE VARIATION WITH TIME, IN THE VIRTUAL MOTION MODEL FOR VARIOUS UNIFORMLY DISTRIBUTED VOID FRACTIONS, IN 100 $/$ DISASSEMBLY

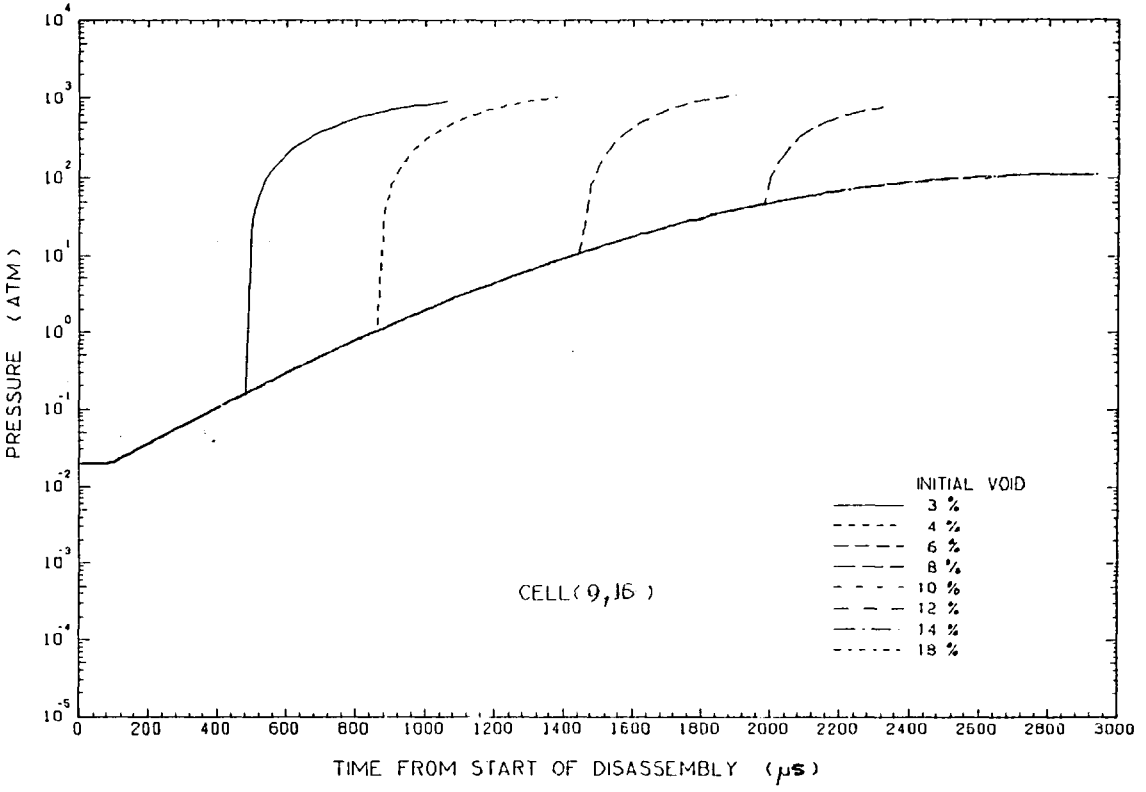

FIG-78 PRESSURE VARIATION IN CELL (2,16)
DURING DISASSEMBLY OF THE CORE VOIDED UNIFORMLY BY 3% ,
AND DRIVEN BY 100 $/s RAMP REACTIVITY

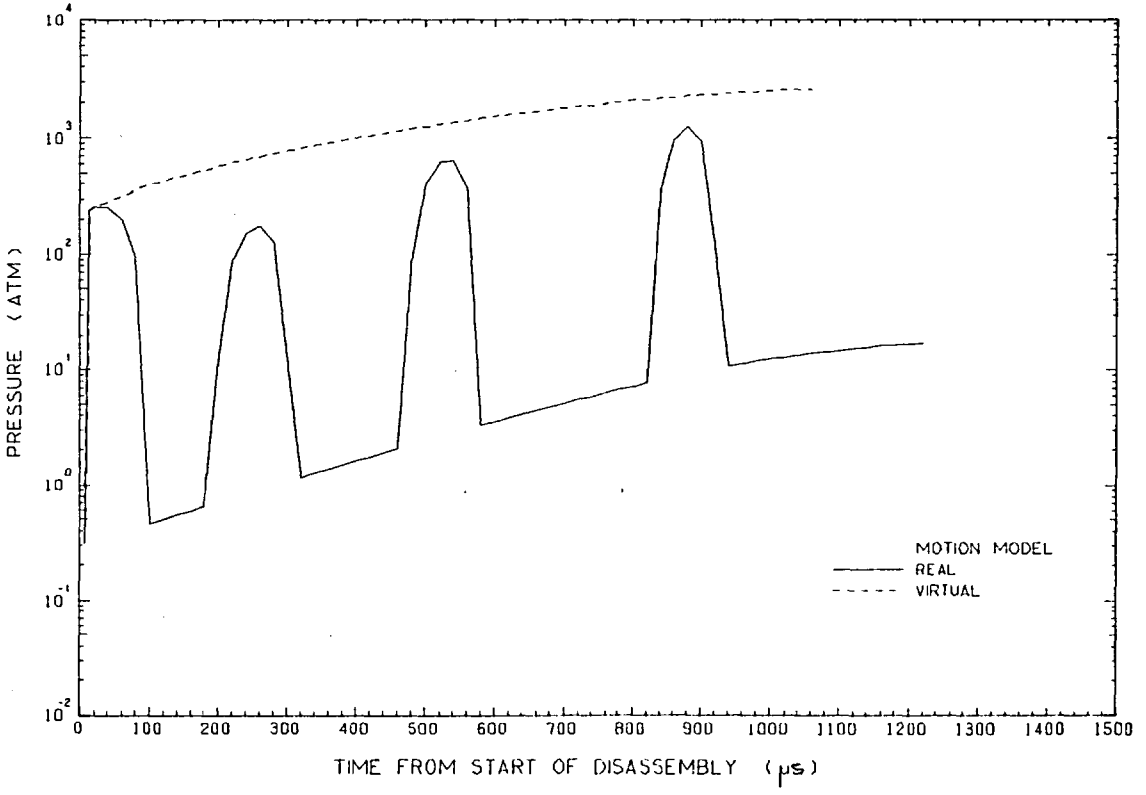

FIG - 79 PRESSURE VARIATION IN CELL (2,16)
DURING DISASSEMBLY OF THE CORE VOIDED UNIFORMLY BY 4% ,
AND DRIVEN BY 100 $/s RAMP REACTIVITY

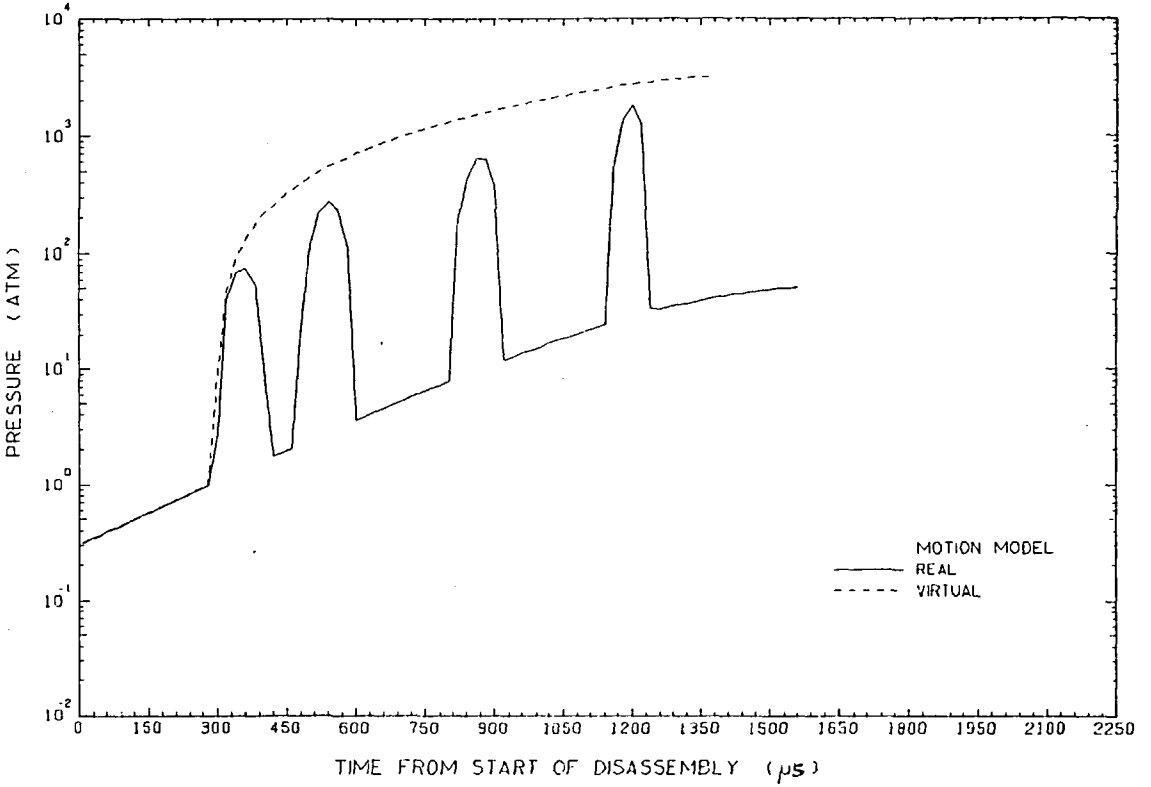

FIG - 80 PRESSURE VARIATION IN CELL (2,16)
DURING DISASSEMBLY OF THE CORE VOIDED UNIFORMLY BY 6%,
AND DRIVEN BY 100 $/s RAMP REACTIVITY

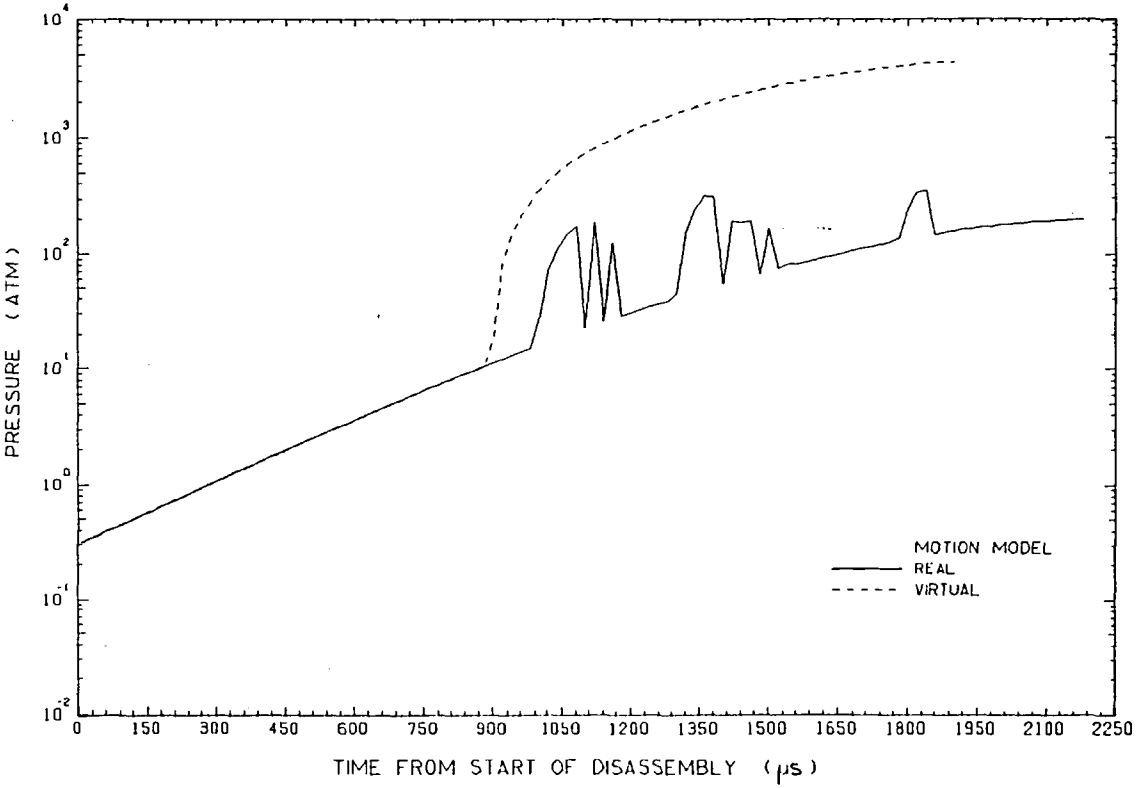

FIG 81 PRESSURE VARIATION IN CELL (2,16)
DURING DISASSEMBLY OF THE CORE VOIDED UNIFORMLY BY 8% ,
AND DRIVEN BY 100 $/s RAMP REACTIVITY

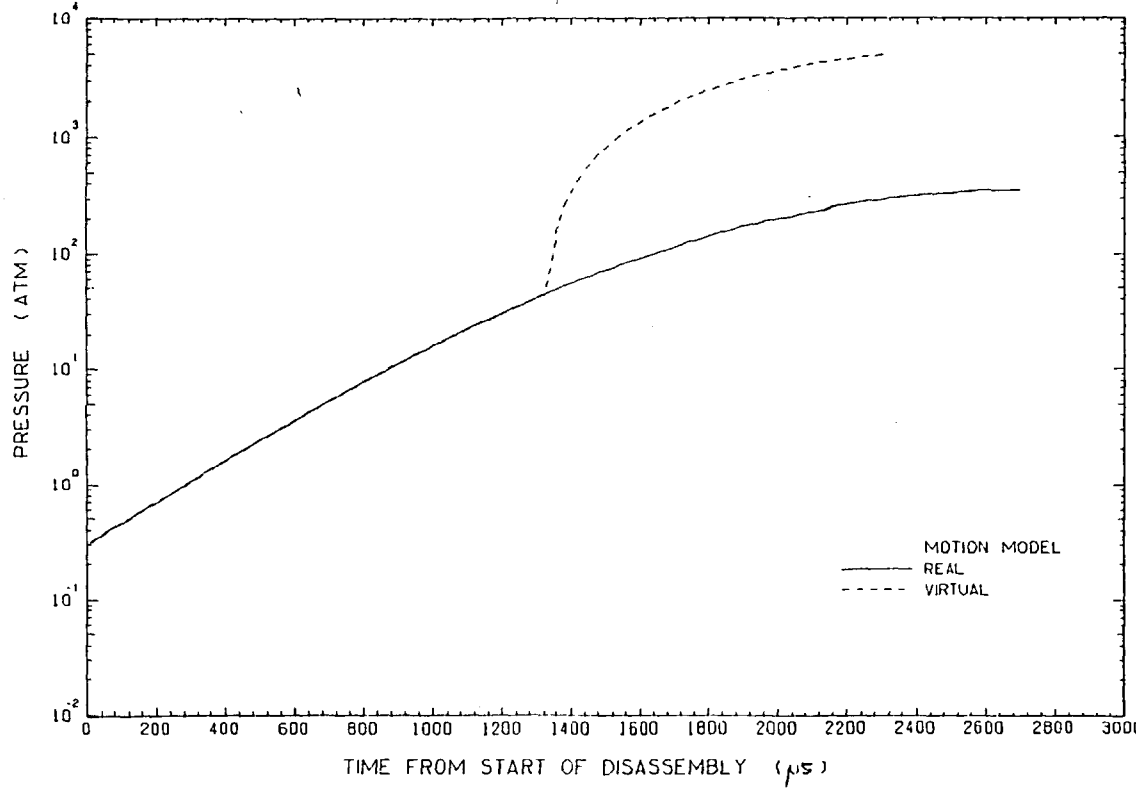

FIG-82 PRESSURE VARIATION
DURING DISASSEMBLY OF THE CORE VOIDED UNIFORMLY BY 10 % ,
AND DRIVEN BY 100 $/S RAMP REACTIVITY

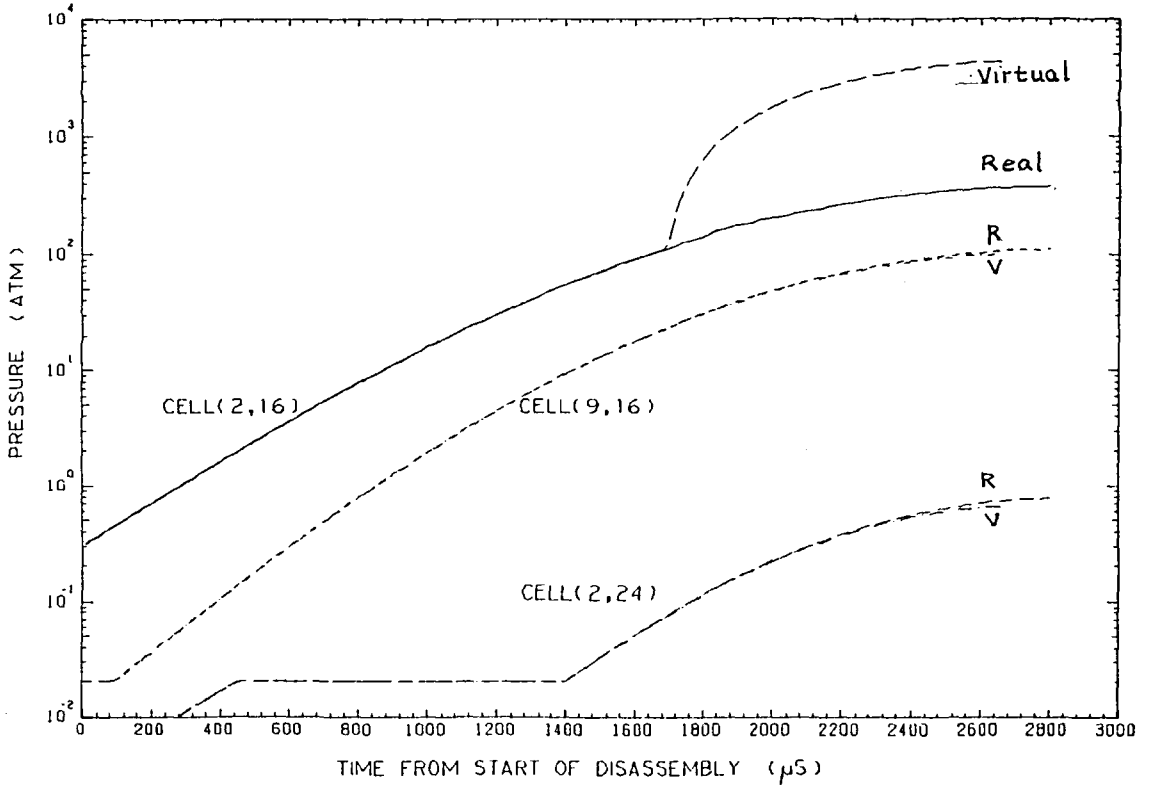

FIG - 83 PRESSURE VARIATION
DURING DISASSEMBLY OF THE CORE VOIDED UNIFORMLY BY 18% ,
AND DRIVEN BY 100 $/S RAMP REACTIVITY

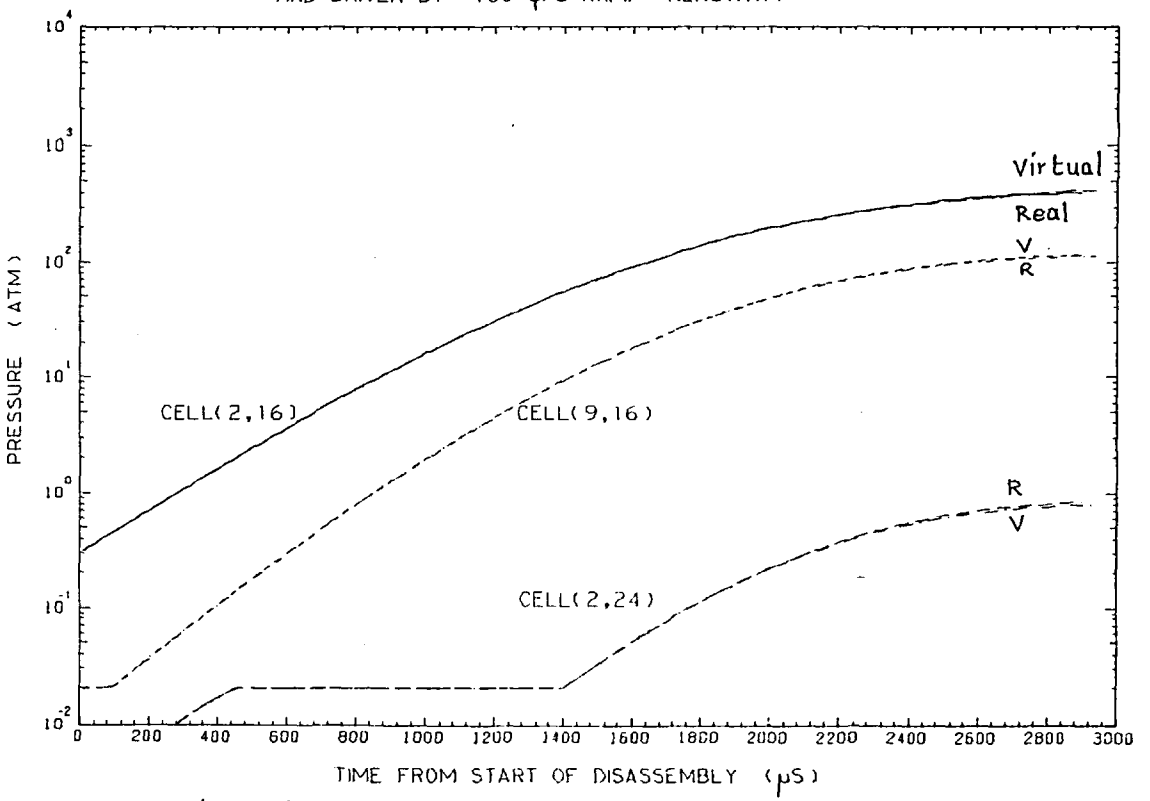

FIG - 84

TEMPERATURE IN CELL (2,16) AT THE END OF DISASSEMBLY DRIVEN BY 100 $/S RAMP REACTIVITY, AS A FUNCTION OF THE INITIAL VOID FRACTION

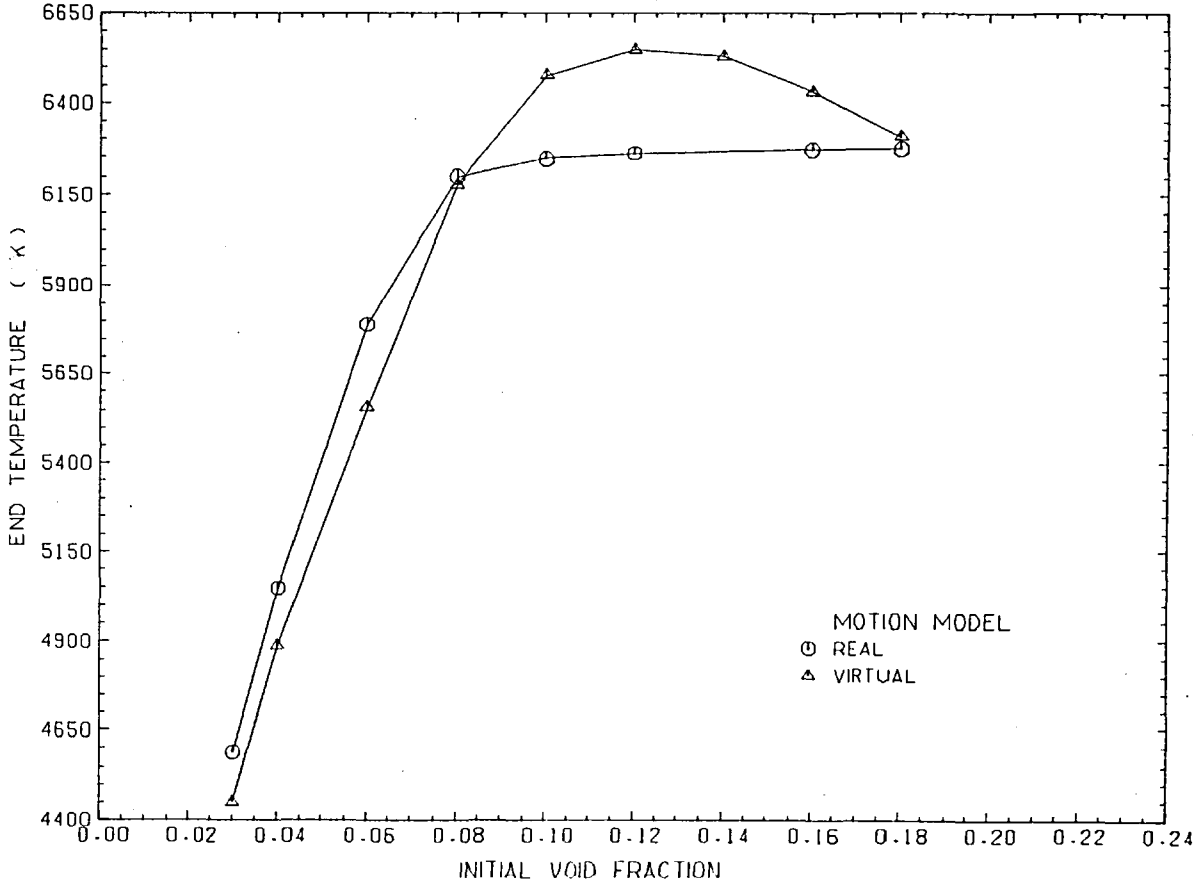

FIG - 85

TEMPERATURE IN CELL (9,16) AT THE END OF DISASSEMBLY DRIVEN BY 100 $/S RAMP REACTIVITY, AS A FUNCTION OF THE INITIAL VOID FRACTION

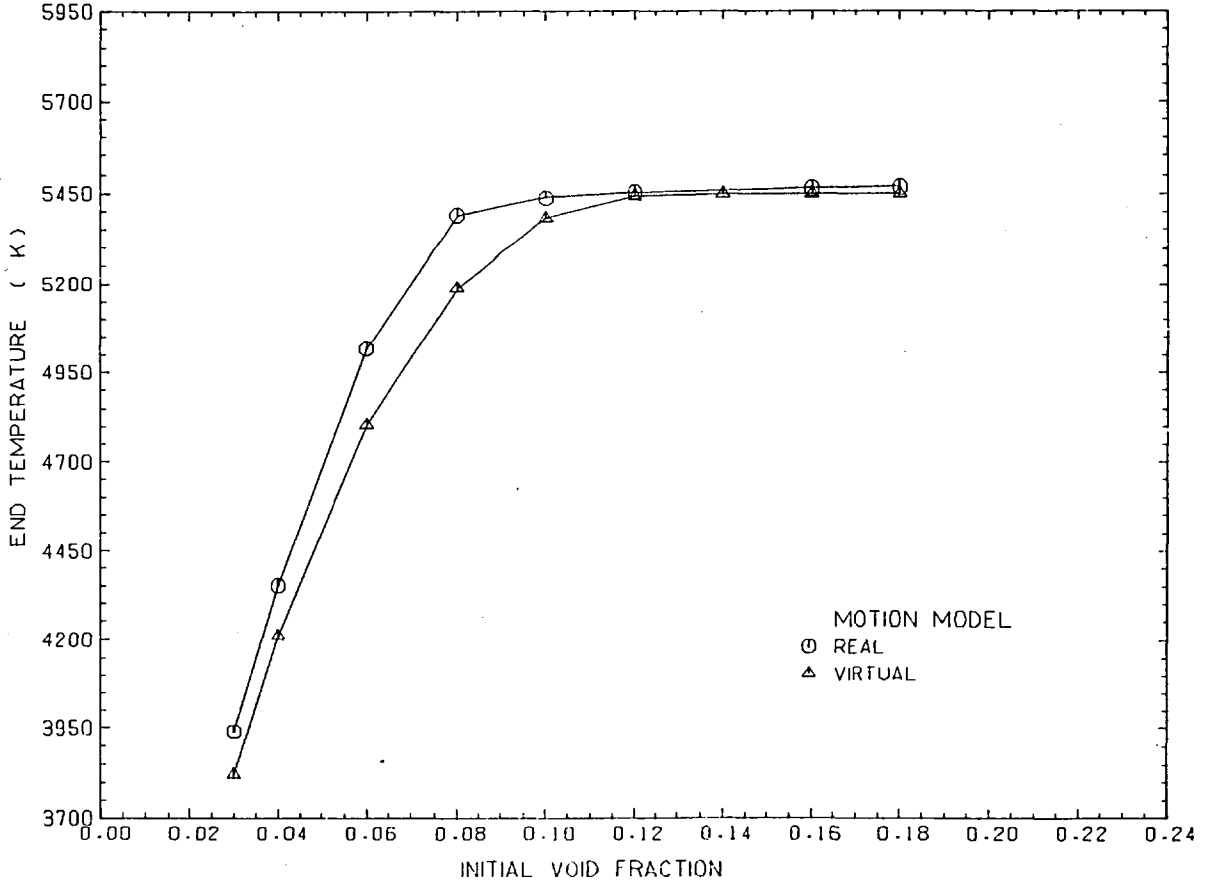

FIG - 86

PRESSURE IN CELL (2,16) AT THE END OF DISASSEMBLY DRIVEN BY
100 $/S RAMP REACTIVITY, AS A FUNCTION OF THE INITIAL VOID FRACTION

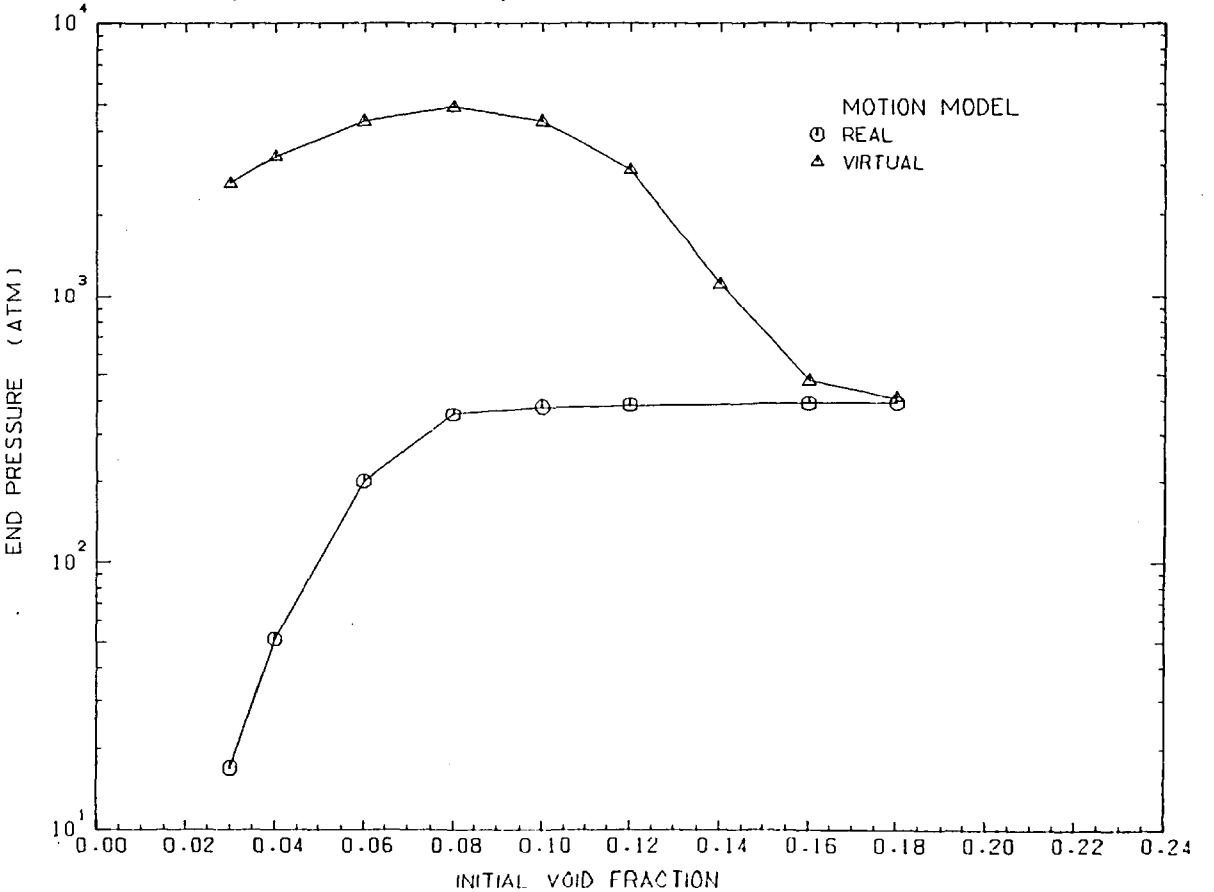

FIG-87

PRESSURE IN CELL (9,16) AT THE END OF DISASSEMBLY DRIVEN BY
100 $/S RAMP REACTIVITY, AS A FUNCTION OF THE INITIAL VOID FRACTION

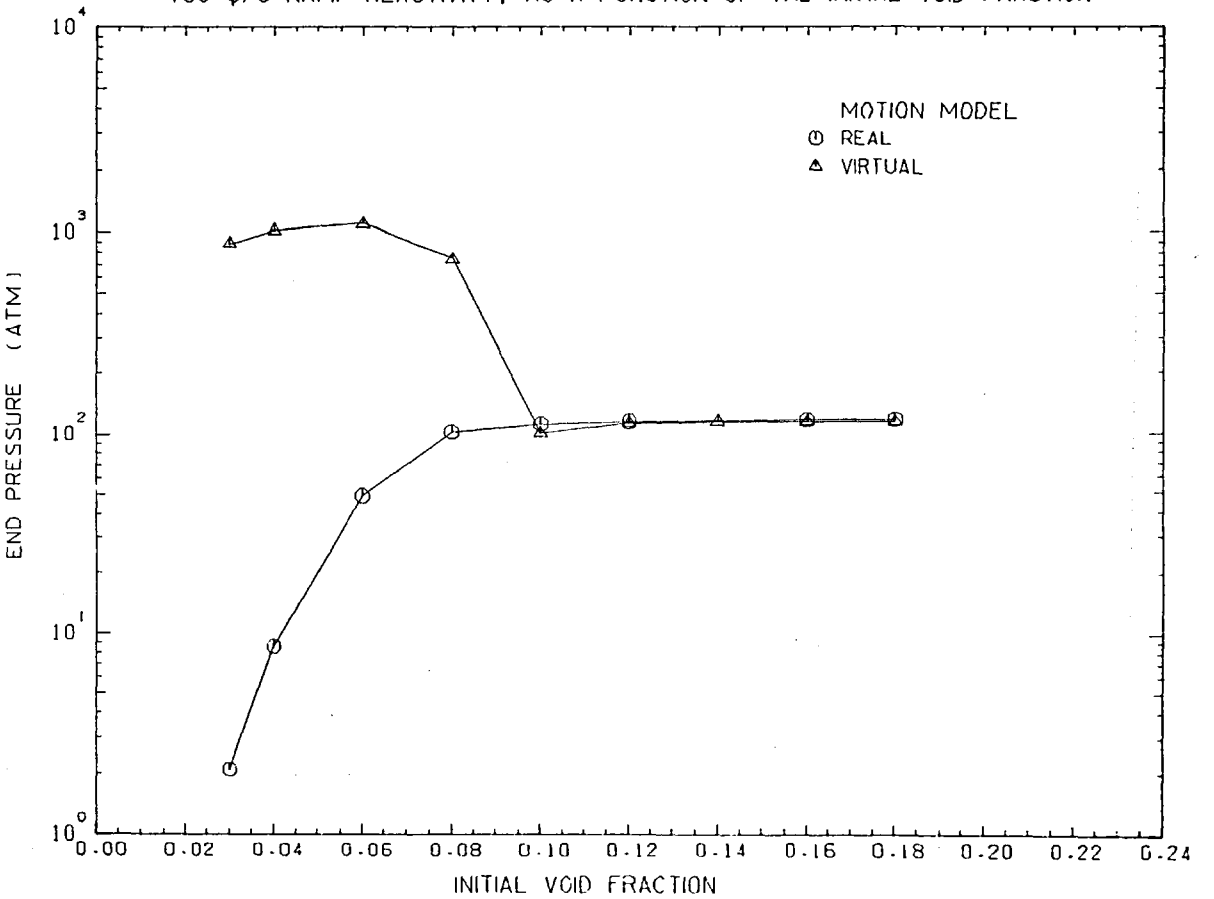

FIG - 88

TIME AT THE END OF DISASSEMBLY PHASE, IN AN ACCIDENT DRIVEN BY 100 $/β RAMP REACTIVITY, AS A FUNCTION OF THE INITIAL VOID FRACTION

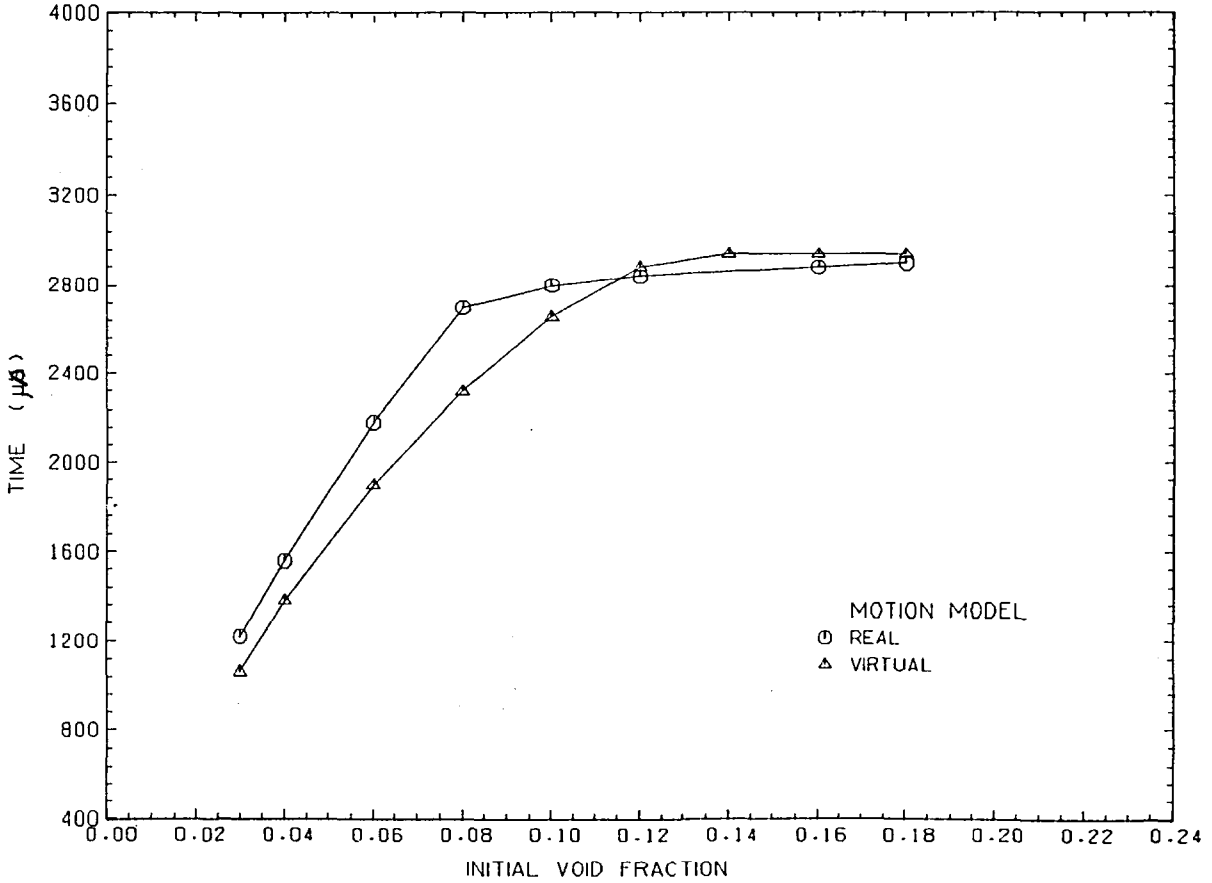

FIG - 89

TOTAL ENERGY GENERATED DURING THE DISASSEMBLY DRIVEN BY
100 $/s RAMP REACTIVITY, AS A FUNCTION OF THE INITIAL VOID FRACTION

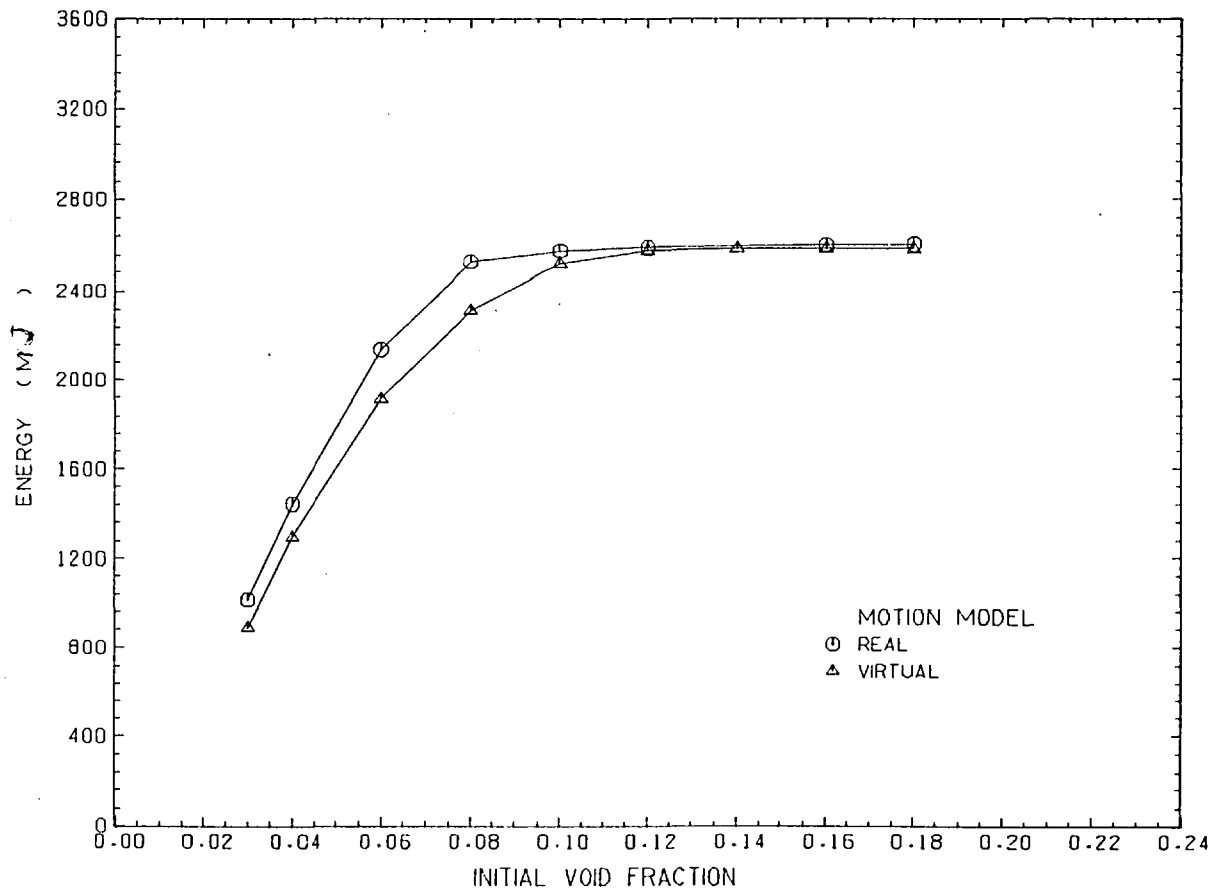

Fig - 9 o

Comparison of quasi steady state flux from NEST with steady state flux from MARC in energy group 1 at the axial mid plane

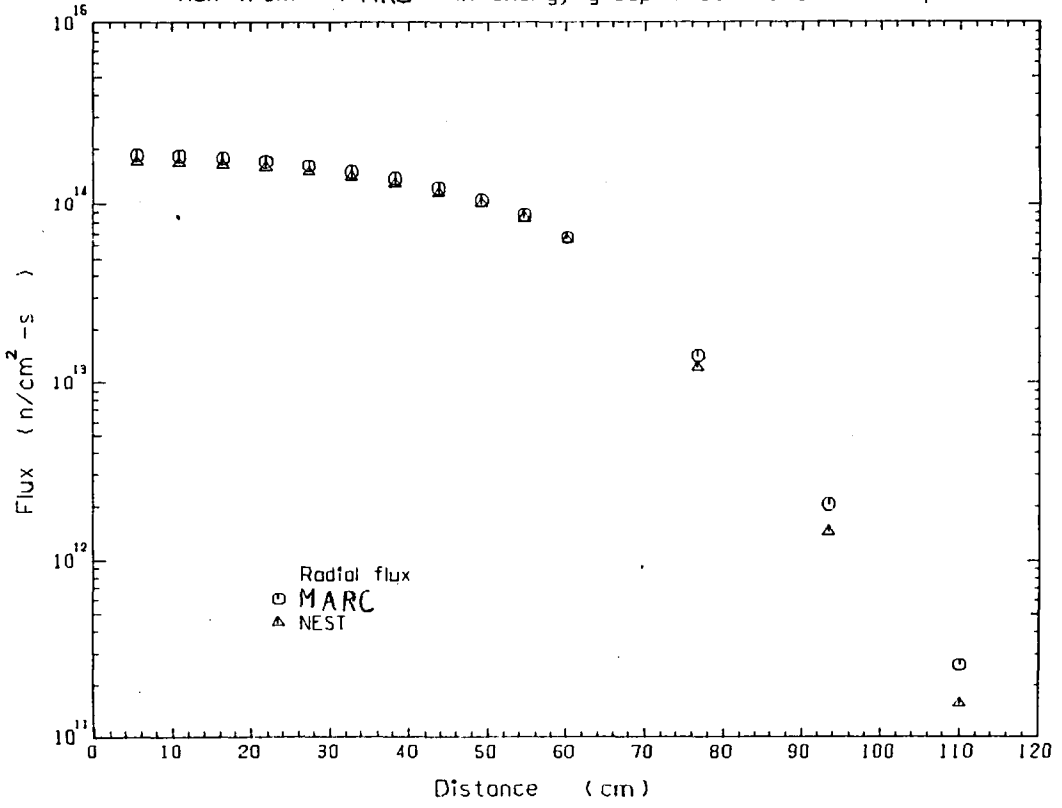

Fig – 91

Comparison of quasi steady state flux from NEST with steady state flux from MARC in energy group 2 at the axial mid plane

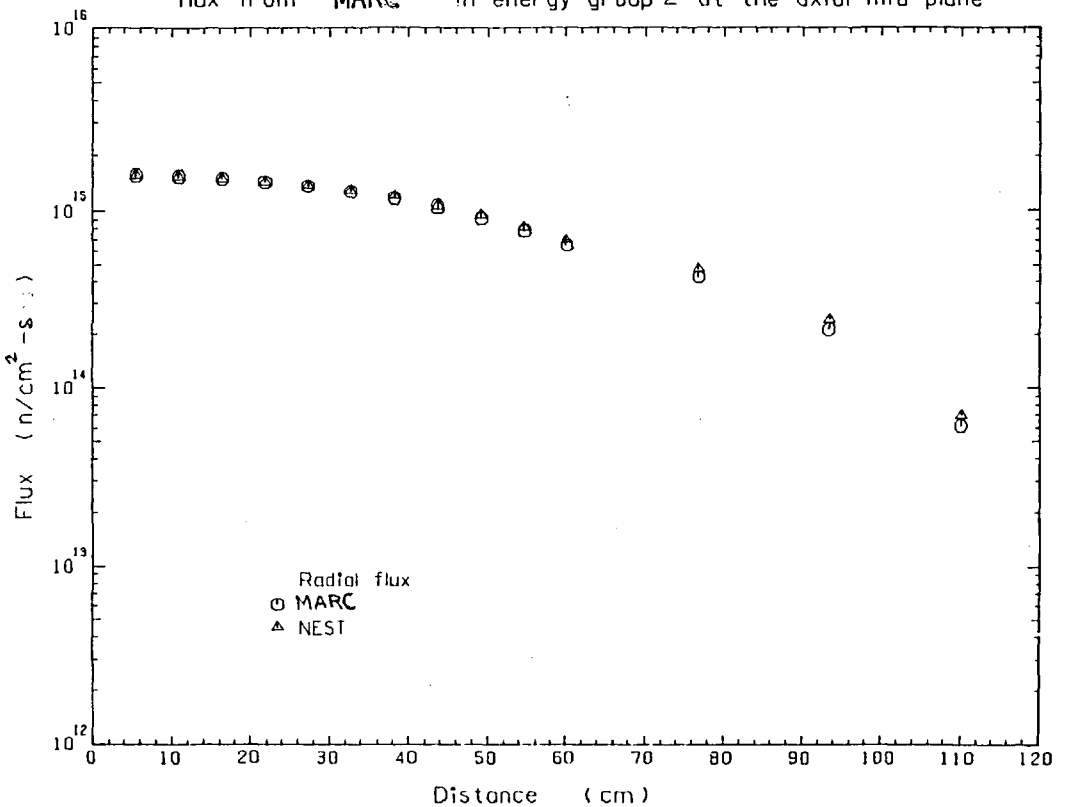

Fig -92

Variation of flux convergence number during quasi steady state calculation of neutron flux using the NEST code

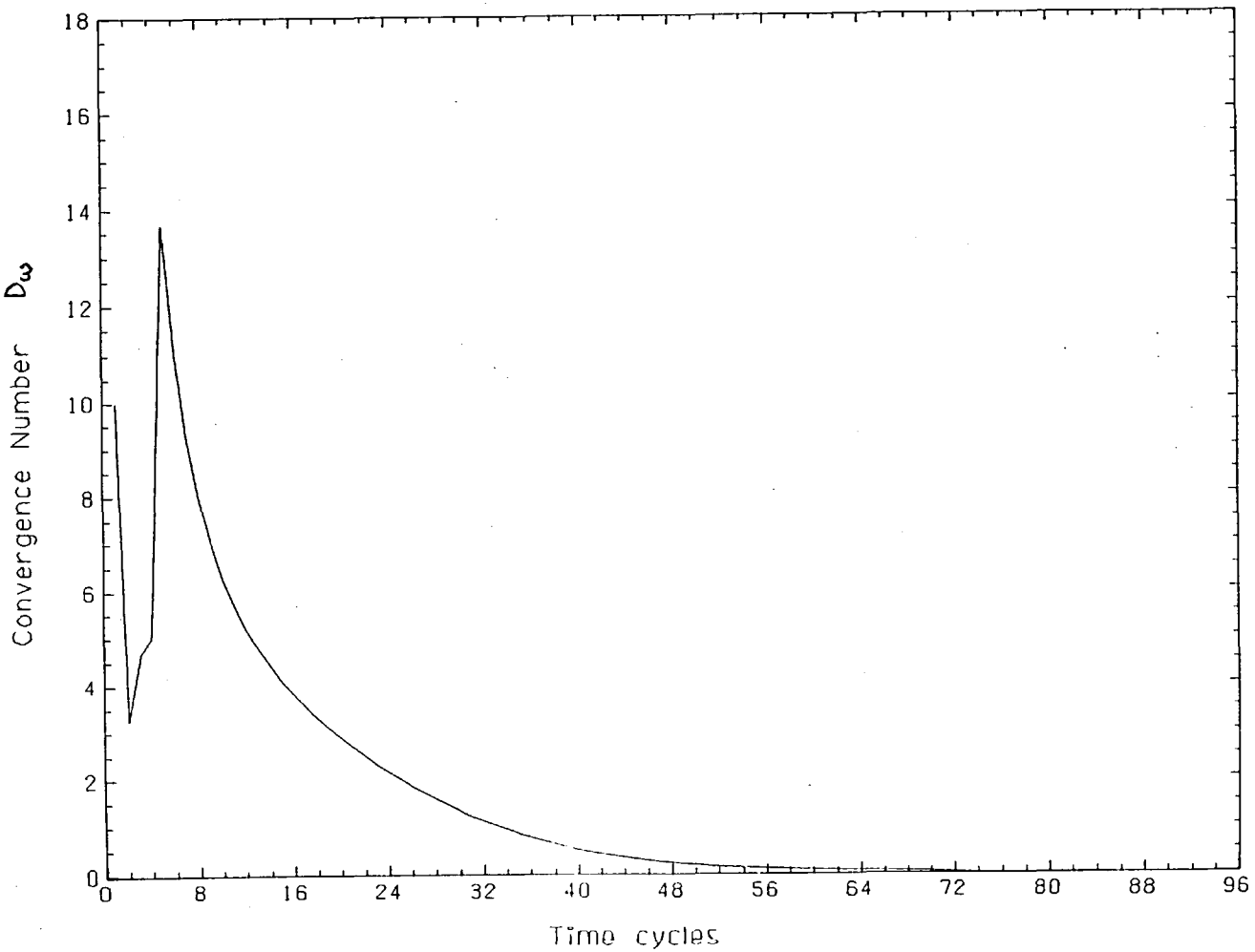

Fig -93

Convergence of effective multiplication fator during quasi steady state calculation of neutron flux using the NEST code

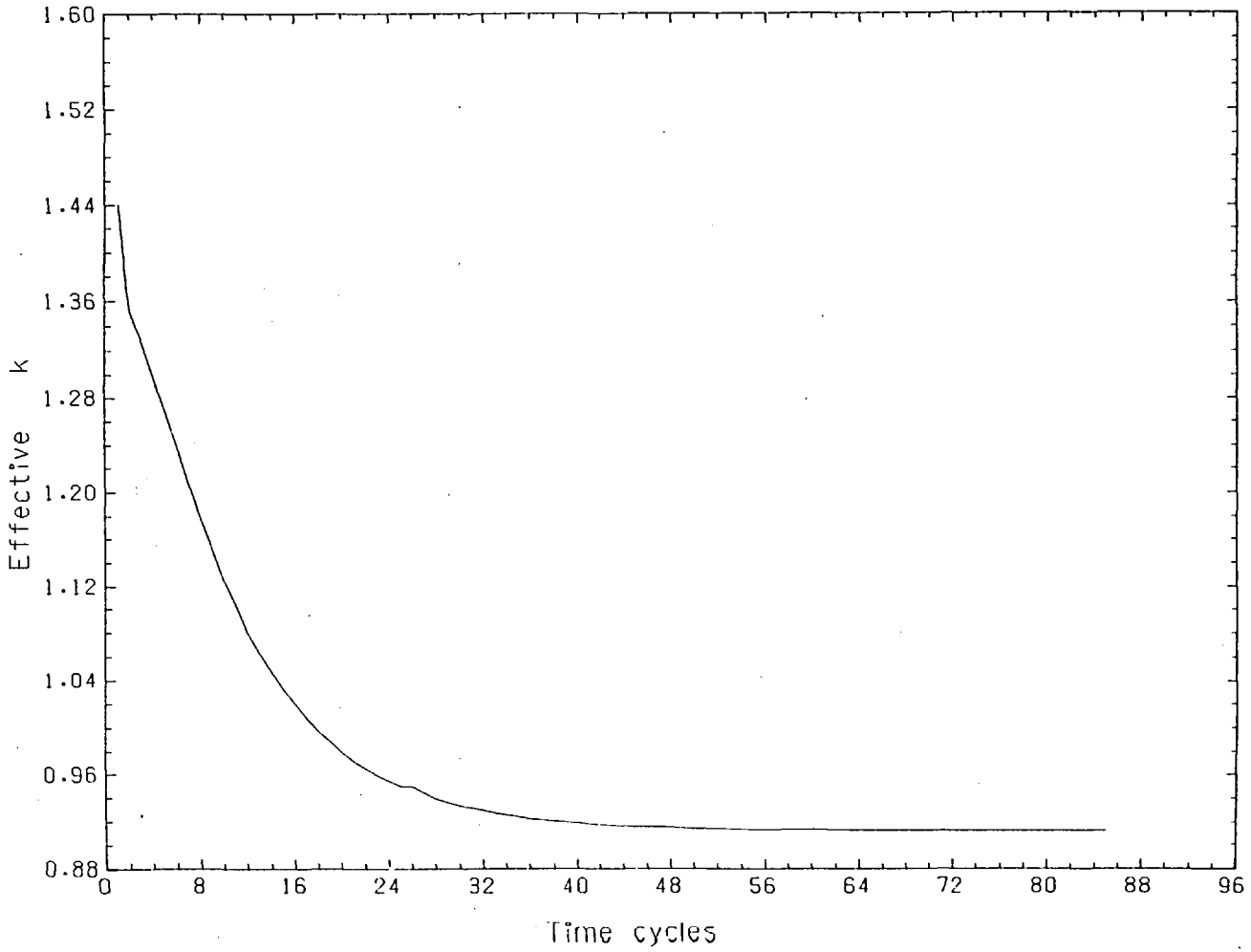

REFERENCES

1. Abagyan L P, Bazazyantz N O, Bondarenko I I, Nikolaeve M N: "Group Constants for Nuclear Reactor Calculations", Consultants Bureau Enterprises Inc., New York (1964).

2. Abramson P B: "FX2-POOL a Two Dimensional Coupled Hydrodynamic Thermodynamic and Neutronic Computer Model for Hypothetical Core Disruptive Accident Analysis", Nucl Sci Eng: 62(1977)195.

3. Adams C H and Stacey W M: "An anomaly Arising in Collapsed Group Flux Synthesis approximation", Trans Am Nucl Soc, 12(1969)151.

4. Allen J.W., Hoskin N.E., Morris E, White P H: "An Equation of State for UO_2 for Fast Reactor Containment Studies" , Paper IAEA-SM-190/21, Proc Sym on "The Thermodynamics of Nuclear Materials" ,Vienna (1974).

5. Alter H, Berk S E: "Current Perspectives on Fast Reactor Containment ", Nucl Eng and Des, 55(1979)153-159

6. Ames F W, "Numerical Methods for Partial Differential Equations", Second Edition, Academic Press New York (1977).

7. Antonakas D, Corcuera r, Govaerts P,: "Accuracy of Coarse Group Calculations in Fast Reactors", Nucl Sci Eng 48(1972)1-9.

8. Arkeri J H, Catton I, Kastenberg W E: "An Experimental Study of Molten Glass/Water Thermal Interaction Under Forced Conditions", Nucl Sci Eng, 66(1978)153

9. Ash M, "Nuclear Reactor Kinetics": 2nd Ed., Mcgraw-Hill, US(1979).

10. Bains M, Board S J, Buttery N E, Hall R W, "The Thermodynamics of Large Scale Fuel Coolant Interactions" UKCEGB Report (1978).

11. Baker L(Jr), "Core Debris Behaviour and Interactions With Concrete", Nucl Eng and Des 42(1977)137-150.

12. Bell C R, Bleiweis P B, Bondreau J E, Parker F R and Smith L L: "SIMMER-1 an Sn Implicit Multi-field Multi-component Eulerian Recriticality Code for LMFBR Disruptive Core Analysis" Los Almos Scientific Lab Rep: LA-NUREG-6467-MS(Jan1977).

13. Belytschko T, "Methods and Programs for Analysis of Fluid Structure Systems", Nucl Eng and Des 42(1977)41-52.

14. Bethe H and Tait J H, "Estimate of the Order of Magnitude of the Explosion When a Fast Reactor Collapses":UKAEA-RM(1956).

15. Bhide M G and Hummel H H: "Calculation of the Doppler Coefficient of Large Ceramic Fueled Fast Reactor", USAEC Report ANL-6601 (1962).

16. Birkhofer A, Langenbuck S, Werner W: " Coarse Mesh Methods for Space Time Kinetics", Trans Am Nucl Soc 18(1974)153

17. Board S J: "A Mechanism of UO_2 / Sodium Thermal Interaction", Nucl Sci Eng 54(1974)233. "Detonation of Fuel-Coolant Explosions",

18. Board S J, Hall R W, Hall R S: Nature 254(1975)319

19. Brooks A: "Some Preliminary Considerations Relating to an Equation of State for Irradiated Nuclear Fuel" , Nuclear Safety 13(1972)467-477.

20. Caldarolla L "A Theoretical Model for the Molten Fuel Sodium Interaction in a Nuclear Fast Reactor", Nucl Eng and Des 22(1972)175-211.

21. Carnahan B, Luther H A, Wilkes J O: Applied Numerical Methods", John Wiley Publishers New York (1969).

22. Chaeseung J L: "Explosive Disassembly of Fast Spectrum Nuclear Reactors", PhD Dissertation, University of California (1969).

23. Chan C K, Min T K, Okrent D: US Nuclear Regulatory Commission, Washington DC, Report NUREG-0259(1977).

24. Chan C K, Min T K, Okrent D: "On Certain Aspects of Alternative Core Disruptive Accidents in LMFBRs", Nucl Eng and Des 51(1979)263-272.

25. Chang Y W: "Application of Containment Codes to LMFBRs in the United States", Nucl Eng and Des 42(1977)53-68.

26. Cho D H, Irvin R O, Wright R W: "Pressure Generation By Molten Fuel Coolant Interaction", Proc Conf on Developements in Reactor Mathematics and Applications: CONF-710302 (idaho Falls,US) (1971).

27. Christensen J A: Thermal Expansion and Change in Volume on Melting for UO_2", Hw-7514B (1962).

28. Clark M(Jr.) and Hansen K P: "Numerical Methods of Reactor Analysis", Academic Press, New YorK, (1964)

29. Crawford R M (1975a): "The Safety Consequences of Local initiating Events in an LMFBR" USAEC Report: ANL-75-73 (1975).

30. Crawford R M (1975b): "Studies in LMFBR Subassembly Boundary Integrity" , USAEC Report ANL-75-27 (1975).

31. Dietrich L W et al. : "Modelling the Response of Fast Reactor Fuel to Hypothetical Accident Transients", Proc Int Mtg Fast Reactor Safety and Related Physics, Chicago, 1976, CONF-761001, US Energy Research and Development Admin

32. Duderstadt J J and Hamilton L J: "Nuclear Reactor Analysis", John Wiley and Sons, New York (1976)

33. Duderstadt J J and Martin W R: "Transport Theory", Wiley Interscience Publication, John Wiley and Sons, New York (1979).

34. Edwards A G and Mather D J: "The Contribution of Bethe-Tait Analysis to the Assessment of Fast Reactor Safety", UK TRG Report 2270(R)1973.

35. Fauske H K : "On the Mechanism of Uranium Dioxide Sodium Explosive Interactions", Nucl Sci Eng, 51(1973)93-101.

36. Fauske H K : "Assessment of Accident Energetics in LMFBR Core Disruptive Accidents", Nucl Eng and Des, 42(1977)19-29.

37. Finneman H: "A Consistent Nodal Method for Analysis of Space Time Effects in Large LWRs", MRR 145, Proc Joint NEACRP/CSNI Specialists meeting on New Developements in Three Dimensional Neutron Kinetics, (1975)145-172

38. Fraser A R and Taylor J B: "Consequences of a Hypothetical Collapse of Fast Reactor Core", UKAEA AWRE Report R44/58 (1958).

39. Frohlich R: "A Theoretical Foundation of Coarse Mesh Variational Techniques", Proc Int Conf on Research Reactor Utilisation and Reactor Mathematics, Mexico, 1(1967)219

40. Furguson D R, Dally D A and Fuller E L: "Improvement of Calculations With Two Dimensional Space Time Kinetics Code FX-2", Am Nucl Soc Proc on Mathematical and Computational Techniques for Analysis of Nuclear Systems, Michigan (1973).

41. Furguson D R and Hansen H F: "Solution of the Space Dependent Reactor Kinetics Equations in Three Dimensions , Nucl Sci Eng 51(1973)189-205.

42. Garland W J, Vlachopoulos J: "A Summation Exponent Analysis of Space Time Dependent Reactor Transients", Trans Am Nucl Soc 18(1974)322.

43. Gear C W: "Numerical Initial Value Problems", in "Ordinary Differential Equations", Academic Press, New York (1971).

44. Gluekler E L, Dayan A, Ways F and Kine T: "Transient Containment Response and Inherent Retention Capability", Nucl Eng and Des 42(1977)151-168.

45. Hancock S L: "Application of Coupled Euler-Lagrange Computer Programs to Structural Response of an LMFBR", Nucl Eng and Des 42(1977)69-74.

46. Henry A F : "Review of Computational Methods for Space Dependent Kinetics", in "Dynamics of Nuclear Systems", University of Arizona Press, Ariz US (1972)

47 Henry A F (1975): "Nuclear Reactor Analysis", MIT Press Cambridge, Mass ,US (1975).

48. Hetrick D: "Dynamics of Nuclear Reactors", University of Chicago Press, Chicago (1972)

49. Hicks E P and Menzies D C: "Theoretical Studies on the Fast Reactor Maximum Accident", Proc Conf on Safety, Fuels and Core Design in Large Fast Power Reactors, CONF-651009 ANL-7120 UC-80-4 (1965).

50. Hirkawa N: "MARS: A Two Dimensional Excursion Code", Atomic Power Development Associates Report APDA-198 (1967).

51. Hummel H H and Okrent D: "Reactivity Coefficients in Large Fast Power Reactors", Published By American Nucl Soc, (1970)

52. Jackson J F and Boudreau J E: Disassembly Energy Release for Mechanical Damage Evaluation", Nucl Eng and Des 42(1977)31-40

53. Jackson J F and Kastenburg W E: "Space-time Effects in Fast Reactor Dynamics", Nucl Sci Eng 42(1970)278-294

54. Jackson J F and Nicholson R B: "VENUS-II an LMFBR Disassembly Program", ANL-7951(1972) LMFBR

55. Jackson J F, Stevensen J F, Marchaterre R H, Avery R H, and

Ott K O: "Trends in LMFBR Hypothetical Accident Analysis", Proc Fast Reactor Safety Mtg, California, (1974)

56. Jagdeep B and Doshi B: "Space Time Dynamics of a Fast Breeder Reactor for Localised disturbances", Nucl Sci Eng 65(1978)106

57. Jankus V Z: "A Modified Equation of State for Hydrodynamic Calculations in AX-1 Numerical Program", Proc Conf on Safety, Fuels and Core Design in Large Fast Power Reactors, CONF-651009 ANL-7120 (1965)

58. Jankus V Z and Weeks R W: "LIFE-II a Computer Analysis of Fast Reactor Fuel Element Behavior As a Function of operating History", Nucl Eng and Des, 18(1972)83-96

59 Kaplan S: "Synthesis Methods in Reactor Analysis", Advances in Nuclear Science and Technology, Ed.: P R Greebler, Vol-III, Academic Press, New York (1966)

60. Kessler G: "Space-dependent Dynamic Behaviour of the Fast Reactors Using Time Discontinuous Synthesis Method", Nucl Sci Eng, 41(1970)115-148

61. Kidman R B : "Cross-section Structure Factors Inter- polation Scheme", HEDL-TME-71-40(1971)

62. Kidman R B: "An Improved F-factor Interpolation Scheme for 1DX", Trans Am Nucl Soc 18(1974)156-157

63. Kidman R B, Schenter R E, Hardie R W: "The Shielding Factor Method of Generating Multigroup Cross Sections for Fast Reactor Analysis" , Nucl Sci Eng, 48(1972)189

64. Kirbiyik M et al: "Hydrodynamics of Post Disassembly Fuel Expansion", Nucl Eng and Des 35(1975)441-460

65. Kramer J M: "Modelling of Fast Reactor Cladding Failure for Hypothetical Accident Transient Analysis", Trans 5th Conf on

Structural Mechanichs in Reactor Technology, Berlin (1979)

66. Kuczera B and Royl P: "Application of Different Criteria in Fuel Pin Melting and Consequences for Over Power Transients in LMFBRs", Trans 3rd Int Conf on Structural Mechanics in Reactor Technology , Vol I(1975)

67. Kuzay T M et al: "Thermo-hydraulic and Thermal Stress Aspects of Porous Blockages in an LMFBR Fuel Assembly", Paper D7/4, Vol D, Trans 5th Int Conf on Structural Mechanics in Reactor Technology, Berlin (1979)

68. Lee J C and Pigford T H: "Explosive Disassembly of Fast Reactors", Nucl Sci Eng, 48(1972)28-44

69. Lee J C: "Explosive Disassembly of Fast Spectrum Nuclear Reactors", PhD Thesis, University of California (1969)

70. Lewis E E: "Nuclear Power Reactor Safety", John Wiley and Sons New York (1978)

71. Little W W and Hardie R W: "Methods for Collapsing Fast Reactor Cross Sections", Nucl Sci Eng, 29(1967)402-407

72. Lorenzini P G and Flangan G F: "Evaluation of Fuel Coolant Interactions During Disassembly of an LMFBR", Proc Conf on New Developements in Reactor Mathematics and Applications, CONF-710302 ,Idaho (1971)

73. Malvern L E: "Introduction to the Mechanics of a Continuous Medium", Prentice-Hall New Jersey, (1969)

74. Marchaterre J F: "Overview of Core Disruptive Accidents", Nucl Sci Eng, 42(1977)11-17

75. Marchaterre J F, Marciniak T, Bratis J, Fauske H: "Work Energy Characterization for Core Disruptive Accidents", Proc Int Mtg on Fast Reactor Safety and Related Physics, Chicago, (1976)

76. MacFarlane D R and Brittan R O (1966): "Transient Sodium Boiling Calculations", Nucl Eng and Des 4(1966)360-374

77. MacFarlane D R and Brittan R O (1967): "Transient Sodium Boiling Calculations", Nucl Eng and Des 6(1967)103-114

78. MacFarlane D R, McNeal N A, Meneley D A, Sananthan C K: "Sodium Boiling Transients in Oxide Fueled Fast Reactors", Nucl Eng and Des, 7(1968)411-426

79. McCarthy W J (Jr) and Okrent D: "Fast Reactor Kinetics", in "The Technology of Nuclear Reactor Safety", Vol 1, Ed. TJ Thompson and JG Beckerely, MIT Press, Cambridge Mass (1964)

80. McCarthy W J, Nicholson R B, Okrent D, Jankus V Z: "Studies of Nuclear Accidents in Fast Reactors", Proc 2nd UN Int Conf 'Peacful Uses Atomic Energy", Geneva , 12(1958)207

81. Marr W W, Wang P Y, Misra B, Padilla A, Crawford R M: "Analytical Investigation of Certain Aspects of LMFBR Subassembly Failure Propagation" , USAEC Report ANL-76-19 (1976)

82. Mathew J R: "Bridging the Gap Between Whole Core Accident and Fuel Behaviour", Trans 5th Conf on Structural Mechanics in Reactor Tech., Berlin, (1979)

83. Meneley D A, Leaf G K, Lindmann A J, Dally T A and Sha W T: "A Kinetic Model for Fast Reactor Analysis in Two Dimensions", Proc Symp on Dynamics of Nuclear Systems, University of Arizona, March(1970)

84. Menzies D C: " The Equation of State of Uranium Dioxide at High Temperatures and Pressures", UKAEA TRG Report 1119(d)(1966)

85. Meyer R A, Wolf B, Friedman N F, Siefert R: "Fast Reactor Meltdown Accidents Using Bethe-Tait Analysis", USAEC Report GEAP-4809(1967)

86. Mitchell B: "A Users Manual for DEFILE: a Code to Generate Multigroup Cross Sections in a Variety of Formats and Group Structures" Private Communication

87. Morewitz H A: "Experiments on Sodium Fires and Their aerosols", Nucl Eng andDes 42(1977)123-135

88. Nakamura S: "A Variational Rebalancing Method for Linear Iterative Solution of Neutron Diffusion Equation", Nucl Sci Eng, 39(1970)278. " A Method for the Numerical Calculation of Hydrodynamic Shocks",

89. Neumann J J and Ritchmeyer R D: J Applied Physics, 21(1950)232

90. Nicholson R B: "Methods for Determining the Energy Release in Hypothetical Reactor Meltdown Accidents", Nucl Sci Eng, 18(1964)207

91. Nicholson R B and Jackson V F: "A Sensitivity Study for Fast Reactor Disassembly Calculations", USAEC Report ANL-7952(1974)

92. O"Dell L D and Walter T H: " Effect of Distributed Voids in LMFBR Core Disassembly Calculations", Trans Am Nucl Soc 15(1)(1972)358

93. Okrent D, Cook J M, Stakus D: "AX-1 a Computing Program for Coupled Neutronics Hydrodynamics Calculations on IBM-704, USAEC Report ANL-5977(1959)

94 Ostensen R W, Henniger R J and Jackson J F: "The Transition Phase in LMFBR Hypothetical Accident", Proc Conf on Fast Reactor Safety and Related Physics, Chicago (1976)

95. Ott K O and Madell J H: "Quasi-Static Treatment of Spatial Phenomena in Reactor Dynamics", Nucl Sci Eng, 26(1966)563-565

96. Ott K O and Meneley D A: "Accuracy of Quasi-Static Treatment of Spatial Reactor Kinetics", Nucl Sci Eng, 36,(1969)402-411

97. Peaceman D W and Rachford H H(Jr.) : "The Numerical Solution of Parabolic and Elliptic Differential Equations", J Soc Indst Appl Math , 3(1955)42-65

98. Peak R D et all: "Response of Liquid Metal Fast Breeder Reactor Containment to a Hypothetical Core Meltdown Accident", Nucl Eng and Des 42(1977)169-180

99. Peckover R S: "The Use of Core Catchers in Fast Reactors", Paper 33, Proc Int Meeting on Reactor Heat Transfer, Karlsruhe , (Oct1973)

100 Pizzica P A and Abramson P B: "EPIC: a Computer Program for Fuel Coolant Interaction", Proc Int Conf on Fast Reactor Safety and Related Physics, Chicago (1976)

101 Rand M H: " The Application of Thermodynamics to Nuclear Fuels", Paper IAEA-SM-190/4, Proc Symp on the Thermodynamics of Nuclear Materials, Vienna (1974)

102 Ritchmeyer R D and Morton K W: " Difference Methods for Initial Value Problems", Intersience Publishers, New York (1967)

103 Schenter R E and Baker J L: "ETOX, a Code to Calculate Group Constants for Nuclear Reactor Calculations", USAEC Report BNWL-1002 (ENDF-127) UC-80 Physics (1969)

104 Schmuck P, Jacobs G, Arnecke G: "KADIS: a Computer Program for Analysis of the Disassembly Phase in Hypo- thetical Accidents in Liquid Metal Fast Breeder Reactors", UKAEA Risley Translation 3371(1978) From German Report: KFK-2497, Kernforshungszentrum, Karlsruhe (1973)

105 Seaborg G T: Proc IAEA Symp on the Enviromental Aspects of Nuclear Power Stations, (New York), (1970)

106 Segev M: "A Brief Summary of a Theory of Self Shielding", Trans Am Nucl Soc, 18(1974)18

107 Sha W T and Walter A E: "An Integrated Model for Analyzing Disruptive Accidents in Fast Reactors", Nucl Sci Eng, 44(1971)135

108 Sha W T , Lindmann A J , Meneley D A , Dally T A , Fuller L L, Leaf G A: "Two-dimensional Fast Reactor Disassembly With Space Time Kinetics", Proc Conf on New Developements in Reactor Maths and Applications, CONF-710302 (Idaho Falls), (1971)

109 Sha W T and Hughs T H: "VENUS, a Two Dimensional Coupled Neutronics Hydrodynamics Computer Program for Fast Reactor Power Excursions", USAEC Report ANL-7701 (1971) Mathematics and Computers.

110 Shapiro H L: "Pekin Man" , Simon and Schuster, New York (1974).

111 Skidmore I C and Morris E: " Experimental Equation of State for Uranium and its Interpretation in the Critical Region", Proc IAEA Symp on " Thermodynamics of Nuclear Materials", Vienna (1962)

112 Smith L L, Ferguson D R, Cahalan J E: "Time Dependent Reactor Physics in the FFTF Unprotected Loss of Flow Accident", in "Advanced Reactors: Physics, Design and Economics", Pergamon Press, Oxford (1975)

113 Soran P D and Dduziak D J: "Bondarenko Formalism Applied to Theta Pinch Reactor Nucleonics", Trans Am Nucl Soc 19(1974)

114 Spurgeon M K et al (The Nuclear Policy Study Group); "Nuclear Power Issues and Choices", Ballinger Pubishing Co, Cambridge, Massachusttes, (1977)

115 Stacey W M (1968): " A Variational Multichannel Space Time Synthesis Method For Separable Reactor Transients", Nucl Sci Eng, 34(1968)45

116 Stacey W M (1971a): " A Review of Spatial and Spectral Flux Synthesis Methods", Trans Am Nucl soc, 14(1971)

117 Stacey W M (Jr.)(1971b): " Treatment of Wide Scattering Resonances in Defining Elastic Removal Cross Sections in the Bondarenko Scheme", Trans Am Nucl Soc, 14(1971)838

118 Stacey W M (1972): "Variational Estimates of Reactivity Worths and Reaction Ratios in Critical Nuclear Reactors", Nucl Sc Eng 48(1972)444

119 Teague H J and Mather D J: " Factors Limiting Prompt Critical Excursions in Irradiated Fast Reactors", Nucl Safety, 14(1973)201-205

120 Teague T J: "Safety of Fast Reactors", In "Nuclear Sci and Tech: Vol-12 ,Ed. Farmer F R, Academic Press, New York (1977)

121 Varga R S: "Matrix Iterative Analysis", Prentice-Hall Publishers, Englewood Cliffs, New Jersey (1962)

122 Wachspress E L, Burgess R D, Baron S: "Multichannel Flux Synthesis", Nucl Sci Eng 12(1962)381.

123 Wallace B and Dobzhansky T: "Radiation, Genes and Man", Henry Holt and Co, London (1960)

124 Walter A E and Padilla A (Jr.): " Mathematical and Computational Techniques Employed in The Deterministic Approach to Liquid Metal Fast Breeder Reactor Safety", Nucl Sci Eng, 64(1977)418-451

125 Walter et al: MELT-III : "A Neutronics Thermal Hydraulics Computer Program for Fast Reactor Safety Analysis", USAEC Report HEDL-TME 74-47 (1974)

126 Weber D P and Ganapol B D: "Multi-field Hydrodynamic Disassembly Calculations With Space Time Kinetics : FX2/VENUS III", Proc Int

Conf on Fast Reactor Safety and Related Physics, CONF-761001 (1976)

127 Werner W: "Solution Methods for Space Time Dependent Neutron Diffusion Equation ", in "Advances in Nuclear Systems and Tech, Vol 10, Ed. Henelley EJ, Lewins J and Becker M, Plenum Press, New York (1977)

128 Wight A L, Hansen K F, Ferguson D R: " Application of Alternating-Direction Implicit Methods to Space Dependent Kinetics Equation", Nucl Sci Eng, 44(1971)239

129 Williams D C: "A Critique of the Board-Hall Model for Thermal Detonation in UO -Na System", Proc Int Conf on Fast Reactor Safety and Related Physics, CONF-761001, US Energy Research and Dev Admin (1977)

130 Williams R: " The Nuclear Power Decisions", Croom Hill , London (1980).

131 Yasinsky J B (1967): "The Solution of Space Time Neutron Group Equations by the Time Discontinuous Synthesis Method", Nucl Sci Eng 29(1967)381

132 Yasinsky J B (1968): " Numerical Studies of Combined Space Time Synthesis", Nucl Sci Eng, 34(1968)158-168

133 Yasinsky J B and Henry A F (1965): "Some Numerical Experiments Concerning Space Time Reactor Kinetics Behaviour", Nucl Sci Eng 22(1965)171-181

134 Yasinsky J B and Kaplan S (1967): "Synthesis of Three Dimensional Flux Shapes Using Discontinuous Sets of Trial Functions", Nucl Sci Eng, 28(1967)426-440

135 Zeuch W R: "Sodium Spillage in Large LMFBRs Resulting from Impact on the reactor Cover", Nucl Eng and Des, 55(1979)207-218

APPENDIX-A

THERMODYNAMIC PROPERTIES OF MATERIALS

A.1 FUEL:

The internal energy density of the fuel in cell(j,k) is given by:

$$E = U^n_{jk} \; / \; \rho_f \; F_f$$

where

$$U^n_{jk} = U^{n-1}_{jk} \; V^{n-1}_{jk} / \; V^n_{jk} + \delta Q^n$$

and where δQ^n is the increment in the internal energy density during the n^{th} time interval.

During the melting transition, the fuel temperature fuel is given by:

$$T_f = T_{sol} + \frac{(T_{liq} - T_{sol})}{(E_{liq} - E_{sol})} (E - E_{sol})$$

where

$$E_{sol} = 10^{-3}(T_{sol} - 273.)\; C_{pf} \qquad (kJ/g)$$

$$E_{liq} = E_{sol} + 10^{-3} \{(T_{liq} - T_{sol})\; C_{pf} + H_f\} \qquad (kJ/g)$$

Outside the melting transition range, the temperature is given by:

$$T_f = \begin{cases} \text{Max } (T_1, T_2) & V_r < 0.6 \\ \text{Max } \{T_1 \text{ , Min } (T_2, T_3)\} & V_r > 0.6 \end{cases}$$

where

$$T_1 = 273. + E / C_{pf}$$

$$T_2 = (4272.5 - 1003\ V_r + 1699\ V_r^2) \\ *(E - 0.237 - 1.882\ V_r)$$

$$T_3 = (4272.5 - 1003 * 0.6 + 1699 * 0.6^2) \\ *(E - 0.237 - 1.882 * 0.6)$$

The saturated vapour pressure is given by:

$$P_v = \exp(69.979 - \frac{76800}{T_f} - 4.34\ T_f)$$

In the liquid phase state, the pressure is estimated from:

$$P_l = \begin{cases} P_{11} & V_r < 1 \\ P_{12} & V_r > 1 \end{cases}$$

where

$$P_{11} = (E_l - 3.59 + 0.119\ V_r + 0.7767 / V_r^2) \\ * 1.554\ 10^{12} \exp(-9.67\ V_r + 4.45\ V_r^2)$$

$$P_{12} = 10^{10\ \frac{(E_l - 3.2213 - 0.173\ V_r)}{(1.9\ V_r - 0.704)}}$$

where the modified energy density E_l is defined as follows:

$$E_l = \begin{cases} E & E < E_{sol} \\ E - 0.001\, H_f \dfrac{(E - E_{sol})}{(E_{liq} - E_{sol})} & E_{sol} < E < E_{liq} \\ E - 0.001\, H_f & E > E_{liq} \end{cases}$$

The density of the liquid fuel is given by the relationship:

$$\rho_f = \begin{cases} 11.2892 - 5.1013\ 10^{-4}\ T_f & T_f < T_m \\ 11.2892 - 5.1013\ 10^{-4}\ T_f - 0.36223\ (T_f - T_m) & T_m < T_f < T_m + 1. \\ 10.9277 + 1.7169\ 10^{-4}\ T_m - 6.8182\ 10^{-4}\ T_f & T_f > T_m + 1. \end{cases}$$

A.2 SODIUM:

The vapour pressure of sodium is given by the relationship:

$$P_s(T_s) = T_s^{-0.61334} \exp\ (15.3838 - 12767.8/T_s)\ 10^6$$

The specific heat of sodium by

$$C_{ps} = 1.6298 - 8.334\ 10^{-4}\ T_s + 4.62729\ 10^{-7}\ T_s^2 \quad (J/gK)$$

The thermal coefficient of expansion of liquid sodium is calculated by the relation:

$$a_s = 0.21968\ 10^{-3} + 0.81226\ 10^{-7}\ T_s + 0.97135\ 10^{-11}\ T_s^2 + 0.68998\ 10^{-15}\ T_s^3$$

The compressibility of sodium and steel is estimated by assuming the following values of β_o and β_l

for sodium:

$$(\beta_o)_s = (74.77 - 0.0505\ T_s + 9.707\ 10^{-6}\ T_s^2)\ 10^9$$

and

$$(\beta_1)_s = 3.59$$

A.3 STAINLESS STEEL:

$$(\beta_o)_{ss} = (507.77 + 4.3\ T_{ss} - 5.53\ 10^{-3}\ T_{ss}^2)\ 10^9$$

and

$$(\beta_1)_{ss} = 5.0$$